# High-power Terahertz Pulse Generation and Nonlinear Terahertz Carrier Dynamics in Semiconductors

by

Ayesheshim Kebie Ayesheshim

A thesis submitted in partial fulfillment of the requirements for the degree of

Doctor of Philosophy

Department of Physics

University of Alberta

# Abstract

This thesis describes the generation, characterization, and nonlinear application of intense terahertz (THz) pulses. Nonlinear THz spectroscopy has emerged as a powerful tool to study the ultrafast time evolution of high-field charge carrier dynamics in semiconductors and nano-materials. The study of such phenomena in semiconductors and semiconductor structures requires intense THz pulses with high electric-field strengths.

We have developed an improved experimental setup for generating high-power, near-single-cycle THz pulses by tilted-pulse-front optical rectification in $LiNbO_3$ with optimized optical-to-THz conversion efficiency, and proper characterization of the THz pulses in the Ultrafast Nanotools lab at the University of Alberta. We have investigated the effects of optical pump pulse pre-chirping and polarization on THz pulse generation using separate compressors for the optical pulses used for THz generation and detection. By down-chirping the 800 nm optical pump pulses to 385 fs, single-cycle THz pulses with energies up to 3.6 $\mu$J were obtained, corresponding to an energy conversion efficiency of $3 \times 10^{-3}$. This high-field THz source is capable of generating electric fields greater than which can induce nonlinear carrier dynamics in semiconductors.

We demonstrate novel high-field THz experiments that explore nonlinear processes in doped and photo-excited bulk semiconductors. As a benchmark and consistency check, a nonlinear THz absorption bleaching Z-scan experiment was conducted on an n-doped InGaAs epilayer on a lattice matched InP substrate. This experiment confirmed that the THz pulses generated by our source are adequate for ultrafast nonlinear measurements in

the THz frequency range. Even more interesting, we have achieved unprecedented THz field absorption bleaching simply by flipping the face of the sample illuminated by the THz pulse pump. That is, we illuminate the insulating (substrate) side of the sample with the THz pulse in the Z-scan experiment rather than illuminating the usual (conducting) face of the sample. In this study considerable insight has been gained into developing an optical diode.

We have also developed a technique to measure transient voltage pulses induced in doped and photoexcited semiconductors due to a shift current generated from the nonlinear THz dynamics of free electrons in the conduction band. This is a fascinating feature with a practical application as an ultrafast and ultra-sensitive THz phtotodetector. A Drude-based dynamic intervalley scattering simulation reveals that the nonlinear THz-induced transient voltage pulses are a result of intervalley scattering driven by high-field THz pulses. It is the first time that THz induced picosecond voltage transients are measured in semiconductors. We find that an intense THz pulse incident on an InGaAs sample excites a transient dipole due to intervalley scattering. Also, THz pulse induced transient voltage signals have been investigated in ZnTe, and doped-Si semiconductors due to a direct flow of free carriers upon THz photon absorption. We have observed nonlinear conductivity responses in Si, ZnTe, photo-excited SI-GaAs, and doped InGaAs, showing the strong THz pulse can heat the electron population and create a momentum distribution leading to saturable absorption in the THz frequency range.

*To my son Emmanuel*

# Acknowledgments

My graduate work at the University of Alberta would not have been a success without the help of many people in various ways throughout my PhD program. First and foremost I am extremely indebted to my thesis supervisor Prof. Frank A. Hegmann for the trust and freedom he gave me to conduct the experiment unconditionally. He always brought a whole new level of imagination to address many of the questions that I encountered throughout my experiments. All the support, advice, critiques, and his ability to understand new ideas quickly will always be an inspiration and motivation to me. His patience and understanding when things were not going well took me to the next stage.

I am very fortunate to know and work with Prof. Richard D. Sydora. I thank him for his kind words of encouragement, valuable discussions, and his financial support for one semester during the last year of my program. He diligently read many of the chapters of this thesis and graciously provided me with in-depth critiques and excellent suggestions for improvement throughout. Thank you so much!

I would like to thank Dr. Fuhai Su for his immense contribution to establish the high-power terahertz experimental setup and to conduct ultrafast nonlinear THz experiments during the early stage of my program while he was a post-doc in the Ultrafast Spectroscopy Lab. Without him a significant portion of the results reported in this thesis would not have been possible.

I always enjoyed the time spent with my friend and colleague Dr. Tyler Cocker. We had valuable discussions and fruitful critiques in our day-to-day interaction while working in the Lab and during the time we spent for lunch and beer, and at conferences. Tyler is an all-round talented physicist who understands new ideas quickly. He definitely has a bright future ahead. There were very enjoyable moments at the OTST 2013 in Kyoto, Japan, despite sleeping at the Karaoke after having sake.

My special thanks to David Purschke, who managed to make time to read the rough draft of most of this thesis chapters and made many useful comments and recommendations.

I am very grateful to my best friend Messele Fetabil who stood firm to save me through

the tough times that I encountered in all directions during my program. All his advice, support, and the countless times we spent on phone conversations with no boundaries are unforgotten for years to come. He is a true friend with great personality.

It is a pleasure to acknowledge all the present and former members of the Hegmann lab, especially, Dr. Lyubov Titova, Dr. Zhenyou Wang, J. R. Hoffman, Dr. Amin Kabir, Glenda De Los Reyes, Vedran Jelic, and David Purschke for helpful discussion on many topics. Also, I want to thank Dr. Lyubov Titova for developing the LabView data acquisition software that I have been using during my experiments. To all the present Hegmann group (by seniority: Glenda De Los Reyes, Vedran Jelic, David Purschke, Peter Nguyen, Ketty Na, and Haille Sharum) I wish great success in their work.

It has been a privilege collaborating with people at the Advanced Laser Light Source (ALLS) at the Varennes campus of INRS-EMT in Canada, especially Prof. Tsuneyuki Ozaki, Dr. Luca Razzari, Dr. Francois Blanchard. Also, Prof. Olga Kovalchuk at the University of Lethbridge.

I would like to thank the great condensed matter technical staff, especially Don Mullin, Tony Walford, Greg Popowich, and Gilbert Lachat for their unreserved technical support whenever I needed their assistance during my graduate program.

Also, I would like to thank the administrative staff of the physics department office especially, Sarah Derr, Sandra Hamilton, and Linda Jacklin.

I would like to thank M. Reid (University of Northern British Columbia, Canada) for providing the infrared camera used for the THz spot measurements.

I am very grateful for all the great friends who shared their lives while this thesis was being completed, Amsalu Yigzaw, Azamed Gezahegn, Wubshet Mekonen, Tizazu Habtie, Desalegn Abera, and Tezera Firew.

Finally, I would like to thank my wife Tadela and my son Emmanuel. Emmanuel did his part by giving his big smile and love while I spent time with him and helped me always to think positive to see the better tomorrow.

# Contents

# List of Tables

# List of Figures

xxi

# CHAPTER 1

## Introduction

The interaction of electromagnetic (EM) radiation with matter has provided an extremely effective and powerful tool for controlling the behavior of condensed materials in all of its phases. This helps to probe and understand the electronic and vibrational states of a wide variety of materials. Each region of the EM spectrum interacts with different degrees of freedom of matter and specific spectral ranges have been made accessible through the advent of suitable sources and detectors. For example, optical radiation predominately interacts with valence electrons, however, whereas THz radiation interacts strongly with many elementary excitations in the meV range [Jepsen et al. (2011); Kampfrath et al. (2013)] within a picosecond time scale.

Since the realization of the first coherent broadband THz sources in the 1980's at Bell Labs, (New Jersey), USA based on the free-space photoconductive switch (or Auston switch) [Auston (1975); Auston and Cheung (1985); Cheung and Auston (1985)] and phonon-polaritons in $LiTaO_3$ [Auston et al. (1984)], major scientific advancements have been made. This includes THz pulse generation, detection, time-domain THz spectroscopy, time-resolved THz spectroscopy and THz imaging which has revolutionized the field of THz optics, leading to enormous advances in both fundamental physics and a wide range of practical applications. THz waves have been widely used as a noncontact probe of material properties with high sensitivity [Jepsen et al. (2011)]. In particular, as a probe of charge carrier dynamics in semiconductors originates from the fact that the dielectric response of charge carriers is strong and dispersive in the THz region of the electromagnetic spectrum [Ulbricht et al. (2011)]. Terahertz time-domain spectroscopy (THz-TDS) and time-resolved terahertz spectroscopy (TRTS) have been the most utilized ultrafast optical techniques to determine the broadband complex conductivities in steady-state and transient systems, respectively. TRTS has also been used to explore ultrafast carrier dynamics in materials.
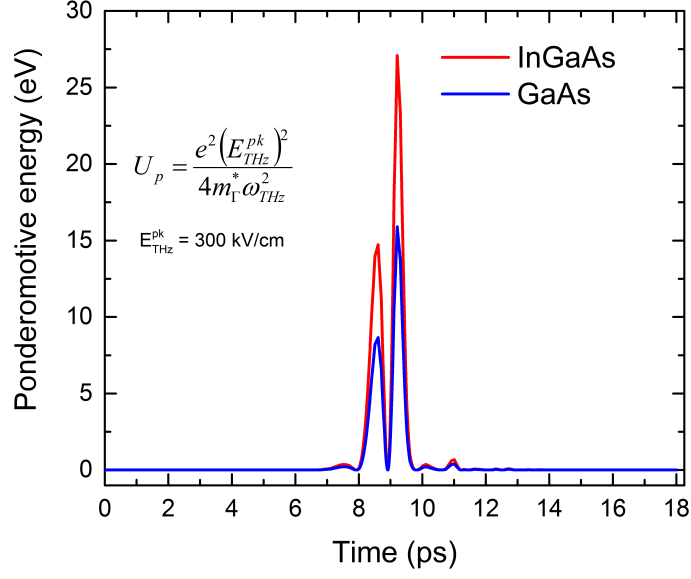
Figure 1.1: Ponderomotive energy induced by THz pulses at an electric field strength of 300 kV/cm. At the peak field, the ponderomotive energy is larger than the band gap of the host materials.

THz radiation is in the frequency range between the upper limit accessible with electronics and the lower limit that can be accessed by optics. Roughly speaking the THz range covers 0.1-10 THz (1 THz = $10^{12}$ Hz) or equivalently the wavelength range from 3 mm - 30 $\mu$m or photon energy scale of 0.4 - 40 meV. A frequency of 1 THz is equivalent to a wavelength of 300 $\mu$m, or a photon energy of 4.1 meV. It is evident that the photon energy in the THz frequency range is below the typical band gap energy of semiconductors (1-3 eV). However, when a high peak field THz pulse is incident on matter, its oscillating field can deposit several times the THz photon energy. It is defined as the average oscillation energy that is acquired by free electron in the radiation field of the incident laser pulse. The work done on a charge carrier with effective mass $m^*$ by a THz field with frequency $\omega_{THz}$, peak amplitude $\mathbf{E}_{THz}^{pk}$ can be estimated by the ponderomotive energy [Turchinovich et al. (2012); Kampfrath et al. (2013)].

$$W_p = \frac{e^2 \left(E_{THz}^{pk}\right)^2}{4m^*\omega_{THz}^2} \tag{1.1}$$

As shown from Eq. 1.1, the ponderomotive energy depends on the square of the wavelength
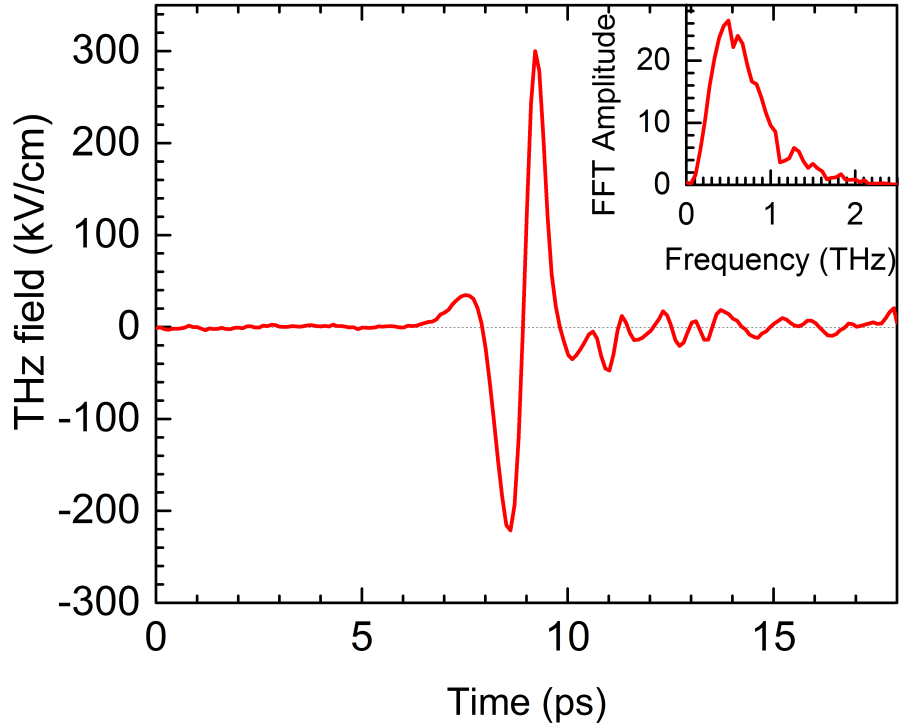
Figure 1.2: Time domain waveform of a high-power terahertz pulse with a peak electric field of 300 kV/cm radiated from a tilted-pulse-front LiNbO₃ optical rectification source and measured by electro-optic sampling using 0.5 mm thick ZnTe crystal. The inset shows the corresponding amplitude spectrum.

and is linearly dependent on the laser field intensity. An example of a ponderomotive energy calculated for both InGaAs and GaAs semiconductors at an incident THz field strength of 300 kV/cm is shown in Fig. 1.1

The transform-limited temporal shape of a typical THz pulse attained from optical rectification sources used for spectroscopy is an approximately single cycle electromagnetic transient with a pulse duration of about 1 ps. The corresponding pulse spectrum is centered near 1 THz with a bandwidth of 1 THz, hence the name "terahertz pulse". An experimentally measured high-power single cycle ultrashort THz pulse generated from a tilted-pulse-front LiNbO₃ optical rectification source is displayed in Fig. 1.2. As shown in the inset of Fig. 1.2, the THz pulse spectrum has a peak of about 0.5 THz and a bandwidth of 0.7 THz. The spectral bandwidth depends on the source crystal as well as the detection system in general.

3

The THz spectrum covers a wide range of fundamental elementary excitations and resonances in solid state materials and molecules. Therefore, the broad spectrum of a THz pulse is a vital spectroscopic tool that provides access to fundamental modes of many physical phenomenon, including free carrier absorption, low energy excitations, and optically active vibrational modes, and collective modes in condensed matter such as phonons, plasma, magnons [Ulbricht et al. (2011); Averitt and Taylor (2002); Kampfrath et al. (2013)]. Typical optically-active vibrational modes lie below 5 THz; however, there are many vibrational modes and low energy excitations above 5 THz. We are generally limited to the 0.2 - 3 THz range because of the sources and detectors we have been using, and the fact that they tend to have vibrational modes above 3 THz. Also, the photon energies of the THz spectrum do not create direct one-photon generation of free carriers in semiconductors due to the THz photon energy being much smaller than the energy gap of typical semiconductors. Hence, THz pulses are an ideal tool for a contact-free probe of materials.

Terahertz optics and technology has sparked an increasingly wide range of scientific applications across many disciplines and brought an almost immeasurable number of breakthroughs. Our Lab has been the source of recent breakthroughs on the topics of ultrafast phenomena in semiconductors, nanoparticles, and DNA damage. One of the greatest strengths of THz spectroscopy and the THz field as a whole, is the ability to generate and coherently detect near single-cycle pulses, enabling the characterization of ultrafast phenomena in semiconductors and nanomaterials on the picosecond time scale. Examples of recent major THz scientific research advancements in our lab include: (1) Ultrafast picosecond voltage transients have been measured in doped and photo-excited semiconductors without applying an external bias for the first time [1]. (2) The invention of THz-coupled STM imaging has enabled direct measurements of the ultrafast excitation and decay of a single nanoparticle with unprecedented simultaneous temporal ($< 0.5$ ps ) and spatial (2 nm) resolutions [Cocker et al. (2013)]. (3) The biological effects of high-power pulsed THz radiation on artificial human skin tissues has been shown for the first time. We have investigated the biological effects of intense pulsed THz radiation on artificial human skin tissues. Exposure of artificial human skin tissue to intense THz pulses for ten minutes was shown to lead to a significant induction of H2AX phosphorylation, indicating that THz pulse irradiation may cause DNA damage in exposed skin tissue. At the same time, we find a THz-pulse-induced increase in the levels of several proteins responsible for cell-cycle regulation and tumor suppression, suggesting that DNA damage repair mechanisms are quickly activated [Titova et al. (2013)]. Furthermore, the intense THz pulses affect expression levels of numerous genes associated with non-melanoma skin cancers, psoriasis, and atopic dermatitis [Titova et al. (2013)]. Our laboratory is also home to time-resolved THz spectroscopy research in a

---

[1]Two papers of ultrafast picosecond voltage transient in doped and photoexcited semiconductors are under preparation to be submitted to PRB

number of novel materials, covering phenomena ranging from ultrafast carrier dynamics in semiconductor nanostructures to insulator-metal phase transitions [Cocker et al. (2012)].

The future exploration of nonlinear THz dynamics in materials demands an efficient, accessible, table-top high power and high intensity THz source. This requires improvements to the usual, low-power optical rectification techniques used for spectroscopy. Recently, advances in intense table top terahertz sources and broadband detection techniques have opened up a new phase of fundamental nonlinear terahertz research of materials to gain deep insight into ultrafast nonlinear phenomena for the next generation semiconductor-based nanoscale electronic devices.

In this thesis, detailed characterization of an improved scheme for high power THz pulse generation using tilted-pulse-front methods are presented. In addition, four main experiments conducted at room temperature utilizing this high-THz-power source have revealed novel ultrafast nonlinear responses under THz excitation.

This thesis is organized as follows: Chapter 2 presents an overview of the basic techniques of the most common table-top THz radiation sources and detectors based on femtosecond laser techniques. In Chapter 3 a brief introduction to the characteristic features of ultrafast nonlinear optics and mechanisms of nonlinear dynamics in the terahertz range are discussed. Chapter 4 is devoted to the presentation of a self-consistent theoretical model, that is the Drude dynamic intervalley scattering model, for hot carrier transport in semiconductors. In Chapter 5, I will present the principles and a brief discussion of optical diffraction by gratings followed by technical details of a novel experimental scheme of high power THz pulse generation using tilted-optical pulse-front through optical rectification in $LiNbO_3$. For the rest of the chapters, we employed intense THz pulses to study the current frontier in the THz technology which is the ultrafast nonlinear THz carrier dynamics in semiconductors, typically the two most technologically-important semiconductors, GaAs and InGaAs. A brief introduction of THz nonlinear optics and novel experimental demonstrates an optical diode by utilizing the intense THz field attained from the high THz power setup are the subjects of Chapter 6. The rest of two chapters are devoted to an experimental and theoretical investigation of THz-pulse-induced picosecond voltage transients in semiconductors, which is the first time such an effect has been observed. Chapter 7 presents novel experimental results of the nonlinear THz induced transient voltage and THz photo-detectors in model semiconductors like InGaAs and GaAs. Chapter 8 presents ultrafast THz induced transient voltages in photoexcited SI-GaAs. Chapter 9 summarizes all the experimental works conducted in this thesis and highlights possible future experiments on "nonlinear THz rectification" in semiconductors.

# CHAPTER 2

## Generation and detection of terahertz radiation

## 2.1 Introduction

Until recently, the THz spectral range remained relatively unexplored due to the lack of suitable sources and detectors at THz frequencies compared with the well established neighboring spectral bands in the microwave and infrared/visible regions. Optical generation of THz radiation is obtained by either ultrafast photoconductive switches (generation of transient photocurrents in semiconductors) or nonlinear optical responses in electro-optic crystals.

Optical methods of THz pulse generation and detection are based on the fundamental principle of electromagnetic radiation from accelerated charges, from an oscillating dipole, $\mathbf{P}(t)$ or time varying current, $\mathbf{J}(t)$. Detailed methods regarding the THz generation, detection, and the principles and achievements of THz spectroscopy, are given in a number of THz reviews and books [Jepsen et al. (2011); Ulbricht et al. (2011); Mittleman (2003); Yun-Shik (2009); Dexheimer (2008)].

## 2.2 Generation of THz radiation

Over the past two decades, ultrashort laser pulses, in conjunction with transient current sources and electro-optic (EO) crystals capable of optical rectification (OR) have become the most versatile and widely used table-top THz generation techniques. This section focuses on the discussion of the most common THz sources, photoconductive switches and OR sources. Illuminating a photoconductive switch with a femtosecond laser pulse induces a

transient electric current that emits THz radiation in the far field [Auston and Smith (1983); Auston et al. (1984); You et al. (1993); Budiarto et al. (1996); Zhao et al. (2002)]. The generated THz field is directly proportional to the first derivative of the transient current, $E_{THz} \propto \frac{\partial \mathbf{J}}{\partial t}$. Conversely, a THz pulse obtained using OR is generated by a second-order, nonlinear transient polarization induced by the mixing of difference frequency components of the pump pulse inside the EO crystal [Hu et al. (1990); Xu et al. (1992)]. The emitted THz field is directly proportional to the second-order derivative of the nonlinear polarization of the material, $E_{THz} \propto \frac{\partial^2 \mathbf{P}}{\partial t^2}$.

OR has several advantages over transient current sources by providing much broader THz spectra [Huber et al. (2000); Stepanov et al. (2003)], required no external bias, and being simpler to implement experimentally. On the other hand, unlike electro-optic crystals, photoconductive switches do not depend on crystal orientation [Reimann (2007)], nor are they strongly influenced by the polarization of the optical pump beam.

In addition to the two common table-top approaches to THz generation discussed above, air-plasmas produced by femtosecond laser pulses have recently emerged as alternative sources of THz radiation [Cook and Hochstrasser (2000); Kress et al. (2004); Bartel et al. (2005); Xie et al. (2006); Kim et al. (2007); Karpowicz et al. (2008); Dai et al. (2009); Klarskov et al. (2013)]. A formal introduction to the general concept and working principles of OR, photoconductive sources, and air plasma generation are provided in the following sections.

### 2.2.1   THz pulse generation by photoconductive switch

Photoconductive switches based on semi-insulating semiconductor substrates have been used to generate and coherently detect THz electromagnetic radiation. THz pulses can be radiated from accelerated photocarriers generated upon illuminating the surface of a biased semi-insulating (SI) semiconductor surface with femtosecond optical pulses. The accelerated photocarriers induce a transient current that in turn emits transient THz radiation into free space.

Photoconductive switches based on semiconductors with high carrier mobility generally achieve the best THz generation efficiency. Materials with high breakdown fields are also advantageous because they allow large voltage biases to be applied, which is directly proportional to the generated THz pulse energy. Meanwhile, laser pulses with short pulse duration enable photocurrent switching on the subpicosecond time scale. Hence, direct band-gap semiconductors, mainly semi-insulating GaAs wafers, are used as ultrafast photoconductive switch devices, with a bias voltage supplied through metallic electrodes deposited on the surface of the wafer. Also Si, and InP are used as photoconductive switches [Rice et al.
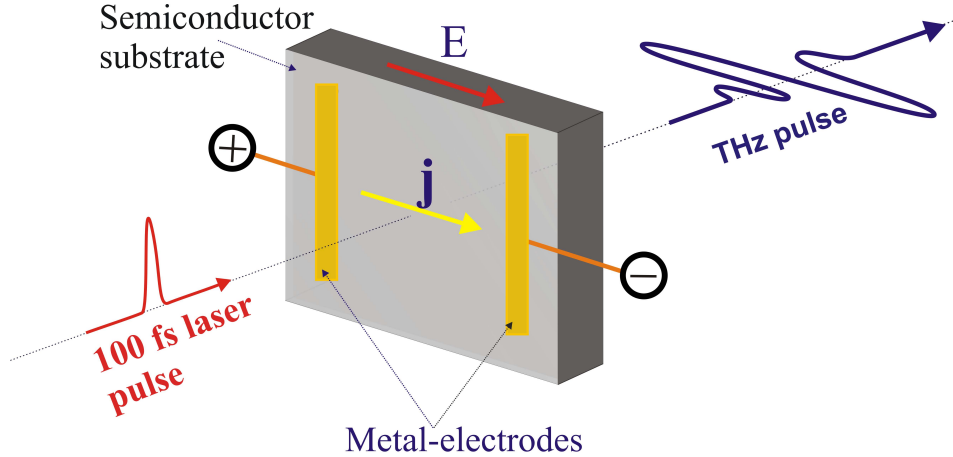
Figure 2.1: Schematic diagram of photoconductive switch THz pulse source.

(1994)]. Generation of THz radiation using photoconductive switch is illustrated in Fig. 2.1, where an ultrashort laser pulse with a photon energy larger than the bandgap of the material, $\hbar\omega \geq E_g$, illuminates at the gap between the electrodes to generate electron-hole pairs. Subsequently, the photoinduced photocarriers are accelerated along the field direction by a static bias field supplied along the metallic electrodes. The resulting accelerated photocarriers (current transients) emit THz radiation in the far field. In the far field approximation, the THz electromagnetic radiation emitted from the photoconductive switch is proportional to the first time derivative of the transient current, $\mathbf{E}(t) \propto d\mathbf{J}(t)/dt$ [S. Jha (1995); Jepsen et al. (2011)]. Analytical analysis of the far field radiation is discussed in Appendix A, Section A.1.

## 2.2.2 THz pulse generation by optical rectification

Optical rectification is a second order nonlinear optical process that involves the frequency down conversion of femtosecond optical pulses to the THz spectral range in electrooptic media. The difference frequency mixing among the frequency components within the spectrum of ultrashort optical excitation pulse that propagates through a noncentrosymmetric crystal results in a rectified (dc) polarization component. The linear ($\mathbf{L}$) and nonlinear ($\mathbf{NL}$)

electric polarization $\mathbf{P}$ in materials is expanded as a power series of $\mathbf{E}$ as,

$$\mathbf{P} = \underbrace{\varepsilon_0\chi^{(1)}\mathbf{E}}_{\mathbf{L}} + \underbrace{\frac{1}{2}\varepsilon_0\chi^{(2)}\mathbf{E}\mathbf{E} + \frac{1}{3!}\varepsilon_0\chi^{(3)}\mathbf{E}\mathbf{E}\mathbf{E} + \frac{1}{4!}\varepsilon_0\chi^{(4)}\mathbf{E}\mathbf{E}\mathbf{E}\mathbf{E} + ...}_{\mathbf{NL}} \quad (2.1)$$

where $\varepsilon_0$ is the electric vacuum permeability, $\chi^{(1)}$ is the second rank tensor of the linear susceptibility, and $\chi^{(2)}$, $\chi^{(3)}$, $\chi^{(4)}$ ... are higher order nonlinear susceptibilities. From Eq. 2.1 the term that is responsible for OR is the second-order nonlinear polarization term, $\chi^{(2)}$.

The idea behind OR is to generate a second order nonlinear polarization inside the nonlinear crystals, which then emits electromagnetic radiation in the THz frequency. The total induced nonlinear polarization by OR inside the emitter is expressed as,

$$\mathbf{P}_i^{(2)}(\Omega) = \sum_{jk} \varepsilon_0\chi_{ijk}^{(2)}(\Omega) \int_{-\infty}^{+\infty} \mathbf{E}_j(\omega + \Omega)\mathbf{E}_k(\omega)d\omega \quad (2.2)$$

where i, j, k are the x, y, z direction in the crystallographic axis of the nonlinear media. The sum adds all the contributions of the induced nonlinear polarization at different points and different generated frequencies associated with the optical rectification. $\mathbf{P}_{THz}^{(2)}(\Omega)$ is the induced dc polarization through difference frequency mixing and is responsible for THz radiation, $\chi_{ijk}^{(2)}$ is the second-order nonlinear susceptibility tensor, and $\mathbf{E}_j(\omega + \Omega)$ and $\mathbf{E}_k(\omega)$ are the amplitude electric field components at two different spectral frequencies of the femtosecond laser pulse. The fundamental electromagnetic wave equation for generation and propagation of THz waves derived from Maxwell's equations is expressed as,

$$\nabla^2\mathbf{E} - \frac{n^2(\Omega)}{c^2}\frac{\partial^2\mathbf{E}}{\partial t^2} = \frac{1}{\epsilon_0 c^2}\frac{\partial^2\mathbf{P}^{(2)}}{\partial t^2} \quad (2.3)$$

where $n^2(\Omega)$ is the refractive index of the medium at a newly generated THz frequency. Detailed derivation of optical rectification mechanism of THz pulse radiation in nonlinear crystal is described in Appendix A section A.2 (or Chapter 2 of my MSc thesis [Ayesheshim (2009)] and [(Ganichev and Prettl, 2006, Chp:6)]). Also, THz pulse generation through difference frequency mixing is possible by exciting the electromagnetic and phonon-polariton modes in ferroelectric crystals like $LiTaO_3$ and $LiNbO_3$. Phonon-polaritons in the THz frequency range can be generated when an ultrashort optical pulse is focused onto such crystals through impulsive stimulated Raman scattering and difference frequency mixing. The detailed analysis of ferroelectric oxide crystals as a THz pulse radiation source through difference frequency mixing (OR) is given in Chapter 5.

Figure 2.2 illustrates generation of THz pulses by OR. An intense femtosecond optical pump pulse illuminates a non-centrosymetric crystal and induces a nonlinear rectified po-
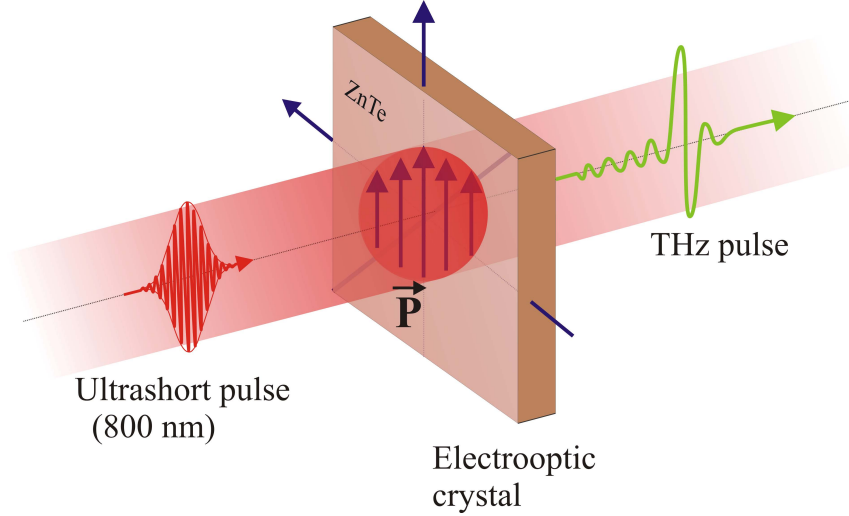
Figure 2.2: Generation of a terahertz pulse by optical rectification in ZnTe. The incident ultrafast optical pulse induces a nonlinear polarization $\vec{\mathbf{P}}$ in the ZnTe crystal.

larization $\mathbf{P}$ via difference frequency mixing and the induced polarization acts as a source of THz radiation. In collinear phase matching, the optical pulse and the generated THz radiation co-propagate in the same direction inside the crystal. As the optical pulse moves through the crystal, the field components of the generated THz radiation superimpose constructively and yields optimal THz generation efficiency.

In optical rectification, a pump laser pulse induces a nonlinear polarization proportional to its intensity envelope [Wahlstrand and Merlin (2003)]. The nonlinear response of optical materials to femtosecond laser excitation gives rise to exchange of energy between radiation fields of different frequencies [(Ganichev and Prettl, 2006, Chp:6)]. During the exchange, conservation of photon energy as well as conservation of momentum should be fulfilled. The efficiency of this technique is highly limited by the collinear phase-matching condition of the group velocity of the optical pulses ($\mathrm{v}_{op}^{g}$) with the phase velocity of THz pulse $\mathrm{v}_{THz}^{ph}$ inside the generating crystal. That is, the optical group velocity must be equal to the phase velocity of the generated THz radiation to achieve collinear phase matching. The requirement of this condition is conveniently fulfilled using a collinear geometry in a Zincblende crystal of ZnTe around 800 nm pump wavelength [Hu et al. (1990); Nahata et al. (1996); Blanchard et al. (2007)] and around 1 $\mu$m in GaP [Chang et al. (2006)].

The achievable THz temporal shape and bandwidth are controlled by both the bandwidth

of the excitation laser pulse, the phase-matching condition [Jepsen et al. (2011); Ulbricht et al. (2011)] and the absorption of the nonlinear material. THz radiation emitters via difference frequency mixing are listed in Ref. [Reimann (2007)] and [Ulbricht et al. (2011)], and these include, ZnTe, GaAs, GaP, InP, GaSe, CdTe, CdZnTe, $ZnGeP_2$, $LiNbO_3$, $LiIO_3$, $LiTaO_3$, $SiO_3$, and DAST. Among these, ZnTe for 0 - 3 THz range, GaP for 2 - 7 THz, and GaSe for 8 - 40 THz (which can go up to 100 THz by tilting the crystal with a short enough pump pulse) are widely used materials for difference frequency generation through collinear phase matching [Ulbricht et al. (2011)], and $LiNbO_3$ can be used for high power THz pulse generation via non-collinear setups [Hebling et al. (2002)]. Both photoconductive and nonlinear electrooptic source are often a challenge for broadband detection due to a limited bandwidth, as mentioned above. In order to completely exploit the THz frequency range for potential applications, ultrabroad bandwidth and scalable THz sources are required. Air plasma induced by intense femtosencod laser pulses has an ability to generate and detect broadband Ho et al. (2010) THz pulses through a third-order nonlinear $\chi^{(3)}$ optical processes Bartel et al. (2005). Unlike photoconductive sources and electrooptic crystals the spectral range is not limited by phonon absorption and dispersion, rather it's only limited by the optical pulse duration. Such that a full bandwidth coverage from 0.3 to 30 THz [Karpowicz et al. (2008)] is able to be detected in this technique.

### 2.2.3  THz radiation in Air Plasma

THz waves are generated in gases during the gas ionization processes induced by mixing of the fundamental femtosecond pulses with 800 nm in wavelength and its second harmonic (SH) laser pulses (400 nm) [Cook and Hochstrasser (2000); Kress et al. (2004); Bartel et al. (2005); Xie et al. (2006); Kim et al. (2007); Karpowicz et al. (2008); Dai et al. (2009); Klarskov et al. (2013)]. It has emerged as one of the most promising broadband and scalable THz sources. Using this method, the THz radiation originates from the transient photocurrent of ionizing electrons driven by the asymmetric electric fields of the superposition of the fundamental and the SH waves [Kim et al. (2007)]. Also, the ponderomotive forces present at the focus of the intense laser pulse, which creates a density difference between electrons and ions. Consequently, the charge separation results in EM transient radiation [Hamster et al. (1993); Yun-Shik (2009)] in the frequency range. However, much stronger THz radiation contribution arising from frequency mixing of the fundamental optical wave of frequency $\omega$ with a second harmonic wave of frequency $2\omega$. Figure 2.3 illustrates the experimental geometry of THz generation from laser-induced plasma in gases. The second-harmonic generation is usually carried out in a type-I $\beta$-barium borate (BBO) crystal as shown in Fig. 2.3. The THz radiation intensity is maximized when the fundamental and SH polarizations are parallel, while it is negligible when they are perpendicular. In this

11
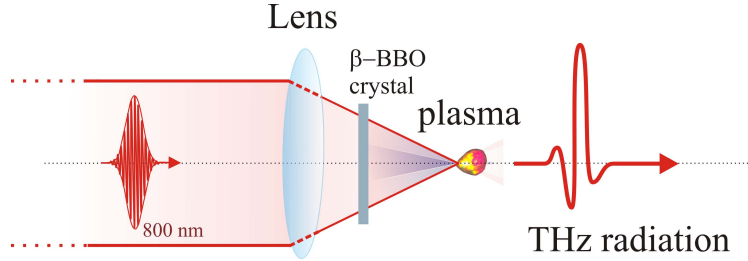
Figure 2.3: Schematic illustration of the experimental setup for generation of THz radiation by mixing the fundamental and second-harmonic (SH) optical pulses. Type-I $\beta$-BBO crystal is introduced after the lens to generate a SH beam.

method, third-order nonlinearity is the dominant processes for THz radiation generation, however, higher-order terms of nonlinearity are also considered at higher optical power. The nonlinear polarization that contributes THz radiation from Eq. 2.1 are $\chi^{(3)}$ and higher order nonlinearity terms. Higher order nonlinear processes are described by nonperturbative analysis [Yun-Shik (2009)].

## 2.3 THz pulse detection

THz pulses can be detected either coherently in the time domain via processes analogous to THz pulse generation, or incoherently using thermal detectors (such as bolometers and pyro-electric detectors). In general, electromagnetic radiation detector performance is limited by sensitivity and signal noise. However, coherent THz pulse detection methods provide high signal-to-noise with ultrafast responsivity. The most advanced ultrafast coherent detection methods mainly rely on photoconductive sampling and electrooptic sampling techniques. Coherent detection schemes measure the transient electric field of a THz pulse. Therefore, with coherent detection techniques, both the actual electric field amplitude and phase information of each spectral component in the pulse is resolved with high precision. This allows for simultaneous extraction of both the real and imaginary components of the conductivity of materials without the need for Kramers-Kronig analysis.

However, incoherent detectors only measure the intensity of the THz field and have slow response time. Incoherent detectors are thermal detectors like liquid-helium cooled bolometers, thermopiles, and pyroelectric detectors. These detectors can measure radiation power over a wide spectral range depending on the coating used. Comparison of THz energy measured using pyroelectric and thermal detectors are shown in Fig. 2.4. The fundamental

THz Energy
reading at focus

(a)       1.5 µJ

(b)       0.4 µJ

(c)       0.12 µJ

(d)       No reading
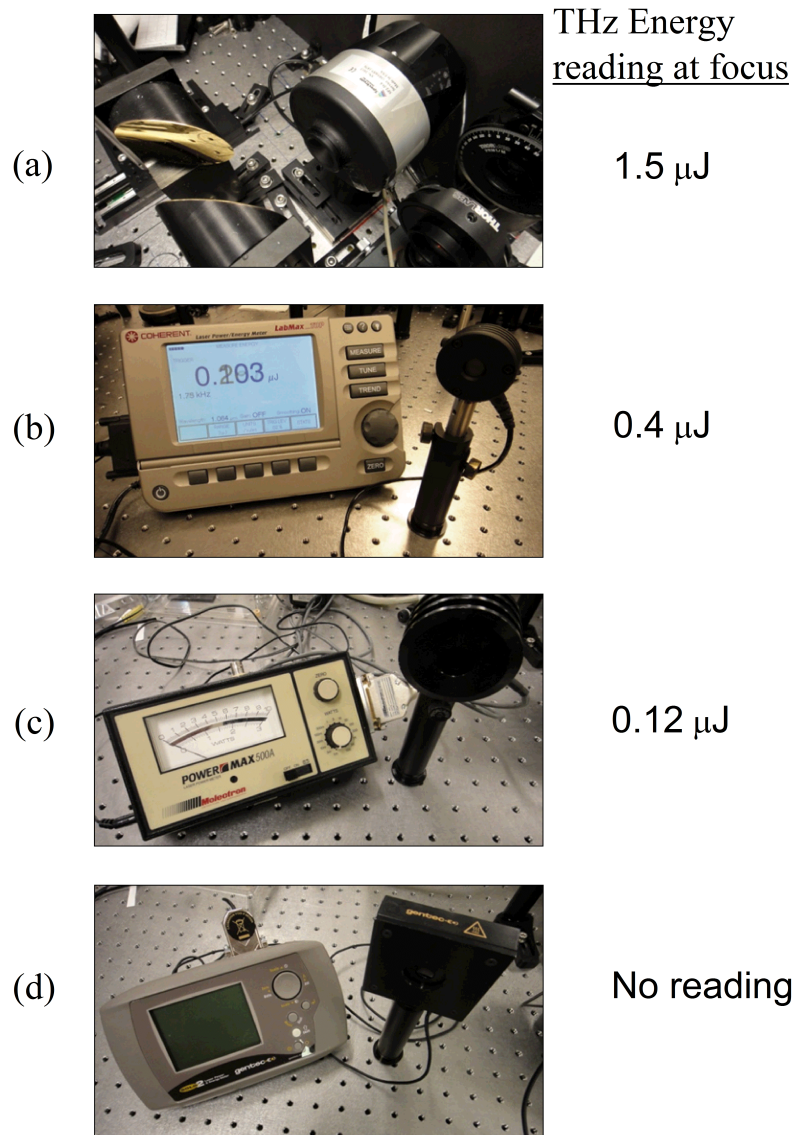
Figure 2.4: THz power and energy detectors: (a) Pyroelectric detector (SPJ-D-8 Spectrum Detector Inc.) used to measure the THz pulse energy at the sample position. (b) Pyroelectric detector, LabMax-Top "Coherent Inc. laser power and energy meter". (c) Thermopile detector, Molectron Detector Inc. PowerMax 500A thermal detector. (d) Thermopile detector. The zero reading is due to the spectral range of the coating used for the detector is not in the THz spectral range.

difference between the different THz pulse energy reading seen by the detectors in Fig. 2.4 is due to the different coating used in the detectors. Thermal detectors respond to the temperature variation due to THz absorption on the detector surface. In pyroelectric detectors, the change in temperature modifies the built-in spontaneous electric polarization of the detector ferroelectric crystal.

## 2.3.1 Photoconductive Sampling

THz pulse detection by photoconductive antenna depends on the current induced by a THz electric field in a photoconductive gap, and the photocarriers are injected by the optical probe pulse. The working principle of a photoconductive antenna as a THz detector is identical to that of a THz emitter carried out through photoconductive sampling in an antenna structure. The difference is that the instantaneous THz field replaces the DC field for photoconductive sampling such that the THz detector antenna is unbiased, as a result the electrodes are connected to a current amplifier rather than a power supply.
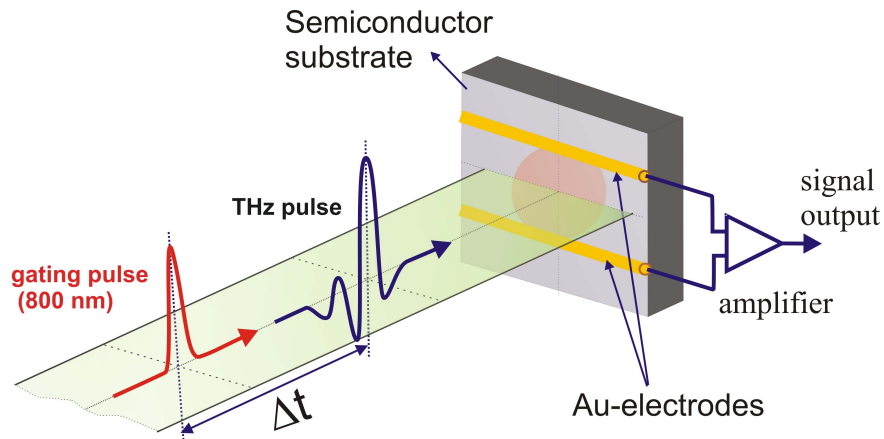


Figure 2.5: Schematic representation of a photoconductive antenna THz pulse receiver. $\Delta$t is the time delay between the THz pulse and an optical detection beams, that controlled by the optical delay stage to map-out the THz signal.

Figure 2.5 illustrates the unbiased photoconductive antenna THz pulse receiver. The optical gate-pulse (probe pulse) delayed by $\Delta t$ with respect to the THz pulse, interacts

with the photoconductive switch in which the optical probe generates charge carriers and the THz field drives them to form a transient photoinduced current. Here the incident THz field amplitude provides a bias voltage to the photocurrent. The photocurrent lasts for the carrier lifetime, which should be much shorter than the THz pulse duration for a time-resolved waveform measurement [Yun-Shik (2009)]. As a result a PC antenna needs a semiconductor with a very short recombination time such as LT-GaAs [Beard et al. (2001); Cooke (2006)] to increase the bandwidth. The temporal electric field of the THz pulse, at the moment of overlap with the optical probe pulse including both its amplitude and sign, is determined from the photoinduced current. The complete THz pulse transient is then retrieved by varying the time delay between the THz pulse that generates photocurrent in the unbiased photoconductive switch and the optical probe pulses [Cai et al. (1998)]. The induced photocurrent is directly proportional to the THz pulse field.

### 2.3.2   Free-Space Electro-Optic Sampling

Free-space electro-optic sampling (FSEOS) is a measurement of the amplitude and phase of the electric field of a THz pulse in the time domain utilizing the linear Pockel's effect [Wu and Zhang (1995)]. The Pockel's effect is the change of the refractive index of an electro-optic medium in proportion to the applied electric field. In FSEOS techniques, the Pockel's effect produces birefringence (changes the refractive index along one polarization axis) in a detection crystal subjected to a THz electric field that in turn modifies the polarization of the probe beam traveling through the crystal. THz field induced birefringence in a nonlinear optical medium is proportional to the applied THz field amplitude [Yun-Shik (2009); Jepsen et al. (2011); Ayesheshim (2009)].

In FSEOS, the phase mismatch between the optical sampling pulse and THz pulse inside the detection crystal limits the efficiency of free-space electro-optic sampling. Hence, electro-optic crystals that fulfill velocity matching near 800 nm, high transparency at optical and THz frequencies, and large EO coefficient are required for efficient EO sampling [Yun-Shik (2009)]. Similar to OR, ZnTe crystal is the most common used for EO sampling due to its large EO coefficient ($r_{42} = d_{14} = 4 \times 10^{-12} m/V$) and collinear phase matching (refer Table 5.1 in Chapter 5).

Figure 2.6 illustrates a typical FSEOS setup for measuring THz field-induced birefringence in electro-optic crystals. The THz pulse and the optical sampling beams are made to coincide and propagate collinearly in the electrooptic detection system. Depending on the THz field strength, a phase modulation is induced inside ZnTe when the THz pulse co-propagates with a sampling beam, see Fig. 2.6. In our high power setup, a piece of ZnTe crystal with thickness about 500 $\mu$m orientated along [110], is used for detection of a THz
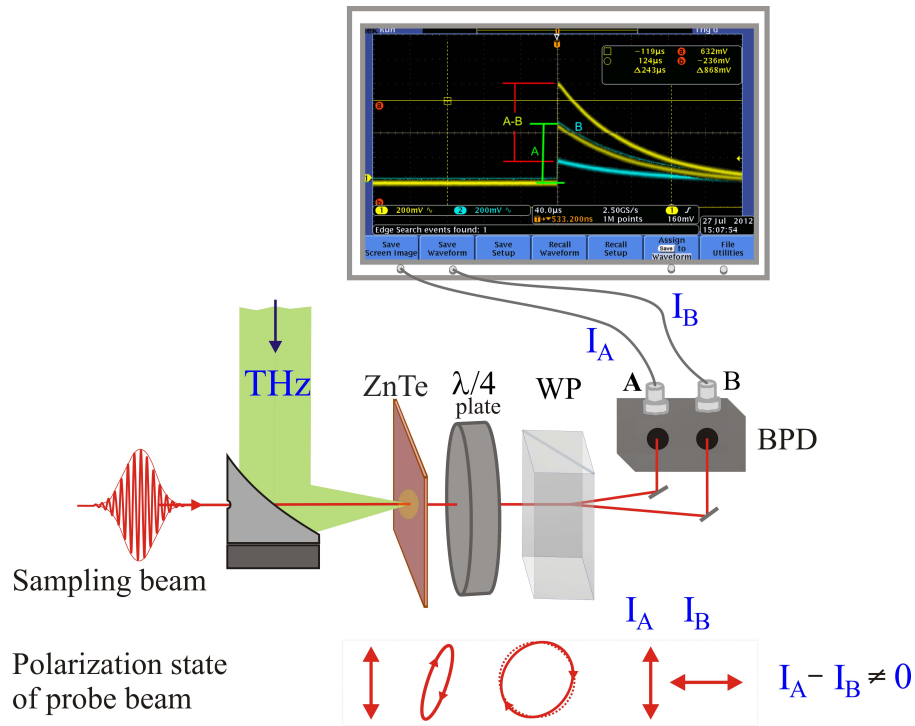
Figure 2.6: Schematic diagram of free space electro-optic detection of THz pulses. Evolution of the polarization of probe beam is shown before and after the ZnTe, $\lambda/4$ plate, and Wollaston prism. The THz modulation is displayed on the oscilloscope that directly connected to the two photodiodes via 50 $\Omega$ SMA cable.

16
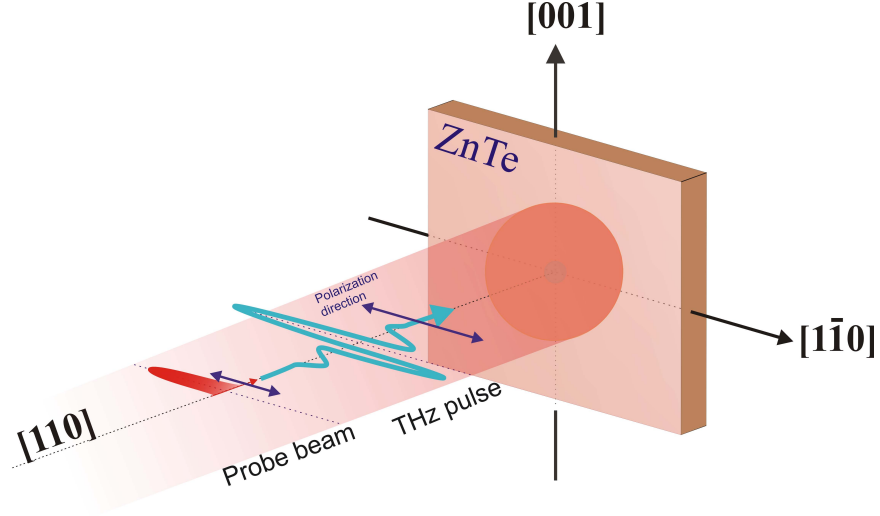
Figure 2.7: Schematic of ZnTe crystal orientation and polarization orientation of probe and THz fields for maximum field induced birefringence. THz pulse and optical probe beams are co-propagated through a thin undoped [110]-oriented ZnTe crystal with field polarizations parallel to [1$\bar{1}$0] direction of the crystal.

beam using free space electro-optic sampling. The balanced photodiodes denoted by **A** and **B**, as shown in Fig. 2.6, measure the intensity of the two beams split by the Wollaston polarizer (WP). Subsequently, an EO signal (the intensity difference detected by the balanced photodetector (BPD)) is collected with a lock-in amplifier phase-locked to an optical chopper which modulates the THz generation beam. The sine of the angle of polarization rotation, $\theta$, is directly proportional to electrooptic signal amplitude modulation measured by the balanced photoconductive diodes as,

$$\frac{I_A - I_B}{I_A + I_B} = \sin\theta \tag{2.4}$$

where $I_A$ and $I_B$ are the intensity measured by photodetector **A** and **B**, respectively.

THz pulse detection at low THz fields creates a linear optical pulse polarization modulation. However, strong THz fields create over rotation of the optical pulse polarization in the detection crystal. Hence, attenuation of THz pulse intensity with a combination of Si-wafers or wire grid polarizers is essential to keep the photodiode detection scheme in the linear regime, where $\sin(\theta) \approx \theta$. Figure 2.8 illustrates a typical THz pulse measured

17

using FEOS after the THz field is attenuated using two Si-wafers to prevent over-rotation that decreases the amplitude of the measured EO signal. The linear electro-optic THz pulse modulation effect inside the nonlinear detector crystal leads to a polarization rotation of the optical beam. When this optical beam propagates through the rest of the FSEO detection units, a phase retardation between the two optical probe beam components are measured by the balanced photodiode. The strength of the THz field is directly proportional to the phase retardation (modulation) measured by the photodiodes, and it has a form,

$$\frac{I_A - I_B}{I_A + I_B} = \sin\theta = \frac{2\pi}{\lambda} n_0^3 r_{41} E_{THz} L \tag{2.5}$$

where $r_{41} = 4.04 \times 10^{-12}$ m/V is the linear electrooptic coefficient for ZnTe, $n_0 = 2.85$ is the index of ZnTe at THz frequencies, L is the thickness of the electrooptic crystal and $\lambda = 800$ nm is the wavelength of the optical pump beam. Small modulation $\frac{I_A - I_B}{I_A + I_B}$ is preferred to maintain linearity in the electro-optic detection system. Without the THz pulse, the linear polarized optical sampling beam travels through the detection, ZnTe crystal without any modification of the polarization condition. Therefore, the polarization is changed to circular by a $\lambda/4$-wave plate placed after the ZnTe detector. The beam splits into two equal amplitude orthogonal components by a Wollaston prism and guided to balanced photodiode detectors **A** and **B** that are connected to an oscilloscope or lock-in amplifier, as shown in Fig. 2.6. The THz field modulation reading by lock-in/oscilloscope, that is the difference in voltage signal measured from the two photodiodes becomes zero. However, when a linearly polarized probe and THz pulse co-propagate through the detection crystal, the THz field induced birefringence tilts the polarization of the probe pulse by a certain angle $\theta$ proportional to the strength of the field given by Eq. 2.5.

Consequently, the probe polarization evolves to elliptical polarization after the $\lambda/4$-wave plate and the balanced photodiode **A** and **B** measures different amplitude levels of the EO signal. The electrooptic signal modulation measured by the lock-in/oscilloscope is directly proportional to the electric field of the THz pulse (see Eq. 2.5).

In the majority of applications utilizing THz pulses generated from both photoconductive switches and OR sources, low energy pulses to drive and probe material responses without perturbation. For example, time-resolved spectroscopy employs a non-contact probe of sample properties to detect and monitor conductivity using weak THz probe pulses, characterization of transient carrier dynamics in semiconductors [Beard et al. (2000); Ganichev and Prettl (2006); Dexheimer (2008); Yun-Shik (2009)], organic crystals [Hegmann et al. (2002)], and semiconductor nanocrystals [Cooke et al. (2006); Titova et al. (2011)] in the THz frequency range. Also, THz intensities generated from transient currents and OR sources have been insufficient to demonstrate sub-picosecond nonlinear THz processes of materials for the last two decades. Moreover, in the THz region, spectroscopic studies have been restricted
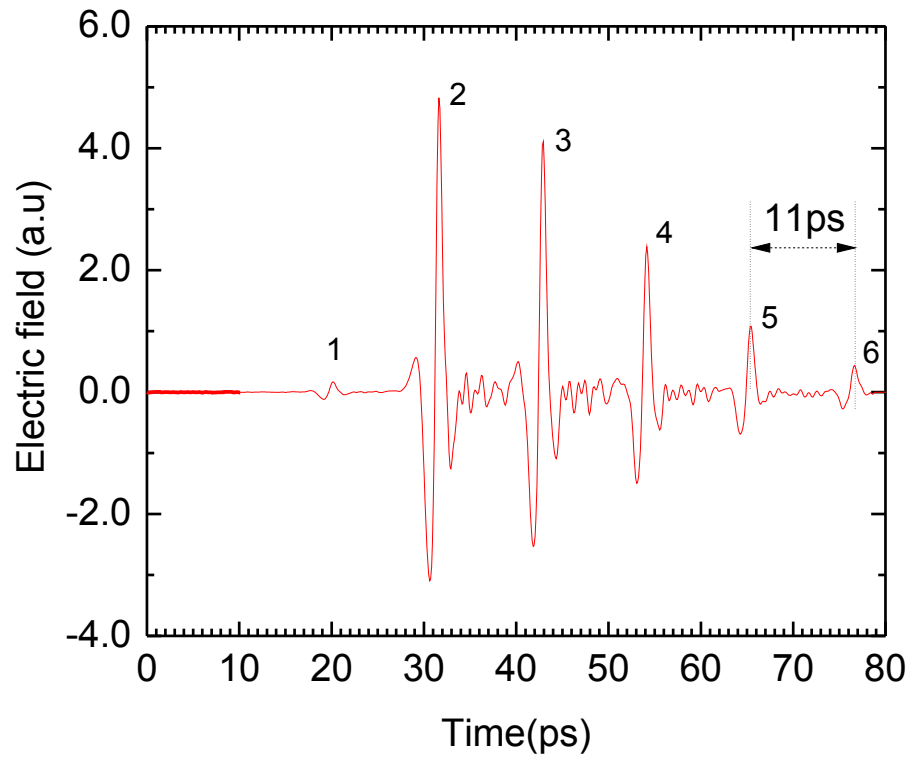
Figure 2.8: THz waveform measured after attenuating the THz energy using a two Si-wafers separated by 35 mm placed on the collimated propagation of the THz beam. The main pulse represented by 2 is followed by a series of reflected pulses as depicted in the figure. The pulses represented by 1 and 2 are pre and main pulses, respectively, while those pulses denoted by 3-6 are due to the multi-reflection between the two Si-wafers. The phase delay between the successive pulses is 11 ps.

to narrow frequency ranges [0.1 - 3 THz] and to the exploration of linear THz effects in materials. The main impediment to broadband THz spectroscopy lies in the limitations on broadband sources. Therefore, the study of THz nonlinear optics, spectroscopy, and other applications were hampered by the absence of efficient, intense, table-top sources. As a result, there is a considerable interest in the development of new sources of ultrashort high-field THz pulses to study the properties of materials under high-field conditions in the THz regime. I believe that ultrafast nonlinear THz dynamics research in matter is going to be the future prospect of this technology. Therefore, the use of ultrashort THz pulses for ultrafast nonlinear THz dynamics studies requires high-power with high peak field amplitudes.

## 2.4 Intense THz pulse generation

High THz electric-field strength as a pump is desirable to drive nonlinear processes in materials, allowing studies of charge carriers and low-energy excitations in the nonlinear regime [Ulbricht et al. (2011)]. Table top intense THz pulses with peak amplitudes beyond several hundredths of kV/cm can be achieved by high-intensity femtosecond laser sources combined with large-aperture emitters [Blanchard et al. (2007)], tilted-pulse-front excitation in LiNbO$_3$ [Hebling et al. (2002); Yeh et al. (2007); Hoffmann and Fulop (2011); Hirori et al. (2011); Blanchard et al. (2014)], and four wave mixing in air-plasma [Cook and Hochstrasser (2000); Bartel et al. (2005); Kim et al. (2008)]. Several improvements have been made on the former two most efficient table-top-high power THz pulse generation techniques [Blanchard et al. (2007)]. With photoconductive switches, improvements made to scale up the THz emissions were made by optimizing antenna structures, increasing electrode separation gaps, increasing the bias field and the optical excitation fluence. For example, [Budiarto et al. (1996)] biased the electrodes with a pulsed voltage of 45 kV and illuminated with 150 fs Ti:sapphire laser pulse energy of 0.5 mJ at 1 kHz repetition rate. The highest THz energy achieved from large-aperture photoconductive THz sources was 0.8 $\mu$J by illuminating the photoconductive switch with 120 fs ultrashort laser pulses at 10 Hz repetition rate [You et al. (1993)]. More recently, [Ropagnol et al. (2013)] reported a THz pulse energy of 3.6 $\mu$J with peak THz field of 143 kV/cm from using an interdigitated ZnSe large aperture photoconductive antenna. From large scale facilities with free-electron lasers (synchrotron), up to 100 $\mu$J THz pulse energy can be generated [Shen et al. (2007)]. However, these large facilities are not easily accessible.

In addition to high power sources, new broadband sources are of interest to fully exploit the entire THz range for THz time domain spectroscopy. Recently, a photo-induced air plasma THz generation and detection technique that provides a broadband THz spectrum with high peak field strength has emerged [Bartel et al. (2005); Xie et al. (2006); Ho et al.

(2010)]. Basic techniques of air plasma-based THz pulse generation is presented in chapter 2 section 2.2.3. However, EO crystals remained attractive for the development of extreme THz sources through the improvement of OR techniques due to their simplicity and their broad range of applications.

### 2.4.1   Intense THz pulse generation by OR

From optical rectification sources in a large aperture 75 mm in diameter ZnTe crystal, a single-cycle THz pulses with 1.5 $\mu$J energy and an energy conversion efficiency of $3.1 \times 10^{-5}$ have been generated [Blanchard et al. (2007)]. Tilted-pulse-front OR [Yeh et al. (2007); Stepanov et al. (2008); Hirori et al. (2011)], have overcome the limitations that hinder achievement of intense THz pulses and boosted the ultrafast nonlinear THz experiments to a new research frontier in a relatively unexplored spectral range at high intensity of THz field excitations.

The most important optical parameters that enhance the efficiency of THz pulse generation by OR is a large effective nonlinear coefficient ($d_{eff}$), small THz absorption, and good velocity matching (phase-matching) between the group velocity of the optical pump and the THz phase velocity [Hebling et al. (2008); Fulop et al. (2010)]. In a collinear phase matched optical rectification scheme of THz generation, the experimental setup is straight forward in which a femtosecond laser pulse excites an electro-optic crystals such as ZnTe and the emitted THz pulse is detected via electro optic sampling technique as discussed before. However, multi-photon absorption leads to saturation of the THz pulse generation efficiency in ZnTe crystals. An alternative candidate of efficient THz pulse generation using nonlinear processes is a large nonlinear electrooptic coefficient crystal, e.g. $LiNbO_3$ [Hebling et al. (2002)] and using higher fluences of the optical excitation pulse. Unlike ZnTe, in $LiNbO_3$, collinear phase matched optical rectification is impossible due to a large refractive index mismatch between THz and 800 nm pulses. As a result, phase matching of the THz and optical pulse can only be achieved using a pulse-front-tilt geometry [Hebling et al. (2002)]. The details and improved version of this setup is presented in Chapter 5.

# CHAPTER 3

## Ultrafast nonlinear THz dynamics

"Physics would be dull and life most unfulfilling if all physical phenomena around us were linear. Fortunately, we are living in a nonlinear world. While linearization beautifies Physics, nonlinearity provides excitement in physics" Principles of Nonlinear Optics-Y. R. Shen.

## 3.1   Introduction

Ever since the advent of the laser in 1960 at the Hughes Research Laboratory in California [Maiman (1960)], researchers have been able to investigate the optical material response to light at higher intensity than ever before. Soon after, the generation of optical harmonics by [Franken et al. (1961)] in quartz crystals, not seen with ordinary light, marked the beginning of the field of nonlinear optics. Since then, numerous nonlinear optical experiments have been carried out that offer a host of fascinating phenomenon which have enhanced our understanding of fundamental light-matter interactions and stimulated a revolutionary change in optics technology. The immediate impact of such physical phenomena in semi-conductors, due to the properties of electrons in the conduction band and their dynamic responses to light, has enabled us to manufacture high performance novel modern optic and optoelectronic devices.

Nonlinear optical phenomenon of a medium, through which light is propagating, is described in terms of the relationship between the incident electric field, $\mathbf{E}(\mathbf{r}, t)$, and the induced time varying electronic polarization, $\mathbf{P}(\mathbf{r}, t)$. The induced time varying polarization can act as a source of new electromagnetic radiation with frequency components not present in the incident radiation field. The interaction is in the regime of linear optics if the relation of the polarization to the applied field is linear, i.e., $\mathbf{P(t)} = \varepsilon_0 \chi^{(1)}(t) \mathbf{E}(t)$. This happens for

low intensity excitation. On the other hand, high intensity interaction is characterized by a nonlinear relation between **P** and **E**, when the magnitude of incident field is comparable to interatomic electric fields[1].

Investigating the nonlinear interactions of THz fields in semiconductors provides unique opportunities to extend our fundamental understanding of high field carrier transport dynamics in materials over the entire spectral range. The study of nonlinear THz dynamics due to the interaction of intense THz pulses with matter is relatively new [Gaal et al. (2006); Danielson et al. (2007); Hebling et al. (2008)]. It is worth mentioning that ultrafast nonlinear THz dynamics has benefited from the advancement and availability of table-top intense THz pulse sources in recent years and the wealth of important phenomena occurring at THz frequencies. Thus, ultrafast nonlinear optics characterization in the THz spectral range (sub-picosecond domain) provides novel and challenging avenues for probing the properties of materials and developing new applications.

Recent years have seen the emergence of a powerful nonlinear THz spectroscopy technique to study transient states (extreme nonlinearities) of materials in the mid-to-far infrared spectral range. Interaction of intense ultrafast THz electromagnetic pulses with solids results in new nonequilibrium phenomena on ultrafast time scales. Ultrafast nonlinear THz interactions of charge carrier dynamics in semiconductors and nanomaterials have attracted attention for potential applications in both modern optics and next generation high-speed optoelectronics.

## 3.2   Nonlinear Ultrafast THz Dynamics

Ultrafast THz nonlinear dynamics represents the study of the fundamental interactions of intense THz radiation with matter. Matter in the presence of an ac electric field of sufficient field strength exhibits phenomena that cannot be understood by treating the field as a small perturbation [Chin et al. (2000)]. Intense light pulses in the THz spectral range provides a new means of controlling material properties through manipulation of fundamental modes, such as free electrons, dipoles, vibrational degree of freedom [Wen et al. (2008); Kampfrath et al. (2013)]. Application of intense THz fields to semiconductors strongly modifies and controls the optical properties [Carter et al. (2005); Chin et al. (2000); Srivastava et al. (2004)]. Currently, the development of intense single cycle pulses in the low-THz regime (a spectral coverage from 0.1 - 2 THz) [Blanchard et al. (2007); Hebling et al. (2008)] have provided a unique tool to study such hot-carrier effects with high time resolution [Razzari et al. (2009); Su et al. (2009); Hoffmann and Turchinovich (2010)].

---

[1]Inter atomic electric fields are typically in the order of $10^8$ V/m

Very recently, significant advances in ultrafast nonlinear THz spectroscopy have allowed exploration of ultrafast phenomenon in materials upon the interaction of intense THz fields with free charge carriers. For example, ultrafast THz induced conduction band nonparabolicity and intervalley scattering [Razzari et al. (2009); Su et al. (2009); Hoffmann and Turchinovich (2010); Blanchard et al. (2011); Turchinovich et al. (2012)], interband tunneling [Kuehn et al. (2010b)], THz-induced impact ionization [Wen et al. (2008); Hoffmann et al. (2009); H. Hirori and Tanaka (2011)], anisotropy of effective mass within isotropic conduction bands [Blanchard et al. (2011)], self-phase modulation [Turchinovich et al. (2012)], photoluminescence quenching dynamics [Liu et al. (2010)], nonperturbative nonlinearities in semicnductors [Lange et al. (2014)], nonlinear THz metamaterials split ring resonators [Fan et al. (2013)], and femtosecond all-optical switching in nanoscale structures [Hoffmann et al. (2010)] are among the interesting ultrafast nonlinear THz induced phenomena observed in semiconductors and semiconductor quantum dots over a time scale of pico- and sub-picoseconds.

The interaction of intense fields in the low-THz regime with matter provides important informations of the fundamental properties of materials. The study of high-field driven carrier transport dynamics in semiconductors plays the central role in the advancement of semiconductor based technologies. This has contributed a great deal to our understanding of the dynamics of electrons in semiconductors. The high intensities of improved large aperture THz sources have allowed for a whole range of novel experiments under strong non-equilibrium conditions.

We have observed significant THz transmission changes in doped and photoexcited semiconductors, due to intervalley scattering processes induced by the electric field of the THz pulse over picosecond time scales. An open aperture Z-scan and OPTP experiments was employed to reveal the nonlinear dynamics responses of free charge carriers in two model semiconductors, namely doped InGaAs and photoexcited SI-GaAs samples initiated by an intense THz pulses, respectively. Single-cycle THz pulses with pulse energy up to 0.8 $\mu$J ($\sim$ 200 kV/cm) generated in a large aperture ZnTe (75-mm) OR source [Blanchard et al. (2007)] were used to drive free charge carriers and probe the nonlinear responses. The observed ultrafast dynamics occurred within the pulse duration of the THz-pump pulse. THz field driven ultrafast nonlinear dynamics of electrons were carried out in the same experimental setup based on our work at the Advanced Laser Light Source (ALLS) in Montreal, Canada [Razzari et al. (2009); Su et al. (2009)]. These will be discussed in section 3.6 and 3.7, respectively. In later Chapters 7 and 8, a completely new type of experiment will be discussed using similar samples that was perform in the Ultrafast Nanotools Lab at the University of Alberta.

The following addresses the physical properties of the samples and provides a brief

overview of the relevant intervalley scattering processes in doped and photoexcited samples following intense THz pulse excitation.

## 3.3 InGaAs

Indium Gallium Arsenide (InGaAs) is widely used for very high mobility optoelectronic devices due to the very small effective mass in InAs as well as a band gap in the telecommunications wavelength range. $In_{0.53}Ga_{0.47}As$ is a direct band gap semiconductor ($E_g = 0.88$ eV) lattice matched with InP. Because of the high strain it is not possible to grow all compositions, and the choice of a substrate is very important. Special properties of $In_xGa_{1-x}As$ alloys have made it an active ingredient in very high speed transistors as well as in fiber optic communication lasers. The $In_{0.53}Ga_{0.47}As$ has found a niche in high speed electronics because of its small effective mass ($m^* = 0.04m_0$) and excellent low and high field transport properties.

## 3.4 Physical properties and band structure of GaAs

Gallium arsenide (GaAs) is a direct bandgap semiconductor ($E_g = 1.43$ eV). GaAs is a material widely used for variety of applications, such as photoconductive switching in ultrafast optoelectronics [Tonouchi (2007); Ulbricht et al. (2011); Jepsen et al. (2011)], high speed transistors, and laser diodes [Mics et al. (2013)]. The detailed understanding and control of the photoconductive behavior of this material in an electric field is, therefore, a key issue both fundamentally and technologically. GaAs has a zincblende crystal structure and a lattice constant of $a_0 = 0.56533$ nm. The zincblende crystal structure and the band structure of GaAs is given in Figure 3.1. At room temperature, this material features a band gap energy between the maximum of the valance and minimum of the central conduction band ($\Gamma$) is, $E_g = 1.43$ eV. The nearest satellite energy gap values are, $E_{\Gamma L} = 0.29$ eV, $E_{\Gamma X} = 0.58$ eV, and $E_{so} = 0.34$ eV as shown in Fig. 3.1 (b).

Photoconductivity of SI-GaAs arises from above-band gap photoexcitation [Mics et al. (2013)], whose cutoff wavelength are given as;

$$\lambda_c = \frac{1240nm}{E_g(eV)} \tag{3.1}$$

The absorbed photons leads to the creation of electron-hole pairs. For GaAs at room temperature $E_g = 1.43$ eV, thus $\lambda_c = 867$ nm. Hence laser pulses below the cutoff wavelength can excite electrons from the valance band to the conduction band. The generation of
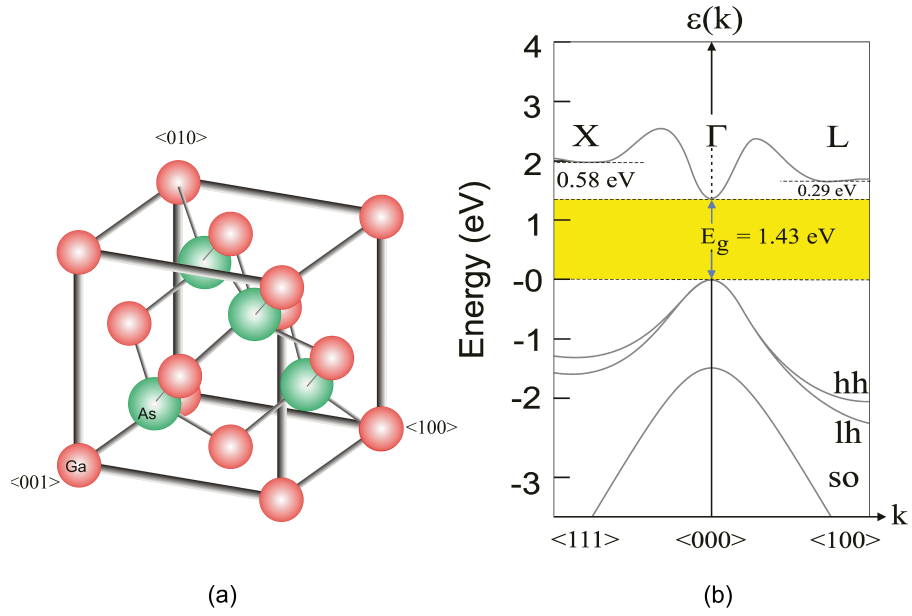
Figure 3.1: (a) Zincblende crystal structure of gallium arsenide (*red spheres: Ga atoms, green spheres: As atoms*). The Ga atom is at ⟨000⟩ and the As atom is at (1/4 ,1/4, 1/4)*a*. (b) Schematic of the band-structure of GaAs. The valance band of GaAs has the standard heavy hole (hh), light hole (lh), and split-off valance band (so). The band gap at room temperature is 1.43 eV. The bottom of the conduction band (Γ- point) is found at **k** =(0,0,0), and satellite valleys at the L- and X-points.

electrons and holes by the absorption of the excitation pulse increases the conductivity of the sample.

## 3.5 Intervalley scattering and band nonparabolicity mechanisms

It is generally accepted that free-carrier absorption is the main loss factor at THz frequencies in conducting materials and the attenuation is directly proportional to the conductivity of the material [Schall and Jepsen (2000); Lui and Hegmann (2001); Hoffmann and Turchinovich (2010)]. The only mechanisms that reduce the conductivity of doped and photoexcited semiconductors for a given carrier density are intervalley scattering and band nonparabolicity [Razzari et al. (2009); Su et al. (2009); Turchinovich et al. (2012)]. These can be achieved through a strong THz electric field excitation that creates a redistribution of free carriers in the energy-momentum space of the conduction band from low momentum Γ-valley to high-momentum satellite-valleys. Also, strong THz fields drive carriers high in the bands when nonparabolicity is significant.

Figures 3.2 and 3.3 display the fundamental scattering mechanisms that dominate high field transport of free carriers and optical properties of a photoexcited and doped semiconductors, respectively. The optical nonlinearity arises from the THz pulse induced change in conductivity of the samples. Free charge carriers are accelerated by intense THz pulses until their energy is sufficient to scatter into various side valleys (intervalley scattering). Scattering from the Γ-valley to the L-valley plays a very important role in high field transport in semiconductors. The scattering process also takes the electron from a low effective mass Γ-valley to the nearest high effective mass L-valley. This results in a negative differential mobility in the high field transport of direct gap semiconductors like GaAs and InGaAs [Singh (2003)]. The rapid initial transfer of electrons to the L-valley produces a lower initial electron temperature than would be found if the electrons remained in the Γ-valley. A significant fraction of the kinetic energy of hot electrons in the Γ-valley is converted to potential energy in the higher energy satellite valleys. By converting this potential energy back into kinetic energy with the return of electrons from the L- to the Γ-valley acts as a source of heating of the electrons in the Γ-valley [Othonos (1998)].

Figure 3.2 shows a schematic representation of the major scattering mechanisms of photoexcitation of SI-GaAs sample followed by intense THz pulse excitation simultaneously or at a later time. At high THz electric fields, photoexcited carriers in the conduction band may scatter to the nearest satellite bands and populate both the L- and X- valleys. Optical excitation creates electron-hole pairs, and simultaneously the free carriers are then accelerated by intense THz pulse in the lowest conduction band that results intervalley scattering.
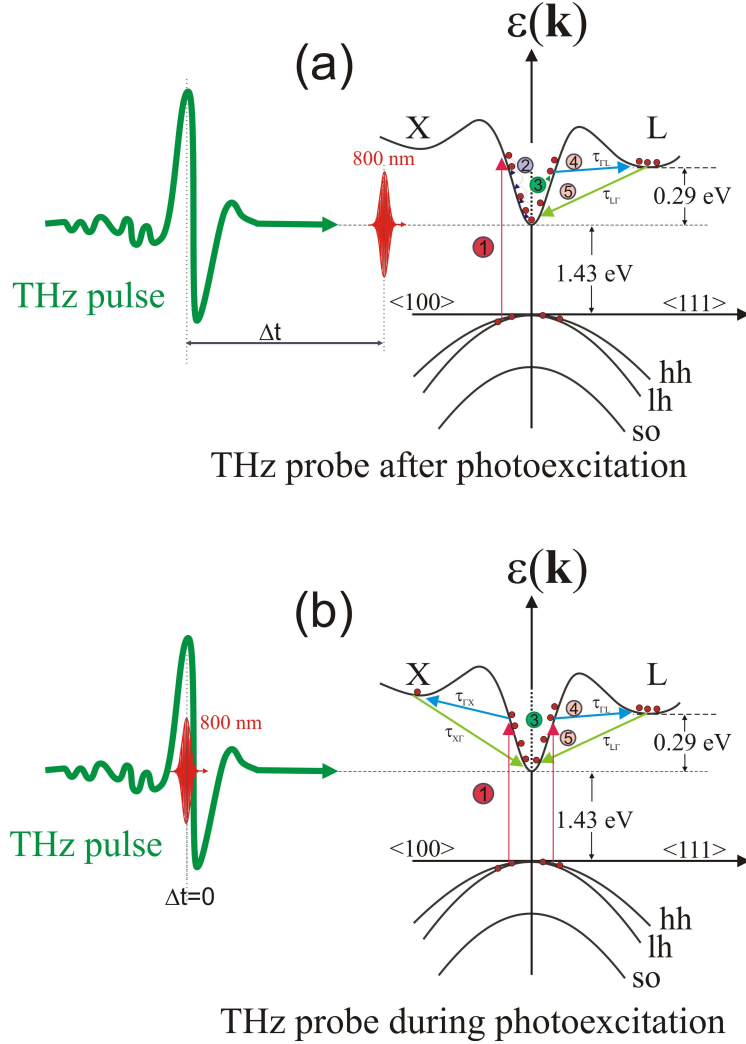
Figure 3.2: Schematic of energy band structure of photoexcited GaAs. (a) Absorption of femtosecond laser pulse creates electron-hole pairs and simultaneously perturbed by intense THz pulse creates intervalley scattering before the photoexcited carriers relaxed to the Γ-valley. Arrow ① represents band-to-band excitation of electrons by 800 nm optical pulse. Arrow ② represent intravalley scattering, and ③ represents electrons at higher k-state in the Γ-valley due to intense THz perturbation. Arrows ④ and ⑤ represents intervalley scattering via THz probe pulse. The conduction electron in the Γ-valley is then accelerated by intense THz pulse simultaneously or at a latter time Δt. (b) is special condition of (a), with OPTP delay time, Δt = 0.

28

Arrow ① represents band-to-band excitation of electrons due to photoexcitation. In ①, the 50 fs laser pump pulse centered at 800 nm photoecxites electrons and holes in the normally insulating GaAs sample, with the electrons being injected into the higher mobility center Γ-valley in the conduction band. The electrons quickly thermalizes ② within 1 ps to the bottom of the Γ-valley. A high-field THz probe pulse can then accelerate the photoexcited electrons to higher energies in the Γ-valley, which may result in intervalley scattering into the nearest adjacent valleys in the band structure the L-valley (labeled ③) that can happen with in 0.1 ps. The reverse intervalley scattering from the satellite valley to the Γ-valley occurs with a time constant of 3.5 ps [Su et al. (2009)]. Figure 3.2 (a) shows the THz probe is delayed by a latter time Δt to allow the carrier relaxes to the lowest conduction band through emission of optical phonon's represented by arrow ②. Arrow ② represents the intravalley scattering, and ③ represents electrons at higher k-state in the Γ-valley due to intense THz perturbation. Arrow ④ and ⑤ are intervalley scattering processes via THz probe excitation. Holes can also scatter from one band to another, however, the effect in the system is omitted due to its large effective mass. In Fig. 3.2 (b) the THz pulse drives photoexcited carriers simultaneously before recombination process, ②, happens.

At high THz field condition, a significant fraction of phtoexcited electrons in GaAs may transfer rapidly into higher conduction side-valleys (L and X-valleys) with lower mobility that give rise to a velocity overshoot in materials like GaAs [Hu et al. (1995)]. Even-though scattering back into the Γ-valley is rather slow because of the smaller density of states in the Γ-valley, the velocity is maintained in the steady state drift. By regulating the amplitude of the THz probe pulse, it is possible to study the intravalley and intervalley dynamics of nonequilibrium free carriers in the conduction band of photoexcited semiconductors. In the linear regime, all the electrons are near the bottom of the Γ-valley. Thus low THz fields perturb electrons only in the lowest energy conduction band (Γ-valley) and results in high electron mobility due to low effective mass, $m^*$, the electron conductivity is given as,

$$\sigma(t) = e n_\Gamma(t) \mu_\Gamma(t) \tag{3.2}$$

where $n_\Gamma$ is the electron density in the Γ-valley, $\mu_\Gamma = \frac{e \tau_\Gamma}{m^*}$, is the electron mobility. It is important to note that the nearest valleys above the Γ point are the L-valleys, which have a much larger effective mass, $m_L^* \approx 0.25 m_0$, than the Γ valley, $m_\Gamma^* \approx 0.067 m_0$ in GaAs. This difference in effective mass is very important for high field transport that leads to negative differential resistance. Thus, as the driving field increases, electrons can gain sufficient energy to transfer into satellite valleys via intervalley scattering. This intervalley scattering competes with intravalley relaxation via scattering by optical phonons. In GaAs the Γ-L intervalley scattering time at room temperature is less than 100 fs. However, the time it takes the electron to backscatter into the Γ-valley is about 3.5 ps [Su et al. (2009)],

due to the density of states of $\Gamma$-valley, $N(E) \propto (m_{dos}^*)^{3/2}$, is much smaller than that of L-valleys. Therefore, high field amplitude ultrashort THz field transient enabling photoexcited electrons to undergo intervalley scattering from the $\Gamma$-valley into the L-valley reveal characteristic change of the transport phenomena due to the picosecond backscattering into the $\Gamma$-valley. As a result the electron conductivity of the system given in Eqn. 3.2 can be modified as;

$$\sigma = e \left( n_\Gamma \mu_\Gamma + n_L \mu_L \right) \tag{3.3}$$

where $n_\Gamma$ and $n_L$ are electron density in the $\Gamma$ and L-valleys and the mobility are $\mu_\Gamma$ and $\mu_L$, respectively. ($\mu_L < \mu_\Gamma$), results a decrease in conductivity with increasing driving field. Above the L-point there is another conduction minimum, the X-valley, with $\Delta\varepsilon_{\Gamma L} = 0.58$ eV and $m_X^* \approx 0.6m_0$. At even higher fields, electrons will populate both the L and X valleys.

Figure 3.3 shows a schematic representation of the major scattering processes in doped InGaAs used in this thesis. Initially, as shown in Fig. 3.3 (a), the n-doped InGaAs high-mobility-$\Gamma$-valley is populated with free electrons in equilibrium. This results in high THz absorption until the THz excitation field induces intervalley scattering, as shown in Fig. 3.3 (b), and the hot electron occupies higher k-values. The band gap between the minimum of the conduction band and the maximum of the valance band is $\varepsilon_g = 0.74$ eV. The energy separation of the $\Gamma$-point in the conduction band and the nearest satellite valley, L, is $\varepsilon_{\Gamma L} = 0.55$ eV. The effective masses at the bottom of the two valleys are $m_\Gamma = 0.03745m_0$ and $m_L = 0.26m_0$, respectively, and the L-$\Gamma$ intervalley relaxation time is known to be about 3.1 ps [Razzari et al. (2009); Su et al. (2009)]. Intense THz field excitation results in bleaching of free-carrier absorption due to intervalley scattering of electrons from the central $\Gamma$- to the nearest satellite L-valleys at a scattering rate of $\tau_{\Gamma L}^{-1}$ [Razzari et al. (2009); Su et al. (2009); Hoffmann and Turchinovich (2010); Sharma et al. (2012)]. To study the dynamic electronic transport properties of a semiconductor, knowledge of the band structure and the effective mass of a charge carriers, $m^* = \hbar^2 \left[ \dfrac{d^2 E}{dk^2} \right]^{-1}$, is important.

The linear and nonlinear band structure are reviewed in Eq. 4.4 and 4.6 of Chapter 4. Besides the mobility differences between conduction band valleys, the nonparabolicity of the valleys in-turn leads to an increase in the effective mass, thereby a decrease in mobility and THz absorption with increasing carrier kinetic energy within a single valley. Consequently, it lowers the overall conductivity of the film, $\sigma = en\mu$ since $\mu$ depends on $m^*$ ( $\mu_\Gamma = e\tau_\Gamma/m^*$). The reduction in conductivity leads a higher THz transmission through the sample. The results from two paper are described here to illustrate THz nonlinear dynamics in doped InGaAs and photoexcited GaAs.
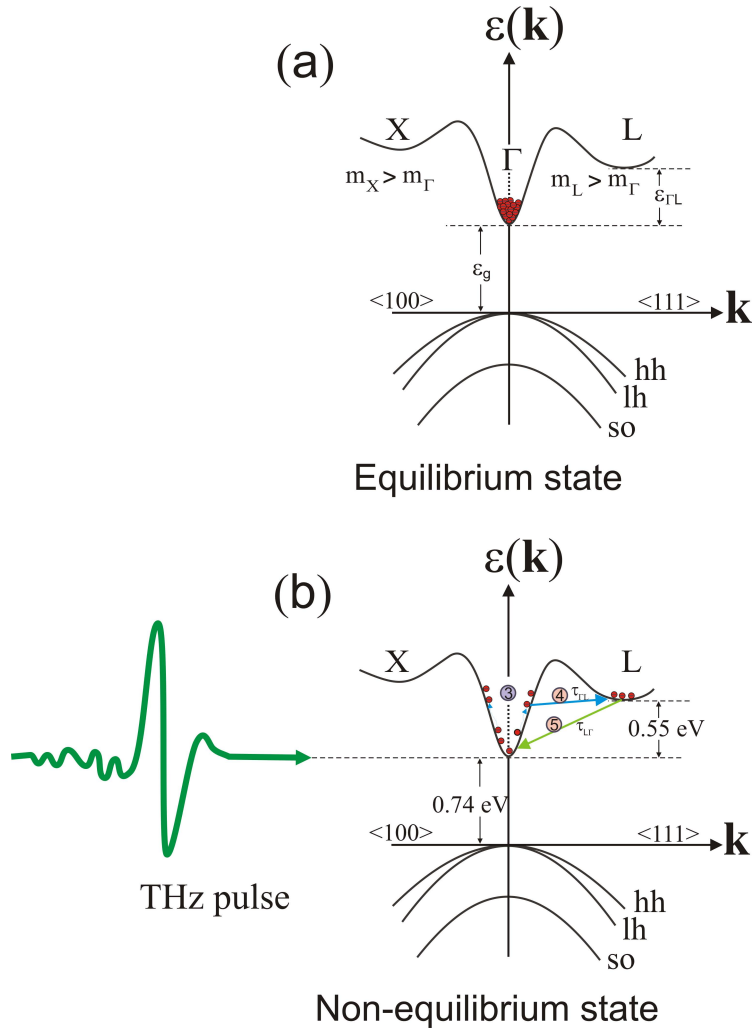
Figure 3.3: Schematic of the energy band structure n-doped InGaAs. (a) Equilibrium states of n-doped InGaAs. (b) Carrier distribution to higher k-states due to electronic band structure of n-doped InGaAs pumped with intense THz pulses. Intervalley scattering mechanisms under intense THz pulse perturbation are shown in (b). The conduction electron in the Γ-valley is accelerated by intense THz pulse, the arrow labeled ③ represents electrons in the higher k-state. Arrows ④ and ⑤ represents intervalley scattering via THz probe pulse.

## 3.6 Intervalley scattering induced by intense THz pulses in doped InGaAs [Razzari et al. (2009)]
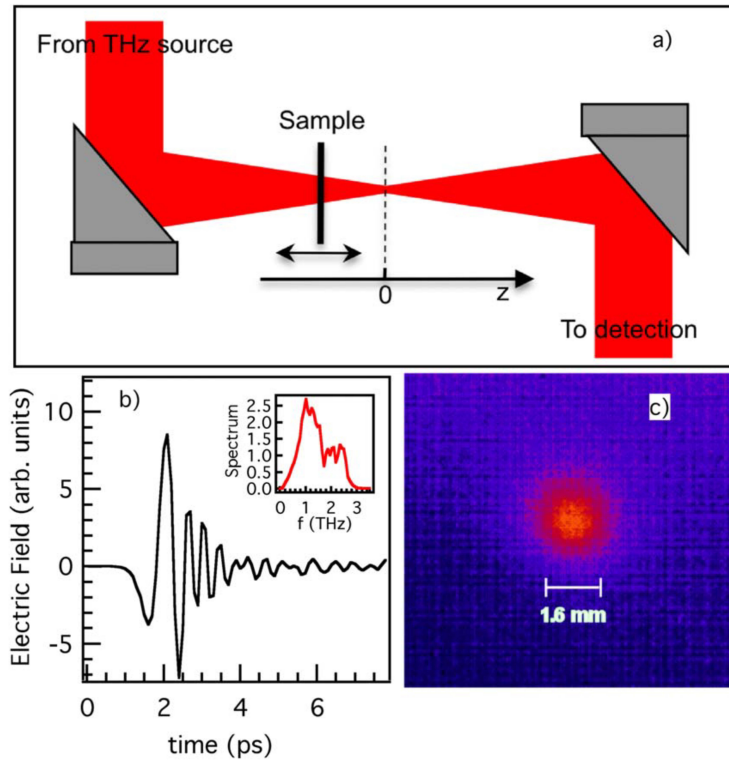


Figure 3.4: (a) Schematic of the THz Z-scan setup. (b) Temporal profile of the THz pulse emitted from the large aperture ZnTe source [Blanchard et al. (2007)]. (c) THz spot intensity profile measured by a pyroelectric camera at the focus. The $1/e^2$ diameter of the THz spot is 1.6 mm.

An open aperture Z-scan experiment was used to explore position and electric field dependent measurements of nonlinear transmission of THz pulses at different position along the propagation axis. A schematic representation of a typical open aperture Z-scan experimental setup is depicted in Fig. 3.4. It consists of a THz pulse focused by off-axis parabolic mirrors and an n-doped InGaAs sample to be scanned along the focus. Figure 3.4 (a) shows the sample scanned through the focus of an intense THz pulse to measure the intensity dependent transmission along the propagation axis through the focus.

A large aperture ZnTe OR source generated picosecond THz pulses in the frequency range of $\sim$ 0.1-3 THz with a pulse energy of about 0.8 $\mu$J at a repetition rate of 100 Hz [Blanchard et al. (2007)]. The temporal profile of the THz pulse generated from this source is shown in Fig. [3.4] (b) and the corresponding power spectrum is displayed in the inset. The $1/e^2$ spot diameter of the THz pulse focused by the off-axis parabolic mirror measures 1.6 mm as shown in Fig. 3.4 (c). Figure 3.5 (a) shows Z-scan normalized transmission of the total THz pulse energy through the sample measured with a standard pyroelectric detector after illuminating the sample with pulse energy of 0.8 $\mu$J (peak electric field of 200 kV/cm). The black curve is a THz Z-scan result for InGaAs epilayer on an InP substrate, and red curve is for InP substrate alone. As evident from the black curve of Fig. 3.5 (a), a significant absorption bleaching effect is observed near the focus of the Z-scan relative to the absorption away from the focus. This bleaching effect is attributed to THz-pulse-induced intervalley scattering that reduces the conductivity of the epilayer, thus increasing THz transmission [Razzari et al. (2009)]. The same scan carried out on a bare InP substrate does not show such enhanced transmission effect at the focus. It is evident that the observed nonlinear bleaching process depends on the conductivity of the InGaAs film alone. The transmission is enhanced only when carriers are scattered to the satellite valleys as discussed earlier. We found evidence to suggest that at low THz field excitation, which is insufficient to induce intervalley scattering, only 3% of the incident total THz pulse energy is transmitted through the sample placed at the THz focus due to the high conductivity of the film. Similar measurements in substrate, InP, shows an overall transmission of about 60%.

Figure 3.5 (b) shows the temporal profiles of the transmitted THz pulses at different Z-scan positions and Fig. 3.5 (c) shows normalized transmission of the time integral of the modulus square of the transmitted electric field as a function of the z position along the scan, which is proportional to the direct measured transmitted THz pulse energy plot of Fig. 3.5 (a). Figure 3.5 (d) shows the temporal profile of the normalized THz electric field differential transmission at different z position along the scan. As shown in Fig. 3.5 (d) at a fixed THz field peak electric field excitation the dynamics of the bleaching process are evident for a Z-scan result plotted for a sample placed at the THz focus than a position far away from the focus. A similar study in a photoexcited GaAs sample using an optical pump/THz probe (OPTP) technique in the same experimental setup has shown intervalley scattering mechanism is responsible for the observed bleaching of the THz pulse absorption effects at high THz fields [Su et al. (2009)].
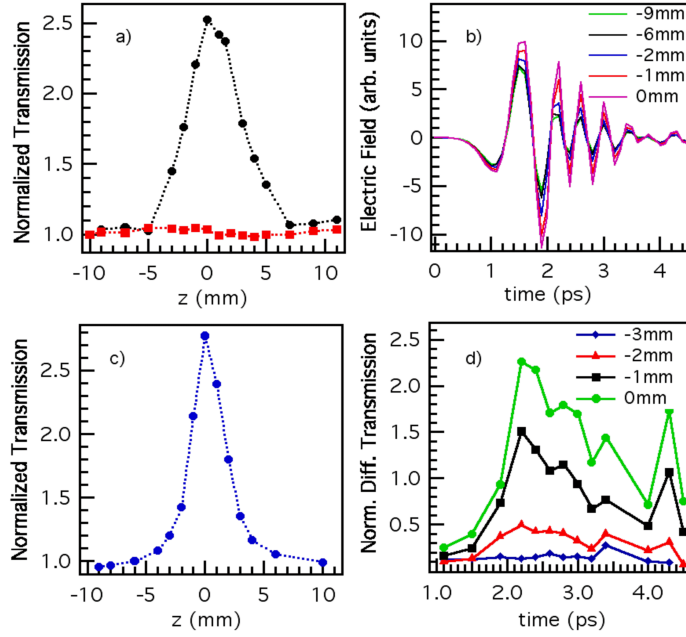
Figure 3.5: (a) Z-scan normalized transmission of the total THz pulse energy measured with a pyroelectric detector after the sample (black curve) and InP substrate alone (red curve). (b) Transmitted THz pulse electric field for different positions of the Z scan. (c) Normalized transmission of the time integral of the modulus squared of the transmitted electric field as a function of the z position along the scan. (d) Normalized electric field differential transmission as a function of time for different z positions along the scan. Note that the initial positive slope is related to the THz pulse duration and the population rate, while the negative slope is indicative of the scattering back of carriers to the $\Gamma$-valley.

## 3.7 Intervalley scattering induced by intense THz pulses in photoexcited GaAs [Su et al. (2009)]

A 0.5 mm thick SI-GaAs sample was used in the OPTP experiment to explore the nonlinear interaction of intense THz pulses with photoexcited carriers by monitoring the field amplitude attenuation at low and high THz fields. High electric field THz probe pulses were generated from a large aperture ZnTe THz source [Blanchard et al. (2007)]. The SI-GaAs sample is placed at the THz focus and an 800 nm optical pump beam of 8 $\mu J/cm^2$ fluence is used to photoexcite electrons and holes. The 800 nm-wavelength optical excitation leads to the injection of electrons to the central conduction band (Γ-valley) and forms the transient conducting layer.
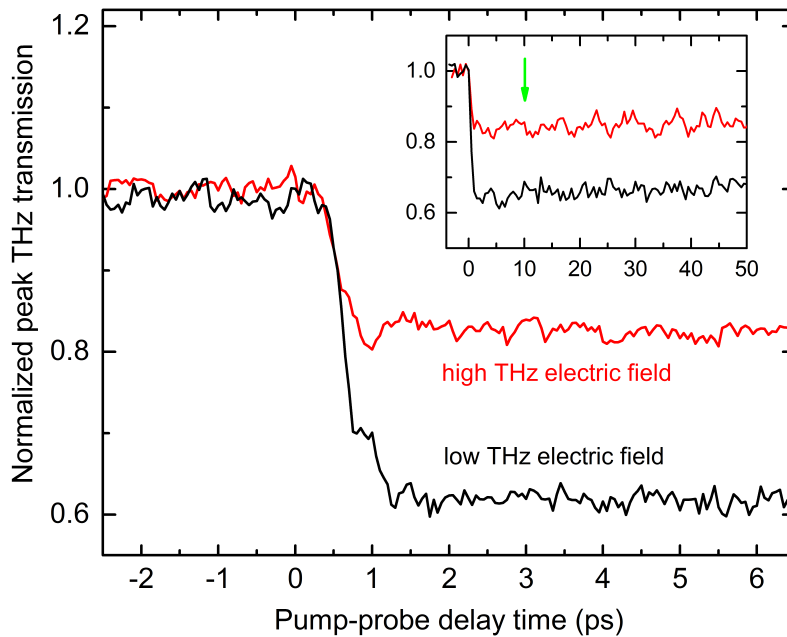


Figure 3.6: Normalized transmission of the peak THz pulse electric field at low (black line) and high (red line) THz fields as a function of pump-probe delay time with respect to a 800 nm, 50 fs, optical pump pulse. The inset shows the corresponding long-term dynamics and the delay at which spectroscopy was performed (green arrow at 10 ps).

Unexcited semiconductors are transparent to THz pulses. However, depending on the strength of the driving fields, phtoexcited SI semiconductors shows nonlinear time-dependent THz transmission. Figure 3.6 shows the normalized transmission of the main peak of the THz probe pulses at low (4 kV/cm) and high (173 kV/cm) THz electric field strengths as function of pump-probe delay time. The optical pump pulse overlaps the peaks of the THz probe pulse at t = 0 ps, and as a result the induced photoconductivity reduces the transmission approximately by 40 % (black line) and 20% (red line) at low and high THz field excitations, respectively. The decrease of the transmission takes about 1 picosecond and arrives at a temporal steady state. The long-term dynamics is shown in the inset.

Figure 3.7 shows the dynamic response with and without optically generated charge carriers for low and high THz fields. The THz waveforms are normalized to the transmission through the unexcited GaAs sample. The blue line in (a) and (b) is the fit by the dynamic intervalley-electron-transfer model to the measured THz waveform transmitted through the photoexcited GaAs. The green lines represent the fraction of photoexcited electrons in the central $\Gamma$-valley as a function of time according to the model calculations. The transmitted THz waveforms are measured through unexcited sample at a negative delay times (thin black line) and in the photoexcited sample after 10 ps of pump-probe delay times (open red circles). The transmission of the high-field beam Fig. 3.7 (b) is significantly enhanced as compared to the low-field case Fig. 3.7 (a), suggesting a bleaching of the charge carrier absorption at higher fields. Moreover, the trailing part of the waveform features almost no change in amplitude or phase compared to the unexcited case at high THz fields. The observed bleaching effect at high THz probe fields is attributed to THz-pulse-induced intervalley scattering of electrons between the central $\Gamma$ and L valleys of GaAs conduction bands. High field THz probe pulse that is able to induce intervalley scattering will effectively see less conductivity in the photoexcited GaAs sample as compared to low-field cases where no intervalley scattering occurs. The deviation obtained from the calculation with and without $\Gamma$-L intervalley scattering is shown in Fig. 3.7(c) in red and black lines, respectively. The grey shaded region between the deviation curves shows how the deviation is minimized in the trailing part of the waveform if $\Gamma$-L intervalley scattering is taken into account.
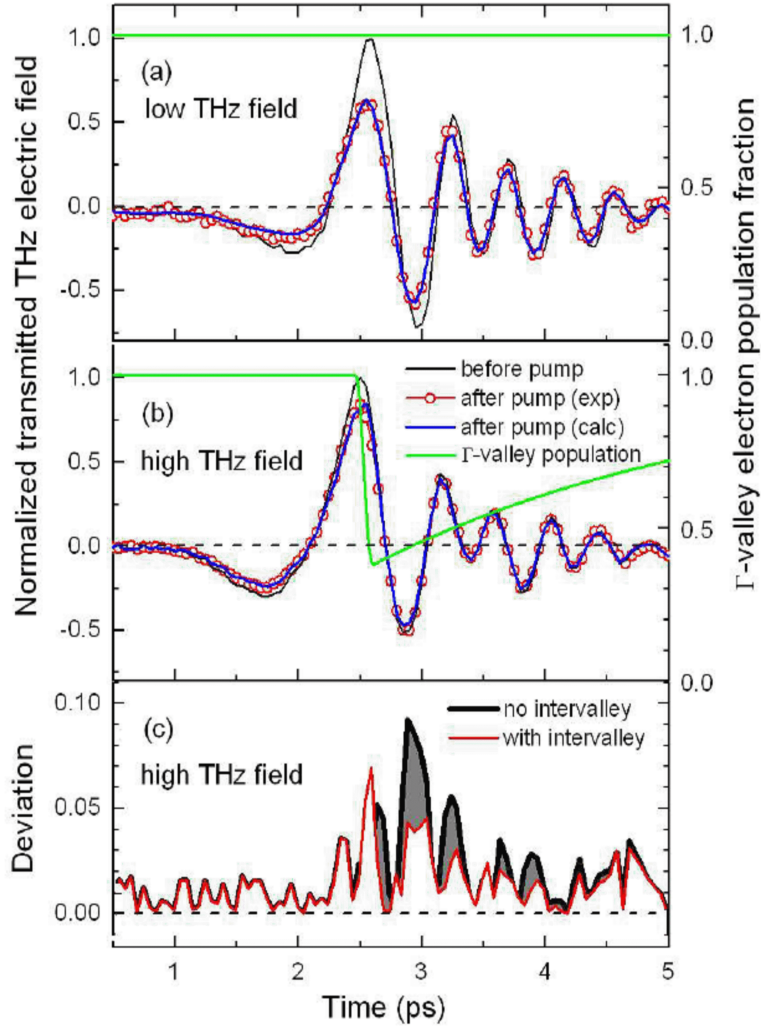
Figure 3.7: Normalized transmitted THz electric fields measured before (thin black line) and 10 ps after photoexcitation (open red circles) of the GaAs sample by the 800 nm optical pump pulse under (a) low and (b) high THz probe fields. The time-dependence of the magnitude through the photoexcited GaAs at high THz probe fields is shown in (c). The red and black lines in (c) correspond to the deviation obtained with and without $\Gamma$-L intervalley scattering included in the calculation, respectively.

# CHAPTER 4

# Dynamic intervalley-electron-scattering model

## 4.1 Introduction

Numerical calculations of carrier transport in semiconductors begin by assuming that electrons behave as classical particles which obey Newton's laws of motion. However, the carrier scattering should be treated quantum mechanically, the dynamics of carrier transport is treated by the wave function $\Psi(\mathbf{r}, t)$ [Lundstrom (2000)]. The dynamical properties of carriers inside semiconductors are thus described by solving the Schrödinger equation,

$$i\hbar \frac{\partial \Psi}{\partial t} = \hat{H}\Psi \tag{4.1}$$

appropriate for a given crystal lattice in the Brillouin zone, where $\hat{H}$ is the Hamiltonian which characterizes the total potential energy, which includes the crystal potential (electrostatic potential due to the atoms) and the built-in or externally applied potential to the crystal. If the applied and induced (built-in) potentials are varying slowly in comparison to the electrostatic potential of atoms, the carrier dynamics are treated by the semi-classical approximation solution of Eq. 4.1. However, for rapidly varying potentials that involve collisions, scattering should be treated quantum mechanically.

The energy of free carriers in an isotropic non-parabolic band with wave vector $\boldsymbol{k}$ is approximated based on $\boldsymbol{k} \bullet \mathbf{p}$ perturbation theory. For a known band structure of semiconductors, the energy of carriers can be expanded in a Taylor series as

$$\varepsilon(k) = \varepsilon(0) + \frac{\partial \varepsilon(k)}{\partial k}\mid_{k=0} k + \frac{1}{2}\frac{\partial^2 \varepsilon(k)}{\partial k^2}\mid_{k=0} k^2 + ... \tag{4.2}$$

and further simplified as,

$$\frac{\hbar^2 k^2}{2m^*} = \varepsilon(k) + \alpha\varepsilon(k)^2 + \beta\varepsilon(k)^3 + ... \tag{4.3}$$

where $\hbar$ is Plank's constant, $k$ is the wave number, m$^*$ is the effective mass of electrons at the bottom of the conduction band, $\alpha$ and $\beta$ are the conduction band parameters. In this model we will consider only the conduction bands in n-doped InGaAs as well as photoexcited GaAs samples. Low field transport creates non-energetic carriers in the conduction band and the electron distribution is centered close to the band minimum at $\mathbf{k} = 0$. The band curvature is approximately parabolic at this minimum, as a result the carrier energy is parabolic and described by the lowest order of the Taylor expansion of Eq. 4.3,

$$\varepsilon(k) = \varepsilon(0) + \frac{\hbar^2 k^2}{2m^*} \tag{4.4}$$

where

$$\frac{1}{m^*} \equiv \frac{1}{\hbar^2} \frac{\partial^2 \varepsilon(k)}{\partial^2 k} \tag{4.5}$$

is the effective mass of electrons and $\varepsilon(0)$ is the thermal energy of carriers.

However, high field transport creates energetic carriers that alters the conduction band curvature for carries from parabolic to nonparabolic. In this high energy regime, the $\varepsilon - \mathbf{k}$ relation varies non-parabolically with $\mathbf{k}$ such that higher order terms of the electron energy given in Eq. 4.3 cannot be ignored and the approximate solution derived by the $\mathbf{k.p}$ approximation becomes,

$$\varepsilon(1 + \alpha\varepsilon) = \frac{\hbar^2 k^2}{2m^*} + \frac{3}{2}k_B T \tag{4.6}$$

where $\alpha$ is the nonparabolicity parameter of the conduction band given by

$$\alpha = \frac{1}{\varepsilon_g}\left(1 - \frac{m^*}{m_0}\right) \tag{4.7}$$

where m$_0$ is the electron rest mass. However, the effective mass of the nonparabolic energy band is modified to, $m^{**} = m^*(1 + \alpha\varepsilon)$, due to the nonparabolicity factor as,

$$\frac{1}{m^{**}} \equiv \frac{1}{\hbar^2} \frac{\partial^2 \varepsilon_k}{\partial k^2} \tag{4.8}$$

Here $\varepsilon_k$ is the energy given in Eq. 4.6. For small $\boldsymbol{k}$, m$^{**}$ is consistent with m$^*$, but increases with $\boldsymbol{k}$. The effect of nonparabolic energy bands induced through high-field interaction with the system is the increase in effective mass of electrons and a decrease in the conductivity

results in the rate of Γ-L valley transfer decreasing. The velocity of carriers is given by,

$$v = \frac{1}{\hbar}\frac{d\varepsilon_k}{dk} = \frac{1}{\hbar}\nabla_k \varepsilon_k \qquad (4.9)$$

## 4.2 Drude model

In the Drude model, charge carriers are considered to move freely in an applied electric field $\mathbf{E}$, with drift velocity $\mathbf{v} = \mu\mathbf{E}$, for a Drude relaxation time $\tau$, where $\mu = \frac{e\tau}{m^*}$ is carrier mobility. The carrier transport rate equation is then given by

$$m\frac{d\mathbf{v}}{dt} = e\mathbf{E} - \frac{\mathbf{v}}{\tau} \qquad (4.10)$$

with an induced current density $\mathbf{J} = en\mathbf{v}$, where $m$ is the carrier mass, e is electron energy, and $n$ is carrier density. In the steady-state (dc or low field), $\frac{d\mathbf{v}}{dt} = 0$, and the rate Eq. 4.10 becomes

$$e\mathbf{E} = \frac{m^*\mathbf{v}}{\tau} \qquad (4.11)$$

For an applied ac field of the form $\mathbf{E}(t) = Re\left\{\mathbf{E}(\omega)e^{-i\omega t}\right\}$ the solution of Eq. 4.10 has the form [Cooke (2006)]

$$\mathbf{v}(t) = Re\left\{\mathbf{v}(\omega)e^{-i\omega t}\right\} \qquad (4.12)$$

where $\omega$ is frequency. Substituting Eq. 4.12 in to Eq.4.10 yields,

$$(-i\omega)\,\mathbf{v}(\omega) = \frac{\mathbf{v}(\omega)}{\tau} - e\mathbf{E}(\omega) \qquad (4.13)$$

After rearranging by using terms of $(\mathbf{J} = en\mathbf{v})$ and $\left(\sigma_{dc} = \frac{\mathbf{J}}{\mathbf{E}}\right)$, Eq. 4.13 simplified to the well known Drude model complex conductivity equation

$$\begin{aligned}
\tilde{\sigma} = \sigma_1 + i\sigma_2 &= \frac{\sigma_{dc}}{1 - i\omega\tau} \\
\sigma_1 &= \frac{\sigma_{dc}}{1 + (\omega\tau)^2} \\
\sigma_2 &= \frac{\sigma_{dc}\omega\tau}{1 + (\omega\tau)^2}
\end{aligned} \qquad (4.14)$$

When $\omega = 0$, the complex conductivity is purely real, i.e., $\sigma_1 = \sigma_{dc}$ and $\sigma_2 = 0$. For ultrashort relaxation times ( $\omega\tau << 1$), $\sigma_1 \approx \sigma_{dc}$ and $\sigma_2 = 0$. Figure 4.1 shows the real ($\sigma_1$) and imaginary ($\sigma_2$) component of a heavily doped InGaAs sample characterized using a THz-TDS system in our lab. The crossover frequency, $\sigma_1 = \sigma_2$ ($\omega\tau = 1$), allows to determine both $\tau$ and plasma frequency $\omega_p$. Based on the analysis, we inferred the carrier scattering
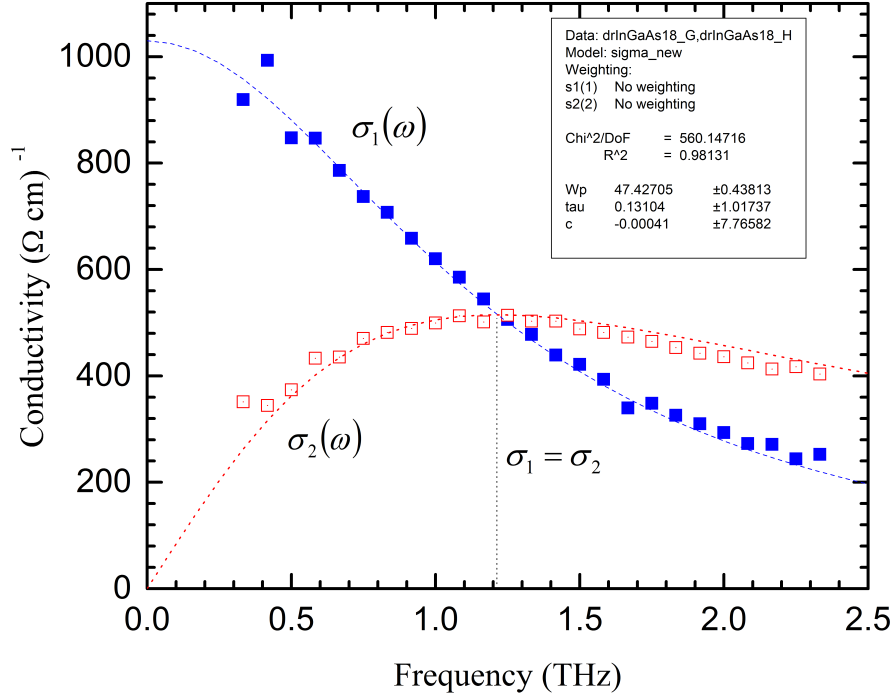
Figure 4.1: Real and imaginary components of the THz conductivity of an n-doped InGaAs sample extracted using Drude model from a THz-TDS measurement. The carrier density and scattering time were determined to be $1.75 \times 10^{18} cm^{-3}$ and 130 fs, respectively.

time $\tau = 130$ fs with carrier density $1.75 \times 10^{18} cm^{-3}$ for an n-doped InGaAs sample.

## 4.3 Drude-based dynamic intervalley scattering model

The Drude model is the most common model used to give a quick, practical and rough physical insight into the most important THz response of free carriers in solids. We utilize a simple but realistic model of Drude based dynamic intervalley-electron scattering, for the band-to band transition of electrons states and their response to THz fields. This model was successfully used for nonlinear THz dynamics characterization in experiments as discussed in the preceding Chapter and later in Chapters 7 and 8. Note that in the model we take

into account the central Γ-valley and the closest satellite L-valleys only. For simplicity, we have neglected scattering into the high-lying X-valleys, as a result the current density $\mathbf{J}$ is determined from the contribution of electrons in both Γ and L-valleys ($\mathbf{J} = en_\Gamma \mathbf{v}_\Gamma + en_L \mathbf{v}_L$), $e$ is charge of electron, $n$ is electron density in the conduction band, and $v$ is the drift velocity given in Eq. 4.9. The total current at any time is taken as the sum of the currents induced in the conduction valleys, $\mathbf{J} = \mathbf{J}_\Gamma + \mathbf{J}_L$. The electron motion driven by the transmitted THz field, $\mathbf{E}_t$, and the population of electrons in the Γ-valley can be described by the two dynamic equations of motion and carrier density rate equations:

$$\begin{cases} \hbar \frac{d\mathbf{k}_\Gamma(t)}{dt} = e\mathbf{E}_t - \frac{\hbar \mathbf{k}_\Gamma(t)}{\tau_\Gamma} \\ \hbar \frac{d\mathbf{k}_L(t)}{dt} = e\mathbf{E}_t - \frac{\hbar \mathbf{k}_L(t)}{\tau_L} \end{cases} \tag{4.15}$$

$$\frac{dn_\Gamma}{dt} = -\frac{n_\Gamma}{\tau_{\Gamma L}} + \frac{n_0 - n_\Gamma}{\tau_{L\Gamma}} \tag{4.16}$$

$$n_\Gamma + n_L = n_0 \tag{4.17}$$

where $\mathbf{E}_t$ is the transmitted field, and $\mathbf{k}$ is the wave vector, $e$ is charge of electron, $n_\Gamma$ is electron density in the central Γ-valley, $n_0$ is total electron density, $\tau_\Gamma$ is the electron momentum relaxation time, $\tau_{\Gamma L}$ is the intervalley scattering times from Γ to L valley, and $\tau_{L\Gamma}$ is the scattering back time from L- to Γ-valleys. $\hbar \mathbf{k}$ denotes the average carrier momentum, which is derived from the total energy in each valley,

$$\begin{cases} \varepsilon_\Gamma(1 + \alpha_\Gamma \varepsilon_\Gamma) = \frac{\hbar^2 k_\Gamma^2}{2m_\Gamma^*} + \frac{3}{2}k_B T \\ \varepsilon_L(1 + \alpha_L \varepsilon_L) = \frac{\hbar^2 k_L^2}{2m_L^*} + \frac{3}{2}k_B T \end{cases} \tag{4.18}$$

and the effective masses for each valley is calculated using Eq. 4.8. where $\alpha_\Gamma$ and $\alpha_L$ are the nonparabolicity parameter of Γ and L-valley conduction bands and $\frac{3}{2}k_B T$ is the lattice thermal energy at room temperature.

Without interband and intervalley scattering, the dynamic equation of an electron Eq.4.15 is described by the dispersion of its band at a constant rate in momentum space as,

$$\hbar \frac{d\boldsymbol{k}}{dt} = eE(t) \tag{4.19}$$

During carrier transport there are various scattering processes that might be independent of each other, the total scattering rate is the sum of all scattering rates [Singh (2003); p261]. In which $\tau_\Gamma^{-1}$ is modified to the sum of the rate of Γ-valley momentum scattering and the $\Gamma - L$ intervalley scattering. There might be an equivalent $L - L$ intervalley scattering as the driving field increases [Lundstrom (2000)], such effects are not included in the simulation. The rate of transfer from the central Γ-valley to the satellite valley, $\tau_{\Gamma L}^{-1}$, is modeled as
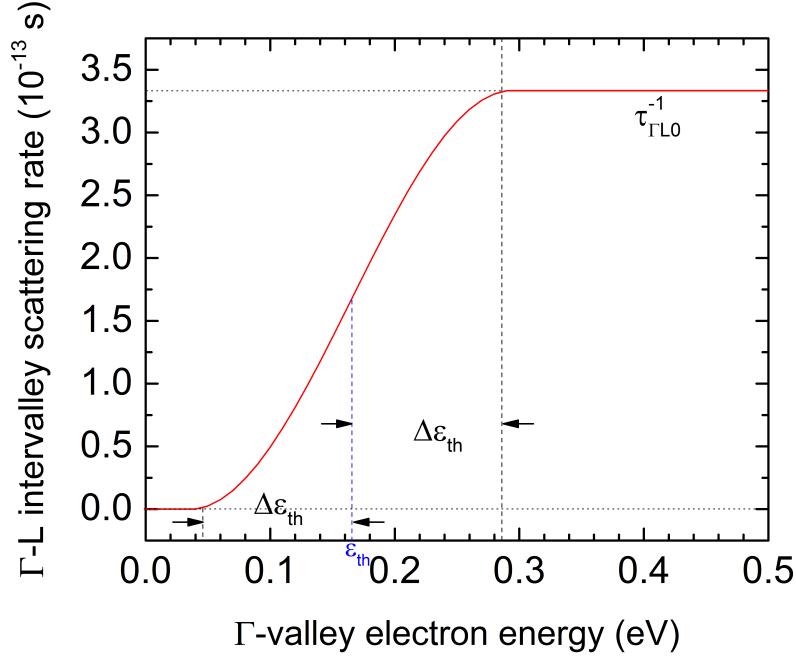
Figure 4.2: The $\Gamma$-L intervalley scattering rate, $\tau_{\Gamma L}^{-1}(\varepsilon_\Gamma)$, as a function of electron energy in the $\Gamma$-valley.

a simplified switch function dependent on the average kinetic energy given in Eq. 4.18 associated to the electrons in the $\Gamma$ valley. However, the reverse rate of transfer of electrons, $\tau_{L\Gamma}^{-1}$, from upper to lower valleys is assumed to be independent of energy within the L-valley [Su et al. (2009)].

$$\tau_{\Gamma L}^{-1}(\varepsilon_\Gamma) = \begin{cases} 0 & \varepsilon_\Gamma \leq \varepsilon_{th} - \Delta\varepsilon_{th} = \varepsilon_1 \\ \tau_{\Gamma L0}^{-1} & \varepsilon_\Gamma \geq \varepsilon_{th} + \Delta\varepsilon_{th} = \varepsilon_2 \\ \text{smooth function} & \varepsilon_1 < \varepsilon_\Gamma < \varepsilon_2 \end{cases} \qquad (4.20)$$

where $\tau_{\Gamma L0}^{-1}$ is the maximum $\Gamma$-L intervalley scattering rate and $\varepsilon$ is the threshold energy with a range given by $\Delta\varepsilon$. Figure 4.2 shows the plot of the intervalley scattering rate equation as a function of the total electron energy. The $\Gamma$-L transfer intervalley scattering rate, $\tau_{L\Gamma}^{-1}$, is made smooth" by inserting a seventh-order polynomial section into the function such that it is continuous up to the third derivative [Anile and Hern (2002); Su et al. (2009)]. For simplicity, we neglect the complicated electron distribution function under conduction band and take average electron momentum as crystal momentum $\hbar\boldsymbol{k}$. The transmission of the

43

THz pulse through a thin conducting film with thickness $d$ on an insulating substrate and index $n$ that is extracted in time domain based on the boundary condition is given as :

$$\mathbf{E}_t = \frac{1}{Y_0 + Y_S}\left(2Y_0\mathbf{E}_i - \mathbf{J}d\right) \tag{4.21}$$

where $\mathbf{E}_t$ and $\mathbf{E}_i$ are the transmitted and incident THz fields, respectively, $Y_0 = (377\Omega)^{-1}$ is free space admittance, and $Y_s = nY_0$ is substrate admittance. The details of the derivation of Eq. 4.21 is given in Chapter 6.

For the incident electric field, $\mathbf{E}_i$, we use an electro-optically measured THz pulse with it's time integral value confirmed to be zero as shown in Fig. 4.3 to avoid any artifacts that can cause unwanted results. The peak field amplitude of the incident THz pulse is scaled in the iteration from low to high electric field amplitude based on the THz pulse energy and spot size measured at the focus. In the simulation linear and nonlinear conditions are considered depending on the driving electric field strength. In the nonlinear condition, nonparabolic effects are taken into account for both $\Gamma$ and L-valleys, i.e., $m_\Gamma^{**}(\varepsilon_\Gamma) = m_{\Gamma 0}^*(1 + \alpha_\Gamma\varepsilon_\Gamma)$ and $m_L^{**}(\varepsilon_\Gamma) = m_{L0}^*(1 + \alpha_L\varepsilon_L)$, respectively.

Figure 4.3 (a) is the original FSEOS measured THz pulse and Fig. 4.3 (c) is the smoothed pulse used in the model. Methods of smoothing and the Matlab code is included in Appendix B. Figures 4.3 (b) and (d) are the corresponding time integral of the pulses, respectively. The transmitted THz electric field, $\mathbf{E}_t$ accelerates the electrons in the conducting film and provides additional momentum by following the transport equation 4.15 and 4.16, which leads to a modification of the curvature of the conduction band as well as the conductivity of the sample. The transmitted THz field through the film is sensitive to the response of free carriers that is proportional to the carrier concentration. However, the change in the distribution of electrons amongst the conduction valleys alters the overall conductivity of the film that in turn controls the transmitted field itself nonlinearly. At high incident fields electrons can acquire high energy, and these energetic electrons driven by the transmitted field can create a population transfer between the lowest conduction $\Gamma$-valley into higher conduction (L and X) side valleys. The scattering of carriers to the satellite valleys leads to a much smaller mobility than the lowest conduction valley due to higher effective mass in the satellite valleys. Table 4.1 shows comparison of the fitting parameters used in the model for different experiments. A step by step flowchart of the model is given in Appendix D.
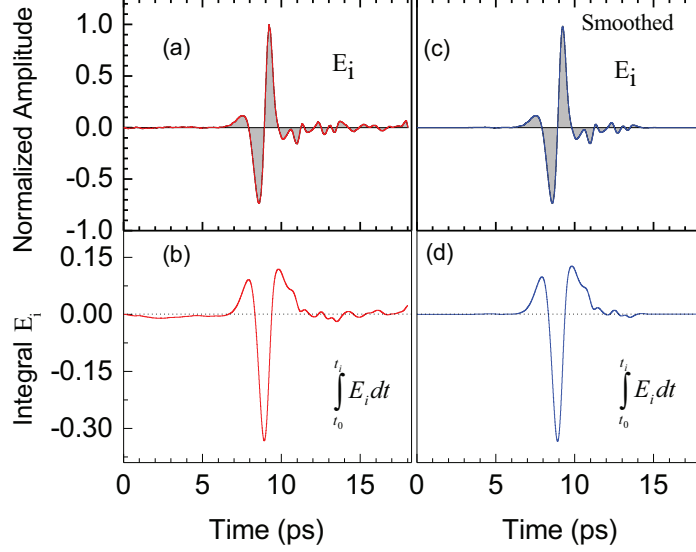
Figure 4.3: EO measured THz pulse used for the model. (a) An electro-optically measured THz pulse signal (red line) and the corresponding smoothed pulse using cosine taper method. (b) Integral of the THz pulse of (a). (c) Smoothed THz pulse of (a) used for the Drude dynamic model calculation. (d) Integral of the smoothed THz pulse in (c).

Table 4.1: Fitting parameters.

| Parameter | Symbols | Z-scan* parameters | TPTP parameters | Ultrafast transient voltage | Units |
|---|---|---|---|---|---|
| Nonparabolicity factor | $a_\Gamma$ | 1.33 | 1.33 | 1.33 | $eV^{-1}$ |
| carrier concentration | $n_0$ | $1.7\times10^{17}$ | $2\times10^{18}$ | $2\times10^{18}$ | $cm^{-3}$ |
| $\Gamma$-valley scattering time | $\tau_\Gamma^{-1}$ | $1.00\times10^{13}$ | $0.56\times10^{13}$ | $1.00\times10^{13}$ | $s^{-1}$ |
| Threshold energy | $\varepsilon_{th}$ | 0.13 | 0.27 | 0.165 | eV |
| $\Gamma$-L intervalley scattering time | $\tau_{\Gamma L0}^{-1}$ | $3.33\times10^{13}$ | $3.33\times10^{13}$ | $3.33\times10^{13}$ | $s^{-1}$ |
| L-$\Gamma$ intervalley scattering time | $\tau_{L\Gamma}^{-1}$ | $2.50\times10^{11}$ | $2.50\times10^{11}$ | $2.50\times10^{11}$ | $s^{-1}$ |

# CHAPTER 5

# High power terahertz pulse generation by OR in LiNbO$_3$

## 5.1  Introduction

THz pulse generation using tilted-pulse-front OR in LiNbO$_3$, first demonstrated by [Hebling et al. (2002)], has been adopted by many THz groups [Yeh et al. (2008); Stepanov et al. (2008); Fulop et al. (2010); Hirori et al. (2011); Blanchard et al. (2014)]. It has become the leading table-top high power THz pulse generation approach in recent years, because it is the most efficient technique for the following two important reasons, LiNbO$_3$ has the highest effective nonlinear electro-optic coefficient relative to other EO crystals which is suitable for OR [Hoffmann and Fulop (2011); Fulop et al. (2010); Blanchard et al. (2011)] and second, LiNbO$_3$ has a large band gap which prevents two photon absorption. This circumvents THz absorption by free carriers generated by the 800 nm pump pulses [Yeh et al. (2008)]. The large band gap, therefore permits high pumping intensities, and consequently almost unlimited up-scaling of THz energy with optical pump power compared with other sources [Hoffmann and Fulop (2011)].

In the past two decades, significant progress has been made towards generation of near-single-cycle THz pulses with several micro-joule THz pulse energies [Reimann (2007)]. Today such sources are common with pulse energies of 10 $\mu$J [Yeh et al. (2007)], 30 $\mu$J [Stepanov et al. (2008)], and 50 $\mu$J [Stepanov et al. (2003)], 125 $\mu$J [Fulop et al. (2012)] having been reported using such a LiNbO$_3$ tilted-pulse-front source. However, the imaging error from the grating to the LiNbO$_3$ crystal leads to an image distortion, an asymmetric THz intensity profile, and scattering, divergence and spatial variation inside the crystal [Fulop et al. (2010); Hirori et al. (2011)]. These issues limit the optimum THz conversion efficiencies and distort the waveform, restricting the utilization of LiNbO$_3$ sources for spectroscopic applications. In a recent study, [Hirori et al. (2011)] were able to overcome the imaging error by re-designing

the imaging geometry. Consequently, the focus of the generated THz pulses approached the diffraction limit, resulting in THz fields at the focus as high as 1.2 MV/cm. More recently, using an 800 nm pump beam [Blanchard et al. (2014)] reported the highest pump-to-THz energy conversion efficiency.

In addition to imaging errors, THz pulse generation in LiNbO$_3$ is critically dependent on the pulse duration of the chirped, femtosecond optical pump pulse. [Yeh et al. (2008)], reported that setting the optical pump pulse duration to 400 fs by adjusting the amplifier compressor optimizes the generated THz energy. Conversely, [Stepanov et al. (2008)] found that increasing the pump pulse duration beyond the minimum, 50 fs setting led to a decrease in conversion efficiency. Therefore, the physics of optimization of THz pulse generation in LiNbO$_3$, particularly the optical pump pulse duration dependence, demands clarification. The main concern in addressing this issue is that when the pump pulse is adjusted to a certain pulse duration, the sampling beam will be chirped as well, which will lead to improper EO characterization of the generated THz pulses. Secondly, the chirp direction of the pump pulse was not addressed in either Ref. [Yeh et al. (2008) or Stepanov et al. (2008)].

This chapter introduces an improved new scheme which clarifies and examines the effect of pre-chirping the input optical pump pulses on the emitted THz pulses from the tilted-pulse-front OR LiNbO$_3$ source. This is realized by introducing two separate compressors to independently control the pulse duration of the generation and detection optical pulses as detailed in section 5.6. By pre-chirping the pump pulse duration, the conversion efficiency, THz pulse peak and spectral bandwidth were mapped out as a function of optical pump pulse duration. We found the optical pump chirp direction to be crucial for pulse energy optimization. The detected field dependence on the polarization of the optical pump pulse was also addressed both experimentally and theoretically.

OR schemes for THz generation have been found to be very useful and simple to implement experimentally, the bandwidth of the generated THz pulses from all OR sources is limited by phonon absorption and dispersion. It was recently suggested that THz pulse generation from air plasmas has opened up the THz spectrum through to the mid-IR [Cook and Hochstrasser (2000); Kress et al. (2004); Bartel et al. (2005); Xie et al. (2006); Kim et al. (2007); Karpowicz et al. (2008); Dai et al. (2009); Klarskov et al. (2013)], the spectral bandwidth from air plasma sources is limited by the gate pulse duration only. Common nonlinear optical crystals that have been used to generate THz radiation using optical rectification of a femtosecond laser pulses at a center wavelength of 800 nm are listed in Table 5.1.

The optical rectification in LiNbO$_3$ occurs through impulsive stimulated Raman scattering, which means the femtosecond optical pulse drive phonon's to emit THz pulses

Table 5.1: Parameters of common nonlinear optical crystals used for optical rectification at $\lambda_0 = 800$ nm pump. $E_g$: energy band-gap, $d_{eff}$: effective nonlinear coefficient, PA, 1PA, 2PA, and 3PA are photon absorption, one-photon, two-photon, and three-photon absorption, respectively. $\alpha_E$: absorption coefficient. [Hebling et al. (2008); Fulop et al. (2010); Hoffmann and Fulop (2011)]

| Material | $E_g$ (eV) | r $(10^{-12}m/V)$ | $d_{eff}$ $(10^{-12}m/V))$ | PA $(\lambda_{800nm})$ | $n_{800}$ | $n_{THz}$ | $\alpha_{THz}$ $(cm^{-1})$ |
|---|---|---|---|---|---|---|---|
| GaAs | 1.43 | 1.43 | 65.6 | 1PA | 4.18 | 3.61 | 0.5 |
| GaP | 2.27 (indirect) 2.48 (direct) | 0.97 | 24.8 | 1PA | 3.57 | 3.34 | 1.9 |
| ZnTe | 2.26 | 4.04 | 68.5 | 2PA | 3.31 | 3.17 | 1.3 |
| GaSe | 2.02 | 1.7 | 28 | 2PA | 3.13 | 3.72 | 0.07 |
| LiTaO$_3$ | | 30.5 | 161 | | 2.22 | 6.42 | 46 |
| LiNbO$_3$ | 3.8 | 30.9 | 168 | 3PA | 2.23 | 5.16 | 16 |
| DAST | | 77 | 618 | | 3.31 | 2.14 | 150 |

[Dougherty et al. (1992)]. Optical rectification methods in nonlinear electro-optic crystals are limited by the crystal response to the ultrafast optical pulse in which the phonon dispersion and multiphoton absorption limits the spectral bandwidth. Taking into account THz absorption, for the absence of optical pump depletion and absorption, the THz generation efficiency $\eta_{THz}$ in nonlinear electro-optic crystals is expressed as [Hebling et al. (2008)],

$$\eta_{THz} = \frac{2\Omega_{THz}^2 d_{eff}^2 L^2 I}{\epsilon_0 n_g^2 n_{THz} c^3} \exp\left\{-\alpha_{THz}L/2\right\} \frac{\sinh^2[\alpha_{THz}(L/4)]}{[\alpha_{THz}(L/4)]} \tag{5.1}$$

where $\Omega_{THz}$ is THz frequency, $d_{eff}$ is effective nonlinear coefficient, $I$ is intensity of optical pump beam, $\epsilon_0$ is vacuum permittivity, $c$ is speed of light in free space, L is crystal length, $\alpha_{THz}$ is intensity absorption coefficient of LiNbO$_3$ at THz frequencies, $n_{NIR}$ is the group refractive index at 800 nm, and $n_{THz}$ is the phase refractive index at $\Omega_{THz}$, respectively.

For $\alpha L \ll 1$, the THz absorption by the nonlinear medium is negligible and Eq. 5.1 is simplified to

$$\eta_{THz} = \frac{2\Omega_{THz}^2 d_{eff} L^2 I}{\epsilon_0 n_g^2 n_{THz} c^3} \tag{5.2}$$

However, the associated spectral bandwidth of the measured THz pulses is limited to the low THz frequency regime by the gate pulse duration and material response, like phonon absorption, and pulse dispersion. However, a recent breakthrough of air plasma (photoionization

of air by the fundamental and SHM ultrashort pulses) THz pulse generation [Petersen and Tokmakoff (2010); Fuji and Suzuki (2007)]-detection scheme overcome the material response issue and extends the THz pulse spectrum beyond the entire THz gap to the mid-IR [Dai et al. (2006); Karpowicz et al. (2008)] that is only affected by the gated pulse duration.

## 5.2 High-power THz pulse generation using tilted-pulse-front optical rectification in LiNbO$_3$

As mentioned previously, efficient THz generation by difference frequency mixing (OR) requires phase matching of the group velocity of the ultrashort pump pulse to the phase velocity of the generated THz pulse inside the generating crystal. Phase-matching and frequency-matching conditions of wave mixing (frequency mixing) are reproduced from the conservation of photon momentum and energy. In the case of THz pulse radiation through OR in nonlinear media the phase matching condition should satisfy the following equation, for collinear generation [Nahata et al. (1996); Hebling et al. (2008); Blanchard et al. (2007)],

$$\Delta k = k(\omega_{NIR} + \Omega_{THz}) - k(\omega_{NIR}) - k(\Omega_{THz}) = 0, \tag{5.3}$$

where $\Delta k$ is the wave vector mismatch, and $k(\omega_{NIR} + \Omega_{THz})$ and $k(\omega_{NIR})$ are the wave vectors of the spectral components of the ultrashort laser pulse that generate the THz radiation of wave vector $k(\Omega_{THz})$. $\omega_{NIR} + \Omega_{THz}$ and $\omega_{NIR}$ are the optical frequency components that lie within the spectrum of the optical pump pulse and $(\Omega_{THz})$ is the emitted THz radiation frequency, respectively.

In a THz optical rectification source with collinear phase matching, the experimental setup is straightforward where a femtosecond laser pulse excites an electro-optic crystal like ZnTe and the emitted THz pulse is detected via electro optic sampling as mentioned in Chapter 2. In this case the pump beam should have as long an interaction length as possible with the generated radiation. This is only possible if the pump travels in the same direction and has the same velocity as the generated THz radiation. This condition is fulfilled collinearly for ZnTe at 800 nm and GaP at $1\mu$m but LiNbO$_3$ has a large index mismatch.

On the other hand, LiNb$O_3$ has a higher electro-optic coefficient than ZnTe and thus potentially higher THz generation efficiency, but collinear phase matched optical rectification is impossible due to a large refractive index mismatch between THz and optical (800 nm) pulses 4.96 and 2.25, at room temperature, respectively. Optical pulses propagate faster than the generated THz pulse, which is consequently emitted at an angle with respect to the propagation direction of the optical pump pulses as depicted in Fig. 5.1 (a). Thus, for
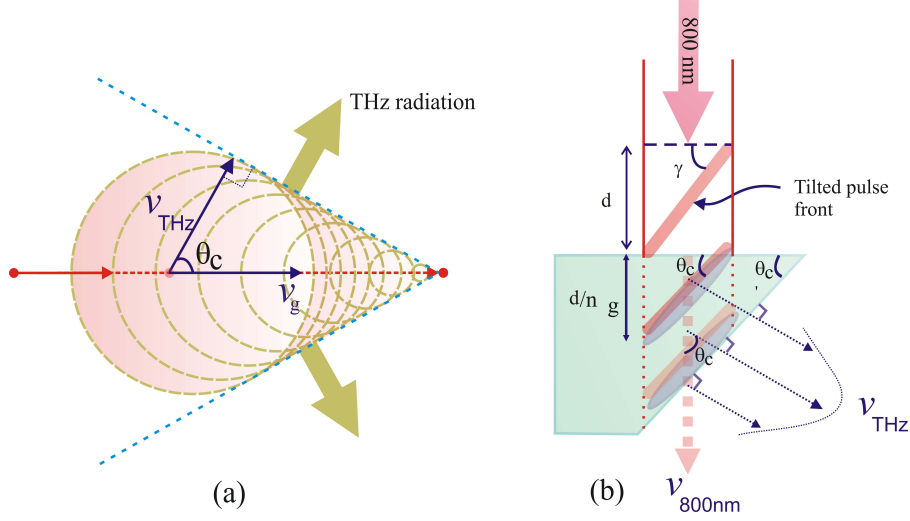
Figure 5.1: Schemes for THz pulse generation in LiNbO$_3$. (a) The THz radiation produced by a focused optical pulse is emitted as a Cherenkov cone. (b) The tilted-pulse-front scheme, the optical pump spot as well as the generated THz radiation are larger in size and in the form of plane waves. This maximizes the optical to THz conversion efficiency. The angle of the tilted-pulse-front incident on the crystal ($\gamma$) is modified upon entering the crystal to $\theta_c$ because the optical group index, n$_g$, is different in LiNbO$_3$ and air.

an efficient frequency down conversion $\Delta k$ in Eq. 5.3 has to be adjusted to become zero. The phase matching condition is given in section A.3 of Appendix A. That can only be achieved using an ingenious way of a pulse-front-tilt geometry proposed by Janos Hebling in 2002 [Hebling et al. (2002)]. Pulse front tilting of the frequency components of the ultrashort pump pulse by grating leads to an angular dispersion. Figure 5.1 shows the non-collinear and collinear scheme of THz pulse generation in LiNbO$_3$. Figure 5.1 (a) illustrates the Cherenkov geometry of THz radiation generated by a point optical pulse propagating through LiNbO$_3$ and Fig. 5.1 (b) details the tilted-pulse-front scheme used to maximize the THz radiation from a LiNbO$_3$ source.

In the case of the Cherenkov geometry, THz radiation is emitted as a cone using a tightly focused optical pulse resulting in inefficient THz generation [Hebling et al. (2002)]. Moreover, it is difficult to collect the emitted THz radiation for applications. In contrast to the focused optical pulse approach, the tilted-pulse-front scheme employs an extended

optical pump spot and improves the optical to THz conversion efficiency through adding up the phases of the generated waves at different position in the material constructively. The THz photons generated at different times will interact with each other and interfere constructively. Therefore, we are adopting the collinear THz pulse generation (tilted-pulse-front) scheme. Thus, the conversion efficiency can be optimized by matching the phase velocity of the THz pulse, $v_{THz}$, to the group velocity of the optical pump pulse, $v_g$ [Hebling et al. (2002)] using the tilted pulse front angle. In the case of Cherenkov radiation, referring to Fig. 5.1, the optical pulse group velocity is related to the phase velocity of THz pulse as,

$$v_g cos(\theta_c) = v_{THz} \tag{5.4}$$

where $v_g$ is the group velocity of the optical pump pulse, $v_g cos(\theta_c)$ is the projection of the group velocity of the optical pump pulse in the direction of the THz pulse propagation direction, and $v_{THz}$ is the velocity of the generated THz pulse. The tilt-angle of the pulse front inside the LiNbO$_3$ crystal can be calculated from Eq.5.4 using the indices of refraction of LiNbO$_3$ mentioned above, yielding

$$\theta_c = \cos^{-1}\left(\frac{v_{THz}}{v_g}\right) = \cos^{-1}\left(\frac{n_g}{n_{THz}}\right) \tag{5.5}$$

For the indices of refraction of LiNbO$_3$ at visible ($n_g = 2.25$) and THz ($n_{THz} = 4.96$) frequencies, the angle $\theta_c$ from Eq. 5.5 is 63$^o$. The LiNbO$_3$ crystal is cut at the tilted pulse-front angle, $\theta_c$, such LiNbO$_3$ the generated THz pulse can be coupled out into free space through the cut surface of the crystal (which is parallel to the wavefront).

## 5.3 Ultrafast Amplifier System in the Ultrafast Nanotools Lab at the University of Alberta

The high-power THz setup is driven by ultrashort femtosecond laser from Micra/Legend Ti:sapphire oscillator-amplifier. Schematic of the standard Legend-Elite amplifier system composed of the seed laser, the pump laser, and the amplifier is shown in Fig. 5.2. The Legend-Elite amplifier laser system amplifies the low energy mode-locked Ti:sapphire short optical pulses in the near infrared provided from the Micra. A cw single-frequency green (532 nm) pump laser of 5 W power pumps the Micra Ti:Sapphire oscillator and producing a mode-locked pulses with bandwidths exceeding 100 nm. A short pulse exits the oscillator and redirect the seed beam into the input port of the Legend, then to the pulse stretcher. The amplifier box contains an optical pulse stretcher, regenerative amplifier (RGA), and optical pulse compressor to amplify the ultrashort pulses from the Micra to the mJ level.
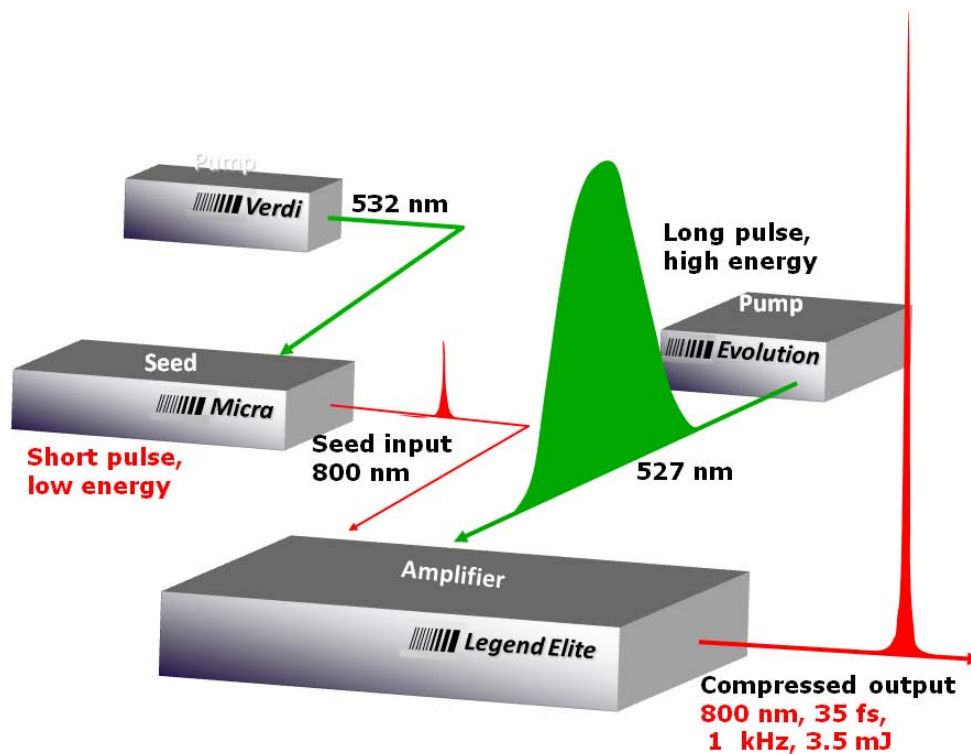
Figure 5.2: Schematic of the Legend-Elite system with Evolution pump and Verdi-pumped Micra seed laser system. The Verdi laser system is a compact solid-state diode-pumped, frequency-doubled Nd:Vanadate (Nd:YVO$_4$) laser that provides single-frequency green (532 nm) output at 5 W power. The Evolution is a diode-pumped, intra-cavity doubled Nd:YLF laser capable of producing Q-switched pulses with average energy greater than 12 mJ at 527 nm at a repetition rates of 1 kHz.

The output pulse from the stretcher then aligned into the RGA, which employs a single Ti:Sapphire laser rod pumped by a pulsed Q-switch, frequency-doubled Nd:YLF laser from the Evolution. The pulse has multi-passed the rod and experienced a gain of $10^6$. Finally, the amplifier delivers a linear horizontally polarized near-IR light pulses centered at a wavelength of 800 nm with average pulse energy of 3.5 mJ at 1 kHz repetition rate and pulse duration of 35 fs.

## 5.4   Tilted-pulse-front scheme

As shown in Fig. 5.3, an amplified down chirped femtosecond beam from the Legend strikes a diffraction grating and the diffracted beam is imaged onto the LiNbO$_3$ crystal using a 75 mm focal length lens that provides a magnification factor that yields the appropriate tilt of the pulse front. There are three distinct regions that affect the tilt angle of the intensity front before illuminating the source crystal: (1) the tilt of the pulse front by the diffraction grating, (2) imaging the diffracted pulse onto the generation crystal using a 75 mm focal length lens, and (3) the change of the tilt-angle from free space (outside of the crystal) to inside the LiNbO$_3$ crystal due to the difference in index of refraction.



$$Demag = \frac{46.2}{9.1} = 5$$
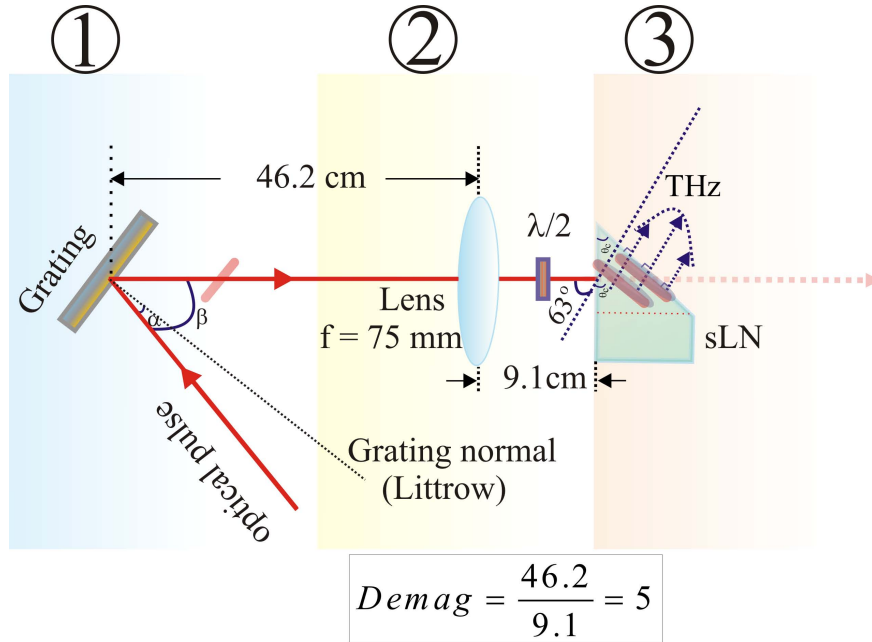
Figure 5.3: Tilted-pulse front scheme in our lab using a grating with 1100 lines/mm. The tilted pulse front at the grating (region ①), between the grating and source crystal (region ② ), and at the source crystal (region ③) are detailed in the text.

Diffraction by the grating affects the wave-front as shown in Fig. 5.3. A beam of 800 nm ultrafast pulse incident on a grating will be separated into its component wavelengths upon diffraction from the grating, with each wavelength diffracted along a different direction. Dispersion is a measure of the separation (either angular or spatial) between diffracted light of different wavelengths. Angular dispersion expresses the spectral range per unit angle,

and linear resolution expresses the spectral range per unit length. The angular dispersion will be discussed in the next section.

## 5.5   Grating equation

Diffraction by a grating is illustrated from the geometry in Figs. 5.4 and 5.5. Figure 5.4
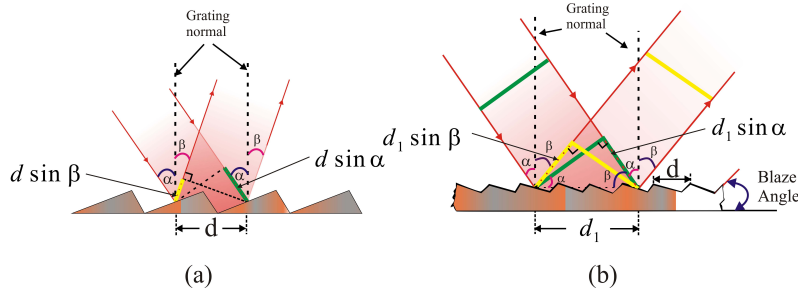


Figure 5.4: Optical beam diffracted by grating. (a) Diffraction at a single groove. (b) Diffraction on a number of grooves. $\alpha$ and $\beta$ denote the incident and diffraction angles, respectively. $d$ and $d_1$ denotes groove spacing (grating constant) and optical beam spot size at the grating, respectively.

illustrates a monochromatic light beam incident at an angle of $\alpha$ on the surface of a grating and diffracted into different directions with discrete angles and wavelength components. The diffracted angle $\beta$ denotes the first order of diffraction. The diffracted light wavefront is constructed by the constructive interference of a number of wavelength components within the bandwidth of the optical pulse. This constructive interference (see Fig. 5.4 (b) and Fig. 5.5 ) follows the grating equation as;

$$d_1 \sin(\alpha) + d_1 \sin(\beta) = m\lambda \tag{5.6}$$

where $\lambda$ is the wavelength and m = 0, 1, 2, ... is the order of diffraction. When m = 0, the wavelengths of the incident optical beam pulse are not separated and the grating acts as a mirror (specular reflection). Thus, from Eq. 5.6, $\sin(\beta) = \sin(-\alpha)$, which means $\beta = -\alpha$, for all $\lambda$. From a conventional argument, the grating equation given in Eq. 5.6 is positive when both the incident and diffracted beams are on the same side of the normal to the grating.

For the Littrow configuration, an incident beam is diffracted back along the direction in

which it comes, that is $\beta = \alpha$, the grating equation 5.6 is modified to,

$$2d_1 \sin(\alpha) = m\lambda \tag{5.7}$$

Here, we are considering a first order diffraction in which the intensity of the diffracted signal is stronger than other orders due to grating design.

### 5.5.1 Intensity pulse-front-tilting at the grating

Figure 5.5 shows the geometrical optics details of the pulse front tilt shown in region ① of Fig. 5.3. The tip of the incident intensity pulse front shown in Fig. 5.5 by a green circle
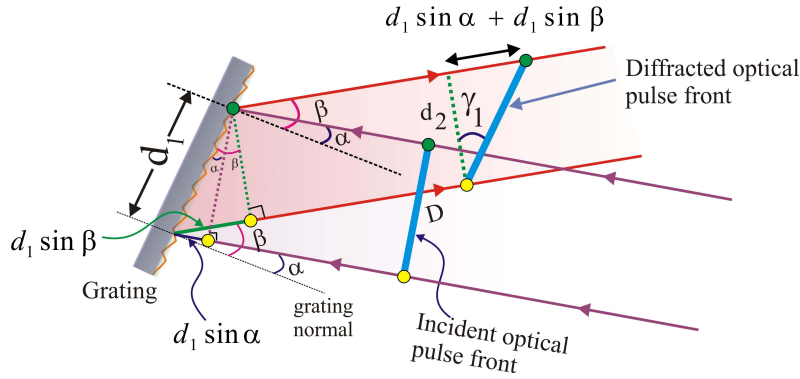


Figure 5.5: Optical pump pulse intensity front tilt by grating: Equivalent scheme of pulse front tilt by grating for part ① of Fig. 5.3. $\alpha$: incident angle on grating; $\beta$: first order diffraction angle on grating; $\gamma_1$: the tilted pulse front angle by the grating with respect to the incident optical pulse front. The deviation is the difference between the incident and diffraction angle on the grating ( dev = $\alpha$-$\beta$). D and $d_1$ are the optical spot sizes before the grating and at the grating, respectively.

arrives at the grating ahead of the yellow circle tip due to the angle at which the grating is tilted. The optical intensity front is tilted by the grating and imaged onto a $LiNbO_3$ crystal. When the yellow ring of the tip arrives at the grating, the green ring tip of the incident pulse front diffracted back from the grating, the same tip travels an additional distance of $d_1 sin(\beta)$. Hence, the green ring tip of the incident pulse front travels an additional optical path length than the yellow ring tips. Thus, as shown in Fig. 5.5 the distance difference

between the two rings after diffraction is represented by the optical path difference between the two beams as;

$$d_1 \sin(\alpha) + d_1 \sin(\beta) \tag{5.8}$$

The tilted pulse front spot size at the grating becomes $\frac{D}{\cos\alpha}$ and the width of the beam after diffraction, most often the first order beam, becomes $\frac{D\cos\beta}{\cos\alpha}$. Thus, the tilt angle $\gamma_1$ after diffraction becomes

$$\tan(\gamma_1) = \frac{d_1 \sin(\alpha) + d_1 \sin(\beta)}{d_2} \tag{5.9}$$

Using Eq. 5.6, it can be further simplified as,

$$\tan(\gamma_1) = \frac{m\lambda}{d_2} \tag{5.10}$$

and in terms of the pulse front tilt angle by the grating, the grating equation can be written as,

$$\cos\beta \tan\gamma_1 = \sin\alpha + \sin\beta \tag{5.11}$$

where $\cos\beta = \frac{d_2}{d_1}$.

## 5.5.2 Intensity-pulse-front at the lens position

Figure 5.6 (a) shows the imaging of the tilted pulse front on to $LiNb_3$ crystal using a lens. Due to the rotation of the pulse front tilt after the focus as shown in Fig. 5.3 and given as,

$$\tan(\gamma) = \frac{d_1 \sin(\alpha) + d_1 \sin(\beta)}{d'} = \frac{d_2 \tan(\gamma_1)}{d'} \tag{5.12}$$

where $\frac{d_1 \sin(\alpha) + d_1 \sin(\beta)}{d'} = d_2 \tan(\gamma_1)$ and the demagnification ratio i.e., the optical pump beam spot size before lens to after lens is, $Demag = \frac{d_2}{d'}$. Hence, Eq. 5.12 can be simplified as,

$$\boxed{\tan(\gamma) = \{Demag\} \tan(\gamma_1)} \tag{5.13}$$

Also, the $Demag$ can be derived from the lens equation. From Fig. 5.6 (b) the lens equation is written as,

$$\frac{1}{S_o} + \frac{1}{S_I} = \frac{1}{f} \tag{5.14}$$

The demagnification is then the ratio of the object distance ($S_0$) to image distance ($S_I$), $Demag = \frac{S_o}{S_I}$. Therefore, the $Demag$ as a function of the focal length of the imaging lens can be simplified as

$$S_o = (1 + Demag)f \tag{5.15}$$
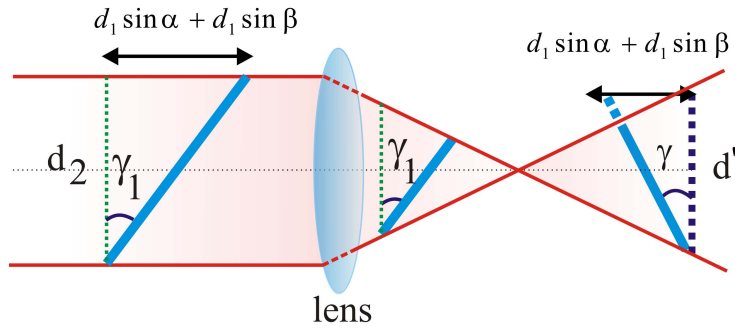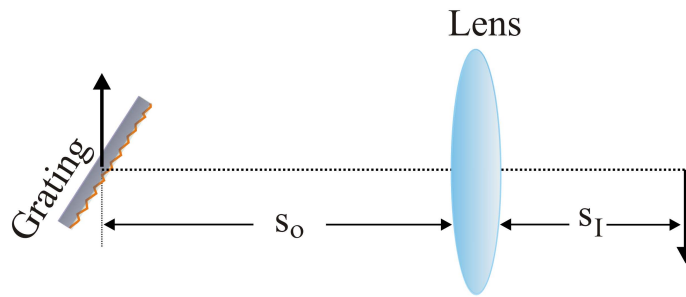
Figure 5.6: (a) Pulse front tilt at the imaging lens position represented by ② in Fig. 5.3: The angle of the pulse front tilt by grating before and after the imaging lens is the same, $\gamma_1$, but it changes to $\gamma$ after the focus. $\gamma_1$ and $\gamma$ denotes the pulse front angle before and after the focus, respectively. $d_2$ and $d'$ are the spot size before the lens and after the focus (before entering into the LiNbO$_3$ crystal.) (b) Lens imaging.

From the lens Eq. 5.15 and grating equation for different demagnification ratios

$$\frac{\Delta(Demag)}{\Delta S_o} = \frac{1}{f} \qquad (5.16)$$

### 5.5.3 Intensity pulse front at the LiNbO$_3$ position

The tilted angles of the pulse front before and after entering into the LiNbO$_3$ crystal is shown in Fig. 5.7. Due to the index of refraction, the optical path length inside shrinks to $s/n_g$ consequently leads to a decrease in the tilt angle. Thus, the tilt angle inside the crystal is related to the tilt angle outside as,

$$\tan(\gamma') = \left(\frac{(d_1 \sin(\alpha) + d_1 \sin(\beta))/n}{d'}\right) = \frac{d_2 \tan(\gamma_1)/n}{d'} = \frac{\{Demag\} \tan(\gamma_1)}{n} \qquad (5.17)$$

Recall, the tilted angle after the grating i.e., between the grating and imaging lens, and after the lens is given by

$$\boxed{d_1 \tan\gamma_1 = d_2 \tan\gamma_2} \qquad (5.18)$$

Thus, the tilt angle after the grating is $\gamma_1$, after lens focus (or before entering to LiNbO$_3$ is $\gamma$), and inside the LiNbO$_3$ crystal is $\gamma'$ (see Fig. 5.7), which is equivalent to the Cherenkov angle, $(\theta_c = \gamma')$. From Eq. 5.17, the tilt angles between grating-lens and lens-LiNbO$_3$, and inside LiNbO$_3$ are related to each other using the demagnification and index of refraction terms as,

$$\boxed{\tan(\gamma) = n \tan(\gamma') = \{Demag\} (\tan\gamma_1)} \qquad (5.19)$$

Where $Demag$ represents the demagnification ratio of the optical spot size at the grating to the spot size imaged by the lens on to the LiNbO$_3$ crystal. The tilted angles inside and outside crystal related as,

$$\boxed{\tan\gamma = n \tan\gamma'} \qquad (5.20)$$

The LiNbO$_3$ crystal cut at an angle of $\theta_c = 63^o$, and index of refraction of LiNbO$_3$, n = 2.26 at 800 nm, results in $\gamma = 77.3^o$.

Based on the above derivations, all the necessary parameters are given in Table 5.4 to develop a tilted pulse-front LiNbO$_3$ OR source for table-top intense THz pulse generation. Most importantly, the grating selection is determined from the demagnification and the angle of deviation. When the groove density of the grating gets smaller, the $Demag$ gets larger. For efficient diffraction of the grating the angle of deviation should not be large. Which is the optical path of the incident beam to the grating should be close to Littrow geometry of the grating. For a selected grating grove densities, 1100 lines/mm and 1800 lines/mm,
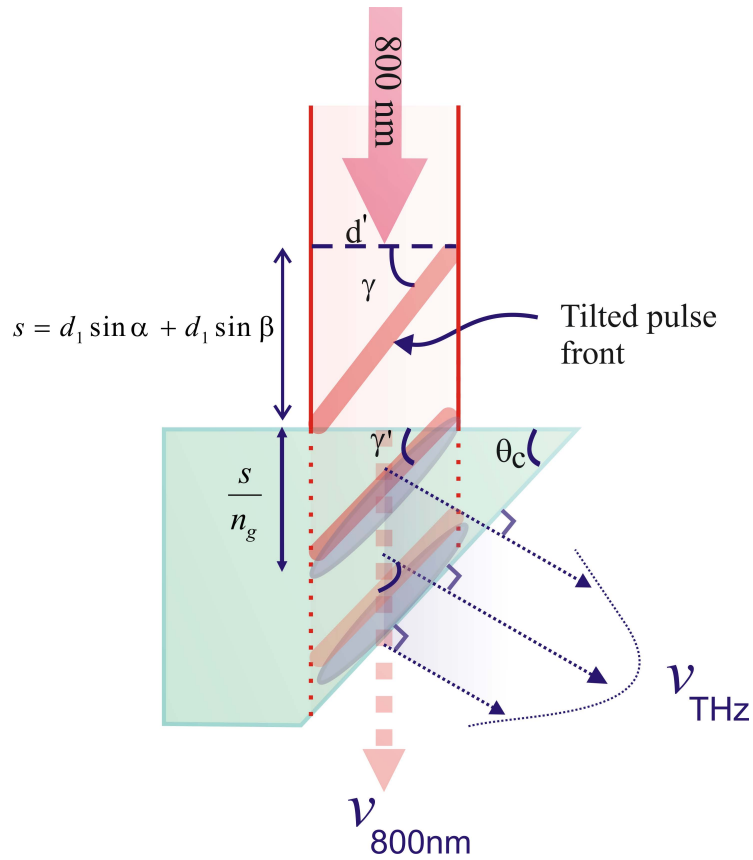
Figure 5.7: Tilted pulse front at the LiNbO$_3$ crystal, as represented region ③ in Fig. 5.3. The spot size and tilt angle before the grating are given by d$'$ and $\gamma$, respectively. $s$ is the optical path length and $\gamma'$ is the tilted-pulse-front angle inside the crystal. When the optical pump gets inside the crystal the angle becomes the Cherenkov angle that matches the cut angle of the crystal at the THz beam exit face.

a **Matlab code** is included in Appendix E to calculate the parameters. To generate both Tables 5.2 and 5.3 we use an optical wavelength of $\lambda = 800$ nm, index of LiNbO$_3$ at such wavelength, $n = 2.26$, and crystal cut angle, $\theta_c = 63^o$.

Table 5.2: 1100 lines/mm grating geometry. Note: the unit of the focal length is in millimeter, object and image distances are in cm, and all angle measurements are in degrees.

| Lens | f = 75 | f = 75 | f = 100 | f = 150 | f = 75 |
|---|---|---|---|---|---|
| Demagnification | 5 | 4.9 | 4.9 | 4.9 | 2 |
| Image distance | 9.0 | 9.03 | 12.04 | 18.06 | 11.25 |
| Object distance | 45.0 | 44.25 | 59.0 | 88.6 | 22.5 |
| Angle of incidence ($\alpha$) | 48.9 | 40.2 | 40.2 | 40.2 | 42.8 |
| Diffraction angle ($\beta$) | 7.3 | 13.6 | 13.6 | 13.6 | -2.2 |
| Angle of deviation (dev) | 41.7 | 26.7 | 26.7 | 26.7 | -68.8 |
| Tilt angle after grating ($\gamma_1$) | 41.6 | 42.2 | 42.2 | 42.2 | 65.7 |
| Tilt angle before crystal ($\gamma$) | 77.3 | 77.3 | 77.3 | 77.3 | 77.3 |
| Tilt angle inside crystal ($\gamma'$) | 63 | 63 | 63 | 63 | 63 |

Table 5.3: 1800 lines/mm grating geometry. Note: the unit of the focal length is millimeter, object and image distances are in cm, and all angle measurements are in degrees.

| Lens | f = 75 | f = 100 | f = 150 | f = 75 | f = 75 |
|---|---|---|---|---|---|
| Demagnification | 2 | 2 | 2 | 2.315 | 1.924 |
| Image distance | 11.25 | 15 | 22.5 | 10.74 | 11.39 |
| Object distance | 22.5 | 30 | 45 | 24.86 | 21.93 |
| Angle of incidence ($\alpha$) | 42.8 | 42.8 | 42.8 | 42.8 | 42.8 |
| Diffraction angle ($\beta$) | 49.5 | 49.5 | 49.5 | 49.5 | 49.5 |
| Angle of deviation (dev) | -6.7 | -6.7 | -6.7 | -10.74 | -10.74 |
| Tilt angle after grating ($\gamma_1$) | 65.7 | 65.7 | 65.7 | 65.7 | 65.7 |
| Tilt angle before crystal ($\gamma$) | 77.3 | 77.3 | 77.3 | 77.3 | 77.3 |
| Tilt angle inside crystal ($\gamma'$) | 63 | 63 | 63 | 63 | 63 |

Table 5.4: Grating parameters for different demagnification and groove density based on the above equations.

| Demag | Groove $(\mathrm{mm}^{-1})$ | Dev (degree) | $\eta_{Gr}$ (%) | $\alpha$ (degree) | $\beta$ (degree) | Littrow angle (degree) | Tilting angle (degree) | Litrow tilting (degree) |
|---|---|---|---|---|---|---|---|---|
| 5:1 | 900 | -33.27 | <40 | 5.43 | 38.70 | 21.10 | 42.69 | 37.66 |
|  | 1100 | 17.93 | <70 | 35.42 | 17.48 | 26.10 | 42.69 | 44.42 |
|  | 1200 | no | no | no | no | 28.68 | 42.69 | 47.58 |
| 6:1 | 900 | 1.13 | <88 | 21.66 | 20.54 | 21.10 | 37.55 | 37.66 |
| 7:1 | 800 | 9.87 | N/A | 23.67 | 13.80 | 18.66 | 33.38 | 34.04 |
| 8:1 | 700 | 4.95 | N/A | 18.75 | 13.80 | 16.26 | 29.97 | 30.25 |
| 9:1 | 600 | -13.11 | <30 | 7.42 | 20.54 | 13.88 | 27.14 | 26.31 |

where $\eta_{Gr}$ is grating efficiency, $Dev$, $\alpha$, and $\beta$ are deviation, incident and diffracted angles.

We investigated the effects of optical pump pulse chirping on terahertz (THz) pulse generation via tilted-pulse-front optical rectification in LiNbO$_3$ using separate compressors for THz pulse generation and optical pulse detection. The basis is presented for the dependence of generated THz pulses on the pulse duration and polarization of the chirped optical pump pulses. By down-chirping the optical pump pulses to 385 fs, single-cycle terahertz pulses with THz pulse energies up to 3.6 $\mu$J (using a correction factor given in Ref. Blanchard et al. (2007)), were obtained corresponding to an energy conversion efficiency of $3 \times 10^{-3}$. The optical-to-THz conversion efficiency is defined as, $\eta = \frac{W_{THz}}{W_{op}}$, where $\eta$ is conversion efficiency, $W_{THz}$ and $W_{op}$ are THz and optical pulse energy, respectively. The THz conversion efficiency comparison with other reported results is given in Section 5.9.1 of table 5.5. Using dual compressors for tilted pulse front scheme allows for optimization of the optical-to-THz conversion efficiency and proper characterization of the THz pulses since the pulse durations of the probe and pump beams were controlled separately, decoupling the electro-optic detection from the optical pump pulse chirping. As a benchmark, the strength of the generated THz fields were confirmed by carrying out a nonlinear THz Z-scan experiment on an n-doped InGaAs epilayer on a lattice matched InP substrate as discussed in Chapter 6.

## 5.6  Experimental setup for intense THz pulse source

A schematic diagram of the experimental setup for generating intense THz pulses is shown in Fig. 5.8, and a photograph of the experimental setup is displayed in Fig. 5.9. As illustrated in the figures, stretched, mode-locked laser pulses amplified in a Ti:sapphire oscillator-amplifier (Micra/Legend: Coherent Inc.) were split into optical pump (80%) for

THz pulse generation and optical sampling (20%) for detection pulses inside the Legend. The detection or sampling pulses were carefully aligned into the ZnTe detector crystal to minimize noise levels. The Micra/Legend system provides a pulse energy of 3.6 mJ at 800 nm with pulse duration of 50 fs and 1 kHz repetition rate. The pulse duration 50 fs is the transform limited pulse duration we measured using a single shot autocorrelator, which is different from the pulse duration specified by the company as discussed in Section 5.3.

The optical pump pulse was directed to compressor 2 and the pulses were up-chirped, down-chirped or made chirp free (shortest pulse duration, 50 fs) as necessary by tuning a variable compressor delay stage. The intensity front of the chirped pulse is diffracted by a 1100 lines/mm grating and imaged into the source crystal using a 75 mm focal length lens. The size of the optical pump pulse was 9.2 mm at the grating and 1.8 mm at the source crystal, yielding a demagnification ratio of 4.9. The optical pump spot on the $LiNbO_3$ crystal was 2 mm in diameter.

The polarization of the optical pump incident on the grating was set horizontally for highest diffraction conversion efficiency. After the grating, the pump light polarization is rotated to vertical using the half-wave plate ($\lambda/2$) to match along the optic axis of the $LiNbO_3$ crystal [Stepanov et al. (2003); Yeh et al. (2007)]. THz pulses are generated by optical rectification of chirped pump pulse excitation in $63^0$ cut 0.6 mol% MgO-doped stoichiometric $LiNbO_3$ (sLN) crystal. Undoped $LiNbO_3$ crystal shows optical damage (photrefractive damage) at high optical pump power that limits its usability as a nonlinear optical medium. A doped stoichiometric $LiNbO_3$ crystal possesses a resistance to optical damage that makes it a much more suitable OR crystal at high optical pump powers than the undoped sLN.

To prevent the optical beam from reaching the pyroelectric or photo-detectors, any transmitted optical and second harmonic generated beams from the source crystal are filtered out using a set of THz transparent black polyethylene absorbers. Before hand, an iris diaphragm adjusted about a 1" diameter is placed close to the $LiNbO_3$ at the THz pulse exiting direction. The THz pulse energy with the iris diaphragm is a bit larger than the THz pulse energy reading without iris diaphragm. Afterwards, the THz pulses collected by a 4″ off-axes parabolic mirror and propagate through a combination of 3″ off-axes parabolic mirrors before focusing collinearly with the sampling beam onto the ZnTe detector crystal.

The detection pulses are delivered to compressor 1 and compressed to the shortest pulse duration, 50 fs, for THz waveform acquisition using free-space electro-optic sampling as discussed in Chapter 2. After being compressed it propagates through an optical delay stage to adjust the variable time delay relative to the THz pulses. The sampling and THz pulses finally meet at the $4^{th}$ off-axis parabolic and co-propagate collinearly through the ZnTe detector crystal. Inside the ZnTe crystal, the optical refractive index is modulated by the transient THz field, which in turn rotates the polarization of the linearly polarized
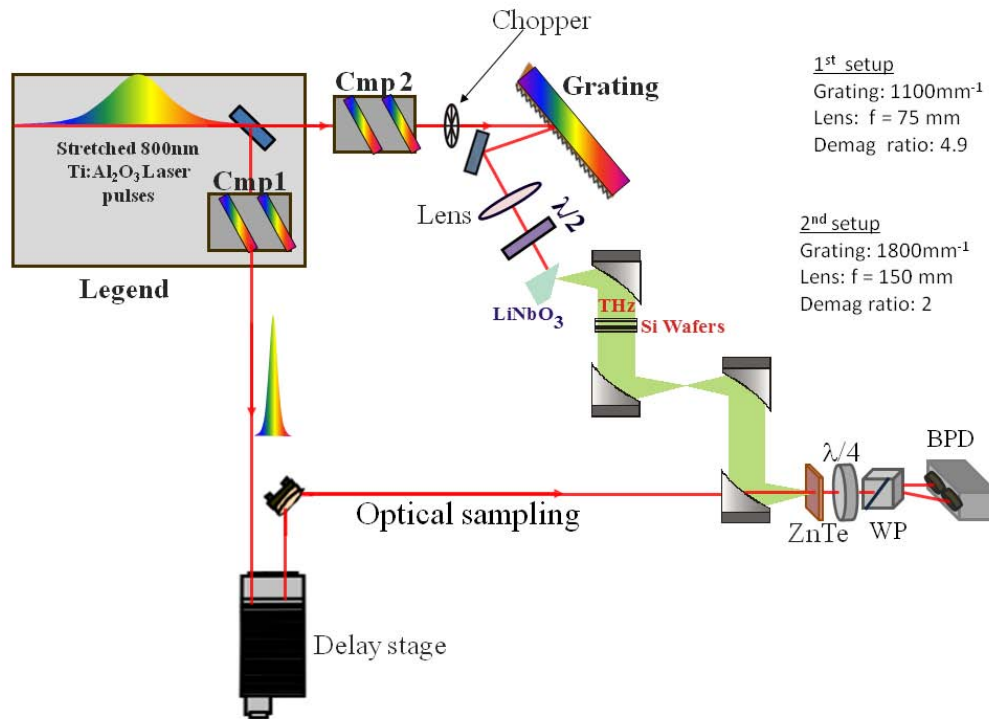
Figure 5.8: Schematic of experimental setup for the generation and detection of intense THz pulses using a tilted-pulse-front OR LiNbO$_3$ source. The pulse duration of the pump pulses was controlled by compressor 2, and the sampling pulse durations were adjusted to transform-limited 50 fs pulses using compressor 1. The optical pump pulse front is tilted by a 1100 lines/mm grating and imaged onto the LiNbO$_3$ crystal. The half-wave plate ($\lambda/2$) rotates the polarization to vertical to match the c-axis of the crystal (Fig. 5.10 (c)). Cmp1: compressor 1; Cmp2: compressor 2; LiNbO$_3$: lithium niobate; Si: silicon wafers; ZnTe: Zinc-telluride; $\lambda/4$: quarter wave-plate; WP: Wollaston prism and BPD: balanced photodiode.
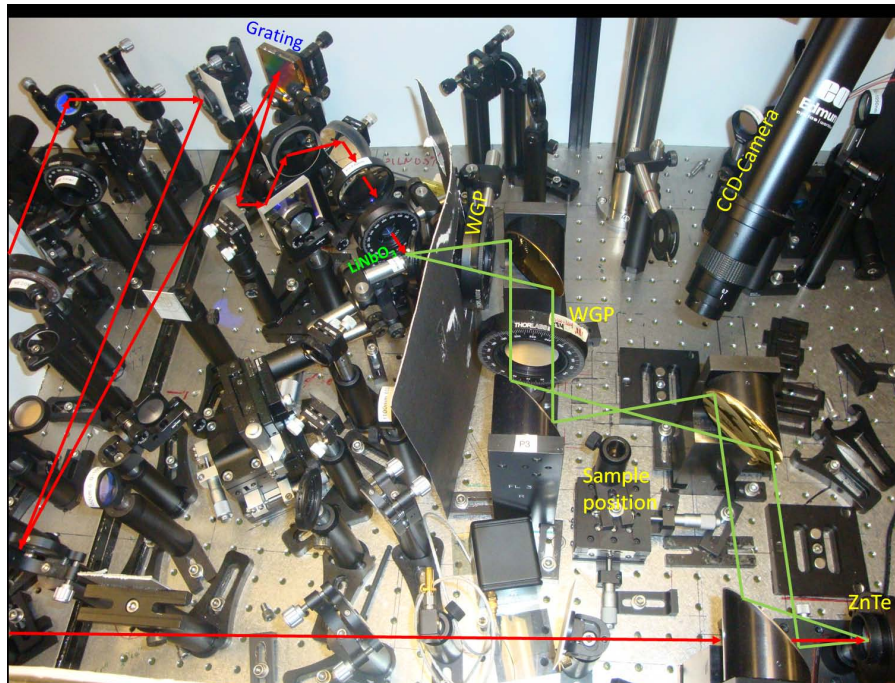
Figure 5.9: Photograph of the experimental setup for generating intense THz pulses. The red line that propagates to the LiNbO$_3$ is the down-chirped 800 nm optical pump beam and the other red line that goes to ZnTe is the detector (gate) beam used to detect the THz pulse. The green lines represnts the propagation of the generated THz pulse from the LiNbO$_3$ crystal.

65
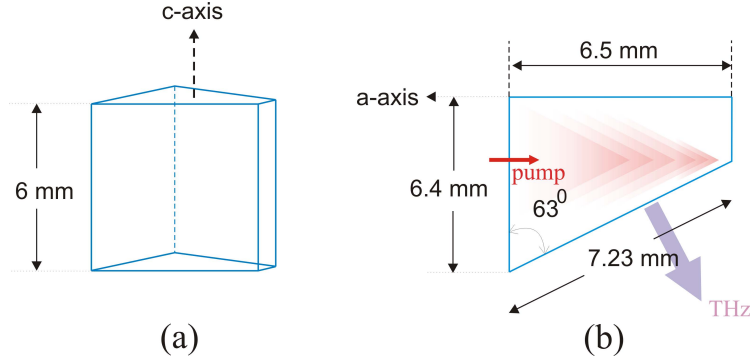
Figure 5.10: Dimension and cut angle of LiNbO$_3$ crystal. (a) A 0.6% MgO-doped stoichiometric LiNbO$_3$ crystal (sLN). (b) Geometry of LiNbO$_3$ crystal. The two faces 7.23 mm × 6 mm and 6.5 mm × 6 mm are polished and the other four faces are AR coated at 800 nm.

probe beam. The polarization-rotated probe beam is analyzed by a quarter-wave plate in conjunction with a Wollaston polarizer. The Wollaston polarizer splits the modulated detection beam into two and the beams are then focused onto two balanced photo-diodes. A set of five 0.5 mm thick silicon wafers were introduced into the collimated section of the THz beam before the sample position (THz focus) to attenuate the THz pulses during waveform acquisition to avoid saturation of the EO detection system. A 0.5 mm-thick [110] ZnTe crystal was used for free-space electro-optic sampling. Finally, the temporal profile of the THz pulse is acquired from the recorded signal of the balanced photo-diodes using a lock-in amplifier. Taking a Fourier transform of the time domain THz pulse reveals the corresponding spectral information. The optical pump beam is chopped to suppress the background light and low frequency noises of the probe beam during data acquisition.

The optical pump pulse energy is 1.7 mJ before the diffracting grating and 1.1 mJ at the position of the LiNbO$_3$ crystal due to losses from the grating, imaging lens, half-wave plate, and other optical components. The loss from the grating is due to reflection and other higher order diffractions modes. The size of the image is slightly larger than the diameter of the imaging lens such that part of the diffracted beam is forced to pass through the edge of the lens and focuses at a slightly different position than the central component of the beam that passes through the center of the lens. Furthermore, the rear edge of the pulse will not be focus with the leading edge of the pulse due to the different speeds for different wavelength components inside the lens. After the beam passes through the lens, its size is still larger than the diameter of the half-wave plate and a large portion of it is blocked before

illuminating the source crystal. Finally, the beam illuminates the source crystal, arranged in such a way that the angle of the tilted-pule-front inside the LiNbO$_3$ crystal is about 63$^o$.

An example of THz pulse generated in this setup is given in Fig. 5.11. The instantaneous
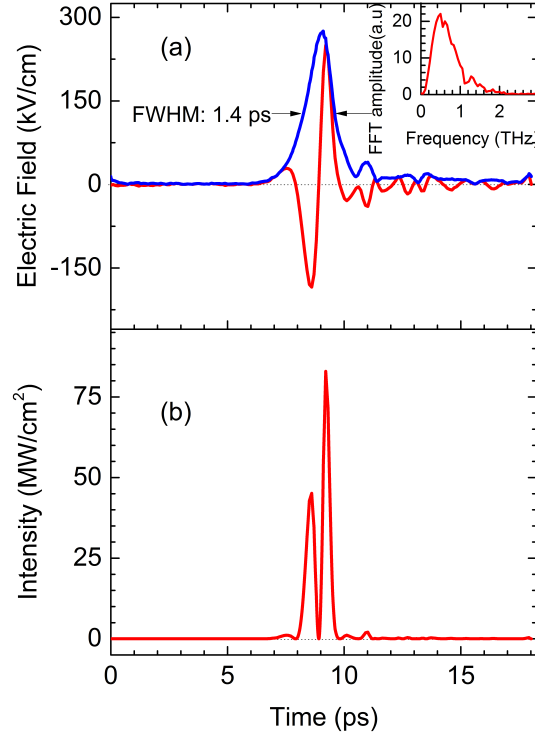


Figure 5.11: (a) Electric field profile of the terahertz pump beam (red line) emitted by the tilted-pulse-front LiNbO$_3$ source measured by electro-optic sampling in ZnTe crystal denoted by the red pulse. The peak electric field strength is 250 kV/cm. The corresponding FFT amplitude spectrum of the THz pulse is shown in the inset. The blue line is the Hilbert transform of the THz pulse used to determine the pulse width. (b) Instantaneous THz intensity at the focus $\left(I_{THz} \propto E_{THz}^2\right)$.

intensity in Fig. 5.11 (b) indicates that the energy of the THz pulse is accumulated mainly in the two main peaks among over many cycles of the field. The temporal THz pulse characteristics is reconstructed by applying the well-known electro-optic sampling technique using a 0.5 mm thick ZnTe crystal. The measured THz spectrum shown in Fig. 5.11. The

the dip shown at 1.6 THz is due to the ambient water vapor absorption line.

## 5.7 Effects of pre-chirping and optical pulse duration on THz generation efficiency

Tuning the optical pump pulse duration by down chirping is crucial for scaling up the optical-to-THz conversion efficiency, but doing so in the conventional single-compressor setup will inevitably lead to a concurrent chirping of the sampling pulse. This problem is avoided in our improved setup. The chirp direction introduced by compressor 2 was identified in a two step processes. First, the optical pump pulse was allowed to propagate through air and then the pulse duration was measured by a single-short autocorrelation at different compressor delay stage settings. Second, the pump pulse duration was measured after the pump pulse propagated through a thick piece of calcite (a glan laser polarizer was used). Then the pulse durations were compared at each variable delay stage position of compressor 2. The two data sets are plotted together in Fig. 5.12. The red curve is the pump pulse duration measured through air, while the blue curve is the pulse duration after the pump pulse from compressor 2 has propagated through a glan laser polarizer.

The green curve is the pulse duration measured after the pump pulse propagates through the $LiNbO_3$ crystal. The pulse duration for the blue and green curves are lower than the red curve for delay stage position $\leq$ 9.2 mm, and hence this region is negatively chirped (down chirped). The propagation of a monochromatic pulse packet in air does not depend on frequency or wavelength, so that for the red curve the phase velocity of the blue and red frequency components of the pulse both travel at the speed of light. However, when the wave packet propagates through a transparent medium (in our case a glan laser polarizer or a $LiNbO_3$ crystal) the different wavelength components of the pulse travel with different speeds due to the group index dispersion of the medium. The minimum pulse duration for all curves is located at the compressor variable delay stage position of about 9.2 mm as shown in Fig. 5.12, and is 50 fs. It shows that the group velocity dispersion in $LiNbO_3$ is consistent with the chirp direction required to produce the highest THz energy. Nevertheless, pre-chirping alone is insufficient to explain the degree to which the optical pump pulses must be initially down-chirped for optimal THz conversion efficiency.

Fig. 5.13 (a) shows examples of THz pulse temporal profiles for pulses acquired at different pump pulse durations. Figure 5.13 (b) illustrates the generated THz energy dependence on the optical pump pulse duration for both the up-chirp and down-chirp cases. In the up-chirp case, light with lower frequencies (or longer wavelengths, on the red side of the spectrum) travel faster through the medium than light with higher frequencies (shorter
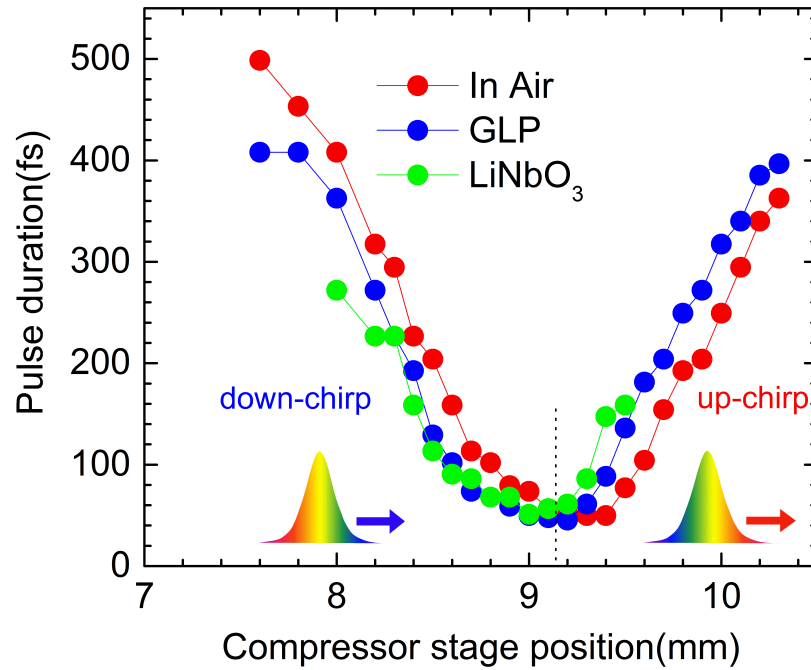
Figure 5.12: Optical pump pulse duration measured by second-harmonic intensity autocorrelation as a function of compressor 2 stage position; (see Figure 5.8). Pump pulse durations of pre-chirped optical pump pulses were measured after the optical pulses propagated through air, a glan laser polarizer (GLP), and a LiNbO$_3$ crystal, respectively. The shortest pulse duration position is shown by the dash line at the crossovers.
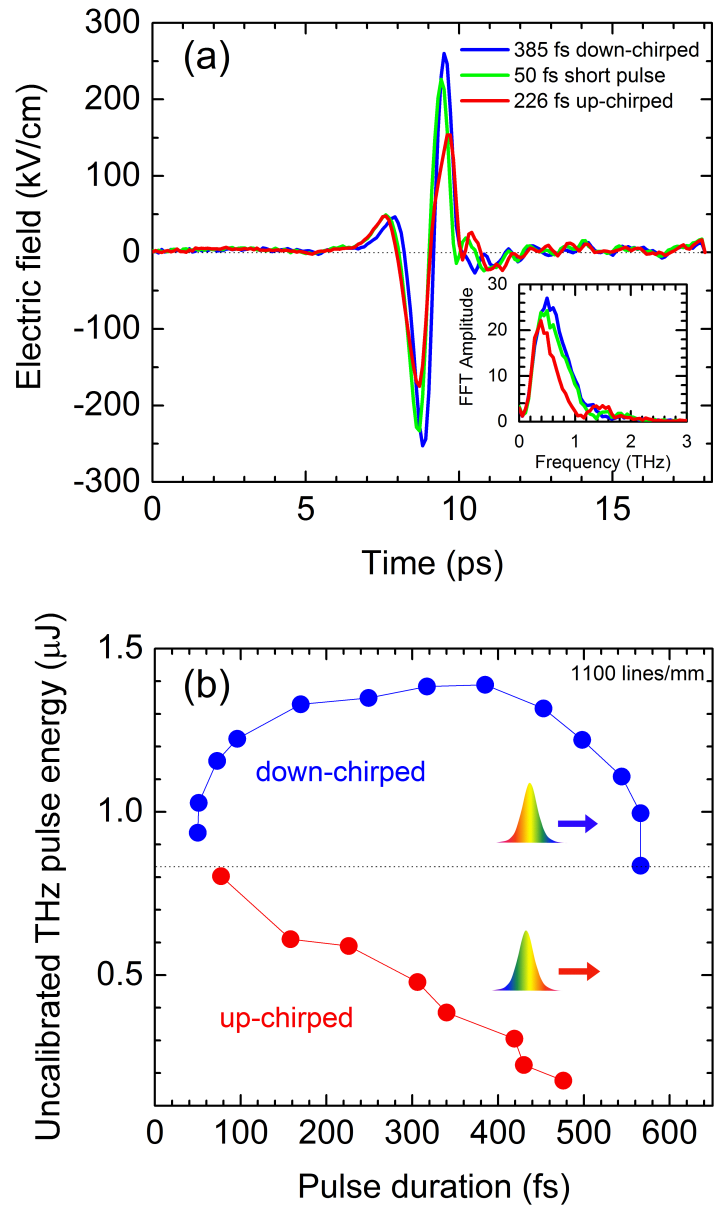
Figure 5.13: (a) Temporal profiles of the radiated THz field and the corresponding frequency spectra (inset) at different optical pump pulse chirp settings. (b) Uncalibrated THz energy measured by a pyroelectric detector as a function of pulse duration and chirp in 1100 lines/mm grating.

wavelengths, blue side of the spectrum). This situation is reversed in the down-chirp case. For up chirp, the THz conversion efficiency decreases linearly with the optical pump pulse duration. Interestingly, this is not the case for down-chirp, where THz energy increases with optical pump pulse duration to a peak value, after which further increasing the pump pulse duration leads to a symmetric reduction in THz pulse energy.

Similar observations of THz pulse energy vs. optical pump pulse duration to that shown in Fig. 5.13 (b) were reported by Stepanov [Stepanov et al. (2010)]. The waveform peak acquired at the chirp free position drops slightly relative to the peak for down chirped pump pulse excitations but is well above the waveform peak produced by up chirped optical pump pulses, as shown in Fig. 5.13 (a). The peak of this pulse is a temporal shift of 120 fs from the peak of the optimum pulse. The spectral peak is located at 0.46 THz for the THz pulses generated by un-chirped optical pulses, as shown in the inset of Fig. 5.13 ( a). However, at a specific down chirped 385 fs pulse duration the generation of THz pulses was improved by more than a factor of 2 and the spectrum shifted to higher frequencies with a central peak of 0.51 THz, shown in the inset of Fig. 5.13 (a). A theoretical model by Fulöp [Fulop et al. (2010)] reported that the optimal pump pulse duration for high energy THz pulse generation is 350 fs, which is consistent with our observation 385 fs. In our measurement we did not account for the extra pulse chirp that arises from the grating due to the angular group velocity dispersion, which may be the reason for the slight discrepancy between ours and Fulop's measurement. We find that the optimum THz pulse bandwidth as well as maximum peak of THz pulse spectrum is attained when the optical pump pulse is down-chirped into the 100-400 fs range, and that reducing the pump pulse width further does not broaden the THz spectral bandwidth. We propose that the THz spectrum from the $LiNbO_3$ source is also affected by the optical pump pulse duration, which determines the dynamics of phonon-polariton excitation inside the sLN.

With 385 fs down-chirped pump pulse duration, a single-cycle THz pulse with an optimal average energy of 1.4 $\mu$J was directly measured using a pyro-electric detector (SPJ-D-8: Spectrum Detector Inc.). The specification and analog conversion of the pyroelectric detector is given in Appendix C. The pyro-electric detector has a $7.8 \times 7.8$ $mm^2$ active pyroelectric detector element and it is calibrated at 1.06 $\mu$m, such that it underestimates the generated THz energy by a factor of about 1.8 [Blanchard et al. (2007)]. After accounting for this calibration factor, a pulse energy of 2.5 $\mu$J is obtained. Recently, after some setup optimization and adjustments pulse energies as high as 2 $\mu$J were measured directly using the pyro-electric detector. This corresponds to 3.6 $\mu$J after using a calibration factor. In general, for the case of up-chirped pump pulses, THz pulse energy drops with increasing pump pulse, duration. For down-chirped pump pulses the THz energy rises to an optimum value and then drops symmetrically as the pulse duration gets larger. On the other hand, increasing the pulse duration with up-chirped pulses leads to a significant reduction in THz

pulse energy. For the shortest optical pump pulses, because of a strong nonlinear effect in sLN [Yeh et al. (2007)] and self-phase modulation [Stepanov et al. (2010)] the generated THz energy is not optimized either.

All the experimental data presented in this thesis were collected under ambient lab conditions (at room temperature and without purging the experimental setup). In this case, there is strong absorption in the range of 2 THz [Stepanov et al. (2003); Bosomworth (1966)] inside the $LiNbO_3$ crystal in addition to absorption from water vapor in the air. Furthermore, there are significant Fresnel losses at the $LiNbO_3$/air interface. Two optical grating geometries with groove densities of $1100 \text{ mm}^{-1}$ and $1800 \text{ mm}^{-1}$ were used to characterize the effect of chirped pump pulse duration on the THz conversion efficiency of the tilted-pulse-front scheme. The demagnification ratios for the two geometries were 5 and 2, respectively. In the latter geometry, a lens telescope was used to minimize the pump beam spot size of 12 mm from the compressor to a spot size of 4 mm at the grating which becomes 2 mm at the source crystal position using a 150 mm focal length lens to yield a demagnification ratio of 2. However, in this geometry a self-phase modulation of the optical pump pulse is observed at the shortest pulse duration (50 fs). This was confirmed by measuring the spectrum of the optical pump pulse before and after the lens telescope which is shown in Fig. 5.14 (a). As can be seen in Fig. 5.14 (a) the spectral shift is a consequence of self-phase modulation at the shortest pump pulse duration setting.

The red line shown in Fig. 5.14 (a) is the reduced spectral broadening of the pump pulse due to self-phase modulation which leads to a less efficient THz pulse generation at the transform limited 50 fs optical pump pulse duration. At such pulse duration, the generated THz pulse energy dropped sharply as shown a dip in Fig. 5.14 (b) at the grating compressor position of 8 mm as well as a dip shown in Fig. 5.15 of the green line. This corresponds to 46% reduction in THz pulse energy with respect to the maximum THz energy measured in the same setup (7.5 mm at the compressor position). As a result, as shown in Fig. 5.14 (b) the reduction in THz pulse energy as a function of grating compressor position is not symmetrical for negatively and positively chirped pump pulse duration. According to Stepanov et al. (2010) using a transform limited optical pump pulse for the tilted-pulse-front source results a 30% reduction in THz pulse generation efficiency. The author suggested that the decrease in generation efficiency could be due to self-phase modulation arising when the shortest pump duration propagates in air from the laser compressor to the experimental setup. However, the decrease in THz pulse energy at the shortest optical pump pulse duration due to self-phase modulation is still an unconfirmed mystery.

In contrast, for the 1100 line/mm geometry self-phase modulation was not observed since there was no lens telescope used to minimize the optical pump pulse size, such that the generated THz energy is symmetrical for both negatively and positively chirped pulses
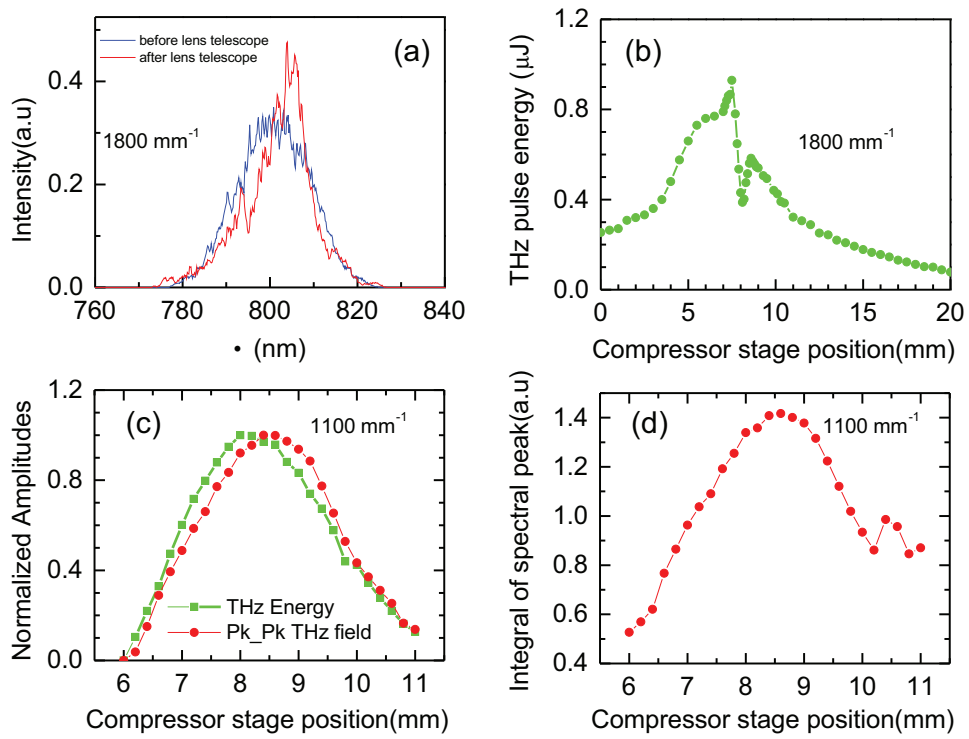
Figure 5.14: (a) Intensity spectrum of the optical pulse measured before (blue curve) and after (red curve) the lens telescope. (b) THz pulse energy as a function of compressor stage position for both 1100 (red line) and 1800 mm$^{-1}$ (green line) grating geometries. (c) Normalized THz pulse energy and peak to peak THz waveforms as a function of compressor stage position of the 1100 mm$^{-1}$ grating setup. (d) The integral of spectral peak as a function of compressor delay stage position.
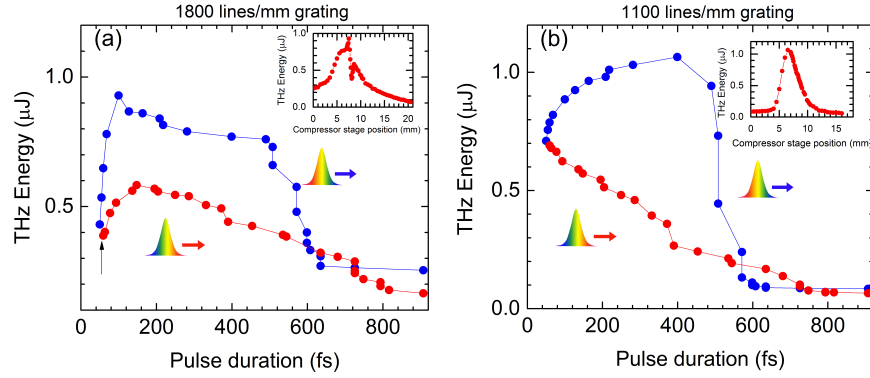
Figure 5.15: THz pulse energy dependence on optical pump pulse duration using 1800 mm$^{-1}$ (a) and 1100 mm$^{-1}$ (b). Blue curve: down chirp and red curve: up-chirp. The inset in each plot are the THz pulse energy measured as a function of compressor position.

shown in Fig. 5.14 (c) green line. The red line represents the peak to peak THz field measured at each compressor position, and Fig. 5.14 (d) shows the integral of the spectral peak at every compressor position. Both plots are in-line with the THz pulse energy plot given in Fig. 5.14 (c) green line. This is one way to retrieve the energy of the THz pulses from the frequency spectrum.

The features of the pulse energy as a function of pump pulse duration is given for both grating geometries in Fig. 5.15 below. In both Fig. 5.15 (a) and (b), the red and blue curve represents the THz pulse energy as a function of pump pulse duration measured for up- and down-chirped 800 nm pump pulses. For the 1100 line/mm grating setup the generated THz pulse energy as a function of pump pulse duration follows the same trend as indicated in Fig. 5.12 (b). However, for 1800 line/mm geometry a sharp reduction in THz pulse energy at the shortest pulse duration (50 fs) occurred as shown on the green line of Fig. 5.15. This might be due to a self-phase modulation in the crystal down shifts the primarily chirped free pump pulse into a negatively chirped pulse that gives reduction in THz pulse energy.

## 5.8    Optical pump polarization dependence

Moreover, the optical pump polarization dependence of the generated THz radiation from the tilted-pulse-front OR source is investigated by rotating the half-wave plate, which changes the optical pump polarization with respect to the optical axis of the source crystal. A quantitative analysis of the generated THz field of optical rectification is directly proportional to the second time derivative of second order nonlinear polarization. That is obtained from a simplified plane wave equation of an electromagnetic wave propagating through a nonlinear source crystal of charge free and non-magnetic medium given by:

$$\nabla^2 \mathbf{E} - \frac{n^2(\Omega)}{c^2} \frac{\partial^2 \mathbf{E}}{\partial t^2} = \mu_0 \frac{\partial^2 \mathbf{P}_{NL}}{\partial t^2} \tag{5.21}$$

where $\mathbf{E}$ is the incident optical pump pulse, n($\Omega$) is the refractive index of the source crystal at THz frequencies, and $\mathbf{P}_{NL}$ is the nonlinear polarization term induced due to the incident pump pulse. The sum of all the pairs of the $2^{nd}$ order nonlinear polarization associated with the OR as function of the incident optical pump pulse field is given by

$$P_i(\Omega) = \varepsilon_o \sum_{jk} d_{ijk}(\Omega) E_j(\omega_1) E_k(\omega_1) \tag{5.22}$$

The pump pulse induces a second order nonlinear low frequency (DC) polarization through $\chi^{(2)}$ via difference frequency generation. LiNbO$_3$ is a uniaxial trigonal crystal with 3m crystal structure. Thus the nonlinear second order polarization leading to difference frequency generation is given by

$$\begin{bmatrix} \vec{P}_x^{(2)}(\Omega) \\ \vec{P}_y^{(2)}(\Omega) \\ \vec{P}_z^{(2)}(\Omega) \end{bmatrix} = \begin{bmatrix} 0 & 0 & 0 & 0 & d_{15} & -d_{22} \\ -d_{22} & d_{22} & 0 & d_{15} & 0 & 0 \\ d_{15} & 15 & d_{33} & 0 & 0 & 0 \end{bmatrix} \begin{bmatrix} E_x^2 \\ E_y^2 \\ E_z^2 \\ 2E_y E_z \\ 2E_z E_x \\ 2E_x E_y \end{bmatrix} \tag{5.23}$$

where d$_{ij}$ is nonlinear susceptibility, P$_{x,y,z}^{(2)}$, and E$_{x,y,z}$ are the second order polarization and optical pump electric field along x, y, and z direction, respectively. The effective nonlinear electro-optic coefficients given in Eq. 5.23 are in terms of the principal axes of the crystal. The product of matrices in the left hand side of Eq.5.23 yields,

$$\vec{E}_{THz} \propto \vec{P}^{(2)}(\Omega) = 2\varepsilon_0 E^2 \begin{bmatrix} 0 \\ d_{22}\sin^2\theta + 2d_{22}\sin\theta\cos\theta \\ d_{15}\sin^2\theta + d_{33}\cos^2\theta \end{bmatrix} \qquad (5.24)$$

where $E$ is the electric field of the optical pump pulse and $\theta$ is the angle between the optical pump pulse polarization and the c-axis of the crystal. In Eq. 5.24, even though there is a y-component of the induced THz field only the Z component survives. This is because the y-polarization component of the THz pulse energy doesn't couple to the z-component polarization to be detected using the pyro-electric detector.
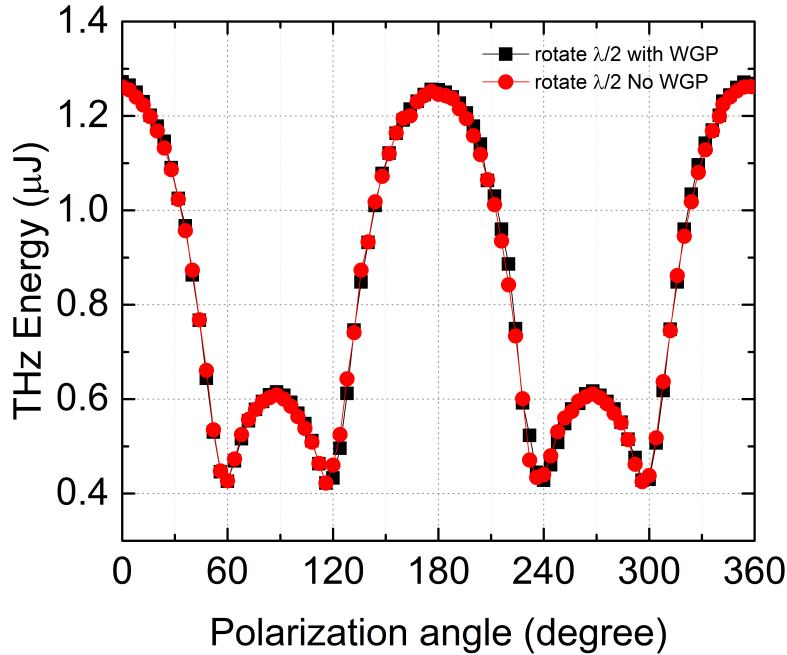


Figure 5.16: Optical pump polarization dependence of a THz pulse radiation generated by OR of a tilted-pulse-front LiNbO$_3$ source. $\theta = 0^o$ corresponds to no pump polarization aligned along the c-axis of the LiNbO$_3$ crystal. Black curve: measured by changing the optical pump polarization by rotating the $\lambda/2$. Red curve: $\lambda/2$ set to allow vertical polarization (parallel to c-axis) of the optical pump and the polarization of the generated THz pulse is changed using wire grid polarizers to check other components of the THz pulse.

Two methods were used to map out the polarization dependence of the radiated THz field from a tilted-pulse-front-optical rectification LiNbO$_3$ source. (i) The wire grid polarizer that controls the output polarization of the THz field placed after the LiNbO$_3$ was set to allow vertical polarization and the $\lambda/2$-wave plate in the optical generation path was rotated through angles $\theta = 0$ to $180^o$, which results in a $2\theta$ change in optical polarization with respect to the c-axis. (ii) The $\lambda/2$ plate in the optical path was set to map the generation crystal with polarization along the c-axis of the crystal and the wire grid polarizers were rotated to check the other components of the generated THz pulses from the LiNbO$_3$ source. As depicted in Fig. 5.16, the result shows that only one polarization component is generated from the LiNbO$_3$ source using the tilted waveform scheme. Figure 5.17 (a) illustrates the normalized generated THz pulse energy as a function of incident optical pump polarization. Figure 5.17 (a) obtained by pumping the source crystal with full optical pump power and Fig. 5.17 (b) were obtained by reducing the optical pump energy by half in which a better fitting between Eq. 5.24 and experimental result achieved. From Eq. 5.24 the intensity of THz radiation is written as:

$$I \propto E^4 \left( d_{15} sin(\theta\pi/180))^2 + d_{33}(cos(\theta\pi/180))^2)^2 \right) \tag{5.25}$$

and the plot of this equation is shown in Fig. 5.17.

The red curve represents the generated THz pulse energy at a fixed optical pump polarization along the optic axis of the crystal while the polarization of the generated THz pulse were mapped out by rotating the wire grid polarizer. The black curve in Fig. 5.17 (a) was attained by rotating the $\lambda/2$-wave plate from $0^o$ to $180^o$ degree, that in turn aligns the optical pump polarization at different angle to the optic axis of the LiNbO$_3$ crystal. By doing so, the generated THz pulse energies were mapped out as a function of optical pump polarization. Regardless of the pump pulse polarization, the THz pulse delivered by tilted-pulse-front OR in LiNbO$_3$ will never have zero amplitude. This is due to the optical rectification of second order polarization is a sum of the square of sine and cosine functions and both trigonometric functions can not be zero at certain polarization angles shown in Eq. 5.24. The generated THz pulse field survives along the z-axis of the LiNbO$_3$ crystal only. As shown in Fig. 5.17 (a) the THz pulse energy has global maxima at $0^o$, $180^o$, $360^o$, and local maxima at $90^o$ and $270^o$. Also, the generated THz energy polarization was demonstrated by setting the $\lambda/2$ wave plate to allow optical pump polarization along the optic axis of the source crystal. Once the $\lambda/2$ wave plate was set to allow vertical polarization of the incident 800 nm beam, the THz pulse energy was recorded at different THz polarization by changing the polarization angle using wire grid polarizers. The result confirms that a single polarization component along z-axis is generated from the tilted-pulse-front LiNbO$_3$ source. It is evident that both results measured by varying the optical polarization at a fixed THz
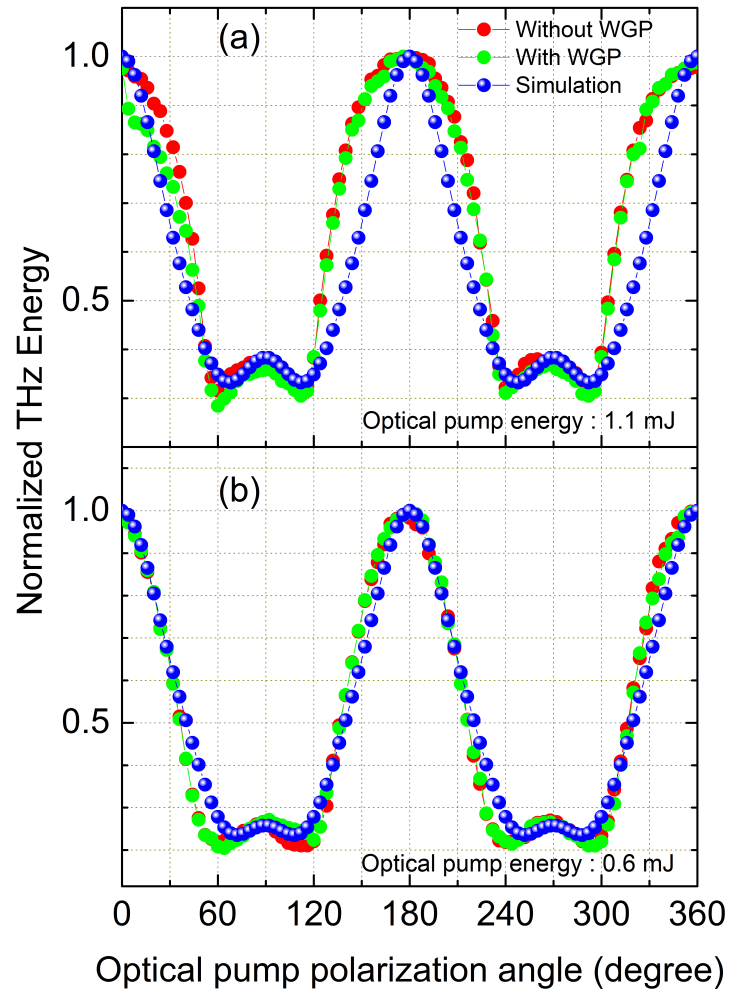
Figure 5.17: Both in (a) and (b) the red and green lines are experimental results and blue line is simulation. (a) is obtained at a THz pulse energy of 1.1 $\mu$J and (b) is measured at 0.6 $\mu$J.

output polarization and vice versa from a tilted wave front are in good agreement.

## 5.9    THz pulse at the optimum pump pulse duration

The optical pump fluence dependence of the experimental setup was characterized with down-chirped pulse at the optimum pulse duration (385 fs). It is found that the temporal profile amplitude increases with pump pulse fluence, as shown in Fig. 5.18 (a). Figure 5.18 (b) shows the corresponding frequency spectra of the temporal waveforms of Fig. 5.18 (a). The THz spectrum generated using the optimal pump pulse duration is broader than that observed for pulses produced using the minimum pulse duration, stretching from 0.2 THz to 2.2 THz. The dip shown at 1.6 THz is due to water vapor absorption.

According to Eq. 5.24, the THz field should scale with the pump energy, which would mean the THz energy should be proportional to the square of the optical energy. The pulse energy dependence on optical pump energy data in Fig. 5.18 (c) indicates that the energy increases linearly with optical pump energy. This observation is similar to experimental data reported by [Stepanov et al. (2010)]. The generated THz energy does not saturate with increasing pump energy because $LiNbO_3$ has a large band gap (Refer Table 5.1) which prevents two photon absorption of the 800 nm pump pulse, and THz absorption by free carriers generated by the pump. Figure 5.18 (d) shows a plot of the peak THz field as a function of optical pump energy and THz pulse energy, and the two plot match closely. This proves that one can retrieve the THz energy from the peak THz field of the temporal waveform.

The peak THz field at the optimum pump pulse duration is evaluated from the measurable parameters of the generated THz pulses. Figure 5.19 (a) shows the THz waveform (red line) obtained at the optimum pulse duration and the green curve is the real part of Hilbert transform of the temporal profile, the FWHM of which is used to evaluate the THz field pulse duration. Figure 5.19 (b) shows the corresponding THz spectrum.
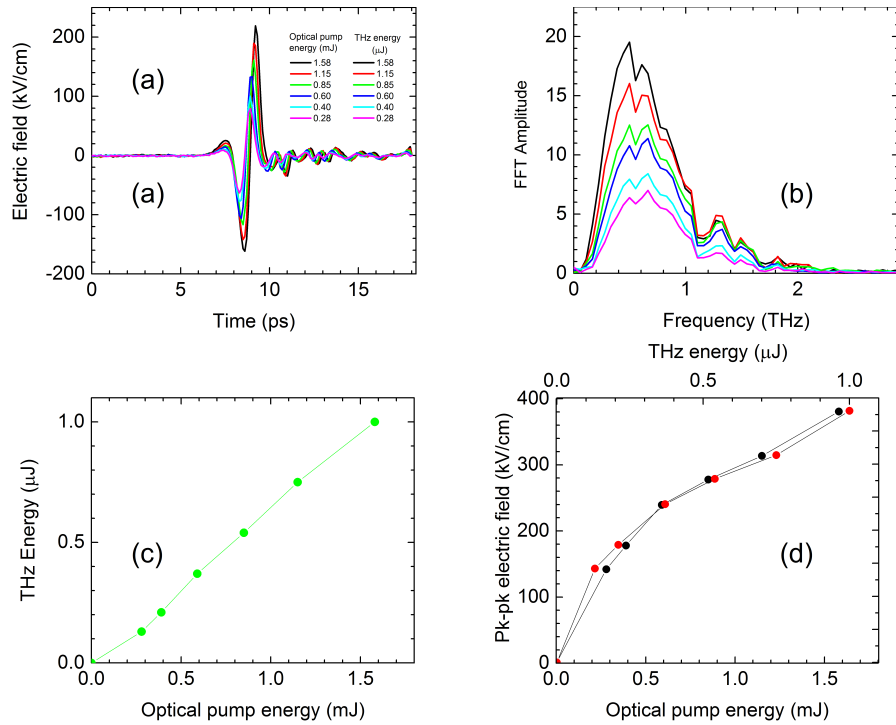
Figure 5.18: Optical pump energy dependence of THz waveforms measured at the optimum pump pulse duration. (a) Examples of THz waveforms for different optical pump excitations. (b) Corresponding frequency spectra of the THz field waveforms. (c) Scaling of generated THz energy with optical pump energy at the fixed optimum pump pulse duration as measured by a pyroelectric detector (uncalibrated). (d) Peak-to-peak THz waveform amplitude as a function of optical pump energy and THz energy.
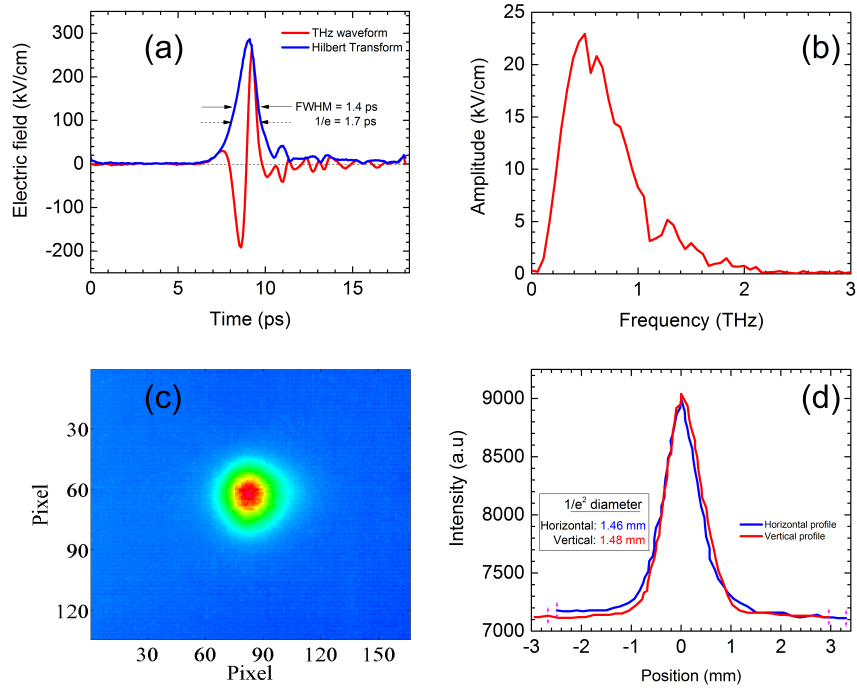
Figure 5.19: Temporal and spectral profiles of generated THz field at the optimal THz energy compressor position. (a) THz field waveform acquired at a direct pyro-electric reading (uncalibrated) THz pulse energy of 1.6 $\mu$J. (b) Corresponding THz spectrum of the THz waveform. (c) Pyro-electric camera image of focused THz spot with $1/e^2$ diameter of 1.5 mm. (d) The horizontal and vertical THz beam intensity profiles of the THz focus spot.

### 5.9.1  THz Peak Electric Field

The peak THz field can be estimated from the electric field modulation in the FSEOS technique given in Eq. 2.5 and the details given in Appendix C.1. Here, determination of the peak field using ultrashort pulse characterization and from the consideration of the THz pulse propagation as a Gaussian beam is given. The peak power is calculated from the FWHM, $\tau_{FWHM}$ or the $\left(\dfrac{1}{e}\right)$ (electric field) THz pulse width as given in Fig. 5.19 (a), area of the THz beam spot at the detector, and from the measured pulse energy given as;

$$P_{pk} = \frac{W_{THz}}{\tau_{FWHM}} = \frac{I(E)}{A} = \frac{1}{2}c\varepsilon_0 |E_{THz}^{pk}|^2 \tag{5.26}$$

The THz peak field as a function of THz pulse energy is given by [Mathew and Fedosejevs (2005); Blanchard et al. (2007)];

$$|E_{THz}^{pk}| \approx \sqrt{\frac{2\eta_0\, W_{THz}}{\tau A}} \tag{5.27}$$

where $|E_{THz}^{pk}|$ is the peak THz field, $W_{THz}$ is THz pulse energy, $P_{pk}$ represents the THz pulse peak power, $\tau$ is the $1/e$ THz pulse width given in Fig. 5.19 (a), A is the area of the THz beam at the focus (detector position), and $\eta_0$ is the impedance of free space. To obtain an accurate value for the THz field, the estimate based on Eq. 5.27 is corrected to account for the Fresnel reflection from the detector face and one has to use the crystal impedance inside the crystal.

However, the propagation of the THz pulse is approximated as a Gaussian envelope as other laser pulses. Thus, the total power, P($\infty$), for a Gaussian envelope is given by;

$$P_{(\infty)} = \left(\frac{\pi\omega_0^2}{2}\right) I(0) \tag{5.28}$$

where $I(0)$ is the THz pulse intensity at the center of the beam ( r = 0, where r is the distance from the center of the beam), and $2\omega_o$ is the full width spot size diameter of the THz pulse intensity profile at $\dfrac{1}{e^2}$ (13.5%). Figure 5.19 (c) shows the THz spot at the focus imaged using uncooled BST pyro-electric infrared camera (PV320: Electrophysics Inc.). The camera has an array of (320×240) pixel with array size of 15.52×11.64 mm (HV), and the size of the pixel is 48.5 $\mu m^2$. The THz spot size is evaluated from the intensity profiles of the spot dimension $\left(\dfrac{1}{e^2}\right)$ of 1.5 mm. The FWHM THz pulse duration is found to be 1.4 ps. In terms of THz pulse energy and pulse duration, the total pulse power is given by;

$$P(\infty) = \frac{W}{\tau} \tag{5.29}$$

where $\tau$ is pulse duration calculated from $\left(\dfrac{1}{e}\right)$ (37%) of the Hilbert transform of the THz waveform at the optimum pulse duration, W is the THz pulse energy measured directly using the pyro-electric detector. According to our maximum measured THz pulse energy at the focus, 1.6 $\mu$J, the corresponding total power calculated was 0.9 MW. The THz pulse intensity at the focus as a function of THz pulse peak is given by

$$I(0) = \frac{1}{2}c\varepsilon_0|E|^2 \tag{5.30}$$

where E is the THz pulse peak field. The peak THz pulse field at the focus can be estimated by substituting Eq. 5.29 and 5.30 into Eq. 5.28 and yields Eq. 5.31.

$$|E_{THz}^{peak}| = \sqrt{\frac{4\eta_0 W}{\tau A}} \tag{5.31}$$

This calculation has a factor of $\sqrt{2}$ difference with the THz field derivation given in Ref. [Blanchard et al. (2007)]. At 1.6 $\mu$J THz energy the calculated peak THz field at the focus becomes 300 kV/cm and the THz field intensity becomes 12 MW/$cm^2$. where $\eta_0 = 377$ $\Omega$, is the free space impedance, W is the THz pulse energy measured directly using the pyro-electric detector, $\tau$ is the $\left(\dfrac{1}{e}\right)$ of THz pulse duration calculated from the Hilbert transform of the THz waveform at the optimum pulse duration. $A = \pi\omega_0^2$ is the spot area of the THz pulse intensity at the focus determined from the $\left(\dfrac{1}{e^2}\right)$ diameter of the intensity profile of THz pulse spot at the focus with a horizontal and vertical diameters of 1.46 mm and 1.48 mm, respectively. Table 5.5 displays summary of the highest THz pulse energies from a tilted-pulse-front LiNbO$_3$ source reported by different group. Also, the peak

Table 5.5: Highest THz pulse energy with conversion efficiency reported from a tilted-pulse front LiNbO$_3$ source.

| Group | Pump energy | Pulse duration | THz Energy | efficiency |
|---|---|---|---|---|
| Fülöp Fulop et al. (2012) | 75 mJ | 1.3 ps | 125 $\mu$J | $25\times10^{-2}$ |
| Stepanov Stepanov et al. (2010) | 120 mJ | 700 fs | 50 $\mu$J | $5\times 10^{-4}$ |
| Stepanov Stepanov et al. (2008) | 28 mJ | 50 fs | 30 $\mu$J | $1\times 10^{-3}$ |
| Nelson Yeh et al. (2007) | 16 mJ | 400 fs | 10 $\mu$J | $6\times 10^{-4}$ |
| Hegmann Ayesheshim et. al. | 1.1 mJ | 385 fs | 3.6 $\mu$J | $3\times 10^{-3}$ |

THz field can be calculated from the EOS signal modulations measured by the balanced

photodetectors as,

$$|E_{THz}| = \frac{\lambda_0}{2\pi n_0^3 r_{41} t_{GaP} t_{Si}^2 L} sin^{-1}\left(\frac{I_A - I_B}{I_A + I_B}\right) \tag{5.32}$$

Refer Appendix C.1 for the details. Figure 5.19 demonstrates the Fourier transform obtained at the optimum pump pulse duration. At this position, the spectral peak is about 0.51 THz with spectral bandwidth of about 2.5 THz. Higher frequency components are absorbed by the LiNbO$_3$ crystal, so that the spectral bandwidth is limited to 2.5 THz only. Examples of comparison of peak THz electric field based on the two methods are given in appendix C.1.

## 5.10    Conclusion

In conclusion, we have demonstrated the detailed characterization of tilted-pulse-front experimental setup. Dual compressor geometry for tilted-pulse-front OR in LiNbO$_3$ optimizes the optical to THz conversion efficiency. It showed that there is an appropriate amount of negatively chirped pulse duration to provide the maximum optical pump to THz conversion efficiency in the tilted-pulse-front scheme. Furthermore, in dual compressor scheme one can characterize the generated THz pulse properly without any cross over pulse duration issues for the sampling and pumping pulses. Table of THz pule parameters generated from a tilted-pulse-front LiNbO$_3$ is given in Table 5.6.

Table 5.6: THz pulse parameters of the tilted-pule-front LiNbO$_3$ setup using 1100 mm$^{-1}$ groove density.

| Parameters | |
|---|---|
| Optimum pump pulse duration | 385 fs |
| Maximum THz pule energy (uncalibrated) | 2.2 $\mu$J |
| Peak electric field[1] | 340 kV/cm |
| Bandwidth | 0.2-2.5 THz |
| Peak frequency | 0.5 THz |
| Pulse width ($\tau_{FWHM}$) | 1.4 ps |
| $\tau_{1/e}$ | 1.78 ps |
| THz spot diameter ($1/e^2$) | 1.46 mm |

[1] Using the given parameters, the THz peak field as a function of measured THz pulse energy is, $|E_{THz}^{peak}| = \sqrt{\frac{4\eta_0 W}{\tau A}} = \left[225\sqrt{W}\right]$kV/cm, where $W$ is THz pulse energy in $\mu$J .

We conducted sets of nonlinear THz dynamics experiments using the apparatus in Fig. 5.9. Therefore, the next chapters uses this experimental setup to study extreme nonlinear THz dynamic responses of carriers in doped semiconductors using a single intense THz

pulse to perturb and probe the nonlinear carrier dynamics and photoexcited semiconductors using optical pump-THz probe experiment. The first set is the demonstration of a significant transmission enhancement of THz pulses in one direction (optical diode) using Z-scan experiment.

# CHAPTER 6

## Ultrafast intense terahertz Z-scan in doped semiconductors

## 6.1 Open aperture Z-scan technique

The open aperture Z-scan technique was first pioneered by Sheik-Bahae in 1990 [Sheik-Bahae et al. (1990)] and it has become a powerful tool for characterizing the nonlinear optical properties of materials. The nonlinear optical absorption can be categorized as: (1) saturable absorption in which the transmittance increases with increasing optical intensity due to intervalley scattering, (2) Multiphoton absorption in which the transmittance decreases with increasing intensity. For practical applications, saturable absorption in semiconductors is used in ultrashort laser pulse generation [Gu et al. (2006); Hoffmann and Turchinovich (2010)]. The Z-scan experiment consists of scanning the sample through the focus of an intense THz beam using a translation stage. The incident pulse energy is kept constant but the sample experiences different incident THz field amplitude at different sample location. The total transmitted THz pulse energy through the sample under investigation is then recorded as a function of sample position relative to the focus to study the nonlinear field dependent transmission dynamics.

In the THz frequency range, the optical nonlinearity of semiconductors arises from the response of free electrons to an intense THz electric field. Therefore, very recently the open aperture Z-scan technique has been employed in the THz frequency range to study nonlinear absorption bleaching due to intervalley scattering in an n-doped semiconductors [Razzari et al. (2009); Hoffmann and Turchinovich (2010)] and an absorption enhancement due to impact ionization effects in an undoped InSb sample [Wen et al. (2008)]. In order to characterize the nonlinear bleaching of absorption effects in doped semiconductors, we employed an open aperture Z-scan technique used for measuring position dependent nonlinear transmission. We have demonstrated intense THz induced nonlinear transmission enhancement

at the THz focus relative to the transmission away from focus in doped InGaAs in the THz frequency range at room temperature with two different carrier concentrations: (a) lightly doped (LD) with carrier concentration, $n_e = 2 \times 10^{17} cm^{-3}$, and (b) heavily doped (HD), with carrier concentration $n_e = 2 \times 10^{18} cm^{-3}$ InGaAs samples. For both samples, the comparison of extremely high nonlinear absorption bleaching of intense THz pulses by illuminating the conducting and insulating faces alternatively is the main subject of this chapter. Note that the abbreviations LD and HD stated above are used through out Chapter 6 and 7.

## 6.2   Experimental setup and measurements

An open-aperture THz Z-scan experimental apparatus that utilizes an intense THz pulse transient generated by optical rectification of a tilted-pulse-front $LiNbO_3$ source, as discussed in Chapter 5, is shown in Fig. 6.1 (a). The THz pulse is collimated and focused to a spot diameter of 1.5 mm at the sample position using a set of off-axis parabolic mirrors. The sample is mounted on a motorized translational stage and illuminated by intense THz pulses at normal incidence while scanned along the axis of the beam focus and monitoring the transmitted total pulse energy. During data acquisition, the sample was scanned along the axis in steps of 100 $\mu$m from -25 to 25 mm over a span of 50 mm with Z = 0 at the position of beam focus. The transmitted THz pulse through the sample was collimated and then re-focused onto the pyroelectric detector by another set of off-axis parabolic mirrors (see Fig. 6.1 (a) ).

In this study, the THz Z-scan was carried out by illuminating both the conducting (InGaAs) and insulating (InP) faces of the sample with intense THz pulse fields alternatively to characterize the nonlinear conductivity responses of free carriers in the sample. The THz energy transmittance through the sample is measured as a function of sample position Z, relative to the focal plane by scanning along the THz pulse propagation axis as shown in Fig. 6.1 (a). Figure 6.1 (b) shows an example of position dependent normalized THz energy transmission resulting from a THz Z-scan experiment in HD sample measured by a pyroelectric detector. The red curve is obtained by illuminating the substrate face of the sample and measuring the transmitted THz pulse energy on the conducting face of the sample, and the green curve is the vice versa. The THz pulse energy without the sample was measured to be 1.5 $\mu$J at the focus. As can be seen from Fig. 6.1 (b), regardless of which face is illuminated first, a considerable enhancement of the total transmitted THz energy is recorded at the THz focus plane relative to away from the focus. The transmitted signal level goes to zero as the sample moves away approximately 10 mm from either side of focus.

The nonlinear absorption bleaching at intense THz pulse that illuminates the conduct-
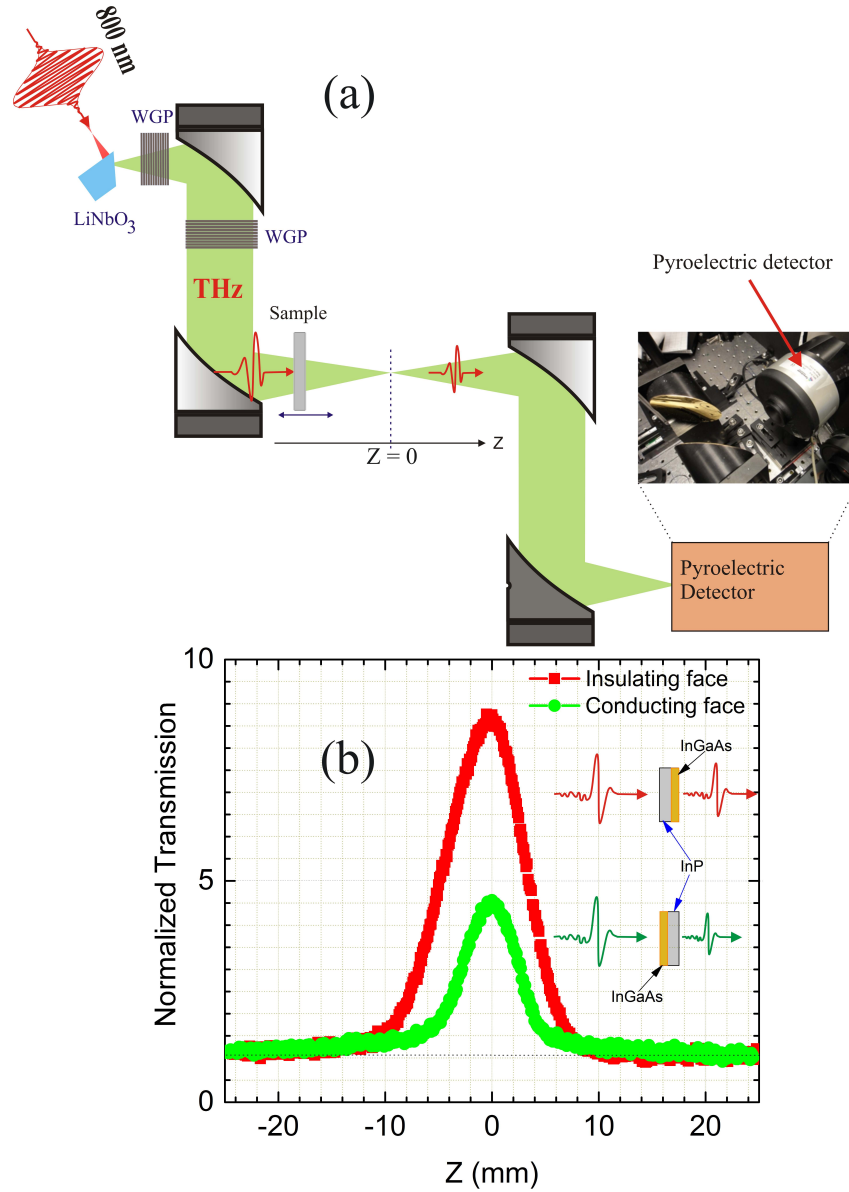
Figure 6.1: Open-aperture THz Z-scan experimental setup. (a) Sketch of THz Z-scan experimental setup that uses the high THz power setup of tilted-pulse-front LiNbO$_3$ source. (b) Example of Z-scan measurement the normalized transmission of the total THz pulse energy through a heavily doped InGaAs sample by illuminating both the conducting and insulating faces alternatively. The THz pulse energy without sample at the focus was 1.5 $\mu$J (uncalibrated) with peak THz field of 275 kV/cm.

ing face of the n-doped InGaAs sample positioned at the focus is indeed anticipated. Most remarkably, we observed exceptionally high enhancement of THz transmission modulation upon illuminating the insulating face (InP) of the sample instead of the conducting face. Commonly in Z-scan experiments the applied field illuminates the conducting surface and record the transmitted total pulse energy. In particular, from Fig. 6.1 (b) we observed a nearly 52% higher normalized transmission modulation in the case of illuminating the insulating face than illuminating the conducting face of the same sample. This amplification of absorption bleaching suggests the development of a practical ultrafast optical diode analogous to current flow in an electronic diode. Understanding the underlying phenomena is desirable for modern semiconductor devices and in designing future devices operating in the THz spectral range, such as photodiodes.

A simple analytical derivation of the transmitted THz fields based on the boundary conditions of the thin conducting film approximation and the Fresnel equations affirms the enhancement effect. Thus, the next section details the derivation and extraction of transmission and reflection coefficients of a thin semi-conducting film on a thick substrate from the electromagnetic boundary conditions for both conditions of illuminating the conducting and insulating faces, respectively. Furthermore, clarification including doping concentration dependent nonlinear THz transmission will be discussed in the next sections as well.

## 6.3 Optical transmission at the air-conducting film interface

In general, part of the light pulse incident on a semiconductor surface is reflected and part of it that enters is absorbed and the rest are transmitted depending on the composition of the semiconductor and the wavelength of the incident light. The pumping THz field can be considered uniform for a film thickness much smaller than the wavelength. The transmission-reflection characteristics of an air-thin conducting film interface on a substrate is detailed in Fig. 6.2 (a), in which the driving field can be found directly by the application of boundary conditions of the electromagnetic field. The theoretical description as well as the experimental analysis of the interaction of any part of the EM spectrum (Microwave, THz, IR, visible, etc) with matter is fully described by Maxwell's equations and its solutions for time-varying electromagnetic fields. Hence, the propagation of a THz pulse through a thin conducting film on a substrate interface should obey the boundary conditions that determine the reflectance and transmittance of EM waves at various boundaries. The boundary conditions require that the tangential components of incident, reflected, and transmitted electric field amplitude from a thin conducting film on a thick substrate be continuous across the film. However, the tangential components of the corresponding magnetic

fields are discontinuous because of the surface current of the film. The amplitudes of the $\mathbf{E}$ and $\mathbf{H}$ illustrated in Fig. 6.2 are continuous across the interface, and are found to satisfy the following boundary conditions.

$$\hat{\mathbf{n}} \times (\vec{H}_1 - \vec{H}_2) = \int_0^\infty J dz = \mathbf{J} d \tag{6.1}$$

$$\hat{\mathbf{n}} \times (\vec{E}_1 - \vec{E}_2) = 0 \tag{6.2}$$

where $H_i$, $H_t$ denotes incident and transmitted magnetic fields, $E_i$, $E_t$ are the incident and transmitted electric fields, and $d$ is the thickness of the conducting film, $\hat{\mathbf{n}}$ is the surface normal, and $\mathbf{J}$ is the surface current density induced in the conducting thin film, respectively. For normal incidence the film equations 6.1 and 6.2 become

$$H_i - H_r - H_t = Jd \tag{6.3}$$

$$E_i + E_r - E_t = 0 \tag{6.4}$$

Figure 6.2 illustrates the normal incident, reflected, and transmitted p-polarized (polarization $\parallel$ to plane of incidence) THz pulse radiation on a plane of incidence of thin conducting film on an insulating substrate. The scheme and the equivalent circuit response of electrons to external field $\mathbf{E}_i$ is displayed in Fig. 6.2 (b). Where $\mathbf{E}_i$, $\mathbf{E}_r$, and $\mathbf{E}_t$ are incident, reflected and transmitted electric fields, respectively.

To simplify the transmitted and reflected amplitude of the field further, the ratios of magnetic fields to electric field for the incident, reflected, and transmitted fields are given by the admittance $Y_j = H_j/E_j$, j = 1, 2, 3, or impedance of the media, $Z = 1/Y$. Thus, $Y_1 = H_i/E_i = H_r/E_r$, and $Y_2 = H_t/E_r$. Substituting impedance equations into Eq. 6.3 and 6.4, the transmitted and reflected field amplitudes on the conducting film can be extracted as,

$$\mathbf{E}_t = \frac{1}{Y_1 + Y_2} (2Y_1 \mathbf{E}_i - \mathbf{J}d) \tag{6.5}$$

$$\mathbf{E}_r = \frac{1}{Y_1 + Y_2} \left((Y_1 - Y_2)\mathbf{E}_i - \mathbf{J}d\right) \tag{6.6}$$

where $Y_1 = H_i/E_i = H_r/E_r$, $Y_2 = H_t/E_r$, and $\mathbf{J} = \tilde{\sigma} \ \mathbf{E}_t$, where $\tilde{\sigma} = \sigma_1 + i\sigma_2$ is the complex conductivity of the film. This approximation 6.5 has been widely used in the treatment of a thin conducting film on a thick substrate and it is valid only when the thickness of the conducting film is much less than the wavelength, d $\ll \lambda$. The complex transmission and reflection coefficient of the film can be then derived by substituting the current density, $\mathbf{J}$ into Eq. 6.5 and Eq. 6.6.

**(a)** InGaAs

InP

$E_i$

$k_i$

$H_i$

$E_r$

$k_r$

$H_r$ →|d|←

$\sigma$

$E_t$

$k_t$

$H_t$

$n$

$d \ll \lambda$

**(b)**

i

t

$Z_0$

r

$Z_s$

$Z_{film}$

impedance of medium

$$Z = \frac{E}{H} = \sqrt{\frac{\mu_0}{\varepsilon\varepsilon_0}}$$

impedance of film

$$Z_{film} = \rho\,\frac{l}{ld} = \frac{1}{\tilde{\sigma}d}$$
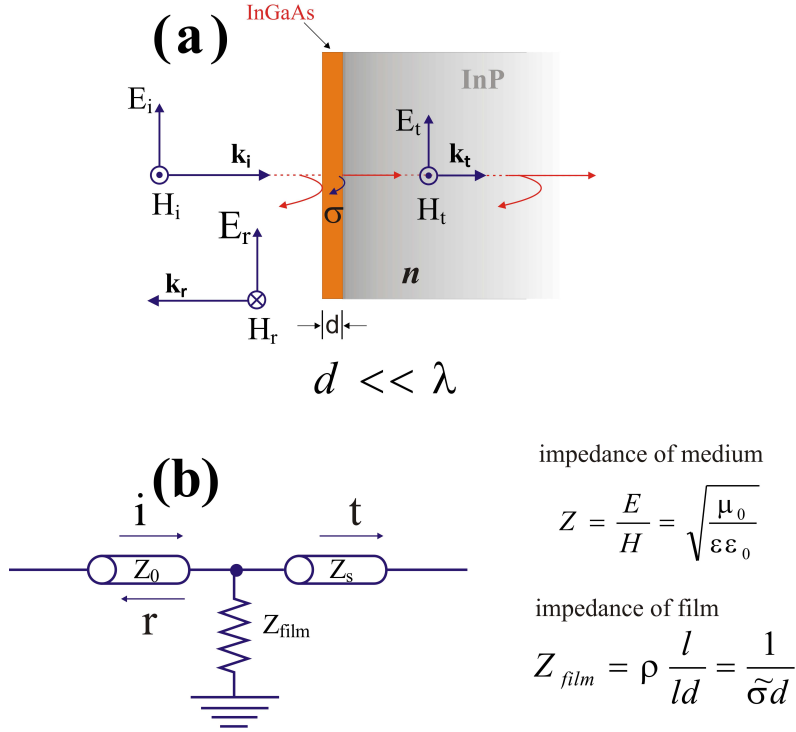
Figure 6.2: (a) Simplified scheme of a field amplitude transmission and reflection of a thin conducting film on a thick substrate with index $n$ illuminated by THz pulse at normal incidence to the sample surface. (b) Corresponding transmission line equivalent circuit of free electron response to external electric field for the thin conducting film substrate of Fig. 6.2 (a). The impedance of the film, $Z_{film}$ is calculated from the resistance of a thin film assuming that the film is a square with length of $l$ and thickness $d$.

$$\tilde{t} = \frac{E_t}{E_i} = \frac{2Y_1}{Y_1 + Y_2 + \tilde{\sigma}d} \tag{6.7}$$

$$\tilde{r} = \frac{E_r}{E_i} = \frac{(Y_1 - Y_2) - \tilde{\sigma}d}{Y_1 + Y_2 + \tilde{\sigma}d} \tag{6.8}$$

The impedance of a medium is, $Z = \frac{E}{H} = \sqrt{\frac{\mu_0}{\epsilon \varepsilon_0}}$ of free space and substrate can be expressed in terms of the admittance as $Z_0 = \frac{1}{Y_1} = \mu_0 c = 377\ \Omega$, and $Z_s = \frac{1}{Y_2} = \frac{n}{Z_0}$. Thus, substituting Y1 and Y2 into Eq. 6.7 results the transmission coefficient is simplified to Tinkham equation [Glover and Tinkham (1957)], given as,

$$\tilde{t} = \frac{1}{1 + n + \tilde{\sigma} Z_0 d} \tag{6.9}$$

and the reflection coefficient is simplified as,

$$\tilde{r} = \frac{1 - n - \tilde{\sigma} Z_0 d}{1 + n + \tilde{\sigma} Z_0 d} \tag{6.10}$$

Also, one can evaluate the transmission coefficient given in Eq. 6.9 and reflection coefficient, Eq. 6.10, using a transmission line equivalent circuit of Fig. 6.2 (b). A THz pulse propagating through air represented by an impedance of $Z_0$ and then effectively terminated with a load impedance $Z_{film}$ and $Z_s$.

Figure 6.3 illustrates the simplified form of the transmission equivalent circuit representation of a light beam transmission/reflection at a material interface of Fig. 6.2 (b), where $Z_{eq} = \frac{Z_{film} Z_s}{Z_{film} + Z_s}$. Thus the transmission and reflection coefficients given by Eq. 6.9 and 6.10 can be calculated from Fig. 6.3 as,

$$t = \frac{Z_{eq}}{Z_0 + Z_{eq}} \tag{6.11}$$

$$\tilde{r} = \frac{Z_{eq} - Z_0}{Z_0 + Z_{eq}} \tag{6.12}$$

Plugging the impedances $Z_0$, $Z_s$, and $Z_{film}$ into $Z_{eq}$ can simplify the transmission and reflection coefficients as,

$$t = \frac{1}{1 + n + Z_0 \sigma d} \tag{6.13}$$

$$\tilde{r} = \frac{1 - n - \tilde{\sigma} Z_0 d}{1 + n + \tilde{\sigma} Z_0 d} \tag{6.14}$$
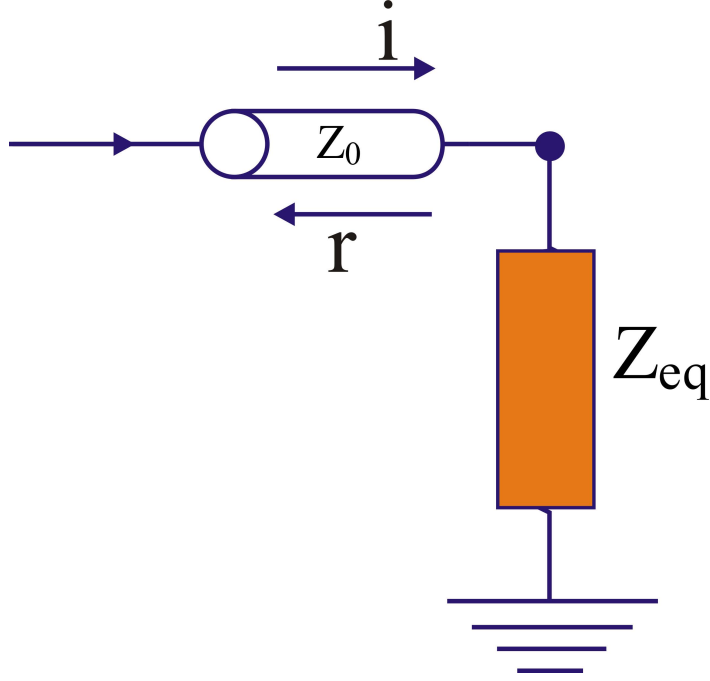
Figure 6.3: Simplified form of the transmission equivalent circuit of Fig. 6.2 (b).

## 6.4 Optical transmission at the air-insulating interface

Here the insulating face of the sample is illuminated with THz radiation as shown in the schematic of Fig. 6.4. Again the boundary condition at the interface require that the tangential component of the amplitude of $\mathbf{E}$ and $\mathbf{H}$ are continuous.

$$H_i - H_r^{'} - H_t^{'} = 0 \tag{6.15}$$

$$E_i + E_r^{'} - E_t^{'} = 0 \tag{6.16}$$

The impedance of the medium is $Z = \sqrt{\frac{\mu_0}{\epsilon \varepsilon_0}}$, where $Z_0$ is impedance of free space, $\frac{Z_0}{n}$ is impedance of substrate, and $Z_{film} = \frac{1}{\sigma d}$ is impedance of conducting film. The magnetic field, $\mathbf{H}$, in terms of impedance can be written as $\mathbf{H}_i = Y_1 \mathbf{E}_i$ , $\mathbf{H}_r^{'} = Y_1 \mathbf{E}_r^{'}$, and $\mathbf{H}_t^{'} = Y_t \mathbf{E}_t^{'}$, thus eq. 6.15 simplified as;

$$E_i Y_i - E_r^{'} Y_r - E_t^{'} Y_t = 0 \tag{6.17}$$

where $Y_i = Y_r = \frac{1}{Z_0}$ for air and $Y_t = \frac{n}{Z_0}$ for the substrate. The equivalent circuit is illustrated in Fig. 6.4 (b). Combining Eq. 6.16 and 6.17, one can obtain the transmitted field amplitude from air to substrate as;

93

**(a)**

InGaAs

$E_i$  $E_t'$  InP  $E_t''$

$\mathbf{k_i}$  $\mathbf{k_t}'$  $\mathbf{k_t}''$

$H_i$  r'  $H_t'$  r"  $\sigma'$  $H_t''$

$E_r'$

$\mathbf{k_r}'$

$H_r'$

$n$

$\rightarrow|d|\leftarrow$

$d \ll \lambda$

**(b)**

impedance of medium

i  t

$Z_0$  $Z_{film}$  $Z_0$

r  $Z_s$

$$Z = \frac{E}{H} = \sqrt{\frac{\mu_0}{\varepsilon\varepsilon_0}}$$

impedance of film

$$Z_{film} = \rho\,\frac{l}{ld} = \frac{1}{\tilde{\sigma}d}$$
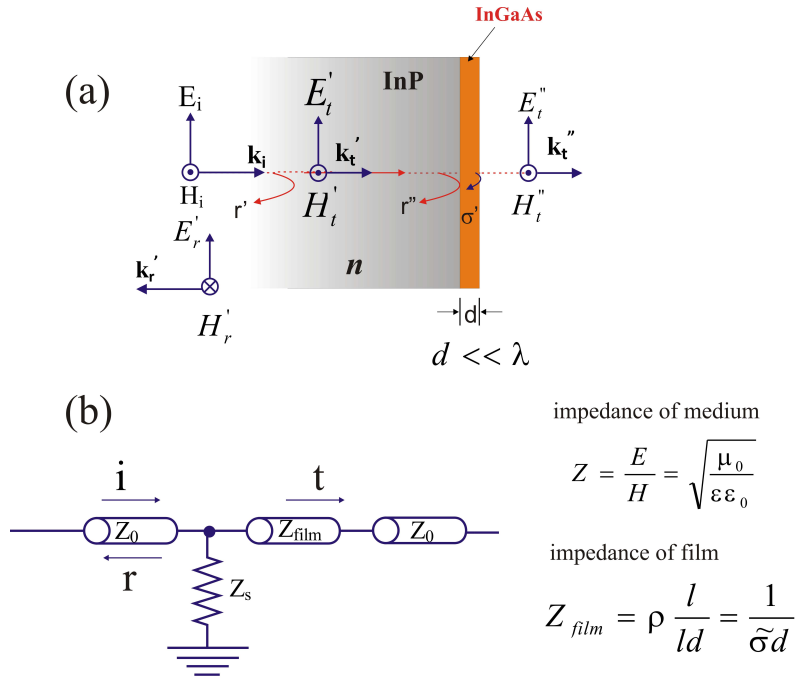
Figure 6.4: Simplified scheme of the field amplitude transmission and reflection of a thin conducting film on a thick substrate with index $n$ illuminated by THz pulse at normal incidence to the sample surface (a) Schematic of a thin conducting film on substrate illuminated on the substrate face. (b) Transmission line equivalent circuit of free electron response to external electric field.

$$E_t^{'} = \frac{2Y_1}{Y_1 + Y_2} E_i \tag{6.18}$$

and the reflected field amplitude at the air-substrate interface becomes

$$E_r^{'} = \frac{Y_1 - Y_2}{Y_1 + Y_2} E_i \tag{6.19}$$

where $Y_1 = H_i/E_i$, $Y_1 = H_r^{'}/E_r^{'}$, $Y_2 = H_t^{'}/E_r^{'}$. Consequently, complex transmission and reflection coefficients of the air-substrate interface are given by

$$\tilde{t}^{'} = \frac{E_t^{'}}{E_i} = \frac{2Y_1}{Y_1 + Y_2} \tag{6.20}$$

$$\tilde{r}^{'} = \frac{E_r^{'}}{E_i} = \frac{(Y_1 - Y_2)}{Y_1 + Y_2} \tag{6.21}$$

In terms of impedance the transmission coefficient is given by

$$\tilde{t}^{'} = \frac{2}{1 + n} \tag{6.22}$$

$$\tilde{r}^{'} = \frac{1 - n}{1 + n} \tag{6.23}$$

Thus, $E_t^{'}$ becomes the incident field to the conducting film in the case of illuminating the insulating face first instead of $E_i$ as listed in Fig. 6.2.

In terms of the given parameter (see Fig. 6.4 (a)), the electromagnetic boundary condition will satisfy Eq. 6.24 and Eq. 6.25 for the substrate-conducting film interface.

$$H_i^{'} - H_r^{''} - H_t^{''} = \mathbf{J}d \tag{6.24}$$

$$E_i^{'} + E_r^{''} - E_t^{''} = 0 \tag{6.25}$$

Again, by plugging the admittances into Eq. 6.24 with Eq. 6.25 the transmitted field through the conducting film can be expressed as

$$\mathbf{E}_t^{''} = \frac{1}{Y_1 + Y_2} (2Y_2 \mathbf{E}_t^{'} - \mathbf{J}d) \tag{6.26}$$

and the reflected field amplitude at the air-substrate interface becomes

$$\mathbf{E}_r^{''} = \frac{1}{Y_1 + Y_2} \left( (Y_2 - Y_1)\mathbf{E}_t^{'} - \mathbf{J}d \right) \tag{6.27}$$

Using equations 6.18, the transmitted field given by Eq. 6.26 can be simplified as

$$E_t^" = \frac{1}{Y_1 + Y_2} \left[ 2Y_2 \left( \frac{2Y_1}{Y_1 + Y_2} \right) E_i - \mathbf{J}d \right]$$ (6.28)

In terms of the index of refraction $n$ of the substrate and complex conductivity $\tilde{\sigma}$ of the film, Eq. 6.28 becomes

$$E_t^" = \left( \frac{2n}{1+n} \right) \left\{ \frac{2}{1 + n + \tilde{\sigma}Z_0 d} \right\} E_i$$ (6.29)

The second term under brace on the right hand side of Eg. 6.29 is simply the transmitted field $E_t$ given by Eq. 6.5, derived from when the applied field illuminates the conducting face of the sample. Therefore, the ratio of the transmitted THz pulse energy through the film during illuminating the insulating face to illuminating the conducting face results,

$$\boxed{\frac{E_t^"}{E_t} = \frac{2n}{1+n}}$$ (6.30)

## 6.5 Electric field variation along the propagation axis

It is known that coherent laser beam oscillations feature a Gaussian envelope of electric field distribution along the beam focus as discussed in section 5.9 of Chapter 2. A Gaussian envelope representation of a THz beam through the focus is shown in Fig. 6.5, in which the sample is scanned. Figure 6.5 shows the Z-scan range in the Gaussian focus of a THz beam that elongates from Z = -25 mm to Z = 25 mm. Figure 6.5 (b) shows experimentally measured pyro-electric infrared image of incident THz field spot variation along the THz pulse propagation axis. Depending on the sample position relative to the THz focus, the sample encounters a variation of THz beam spot radius and consequently variation in THz pulse intensity, peak THz field estimated from Eq. 5.31. Similarly, the THz electric field at different positions can be calculated as

$$|E_{THz}^{peak}(\omega)| = \sqrt{\frac{4\eta_0 W}{\tau A(\omega)}}$$ (6.31)

where $A(\omega)$ is the THz spot area, $A(\omega) = \pi\omega^2$ and $\omega(z) = \omega_0 \sqrt{1 + \left( \frac{z}{z_R} \right)^2}$ is the THz spot radius along the Z-scan axis. Thus, the peak THz field along the Z-axis will be simplified as

$$|E_{THz}^{peak}(\omega)| = E_0 \frac{1}{\sqrt{1 + \left( \frac{z}{z_R} \right)^2}}$$ (6.32)
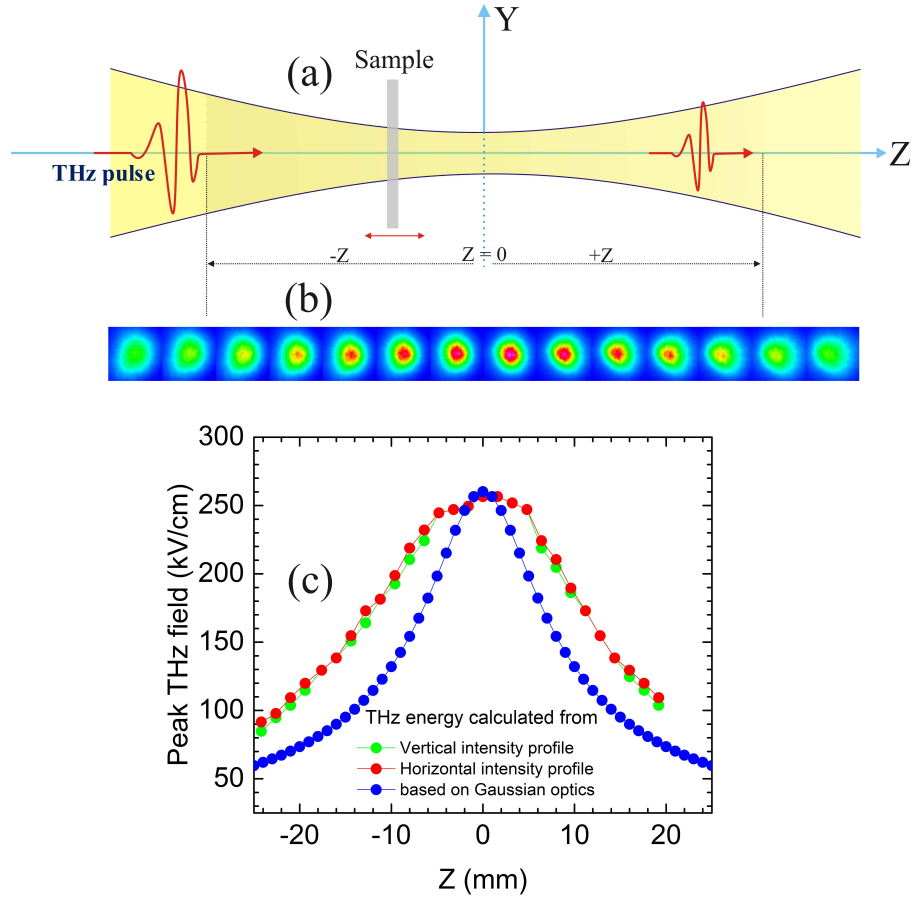
Figure 6.5: (a) Gaussian field envelope. (b) Corresponding THz spot measured along the z-scan range using pyro-electric infrared camera. (c) Peak electric field of a THz pulse with total energy 1.3 $\mu$J (peak electric field of 260 kV/cm at z = 0). for different positions along the Z-scan axis of a Gaussian envelop. Blue curve is a peak THz field calculated based on Eq. 6.32 and red and green curves are peak THz field calculated from the horizontal and vertical intensity profile of the THz spot shown in (b).

where $E_0 = \sqrt{\frac{4\eta W}{\tau A(z=0)}}$ is the THz field calculated at the focus using equation 5.31, $\omega_0$ is the Gaussian beam radius (beam waist radius). At z = 0, the THz field becomes the peak field at the focus, $E_{THz}^{peak}(0) = E_0$. In terms of the sample position other than z = 0, the peak field depends on z and the Rayleigh range $z_R = \frac{\pi \omega_0^2}{\lambda}$ that is given in Eq. 6.32. Using Eq. 6.32 the THz field distribution for a THz pulse of total energy 1.3 $\mu$J is plotted in Fig. 6.5 (c). As the sample is moved closer to the THz focus, the rise in transmission can then be understood as a result of a decrease in conductivity due to the intervalley scattering by the intense THz pulse. From Fig. 6.5 it can be seen that the calculated peak electric field along the z-scan follows the same pattern with the peak field calculated from the intensity profiles of the THz spot along the propagation axis. Similar behavior is observed in all Z-scan results of measured data (see Fig 6.6 and 6.8).

## 6.6 Nonlinear absorption bleaching induced by intense THz pulses in the Z-scan experiment

In this Z-scan experiment, we have exploited an intense THz pulse with an energy of 1.3 $\mu$J and peak electric field of $\sim 260$ kV/cm to illuminate the samples. The total transmitted THz pulse energy is measured using a pyroelectric detector (SPJ-D-8: Spectrum Detector Inc.). As discussed earlier, the samples are n-doped 500-nm thick InGaAs films with carrier concentrations of approximately $2 \times 10^{17} cm^{-3}$ (LD) and $2 \times 10^{18} cm^{-3}$ (HD) grown by metal-oxide chemical vapor deposition on a lattice-matched, 500 $\mu$m thick semi-insulating InP substrate. The Z-scan experimental reveal high nonlinear absorption bleaching of intense THz pulses in both samples by illuminating the conducting and insulating faces alternatively as shown in Fig. 6.6.

It should be noted that from our previous THz Z-scan experimental result a nonlinear absorption bleaching effect is not observed in a bare InP substrate alone scanned in a THz Z-scan setup [Razzari et al. (2009)]. The THz Z-scan experimental results have also shown that the measurement of nonlinear transmission in InP substrate results in a 60 % transmission (see Reference [Razzari et al. (2009)]). Therefore, the overall nonlinear dynamical effect arises from the intense THz field driven free electrons in the conduction bands of InGaAs the sample. Figure 6.6 (a) and (b) shows the results of a THz Z-scan experiment on a LD sample by illuminating the insulating (red curve) and conducting (blue curve) faces, respectively. While, Fig. 6.6 (c) and (d) shows the results of a THz Z-scan experiment on a HD InGaAs sample.

As evident from Fig. 6.6, for both samples regardless of which face illuminated first results a high transmission modulation near the focus relative to the transmission far from
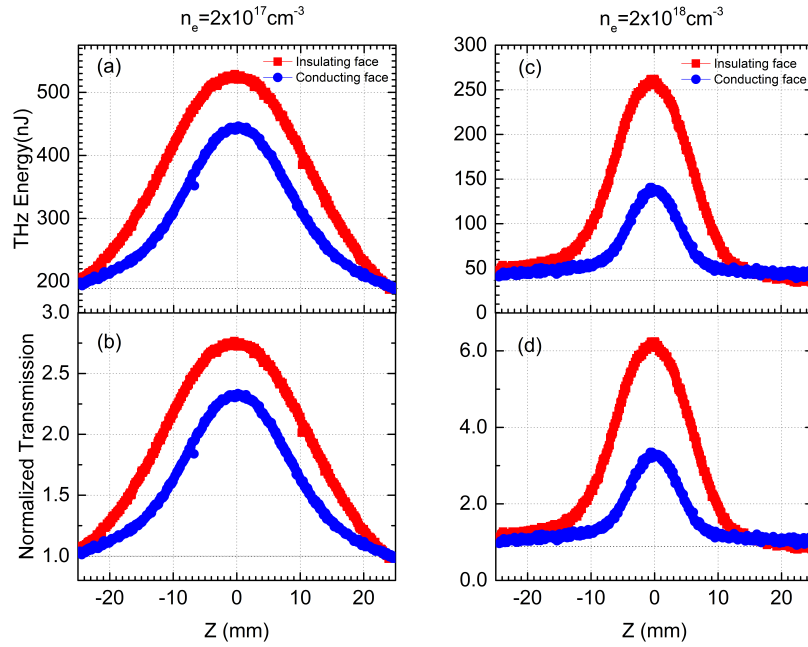
Figure 6.6: Nonlinear THz Z-scan experimental results of the total THz pulse energy transmission through LD InGaAs sample (a) and (b), and HD InGaAs samples (c) and (d). The red curves in all plots are obtained by illuminating the insulating face of the sample with THz pulse energy of 1.3 $\mu$J ($E_{THz}^{peak} = 260$ kV/cm), and the blue curves are obtained by illuminating the conducting faces of the samples.

the focus. The prominent nonlinear bleaching of absorption in both samples are known to arise from intense THz pulse induced intervalley scattering of carriers from the minimum of the conduction band (Γ-valley) to the nearest satellite (L-valley) bands as discussed earlier in Chapter 3 and 4. The data collected by [Razzari et al. (2009)] on a similar InGaAs sample (see section 3.6) was performed at THz energy of 0.8 $\mu$J and field strength of $\simeq 200$ kV/cm produced via OR in a large aperture ZnTe crystal. However, the new normalized transmitted THz pulse data obtained by illuminating the conducting face of the sample (the green line in Fig. 6.1 (b)), displays significantly higher transmission modulation than that reported by Razzari et al. (2009). This is compelling evidence that the generated THz pulse energy from our high power THz pulse generation setup is on the order of micro-joules and more intense than in the previous study. Therefore, the reading of uncalibrated pyroelectric detector appears to be reasonable. In Fig. 6.6 (c) and (d) the Z-scan result of total transmitted THz pulse energy is normalized to the corresponding transmitted THz pulse energy reading away from focus (Z = 25 mm) to obtain the normalized transmission.

As can be seen from Fig. 6.6, in addition to a nonlinear absorption bleaching a broadening of a nonlinear THz transmission for a THz pulse propagates from the substrate to the epilayer for both doping levels are observed. This is due to the higher THz field transmission creates a stronger nonlinearity for the case of illuminating the insulating faces of the sample.

The nonlinear transmission of the total THz pulse energy in both samples is dominated by free-carrier contribution that is in turn affected by scattering into satellite bands at high THz pulse energy and lowers the overall conductivity of the sample to enhance transmission at the focus (Z = 0). When the sample's insulating face is exposed to intense THz pulses, higher modulation of nonlinear THz absorption bleaching at the focus compared to the conducting face illuminated suggests the possibility of a nonlinear THz diode. As can be seen in Fig. 6.6, a strong nonlinear normalized transmission (absorption bleaching) is found to occur at high THz intensity (Z = 0) above 200 nJ transmitted for a given range for low carrier density InGaAs and above $\sim$70 nJ transmitted for the highly doped sample; this is due to carrier heating and hot carrier transfer into satellite valleys at high THz intensity which in-turn lowers the conductivity and enhances transmission.

A summary of the THz transmission ratios for lightly and heavily doped InGaA samples measured by the pyroelectric detector connected to a 300 MHz oscilloscope are given in Tables 6.1 and 6.2, respectively. The data collected by both instruments provided exactly the same transmission ratios for all conditions. For LD samples placed 25 mm away from the focus, approximately 12% of the incident THz pulse energy is transmitted during both illumination conditions. However, the sample transmits over twice as much as at the THz focus for conducting face illumination and three times for insulating face illumination. For the HD sample placed 25 mm away from the focus, approximately 4% of the incident THz

pulse energy is transmitted for both illuminations. On the other hand, when the sample is placed at the focus the THz pulse energy transmission is doubled and quadrupled for conducting and insulating face illuminations, respectively.

According to the derived transmission ratio equation based on the Fresnel and Tinkham approximation for thin films in Sections 6.3 and 6.4 of Eq. 6.30, the ratio of the forward transmitted THz electric field (for a THz pulse propagating from insulating to conducting) to the backward transmitted THz electric field (for a THz pulse propagating from conducting to insulating) results a factor of ∼1.5 . Such a nonreciprocal light transmission suggests the possibility of an optical diode. In the linear regime, light transmission is reciprocal regardless of whether the symmetry is broken or unbroken [Peng et al. (2014)]. However, in our nonlinear bleaching of absorption experiment we measured a nonreciprocal light transmission when the semiconductor face is filliped to the illuminating light pulse. It is highly desirable to develop an optical diode capable of enhancing a transmission of light in one direction and blocking the transmission of light in the reverse direction for future optical information processors.

Analogous to electrical diode, optical diodes allow a one-way transmission of light. This could allow the advent of light based computing (optical computer) and it can be used as an alternative for optical isolators. Figure 6.7 shows a representation of forward and reverse bias optical diodes. The mechanism that controls transmission in forward and reverse bias cases are different in reflective and refractive properties at the air-substrate and air-conducting film. Also, at the substrate-conducting to conducting substrate are different inside the sample. Therefore, a more versatile optical diode based on semiconductors can be achieved by increasing the thickness of the substrate or placing extra insulating layers or saturable glasses at a specific wavelength of large excited state absorption cross section [Philip et al. (2007)] adjacent to the substrate, and decreasing the thickness of the conducting film.

Figure 6.8 (a) shows, the plot of Z-scan experimental results of the two samples by exciting the conducting face Fig. 6.8 (a) and insulating face Fig. 6.8 (b). As seen in Fig. 6.8 the Z-scan result shows a twofold spatial broadening for lightly and heavily doped samples, when the THz pulse is propagated form insulating to conducting face.

It has been suggested that carrier scattering time decreases by a factor of 4 as the electron density is increased from $10^{15} - 10^{19} cm^{-3}$ [Sharma et al. (2012); Mics et al. (2013)]. That is, the electron momentum scattering time increases as the electron density decreases so that the electrons can drift in the THz field for longer time and attain a higher velocity before relaxing to the conduction band. Therefore, for LD sample the transmission curve becomes broader than the HD samples and the peak of the normalized transmission of HD sample is higher than the LD sample.
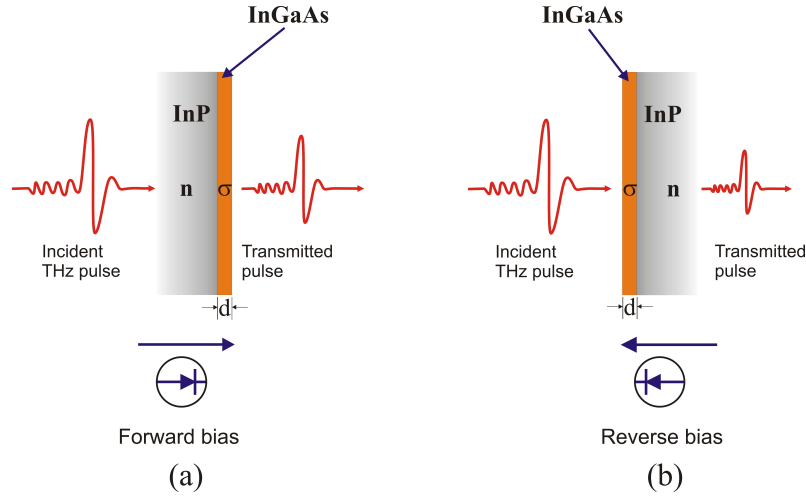
Figure 6.7: Optical diode: (a) Forward bias configuration. THz pulse propagating through the InP layer to InGaAs film results in an increase in transmission than the reverse bias. (b) Reverse bias configuration. THz pulse propagating through the InGaAs film to the InP substrate results a lower transmission with respect to the forward bias. In the figure, **n**, $\sigma$, and $d$ are index of refraction of the substrate, conductivity of the doped InGaAs sample, and thickness of the film, respectively.

Table 6.1: Comparison of THz energy transmission at focus and away focus during an intense THz pulse irradiates the conducting and insulating faces of LD InGaAs film.

| THz illuminates conducting face of LD InGaAs samples | | | | | | |
|---|---|---|---|---|---|---|
| Detector | Pre-focus | T(%) | On focus | T(%) | Post-focus | T(%) |
| | z = -25 mm | | z = 0 mm | | z = 25 mm | |
| Scope reading | 0.152 $\mu$J | 12 | 0.378 $\mu$J | 28 | 0.152 $\mu$J | 11 |
| Pyroelectric | 0.172 $\mu$J | 12 | 0.422 $\mu$J | 28 | 0.164 $\mu$J | 11 |

| THz illuminates insulating face of LD InGaAs samples | | | | | | |
|---|---|---|---|---|---|---|
| Detector | Pre-focus | T(%) | On focus | T(%) | Post-focus | T(%) |
| | z = -25 mm | | z = 0 mm | | z = 25 mm | % |
| Scope reading | 0.184 $\mu$J | 13.8 | 0.4763 $\mu$J | 35.59 | 0.1851 $\mu$J | 13.8 |
| Pyroelectric | 0.203 $\mu$J | 13.6 | 0.522 $\mu$J | 34.9 | 0.203 $\mu$J | 13.6 |
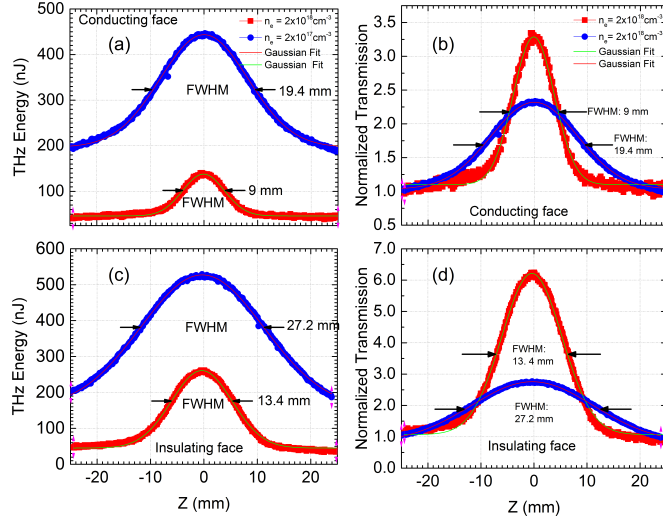
Figure 6.8: Nonlinear THz Z-scan experimental results of a total THz pulse energy transmission through a LD (blue circle lines) and HD ( red rectangle lines) $In_{0.47}Ga_{0.53}As$ samples, respectively. (a) and (c) are obtained by illuminating the conducting faces of the samples. (b) and (d) are obtained by illuminating the insulating faces of the samples. FWHM of red curve in (a) or (c) is 9 mm and 13 mm in (b) or (d), respectively; while for blue curve it is 19 mm in (a) or (c), and 27 mm in (b) or (d).

Table 6.2: THz energy transmission at focus and away focus during the conducting and insulating faces of heavily n-doped InGaAs film irradiated by intense THz field.

| THz illuminates conducting face of HD InGaAs sample | | | | | | |
|---|---|---|---|---|---|---|
| Detector | Pre-focus | T(%) | On focus | T(%) | Post-focus | T(%) |
| | z = -25 mm | | z = 0 mm | | z = 25 mm | |
| Scope reading | 0.5028 $\mu$J | 3.76 | 0.123 $\mu$J | 9.14 | 0.51.4 $\mu$J | 3.84 |
| Pyroelectric | 0.066 $\mu$J | 4.42 | 0.138 $\mu$J | 9.24 | 0.066 $\mu$J | 4.42 |

| THz illuminates insulating face of HD InGaAs sample | | | | | | |
|---|---|---|---|---|---|---|
| Detector | Pre-focus | T(%) | On focus | T(%) | Post-focus | T(%) |
| | z = -25 mm | | z = 0 mm | | z = 25 mm | % |
| Scope reading | 0.0496 $\mu$J | 3.7 | 0.238 $\mu$J | 17.7 | 0.04875 $\mu$J | 3.6 |
| Pyroelectric | 0.063 $\mu$J | 4.22 | 0.258 $\mu$J | 17.29 | 0.0.064 $\mu$J | 4.28 |

## 6.7    Conclusion

In conclusion, we have demonstrated the first optical diode in the THz frequency range analogous to current flow in an electronic diode, by utilizing an intense THz pulse to illuminate the conducting and insulating faces of a doped semiconductors alternatively using an open aperture Z-scan technique. By simply flipping the illuminated faces of the sample from the film (InGaAs) to the substrate (InP), the THz pulse transmission at the focus increases. For a sample thickness of 500 nm we have demonstrated a nonreciprocity factor of 1.5.

# CHAPTER 7

## Ultrafast THz induced transient voltage pulse in InGaAs

## 7.1 Introduction

Interactions of intense THz radiation with different degrees of freedom of matter provides the nonlinear responses of highly doped or photoexcited semiconductors [Wen et al. (2008); Bowlan et al. (2011); Kampfrath et al. (2013)]. In doped semiconductors, the nonlinear carrier dynamics predominantly arises from interband transition of free-carriers, which can be monitored by a nonlinear THz spectroscopy using single cycle ultrafast THz probe pulses.

The last three decades have seen a surge in interest for improving and developing high-speed devices operating in the THz frequency range that have the capability to detect very-low-power transient signals at ultrafast speeds. The photo-response of biased semiconductor materials to optical pulses has been extensively studied since the development of picosecond laser sources [Turchinovich et al. (2012)]. Transient current generation dynamics using femtosecond lasers in semiconductors occurs due to induced polarization resulting from charge separation and excitation, spin rotation, and molecular rotations [Haché et al. (1997); Kampfrath et al. (2013)].

## 7.2 Brief introduction to transient current generation in semiconductors

All nonlinear optical processes can be used to generate electrical currents in solids [Ganichev and Prettl (2006); Laman et al. (2005)]. The electrical transient current arises due to the change in spin degrees of freedom [Haché et al. (1997); Ganichev et al. (2001); Stevens et al.

(2003); Hübner et al. (2003); Zhao et al. (2005)] and normal charge current without spin polarization [Zhang et al. (1992); Cote et al. (2002); Bieler et al. (2006)] can be generated in a higher order optical nonlinear processes. Nonequilibrium carrier transport in semiconductors results in a transient current associated with the occurrence of free carrier redistribution and other various dynamical electric charge transport phenomena. The most common techniques of normal charge current generation in semiconductors are optical rectification, shift currents, and injection currents [Chuang et al. (1992); Laman et al. (2005); Bieler et al. (2006)]. OR is the usual near-dc rectification current associated with a completely non-resonant response. However, shift and injection currents are induced due to above band gap (resonant) excitation of charge carriers.

Electron displacement during excitation leads to generation of the so-called shift current [Laman et al. (2005); Nastos and Sipe (2006); Bieler et al. (2006)]. The current induced by the electron shift distance, $\mathbf{r}_{shift}$ is, given by

$$\mathbf{J}_{shift} = \frac{e\alpha I_P}{\hbar\omega}\mathbf{r}_{shift} \tag{7.1}$$

where $\mathbf{J}_{shift}$, is the shift current density, $\alpha$ is absorption coefficient, $I_p$ is intensity of the pump pulse, $\hbar\omega$ is photon energy, and $\mathbf{r}_{shift}$ is displacement of the charge center. Whereas, injection current is associated with quantum interference of different polarization components of the incident beam that leads to injection of carrier distribution and then an injection current. It vanishes for zincblende crystal structures like GaAs and is generated only for circularly polarized light [Chuang et al. (1992)]. The rectification and shift current induced by optical pulses in semiconductors takes the form [Cote et al. (2002)]:

$$\mathbf{J}_{rect} = 2\epsilon_o\chi^{(2)}\frac{\partial}{\partial t}\left\{\mathbf{E}(t)\mathbf{E}^*(t)\right\}, \tag{7.2}$$

and

$$\mathbf{J}_{shift} = 2\epsilon_o\sigma^{(2)}\mathbf{E}(t)\mathbf{E}^*(t), \tag{7.3}$$

where $\mathbf{E}$(t) is the incident electric field and the asterisk, $\mathbf{E}^*$(t) denotes its complex conjugate. $\chi^{(2)}$ and $\sigma^{(2)}$ are susceptibility and conductivity tensors, respectively. Rectification current is the only second order nonlinear current induced in solids that is associated with photon energies below the band gap ( $\hbar\omega < E_g$) [Laman et al. (2005); Nastos and Sipe (2006)]. However, for a laser beam of photon energy $\hbar\omega > E_g$, the shift current dominates the current response [Chuang et al. (1992); Cote et al. (2002); Laman et al. (2005); Nastos and Sipe (2006)]. Hence, our main focus is on the shift current that arises due to upper band transitions of carriers at intense THz pulse excitations. The mechanism of intense THz pulse induced shift current generation is displayed in Fig. 7.1. The time dependent induced polarization by the low field driving THz pulse leads to a generation of weak shift currents

that follows the laser pulse envelope [Laman et al. (2005)].

As noted in the introduction chapter, THz frequency photons do not have enough energy to directly excite electrons across the band gap of semiconductors. Instead, the low THz electric field interaction enhances redistribution of free charge carriers in momentum space that in turn induces a net electric current in the conduction band. Consequently, it is possible to induce larger photo currents at THz frequencies, as one can increase the number of photons without damaging the sample. Rather, it is suggested that strong THz excitation on an n-type GaAs layer causes coherent THz emission [Kuehn et al. (2010b)].

In this chapter, the generation of ultrafast nonlinear picosecond voltage pulses in n-doped InGaAs by intense single cycle THz pulses without external bias is shown for the first time. Also, the dependence of the voltage transient on polarization, field strength, and carrier density level provides detailed insights into the phenomena governing the dynamics of nonlinear electron transport. The THz pulse induces a nonlinear response that modulates the carrier mobility and affects the conductivity of the sample. This in turn increases the peak field strength of the transmitted THz pulse responsible for picosecond voltage transient generation. The observed nonlinear nature of the transient voltage pulses is attributed to a reduction in the total conductivity of the sample due to intervalley scattering into satellite valleys and conduction band nonparabolicity pronounced at high-momentum states. Our experimental observations are well described by a Drude-based dynamical electron transport model by incorporating intervalley scattering and effects of energy band nonparabolicity. The model reproduces the experimental data quantitatively, and shows that intervalley scattering and band nonparabolicity are the leading effects for the observed nonlinear behavior of the measured voltage transients at high THz field excitations.

## 7.3 Picosecond transient voltage pulse generation in n-doped InGaAs

Voltage transients as high as 20 V with durations as short as 30 ps are measured in n-doped InGaAs as describe in more detail later. The observed voltage transients arise from THz induce polarization response of charge carriers in the conduction band which forms an induced dipole in the semiconductor. Conventional electronic instrumentation cannot be applied to detect such ultrafast transient signals. The transient voltage, therefore, is related to the integrated polarization response of charge dynamics of electrons in the sample. Understanding the microscopic processes responsible for its generation is the subject of the main motivation of this study, which leads to a fundamental understanding relevant to the development of fast THz photodetectors.

A single-cycle intense THz pulse is used to simultaneously perturb and probe carriers in the lower and upper conduction bands of the sample. Acceleration of electrons inside the sample are governed by different temporal parts of the driving field that leads to generation of transient polarization (current). The response of electrons to the THz-field are then monitored by measuring the induced transient radiations. The resulting transient polarization density gives rise to the emission of a picosecond voltage pulse in the reflected and transmitted directions as portrayed in Fig. 7.1 (c) and (f). Such signals are composed of a fast electronic response that follows the individual transmitted THz field cycles.
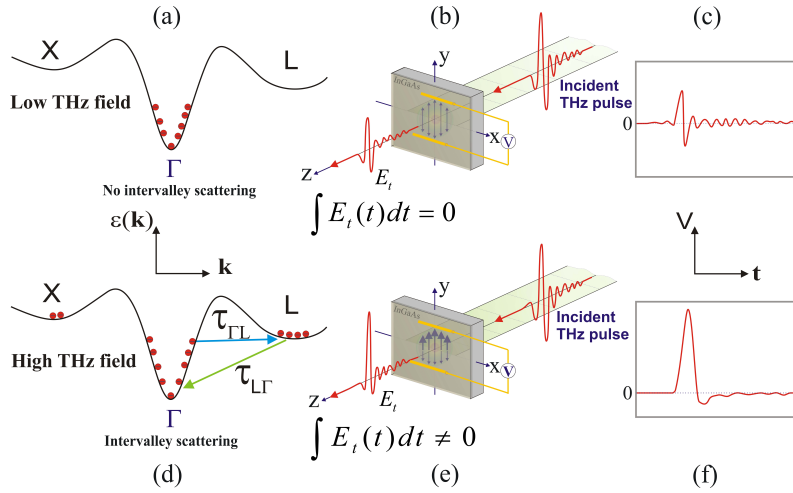


Figure 7.1: Temporal profile of the driving (transmitted) field at low and high THz fields. Free carrier dynamics of the momentum distribution of electrons in the lowest conduction band. (b) At low THz field excitation, the transmitted field is linear and the time integral of the pulse is zero. As a result, the induced voltage transient replicates the shape of the driving (transmitted) field as shown in (c). (d) Intervalley scattering of electrons at high THz field. (e) At high field, the transmission is nonlinear and the driving field becomes unipolar resulting in a nonzero integral. This in turn induces a strong unipolar shift current, as shown in (f).

Figure 7.1 shows the mechanism of the electron momentum distribution and scattering in different **k**-states. Features of the polarization of the driving field and the induced voltage signals are displayed both at low and high field excitations. Figure 7.1 (a) and (d) illustrates

the scattering of electrons at low and high THz field excitation, respectively. Low THz field excitation corresponds to the linear interaction of the field with charge carriers and high field excitations corresponds to the nonlinear interactions.

Low THz fields do not induce any nonlinear response in the sample. Rather it weakly affects the carriers in momentum space via scattering of electrons with the lattice in the Γ-valley [Ganichev and Prettl (2006); Blanchard et al. (2011); Turchinovich et al. (2012)]. The randomization of the electron motion limits the drift velocity. This results in the observed voltage transient pulse mimicking the time profile of the incident THz pulse. Low THz field excitation is strongly affected by lack of inducing strong polarization effects. Hence, the overall time integral of the transmitted (driving) field goes to zero similar to that of the incident field. However, it induces an oscillatory polarization and the radiation generates a low amplitude oscillatory voltage signals identical to the temporal shape of the driving field as shown in Fig. 7.1 (c).

On the other hand, at high THz field excitation, one-half of the driving field ($\mathbf{E}_t$) is much stronger than all other oscillatory parts as shown in the transmitted field of Fig. 7.1 (e), and results in a non-zero time integral of the transmitted THz field. This is because different temporal parts of the pulses experience different absorption efficiencies [Hoffmann and Turchinovich (2010)], and leads to its partial reshaping of the driving field into unipolar. Hence, for a short time, the THz pulse act as a unipolar field. Therefore, the overall induced polarization density within the time duration of a single cycle THz pulse induces a unipolar transient voltage signal, as displayed in Fig. 7.1 (f). The induced voltage transients are then launched into a coaxial cable and recorded on a high speed digital sampling oscilloscope.

## 7.4 Experimental Setup

We developed a novel experimental scheme to study ultrashort THz induced picosecond voltage transients in semiconductors. Figure 7.2 shows a schematic diagram of the experiment that contains an intense THz pulse source, doped sample, transient voltage detectors, and a fast digital oscilloscope. Linearly polarized intense single-cycle THz pulses from a tilted-pulse-front LiNbO$_3$ source (Fig. 7.2 (a)) with peak THz field strengths up to 300 kV/cm are focused onto the sample mounted on an SMA launcher (Fig. 7.2 (b)) or in contact with a high-bandwidth microwave probe (MWP), as illustrated in Fig. 7.2 (c). Any induced voltage transients by hot electrons driven by the transmitted THz fields are then launched into a coaxial cable and recorded on a high speed digital sampling oscilloscope (digital serial analyzer (DSA)).

All the possible scenarios that could lead to the measured transient voltage pulses such as heating, Schottky and contact effects, photogalvanic and substrate effects are investigated
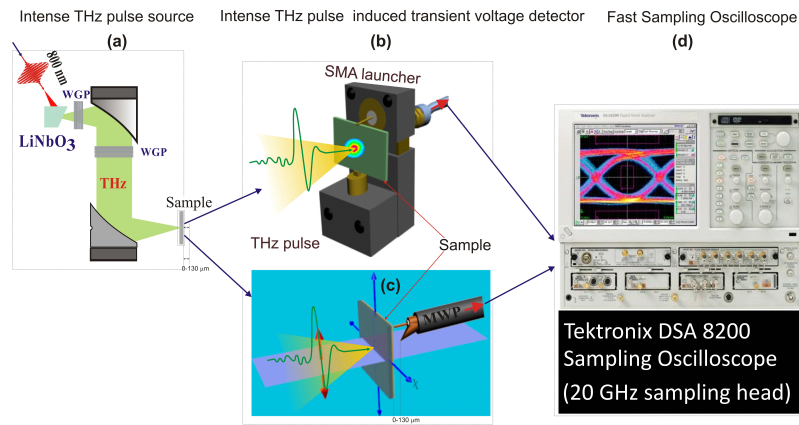
Figure 7.2: Schematic diagram of the experimental setup. (a) Intense THz pulse source. (b) Scheme of transient voltage pulse detectors SMA and (c) MWP. In (b) the sample is mounted between the signal and ground tip of the detector, however, in (c) the sample is mounted on a $1''$ washer and the microwave probe couples the signal either in-contact or non-contact schemes. The picoprobe MWP detector is placed behind the sample (opposite side of the illuminated face of the sample) in the range of 0-130 $\mu$m to characterize the radiated signals. (d) Fast sampling oscilloscope used to display time domain THz induced ultrafast transient voltage signals.

using a systematic variation of the two detection schemes in later sections. This provides a clear insight into the origin of the measured transient voltage signals. The experimental geometry is classified according to the position of the detector with respect to the back face of the sample. The experimental details will be discussed in the next sections. Figure 7.2 (a) represents the simplified THz pulse generation schemes of a tilted-pulse-front experimental setup. A pair of wire-grid polarizers (WGP) shown in Fig. 7.2 (a) were introduced into the collimated section of the beam after the source crystal and prior to the sample position. This is done to controllably attenuate and validate the polarization state of the pump field with respect to the contacts of the detector. After introducing a pair of wire grid polarizers and extra black-polyethylene, the maximum THz excitation pulse energy drops about 1.1 $\mu$J (250 kV/cm) at the focus.

In both detection schemes, the detectors were placed on the conducting side of the film to detect the near- and far-field radiations. The detectors are then connected to either the fast digital scope, slow scope, or even to a Lock-in amplifiers to display the generated voltage signals and current amplitudes. For example, at a THz pulse energy of 0.87 $\mu$J, the pk-pk voltage signal measured using a 300 MHz oscilloscope is 1.1 mV, while it is 770.3 mV using the DSA.

The signals picked up by the detectors are guided to a 20 GHz sampling head of the DSA (Tektronix DSA 8200 sampling oscilloscope) shown in Fig. 7.2 (d). Each detection scheme has its own advantages and disadvantages for exploring the origin of the THz induced voltage pulses by characterizing their dependence on; THz pulse polarization with respect to contacts, heating effects, crystal orientation, and sample-detector separation. The first three effects are easier to be characterized using SMA detection schemes, but it requires more complicated experimental procedures using MWP. However, the last effect is characterized by the MWP detection scheme only. The MWP scheme also give the fastest voltage transients.

### 7.4.1 SMA detector scheme

In this detection technique, the sample is mounted on a 20 GHz SMA launcher between the probing tab connector at the top and ground plane at the bottom. As illustrated in the photograph of Fig. 7.3 (a), a piece of 7×7 mm$^2$ n-doped bare InGaAs sample is mounted on the SMA launcher. The corresponding electronic circuit of the scheme is displayed in Figure 7.3 (b). The THz pulse illuminates the center of the sample at normal incidence. The induced transient voltage signal propagates through a resistive un-illuminated section of the sample to be picked up by the SMA tab connector. This detection scheme is ideal for polarization dependence measurements, where the polarization of the THz pulse can be
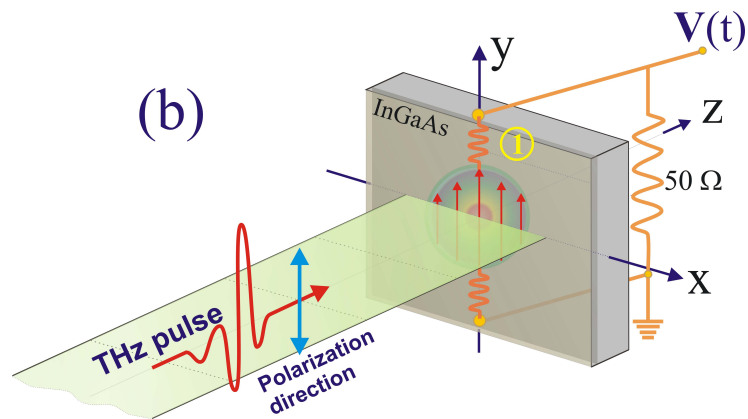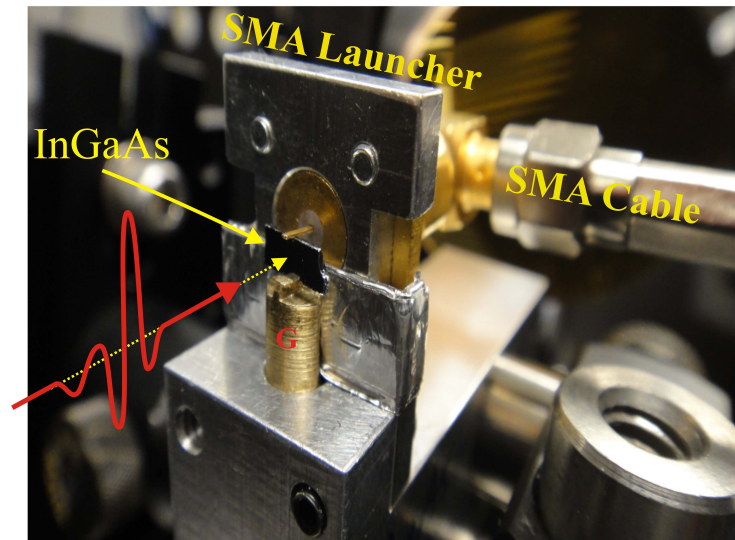
Figure 7.3: Experimental details of the SMA detector scheme of SMA detector. (a) Photograph of an InGaAs sample mounted on the SMA launcher and illuminated with a THz pulse. (b) Simplified electronic circuit scheme of an InGaAs sample mounted on a 20 GHz SMA launcher.

fixed and the sample with SMA contacts can be rotated. The details of this scheme will be discussed in Section 7.5.

### 7.4.2 MWP detector scheme

In the MWP detection scheme, the sample is mounted on a $1''$ washer and placed at the THz focus. The face of the sample is illuminated with THz pulses at normal incidence, and the detector is set to pick up the radiated transient voltage signal at the back face of the sample. The MWP has flexible tips **MODEL 40A**, 40A-GS-1250-EDP (picoprobe by GGB industries Inc.) with a frequency response of DC to 40 GHz, insertion and return losses of about 0.8 dB and 18 dB, respectively, and a ground-signal line pitch of 1.25 mm. The flexibility of the tips allows a highly reproducible measurement scheme for different sample surfaces.

The MWP detector does not necessarily have to be in-contact with the sample. Rather, it can be in-contact with a bare sample or metal transmission electrodes deposited on the sample surface and non-contact measurement methods. The contact and non-contact conditions are determined by a CCD camera mounted on a telescope for precise positioning of the probe with respect to the sample surface in a repeatable manner. All these cases are illustrated in Fig. 7.4. In both the first and second cases, the detector collects the photocurrent transients directed along the surface of the sample. However, in the third case the picoprobe collects the dipole radiation emitted perpendicular to the surface in the far-field (the signals are radiated through space directly from the point of generation to detection). This scheme is ideal for imaging the electric dipole radiation pattern of the illuminated surface by placing the picoprobe few micrometers away from the face of the sample and scanning the MWP. The details off this will be discussed in Section 7.6. A closer view of the MWP in InGaAs sample is shown in Fig. 7.5. In all cases in the MWP scheme, the samples were illuminated on the substrate side as labeled by ② in Fig. 7.4 (a) and the detector was placed on the conducting side of the sample labeled by ①. For a MWP in-contact with a gold-transmission line of the HD film, the pk-pk voltage amplitude reaches up to 20 V, at an excitation pulse energy of 1.1 $\mu$J (corresponding peak field is 236 kV/cm) and up to 8 V is measured from a bare sample at the same THz pulse energy. The pk-pk voltage measured about 130 $\mu$m away from the sample is 450 mV. The MWP is in-contact either with the bare sample as depicted in the photograph of Fig. 7.4 (a) with equivalent electronic circuit displayed in (b), or it is in-contact with gold transmission lines deposited on the InGaAs whose electronic equivalent circuit displayed in Fig. 7.4 (c). The MWP can also pick a voltage transient in free space propagation mechanisms (non-contact measurement).
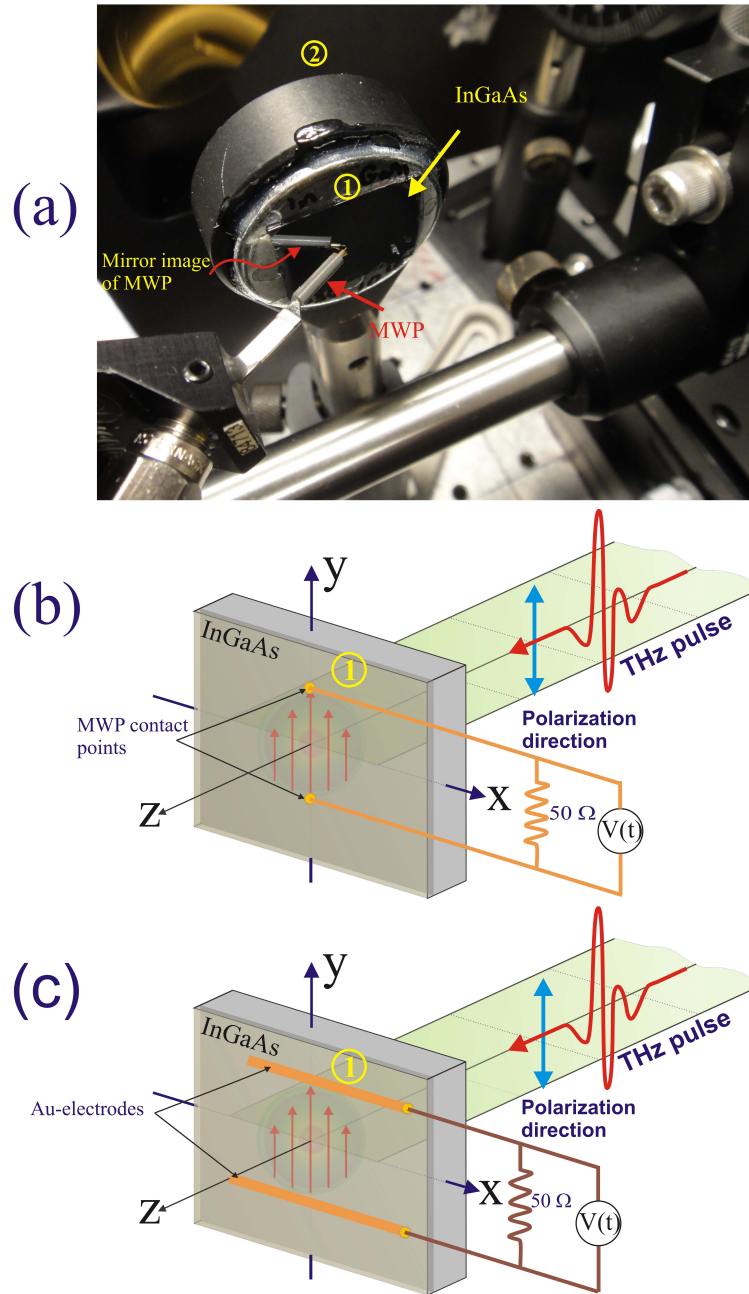
Figure 7.4: (a) Photograph of the MWP non-contact with a THz illuminated bare sample. (b) Electrical equivalent circuit of a 40 GHz bandwidth microwave probe detector in-contact with a bare sample, and (c) in-contact with gold transmission lines deposited on the sample. The non-contact electrical circuit is similar to (b) the only difference is the tip is non-contact with bare sample.

114
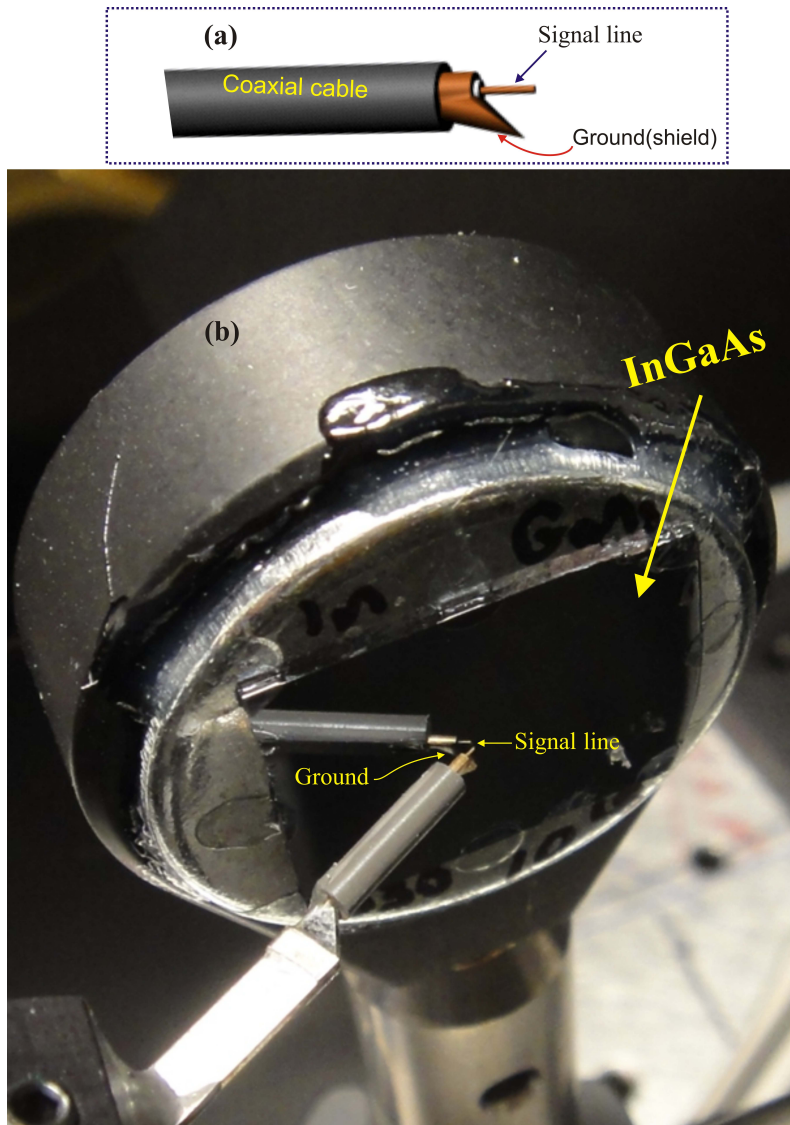
Figure 7.5: (a) The signal and ground line of MWP. (b) Closer view of the microwave probe positioned 100 $\mu$m away from the face of a bare InGaAs sample mounted on a 1″ diameter washer. The MWP is non-contact with the InGaAs sample as shown from the gap between the ground-signal tip of the picoprobe with its mirror image on the face of the sample.

Examples of a picosecond transient voltage pulse generated in a HD sample at a peak THz field amplitude of 225 kV/cm are displayed in Fig. 7.6. Figures 7.6 (a) and (b), show the voltage transients measured by a microwave probe (MWP) in-contact with gold electrodes and a bare sample, respectively.

Gold electrodes were deposited on the film to maximize the radiative coupling of the measured signal. The highest peak transient voltage radiation is recorded, followed by long oscillatory small amplitudes due to parasitic capacitive capacitances and inductances in the circuit. As evident from Fig. 7.6 (a) and (b), the amplitude of the voltage signal measured from the gold electrode sample is more than twice stronger than the signal measured in a bare sample. The FWHM of the voltage transients are 34 ps and 29 ps, respectively. The variation of the width of the voltage pulse is due to the impedance mismatch between the detection components, such as the detector-tip, metal electrode, and bare samples. That is, $Z_{Au} \neq Z_{probe} \neq Z_{InGaAs}$, where $Z_{Au}$ is the impedances of the gold electrodes, and $Z_{probe}$, and $Z_{InGaAs}$ are impedances of MWP, and bare sample, respectively. Moreover, the FWHM pulse duration of the measured voltage pulses is strongly dependent on doping level and detector position with respect to the sample. Figure 7.6 (c) shows the capacitive coupled measured voltage pulse by setting the MWP 130 $\mu$m away from the face of the bare sample. Figure 7.6 (d) is the first time derivatives of the voltage waveforms of Fig. 7.6 (a) and (b). Figure 7.7 shows a typical voltage transient measured by SMA in a HD sample at an incident THz field of 172 kV/cm. The insets shows the corresponding voltage signal spectrum (red signal) and blue curve is the background pick up of SMA measured without sample in place.
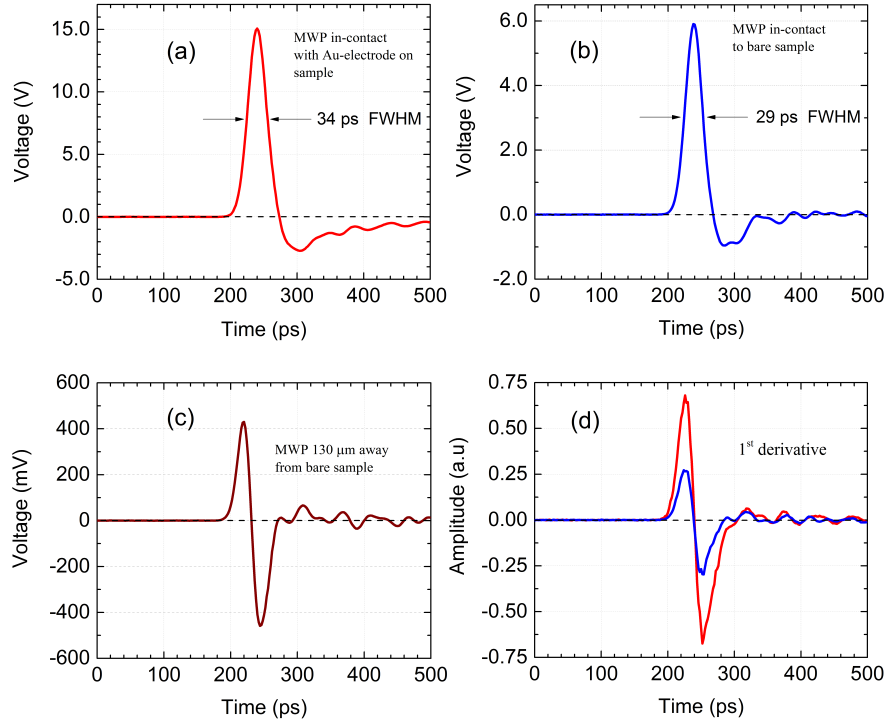
Figure 7.6: Examples of an intense THz field induced transient voltage signals measured by MWP from HD sample with incident THz pulse energy of 1 $\mu$J (peak field of 225 kV/cm). The FWHM of the voltage transients measured varied from 28 ps - 38 ps, depending on the doping level and the position of the detector with respect to a bare or a Au-contacted transmission line samples. Also, the THz pulse spot at the focus affects the spectral width of the induce transient voltage pulses. Transient voltage signals measured by MWP in-contact with a Au-electrode transmission line (a), in-contact with a bare sample (b). (c) 130 $\mu$m away from the sample. (d) The first time derivative of voltage signals in (a) and (b). (Red curve is with Au-electrodes transmission sample and blue curve is bare sample.
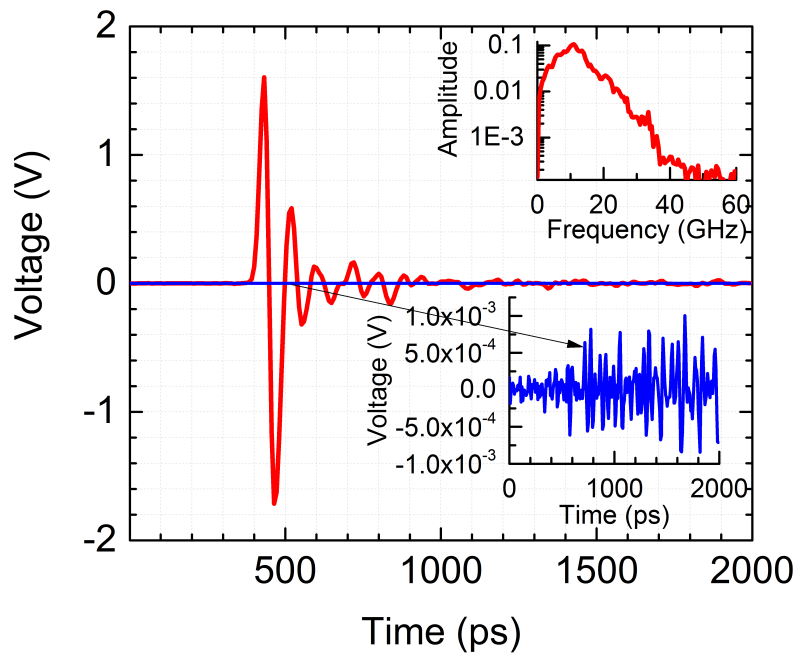
Figure 7.7: Examples of transient voltage signal measured by SMA at an incident THz energy of 0.585 $\mu$J (peak THz field 172 kV/cm) in HD sample. The top inset shows the corresponding spectrum of the voltage transient and the lower panel, the blue curve in the lower inset, is the SMA pick up without the sample in place.

Depending on the strength of the voltage amplitudes, a series of attenuation were used to adjust the amplitude of the measured signal without appreciably distorting the waveform of the pulse. With a carefully aligned setup and a THz pulse energy of 1 $\mu$J, up to 36 dB attenuator was used for a MWP in-contact with a gold electrodes during data acquisition. The voltage loss by the attenuators is given in decibels (dB) from the voltage ratio between the input ($V_{in}$) and output ($V_{out}$) as;

$$dB_{atton} = 20 \, log_{10} \left( \frac{V_{out}}{V_{in}} \right) \qquad (7.4)$$

and the out put voltage becomes;

$$V_{out} = V_{in} 10^{\frac{-dB_{atton}}{20}} \qquad (7.5)$$

where $\frac{V_{in}}{V_{out}}$ is the voltage reduction factor. Table 7.1 displays list of attenuators with equivalent voltage reduction factors.

Table 7.1: Conversation of decibel into voltage gains.

| Attenuators loss in decibels (dB) | 6 | 10 | 16 | 20 | 26 | 30 | 36 |
|---|---|---|---|---|---|---|---|
| Voltage reduction factor $\left( \frac{V_{in}}{V_{out}} \right)$ | 2 | 3.16 | 6.3 | 10 | 20 | 31.6 | 63.1 |

The evolution of the nonlinear THz induced transient voltage dependence on incident field strength, carrier density, and incident THz field polarization are presented. Moreover, it was verified that the induced signals were not due a: (i) heating effects, (ii) substrate or antenna pick-up effects, and (iii) sample orientation dependences. Gouy phase shift effects are also demonstrated by placing the sample at the second focus and measure in polarity reversal in voltage signal. The experimental investigation of such effects are addressed in the next sections.

### 7.4.3    Field and carrier density dependence

Based on the measured parameters and THz peak field calculation as discussed in Chapter 5, a guide to the conversion of THz pulse energy into THz peak field is shown in Fig. 7.8.     Figure 7.9 is examples of THz induced voltage transients in LD and HD InGaAs samples at an incident THz field of 236 kV/cm with corresponding bandwidth limited Fourier
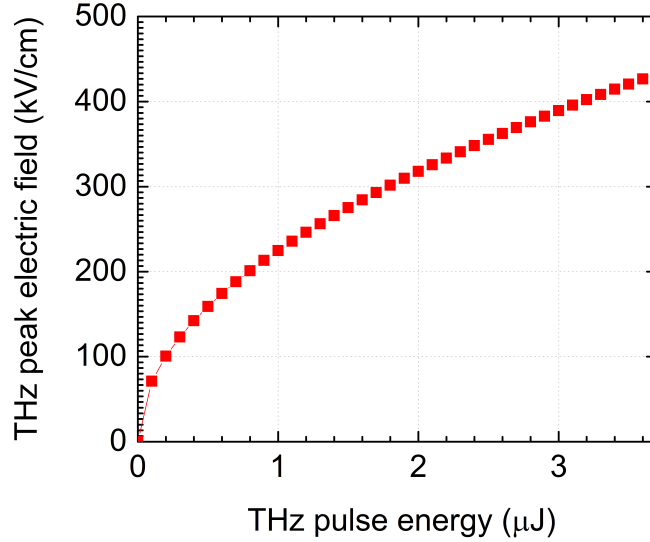
Figure 7.8: THz peak field vs. THz pulse energy.

spectrum. Fast transients of 34 ps and 38 ps pulse width have been observed for HD and LD samples, respectively. The spectral bandwidth is limited by impedance mismatch of the detector components. Figure 7.10 (a) shows the THz incident pulse energy measured by the pyroelectric detector scope reading as a function of wire grid polarizer angle. The wire grid polarizer angle is the orientation of the first wire grid polarizer with respect to the crossed polarization position to the second wire grid polarizer (see Fig. 7.2 (a)). Figure 7.10 (c) and (d) shows the pk-pk voltage measured in Au-electrode contacted and bare samples by placing the detector 130 $\mu$m away from face, respectively. The pk-pk current measured using a Lock-in amplifier is displayed in Fig. 7.10 (c). From the right panel of Fig. 7.10 the dynamics showed a similar evolution for all cases. At an incident pulse energy of 373 nJ (peak field $\approx$ 137 kV/cm), the MWP detector in-contact with a bare sample and connected to Lock-in amplifier in the current mode reads 0.8 nA. The corresponding measured transient voltage, after introducing a 20 dB attenuator, the pk-pk amplitude becomes 1.3 V at 50 ps pulse duration. Thus the pulse current becomes $\frac{1.3V}{50\Omega} \times \frac{50ps}{1ms} = 1.3$ nA, which is close to the Lock-in reading of 0.8 nA.

Figure 7.11 shows examples of the field dependence of fast and slow oscilloscope traces of THz-induced transient voltage signals in HD and LD InGaAs samples. Figure 7.11 (a) and (b) are results measured with the MWP in-contact with an a Au-electrode on HD

120
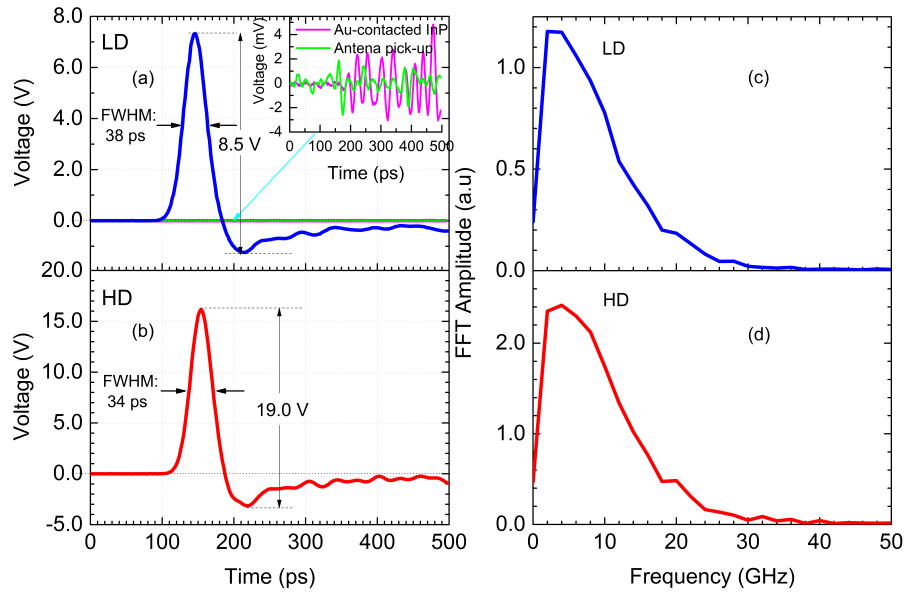
Figure 7.9: Examples of intense THz pulse induced picosecond transient voltage pulses in n-doped InGaAs sample measured by MWP in-contact with gold transmission lines deposited on LD samples (a) and HD sample (b). (c) and (d) are the corresponding frequency spectra of the voltage transients. The inset in (a) displays the measured voltage signal in a Au-contacted substrate (InP) colored pink and antenna pick-up (green) lines, respectively. The THz peak field is 236 kV/cm.
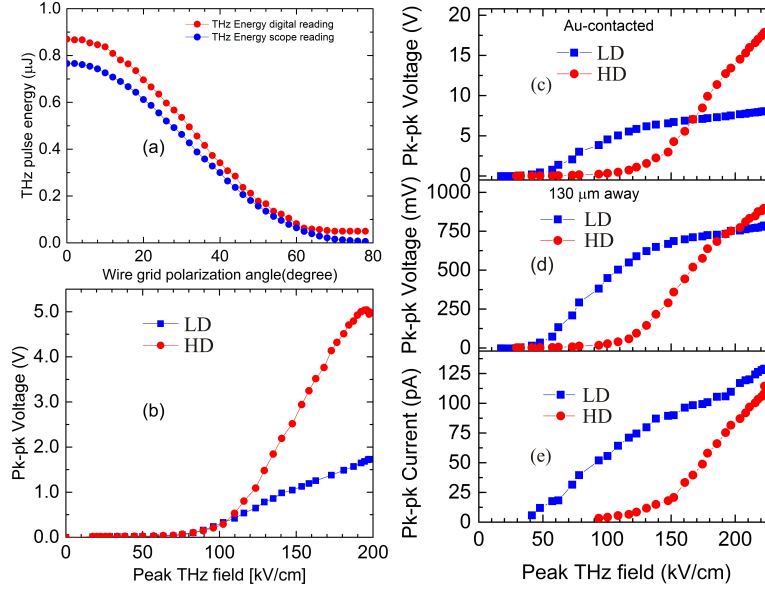
Figure 7.10: THz field dependence of the peak-to-peak values of the transient voltage. (a) THz pulse energy measured using pyro-detector and oscilloscope. The peak to peak voltage measured in lightly (blue curves) and heavily (red curves) doped samples. (b) Peak-to-peak voltage measured with the SMA scheme from bare InGaAs samples. (c) Pk-pk voltage measured with the MWP in-contact with Au-electrode n-doped InGaAs samples. (d) Pk-pk voltage measured in a non-contact (MWP placed 130 $\mu$m away) from bare InGaAs samples. (e) Pk-pk transient current measured using a MWP displayed on a lock-in amplifier. The dynamic model fitting for (c) and (d) will be discussed in the later sections. All the field dependence measurements (b)-(c) follows the same trained. The exception in case of SMA detector the maximum THz field applied was 223 kV/cm whereas the maximum field strength for MWP measured data's was 236 kV/cm.
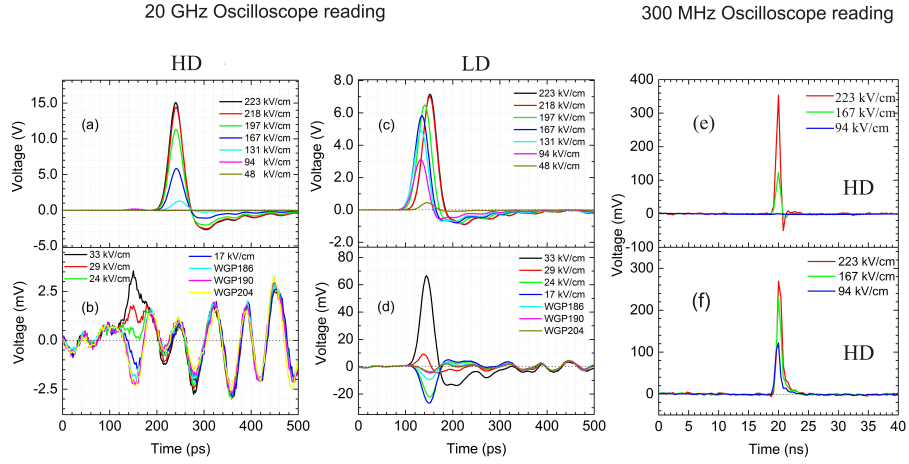
Figure 7.11: Examples of a fast and slow oscilloscope traces of THz-induced transient voltage signals measured from HD and LD InGaAs samples at different THz field excitation strengths. (a) and (b) are experimental results measured by MWP in-contact with a gold transmission line on a HD sample displayed on a fast scope. (c) and (d) are voltage transients for LD samples. In the legend of (b) and (d) WGP186, WGP190, and WGP204 represents for the rotation angle of the first wire grid polarizer with respect to the second wire grid polarizer is $72^o$, $80^o$, and $90^o$, respectively. For both samples, when the THz polarization is rotated by $70^o$ with respect to MWP pitch the polarity of the measured voltage signal is reversed. (e) and (f) are transient voltages measured by MWP connected to a 300 MHz oscilloscope for both HD and LD samples.

sample displayed on the fast scope. As mentioned before, two WGP were used to vary the strength of the applied field. For example, when the two wire grid polarizers are set to be crossed polarization the THz field of $\sim$223 kV/cm is obtained. However, when the first WGP rotated about $72^o$ with respect to the second WGP that controls the polarization states of the incident THz field, the sensitivity of the pyroelectric detector deteriorates, such that a very sensitive instrument is desirable to measure the low THz pulse energy close to a cross polarization accurately. Figure 7.11 (c) and (d) are voltage transients for LD samples. Hence, for the THz field obtained by rotating the WGP by $72^o$ ( WGP186), $80^o$ (WGP190), and $80^o$ (WGP204) are not displayed as shown in the legend of Fig. 7.11 (b) and (d). The temporal shift observed in 7.11 (c) is due to a changing of the attenuators at the scope for each measured signal. Also, with the same experimental conditions, the slow voltage transient measured in HD and LD samples by connecting the MWP directly to a 300 MHz oscilloscope is displayed in Fig. 7.11 (e) and (f), respectively.

Due to intervalley scattering and band nonparabolicity at high field excitation the conductivity of the sample decreases; consequently, the amplitude of the transmitted field strength increasing nonlinearly. The amplitude of the generated voltage pulse then increases nonlinearly with incident field strength.

### 7.4.4   Contact effect

Schottky and contact effects were characterized by blocking and unblocking the tap connectors of SMA detector with a metal ruler as shown in Fig. 7.12 (a) and (b). The tab connector is 0.5 mm wide. In both cases, the same amplitude of transient voltage pulses were able to be measured as shown an overlap plot for both cases in Fig. 7.12 (c). It is confirmed that the measured voltage signals are not due to contact or heating effects of the signal tip.
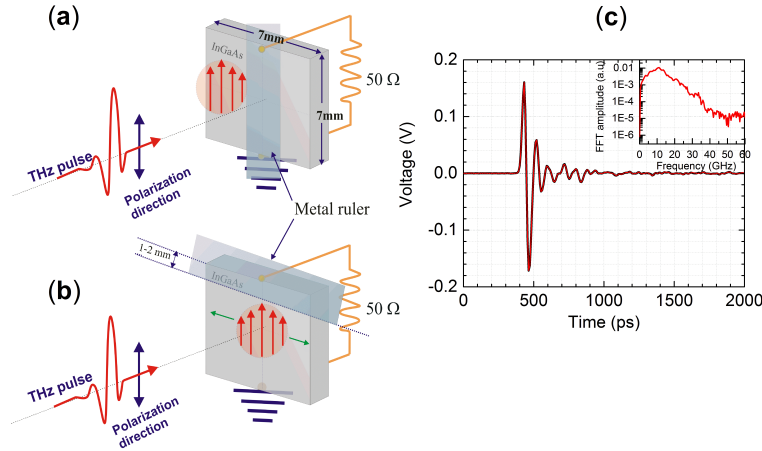
Figure 7.12: Testing for Schottky contact effects: (a) Blocking the probe tip of the sensor with a metal ruler vertically and the THz pulse illuminates at the edge of the sample and we observed a voltage transient. (b) a metal ruler blocks the tip of the detector horizontally and a THz pulse illuminates the sample at the center and still it gives the same amplitude of voltage signals. (c) The measured transient voltage signal and the inset shows a bandwidth limited Fourier spectrum.

## 7.5   Polarization dependence

The THz electric field polarization dependence of the THz induced voltage signal was measured using the SMA detection scheme. In order to study the polarization dependence of the main peak of the transient voltage pulses, the conducting face of the sample in-contact with a thin Au-transmission line on a PC board, as shown in Fig. 7.13, rotates together with the SMA holder with respect to a fixed linearly-polarized THz electric field direction labeled by blue double arrow. That is equivalent to rotating the plane of polarization of the incident THz field with respect to a fixed sample-holder arrangement. The polarization of the incident THz pulse is adjusted using a pair of WGPs as shown in Fig. 7.2 (a). The first wire grid polarizer controls the THz energy amplitude and the second wire grid polarizer is set to allow specific polarization direction to the sample. The conducting face of the sample was in-contact with a thin Au-transmission lines and the THz pump is illuminated between the transmission gap lines on the insulating face of the sample. The transmission line has a 2 mm gap and 2 mm strip width printed on the PC board. The modulation of the transient voltage pulse peak is largest when the polarization of the incident THz field is perpendicular

125
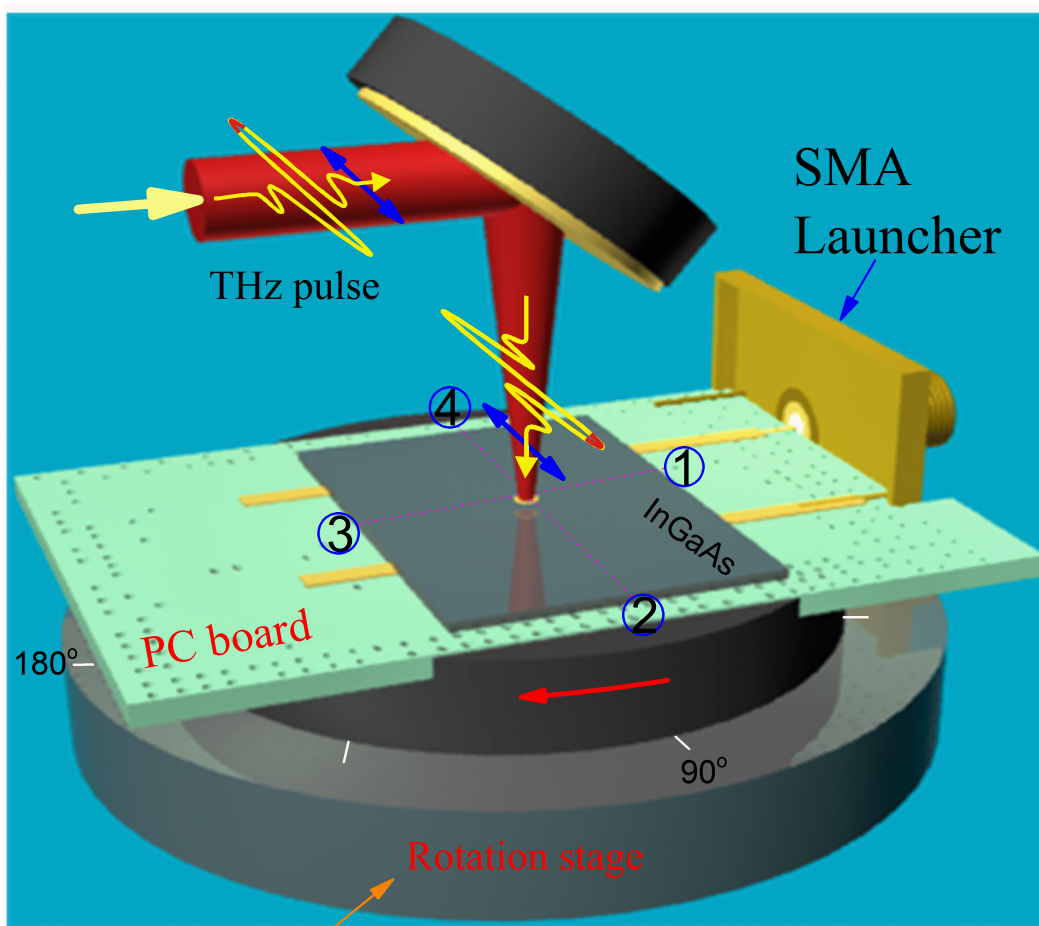
Figure 7.13: Experimental geometry of THz polarization dependence measurement. The conducting InGaAs face of the sample is placed face down on the metal electrodes extended from the negative and positive terminal of the detector attached on a PC board. The THz pulse illuminate on the substrate side of the sample. The rotation stage allow the InGaAs sample to be rotated with respect to the incident THz polarization.
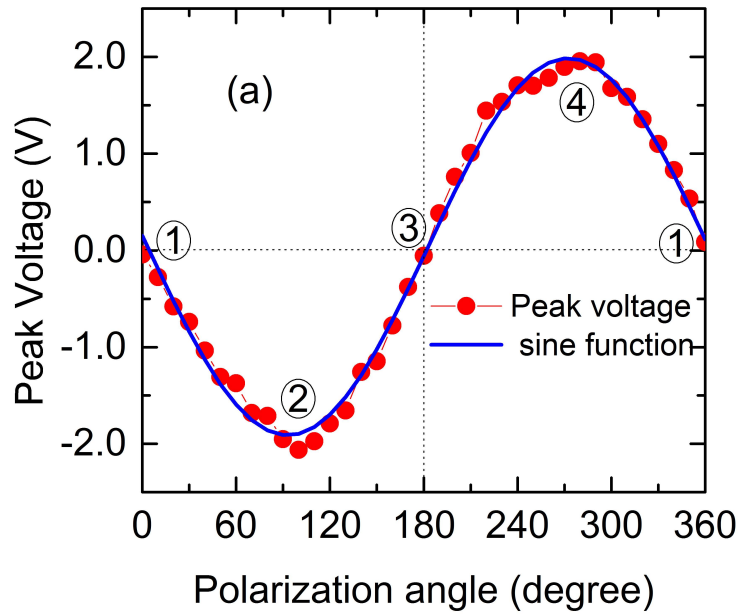
Figure 7.14: Illustration of the polarization dependence of the peak amplitude THz-induced transient voltage pulse. The red circles are the experimental peak-to-peak values of the voltage pulses measured by rotating the sample in-contact with the electrodes in Fig. 7.13 with respect to the fixed polarization of applied THz pulses. The blue line is a fit to the data with a simple sine function.

to the transmission line ($\theta = 90^o$). It can be observed that the magnitude of the voltage transient in Fig. 7.14 reaches its minimum when the THz pulse polarization is parallel to the transmission line.

The azimuthal angle shown in Fig. 7.14 is measured between the plane of polarization of the incident field with respect to the transmission lines in-contact to the sample. The polarization angle $0^o$, $180^o$, and $360^o$ represents an incident field polarization parallel to the electrodes of the detector with sample in-contact denoted by ① and, ③ in Fig. 7.13, respectively. The largest transient voltage amplitude is measured for a THz pulse polarization perpendicular to the contacts. However, the measured voltage pulse is independent of orientation of the sample itself on the PC board. This is because, the thin InGaAs sample is cut along (100); as a result, rotating the sample alone about the normal axis through $360^o$ for a fixed polarization of applied field does not reverse the polarity of measured signal. Upon rotation of the sample with the sample holder, the magnitude of the observed transient voltage depends on the angle $\theta$ between the polarization vector and the electrode in-contact with the sample. The pk-pk transient voltage amplitude traces versus the excitation field polarization angle with respect to the optic axis of the sample, as shown in Fig. 7.14, agrees with the sinusoidal fitting as $V(\theta) = V_{max}\sin(\theta)$. Red dot and blue curves are experimental data and sinusoidal fits, respectively.

The origin of the directionality of the THz induced dipole radiation polarization lies in the transverse variation of the current transients. This property is reflected, through the temporal sequence of the excitation, and the angle of incidence of the pump radiation. For this reason the polarity of the emitted current/voltage pulse polarization can be changed by varying the direction of the THz pump polarization with respect to the contacts.

Also, we have demonstrated a Gouy phase shift effect [Ruffin et al. (1999)] by measuring the voltage signals at two foci represented by focus1 and focus2, as shown in Fig. 7.15 (a). Figure 7.15 (b) shows the pk-pk voltage measured by scanning the sample mounted on an SMA holder through focus 1, and (c) shows examples of voltage pulses measured at the two foci represented by focus 1 and focus 2 in (a). The $\pi$ phase reversal is due to the Gouy phase shift. Figure 7.15 (d) shows the THz induced transient voltage measured using SMA scheme along the axis of the THz focus. As the sample mounted on the SMA scanned along the THz pulse propagation axis the THz beam becomes larger away from the focus.
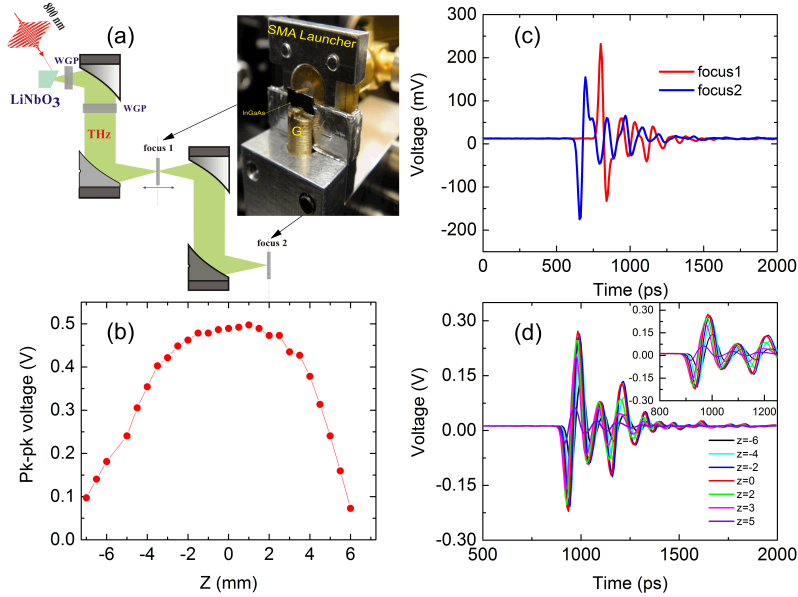
Figure 7.15: (a) An InGaAs sample mounted on an SMA launcher. (b) Peak-to-peak voltage measured along the THz focus (focus1). (c) Voltage transients measured at focus1 (blue line) and focus2 (red line). (d) Examples of voltage transients measured at different position along the axis with SMA detector

## 7.6 Terahertz Induced Transient Dipole Radiation

A nonlinear polarization induced by an intense THz probe excitation acts as the source of the transient picosecond voltage radiation measured in the sample. The ability to characterize the radiation properties in a non-contact fashion is necessary to understand the spatial distribution of the nature of freely propagating radiation. Intense THz pulses are useful for performing THz probe charge carrier dynamics measurements in the near-field [Bitzer et al. (2011); Huber et al. (2008, 2009); Cocker et al. (2013)] and can resolve issues we have not addressed so far. However, when used as a far-field probe of carriers, the spatial resolution is at best in the range of tens of microns, owing to the diffraction limit of the probe radiation [Ulbricht et al. (2011)]. Figure 7.16 shows the MWP used to monitor the nonlinear carrier dynamics without direct contacts to the sample.

In this experiment, the sample is placed at the THz focus and the MWP was placed 100 $\mu$m away from the face of the InGaAs sample in order to map out the free space propagating
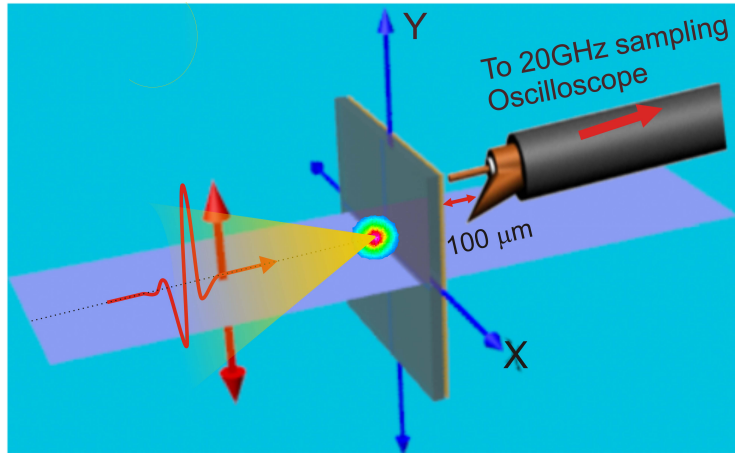
Figure 7.16: THz induced dipole radiation setup: the MWP probe was set at 100 $\mu$m away from the back face of the sample and raster scanned along x and y to image the dipole radiation in the far field.

signals induced by THz driven dipole radiation. The MWP was scanned vertically about 3.6 mm in both directions from the center of the THz spot and horizontally 4 mm on each side while monitoring the amplitude of the generated transient voltage pulses. Figure 7.17 shows the spatial pattern of the transient voltage radiation close to the surface of the sample at a THz peak electric field excitation of 190 kV/cm. In Figure 7.17 (a) the potential has a large gradient between the charges. The surface plot is colored red for positive and blue for negative polarities. Figure 7.17 (b) is the corresponding contour plot of the transient voltage signal, which represents the equipotential lines. Vertical scanning along the center of the THz irradiation spot results a sign reversal for the measured radiation. The MWP is raster scanned along the x and y planes of the sample. The blue and the red concentric ellipses represents the negative and positive polarity of the induced dipole. Figure 7.17 (d) shows simulation result of a dipole radiated inside a material medium from a spatially shifted electrons by dc electric field. A spatially shift from a dc electric field causing charge and current density perturbation, this results dipole radiation pattern which is obtained by solving Maxwell's equation using the source charge and current density. The magnitude of the shift is may consistent with the maximum amplitude of the applied field. The THz spot in Fig. 7.17 (c) and the dipole size in (a), (b) and (d) are exactly equal in diameter as shown a dotted red thin circle. The spatial pattern of the transient voltage shows a dipole pattern related to the spatial shift of charge carriers. By moving the picoprobe in Fig. 7.16 away from the back face of the sample along the THz propagation direction, we
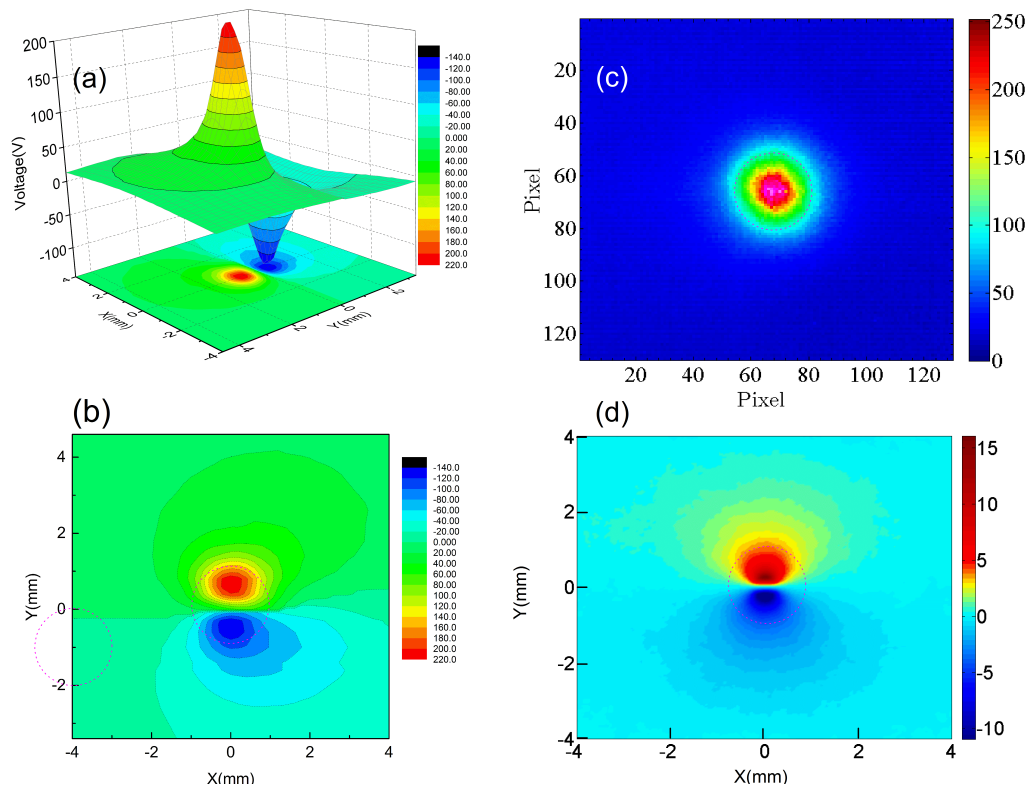
Figure 7.17: THz induced nonlinear dipole radiation pattern. (a) Picosecond transient voltage measured from a THz induced dipole radiation 100 $\mu$m away from the conducting face of the InGaAs sample. (b) Corresponding contour plot, which represents the equipotential lines on the plane of sample. (c) THz spot at the focus. The diameter of the THz spot matches exactly with the size of the induced dipole as shown a thin red dotted circle. The blue and the red concentric ellipses represent the negative and positive polarity of the nonlinear induced THz dipole. (d) A shift current simulated by spatially shifting the electrons by a dc field in a medium causes a dipole radiation pattern.
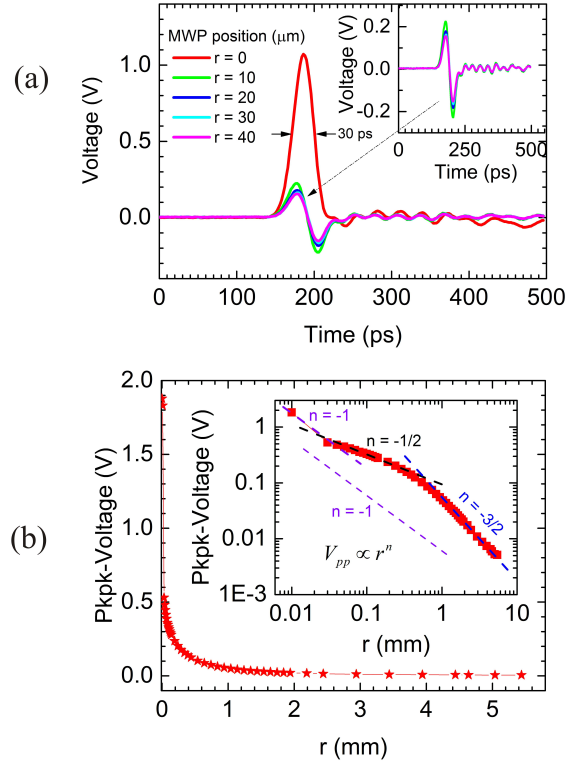
Figure 7.18: (a) Voltage signals measured using MWP at different locations along the propagation direction. The MWP is in-contact with the bare InGaAs sample at $r = 0$. (b) Peak-to-peak voltage measured with the MWP in-contact to non-contact a distance $r$ from the sample.

have characterized the near and far field radiation. A selected spatial dependence of the voltage waveforms, measured at a peak THz field of 196 kV/cm, are shown in Fig. 7.18 (a). The amplitude of the positive peak of the voltage pulses decreases as the MWP detector is far away from the face of the sample. In Fig. 7.18 (a) the free space propagated measured transient voltage waveforms at different detector position is observed to be a bipolar, that is due to the capacitive coupling. Figure 7.18 (b) illustrates the position dependent nonlinear pk-pk voltage measured with the MWP in-contact to non-contact a distance $r$ from the sample in the linear and log-log scale.

## 7.7 Dynamic intervalley electron transfer model

The effect of direct THz induced picosecond voltage transient generation in an unbiased semiconductor was analyzed theoretically. In order to quantify the basic features and gain deeper insight into the time-resolved intense-THz-field transport dynamics, the measured data is compared with a simple dynamical model. Sufficient quantitative insight was obtained using this model for the characterization of linear and nonlinear carrier dynamics.

We employ a modified Drude-based dynamic intervalley electron transfer model [Razzari et al. (2009); Su et al. (2009)] to estimate and explain the measured nonlinear transient picosecond voltage pulses induced by intense THz fields (see the details of the model in Chapter 4 and Appendix D). The simplified model which incorporates interband transitions between two valleys ($\Gamma \longrightarrow$ L and L$\longrightarrow \Gamma$) provides valuable insight into the qualitative nonlinear carrier dynamics in n-type semiconductors. In this model, the nonlinear THz interactions are analyzed in the time domain. The frequency domain analysis may lead to misleading results due to the chirp in the waveform [Razzari et al. (2009)].

As discussed in Chapter 4, for the model we used an electro-optically measured THz pulse (red pulse in Fig. 7.19 (a)). To get rid of any artifacts in the simulation, the overall time integral of the incident THz electric field is forced to be zero. This field is not measured at the sample position, rather it is a far field measured at the second focus using an EOS technique. Thus, the original EOS signal (red signal in Fig. 7.19 (b)) was smoothed out using a cosine taper technique to ensure that the effect of the oscillatory portion of the signal over long time on free charge carriers are minimal and to give carriers enough relaxation time. The Matlab code of the cosine taper smoothing function is given in Appendix B. However, the reflection loss and dispersion added by the substrate for the driving field were not corrected. The smoothed signal (blue signal in Fig. 7.19 (a)) is used as an excitation field in the model and the driving field is numerically solved from the dynamic equations given in Eq. 4.21 of Chapter 4 for incident peak electric fields adjusted to in the range of 0 to 250 kV/cm.

As discussed in Chapter 4, the analytical form of the driving field inside the film is the transmitted field derived from a thin conducting film of thickness $d$ and can be expressed in terms of the incident field, $\mathbf{E}_i$, and current density $\mathbf{J}$ as given in Eq. 4.21 and 6.5. The strength of this field is affected by the modulation of the conductivity of the sample due to the nonlinear electron transport caused by intense electric fields. In the model, it is assumed that every free carrier in the sample experiences equal effects to the transmitted THz electric field. Using standard values of the transport parameters, solutions to the Drude dynamic intervalley model predicts the experimental trends in the time-domain. The nonlinear carrier transport associated with different temporal parts of the driving field induces a transient
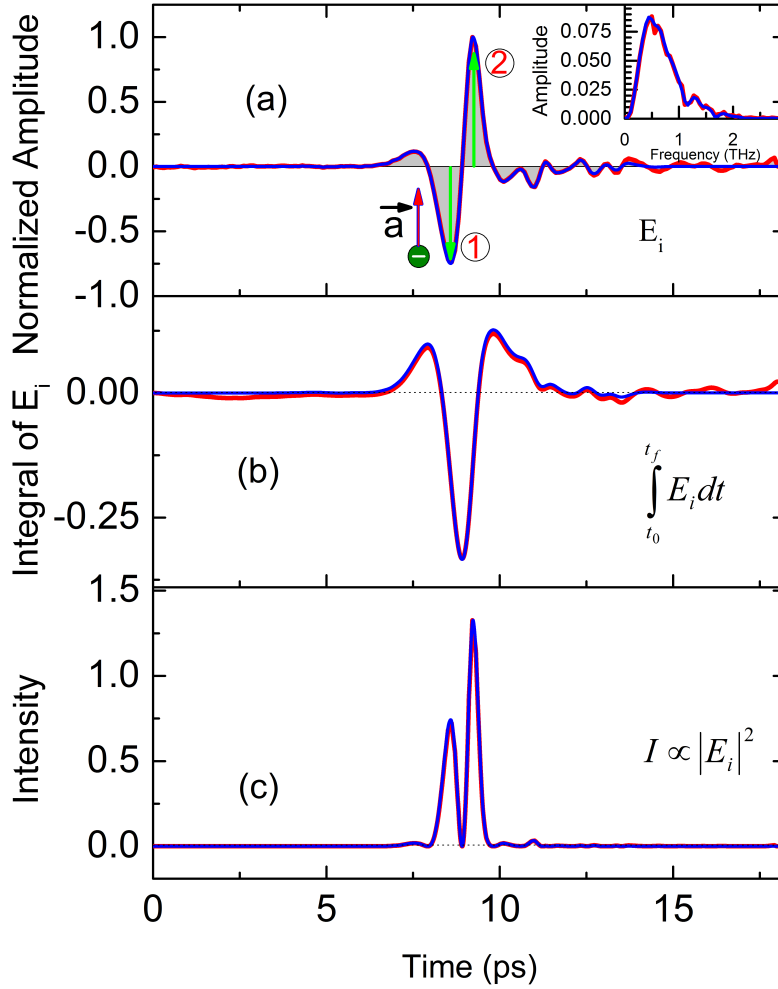
Figure 7.19: (a) An electro-optic measured terahertz pulse (red signal) and after smoothed (blue signal)used for the model. The red line is the temporal profile of an electro-optic measured THz signal and blue line is the corresponding smoothed out signal using a cosine taper method (See Appendix B). (b) Integral of both pulses of (a), which are the algebraic sum of trapezoids of a single cycle THz pulse within the given time window in Fig. 7.19 (a). (c) Corresponding intensity envelope of the pulses that shows regions of the waveform energy contained in the pulse.

134

polarization envelope that follows the shape of the driving field. As shown in the intensity envelope, Fig. 7.19 (c), a strong carrier modulation occurs at the two main peaks of the driving pulse. The induced voltage transient at the sample position is then calculated from the product of the transmitted field and the THz spot diameter, $d$, or the pitch size of the MWP detector as,

$$V_{sample} = E_t d \tag{7.6}$$

However, the voltage displayed at the oscilloscope is determined after losses due to impedance mismatch between connectors and bandwidth limitations air-film-substrate interfaces. If the measured voltage transients are not limited by the bandwidth of the system and by the impedance mismatch between the detector circuits, a faster and high-peak voltage transients are possible. Figure 7.20, shows the calculated transient voltage using Eq. 7.6 at the sample position (without taking into account the limiting effects). However, to estimate the displayed voltage signals at the oscilloscope, all such effects should be taken into account in the simulation. Such effects can be governed by the impulse response of the system. The impulse response of the scope is represented by a Gaussian pulse that has the same pulse width as the experimentally measured voltage transients. Therefore, the voltage pulse displayed at the sample is the convolution of the numerically calculated voltage signal at the sample position with the impulse response, given by;

$$V_{DSA} = [V_{sample} \otimes IR] \tag{7.7}$$

where $V_{DSA}$ is the voltage signal displayed on the oscilloscope and $IR$ is the impulse response of the system. The shape and magnitude of the simulated voltage transients are then retrieved in this manner and compared with experimentally measured voltage signals after adjustment by a small correction factor for circuit resistances. One can also estimate the voltage signal displayed on the scope from the product of the simulated voltage signal at the sample position with the transfer function of the system (oscilloscope) by considering RC low pass filters as the transfer function of the system. The details are given in Appendix F. Figure 7.21 shows the incident, transmitted, and time integral of the THz waveforms, the corresponding total electron energies, the $\Gamma$-valley fractional population, and the convoluted voltage signal obtained from the model in a HD InGaAs sample for both low and high THz pump fields. Low and high THz fields corresponds with THz peak fields of 5 kV/cm and 230 kV/cm, respectively. The low field calculations are listed in the left panel of Fig. 7.21 (a) to (f) and the high field calculations are listed in the right panel from (g) to (l).

At low THz fields, i.e., for low amplitudes of $E_i$, carriers in the sample are accelerated by an external field transient with maximum peak field of 5 kV/cm in the lowest energy valley of the conduction band. As evident from the transmitted field in Fig. 7.21 (d) the field amplitude of 5 kV/cm is low enough to show a linear response. That is, the transmitted

135
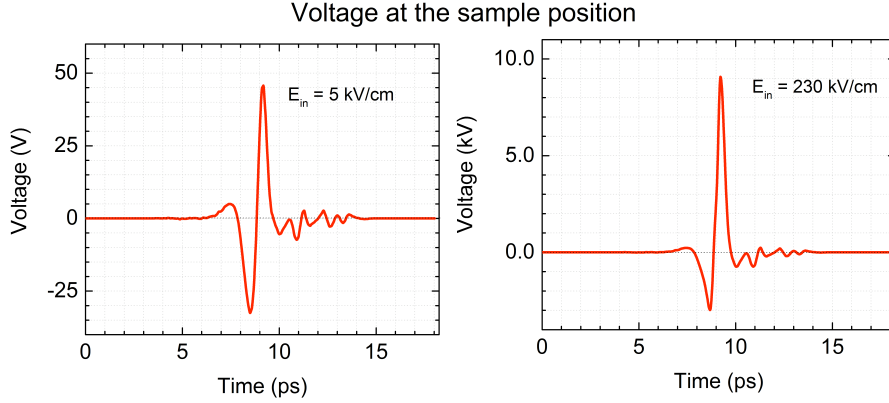
Figure 7.20: Calculated voltage transients using Eq. 7.6 at low ($E_{in} = 5$ kV/cm) and high ($E_{in} = 230$ kV/cm) THz fields. The temporal profiles of the signals are similar to the simulated driving field shown in Fig. 7.21 (d) and (j).

field is similar in shape to $E_i(t)$. The amplitude of the driving field retrieved numerically is less than 1 kV/cm as we can see in Fig. 7.21 (d) and the temporal waveform of the driving field mimics the incident THz field (bi-polar in nature) and its time integral is still zero, as evident from Fig. 7.21 (e). At such low field, intervalley conduction band transfer ($\Gamma \longrightarrow L$) is not likely, rather, the net spatial shift of carriers arising from symmetrically negative and positive peaks of the driving pulse is minimal; and the overall effect of the electromagnetic radiation by such carriers are week. In this case, the non-equilibrium electrons approach the conduction-band minimum by the dominant intravalley scattering rate of longitudinal optical phonons (LO) (emitting a series of LO phonons in a cascade process). This permits the study of ultrafast intraband dynamics of carriers driven out of their equilibrium [Ulbricht et al. (2011)]. The interaction at such low field is in the linear regime and the conduction electrons remain in the high-mobility $\Gamma$-valley, which is confirmed by the corresponding calculated evolution of the $\Gamma$-valley fractional electron population, which is unity, as shown in Fig. 7.21 (c). The transient voltage induced by those low field driven carriers are proportional to the driving field strength and is very small in amplitude, as shown in Fig. 7.21 (f). However, as the incident peak THz field strength increases (see Fig. 7.21 (g)), the temporal shapes of transmitted field differs sharply from the incident wave due to the modification of the overall conductivity of the sample as well as the modification of the spectral content of the driving pulse at the focus as shown in Fig. 7.21 (j)).

At high THz fields the positive peak of the driving field of the half-cycle is much
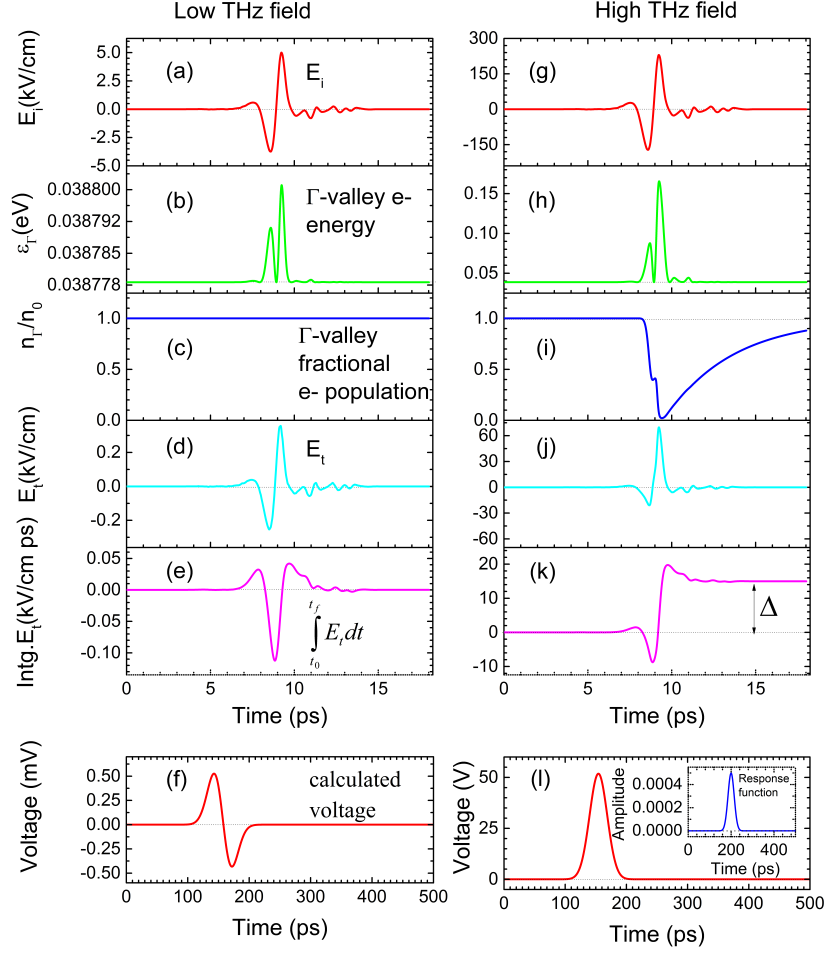
Figure 7.21: Illustration of Drude dynamic calculation for low field ( 5 kV/cm) and high field ( 230 kV/cm). Incident THz fields, $E_i$, at low (a) and high (g) peak THz fields. Calculated total $\Gamma$-valley electron energy at low (b) and high (h) incident THz fields. Calculated relative $\Gamma$-valley population as a function of time, for low (c) and high THz fields (i). Calculated transmitted THz pulses, $E_t$, at low (d) & high (j) electric fields. Integral of driving fields at low (e) and high (k) incident fields. Calculated transient voltage pulses at low (f) and high (l) fields. The inset in (l) is the Gaussian response function used in the model.

137

stronger than the negative peak. This results in a non-zero time integral, as shown in Fig. 7.21 (k), and acts as a net positive field. The high field of the transmitted THz pulse induces intervalley scattering and the Γ-valley fractional population gets to its lowest value, as shown in Fig. 7.21 (i). Within the THz pulse duration, almost 96% of the electrons have scattered into the L-valley, which agrees well with proximately 80% of the electrons in the Γ-valley have scattered into the L-valley within 200 fs reported using Monte Carlo simulation [Osman et al. (1987); Nuss et al. (1987)]. The change in electron population in Γ-valley suggests that electrons are scattered into the low curvature satellite valleys with an energy dependent scattering rate of $\tau_{\Gamma L}^{-1}$. Moreover, the highest number of electrons transfered into the satellite valleys occurs at the main peak of the driving field as detailed in Fig. 7.21 (i) and (j). The curve indicates that the reduction of the fractional population of the conduction band over 1.07 ps time interval is followed by a slower recovery due to the back return of electrons from the satellite L-valleys to the central Γ-valley with a time constant given by the $L \longrightarrow \Gamma$ intervalley scattering time. The cooling of electrons in the Γ-valley allows a net flow of electrons from L-valleys into the Γ valley [Stanton and Bailey (1992)]. The reduction of a fractional population of electrons in the conduction band is comparable with the THz pulse width, 1.5 ps. The temporal dynamics of the observed nonlinear transport is consistent with our previous Z-scan results and model developed by Fuhi Su [Razzari et al. (2009); Su et al. (2009)], in which this phenomenon was attributed to electric-field-driven intervalley scattering and band nonparabolicity at high momentum states.

A striking illustration of the effect of intervalley scattering can be seen in Fig. 7.21 (e) and (k) of the time integral of the driving field for low and high field excitations, respectively. The curve shows the symmetrical nature of the driving field in the low field case results in zero integral, whereas the nonzero integral value, $\Delta$, in case of the high field condition that arises from the unipolar temporal shape of the driving field which is responsible for the observed field dependent temporal nonlinear dynamics. It can be seen in Fig. 7.21 (f) and (l), the simulation gives an excellent estimate of the induced picosecond voltage transient at low and high peak electric fields, respectively. To obtain these pulses, the voltage transient estimated at the sample position is convoluted with the impulse response of the system (photodetectors, fast oscilloscope, and SMA cables). The response is shown in the inset of Fig. 7.21 (l) and the details are given in Fig. F.4 of Appendix F. We see that the numerical model tends to give predictions that are parallel to the experimental data shown in Fig. 7.6.

Linear and nonlinear dynamics are reported in Fig. 7.22 and 7.23 at both low and high THz fields for HD InGaAs sample. In each case, the simulation is performed for a carrier response to the THz field that is linear (LN), linear with nonparabolic (LN-NP) band structure, nonlinear with no intervalley (NL-NI) scattering, nonlinear with parabolic band (NL-P), and nonlinear (NL). In linear conditions, the conduction bands are parabolic

138

Table 7.2: Different conditions of carrier response parameters taken into account in the model. Note: P is for parabolic and NP is for nonparabolic. Refer Chapter 4 for the details of the nonparabolicity factors $\alpha_\Gamma$ and $\alpha_L$, and the rate of carrier density, $\frac{dn_\Gamma}{dt}$.

| Parameters | LN | LN-NP | NL-P | NL-NI | NL |
|---|---|---|---|---|---|
| Energy band | P | P | NP | NP | NP |
| $\alpha_\Gamma$ | 0 | 0 | $\neq 0$ | $\neq 0$ | $\neq$ |
| $\alpha_L$ | 0 | 0 | $\neq 0$ | $\neq 0$ | $\neq$ |
| Intervalley scattering | no | no | yes | no | yes |
| $\frac{dn_\Gamma}{dt}$ | 0 | 0 | $\neq 0$ | $\neq 0$ | $\neq 0$ |

and intervalley scattering is not included in the calculation, which leads to all the carriers remaining in the lowest conduction band. In case of nonlinear effects, intervalley scattering and band nonparabolicity are included in the model. The different parameter assumptions taken into account for the model is summarized in Table 7.2.

It can be observed from Fig. 7.22 (b) and (c) that similar behavior was observed in all cases of the transmitted THz pulses, with no appreciable time shift and change in the pulse shape. Furthermore, it mimics the temporal shape of the incident THz pulse of (a) and all the integrals are zero, as shown in Fig. 7.22 (e) and (f), thus the low field interaction does not create any net change on the free carrier conductivity in the time duration of the pulse. Figure 7.23 illustrates the linear and nonlinear characterization of the dynamical model at high peak THz electric field. As can be seen in Fig. 7.23 (b) and (e), there is a noticeable nonzero integral for the transmitted field of linear and nonparabolicity (LN-NP) condition as compared with the linear (LN) condition. The nonlinear dynamics due to intervalley scattering and nonparabolic effects at high THz peak electric is evident from the time integral plot of Fig. 7.23 (f). The plot shows the nonzero integral of the driving field due to the unipolar nature of the transmitted field at high peak electric field as compared with the low field cases.

We see that the numerical model tends to give predictions of pulse shortening for the transmitted pulse with an increase in peak electric field as detailed in Fig. 7.24, which is consistent with results obtained in [Hoffmann and Turchinovich (2010)]. The author addressed THz pulse shortening, as it propagated through the n-doped semiconductors with increase in peak electric field of the THz pulse.

Figures 7.25 (a) and (b) show picosecond voltage pulses measured in a gold-electrode-contacted HD and LD InGaAs samples, respectively. As a result, the low THz field response
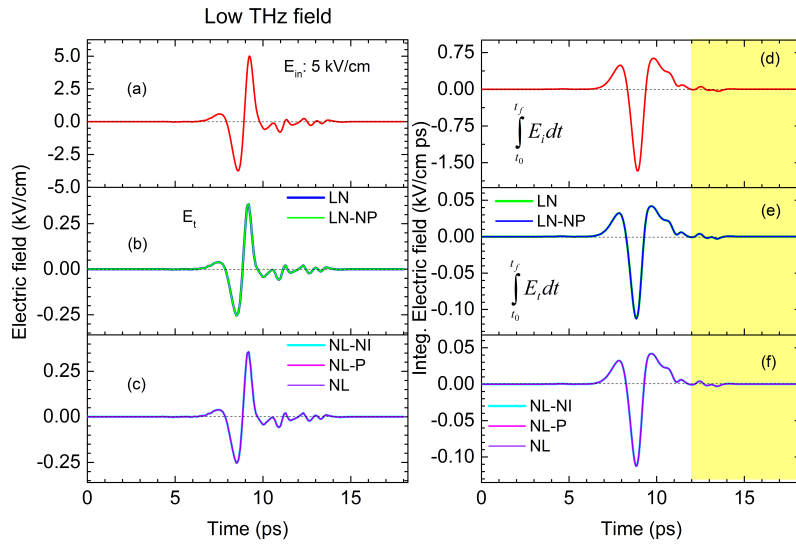
Figure 7.22: Left panel (a)-(c) are the incident field at low field for $E_{in} = 5$ kV/cm, and the transmitted fields for linear (LN), linear and nonparabolic band (LN-NP), nonlinear no intervalley (NL-NI), nonlinear with parabolic band (NL-P), nonlinear (NL). The right panel (d)-(f) are the corresponding integral of the incident (d) and transmitted fields (e), and (f), respectively.
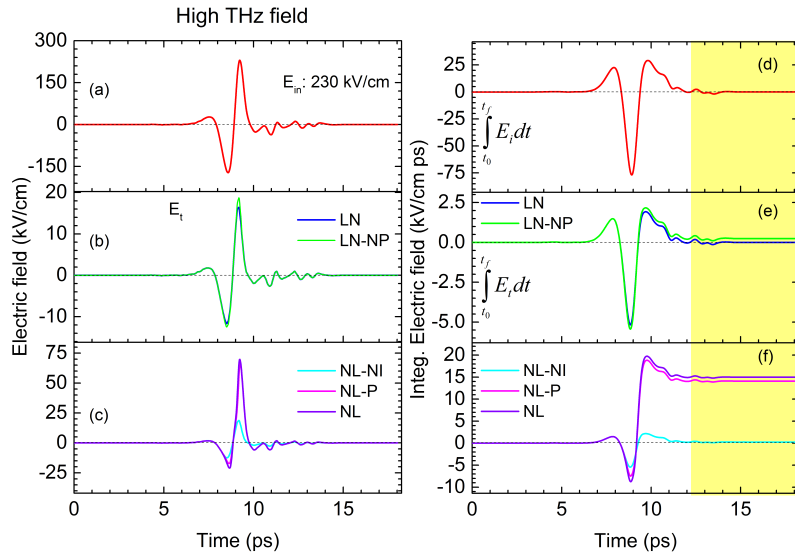
Figure 7.23: Left panel (a)-(c) are the incident field at high THz field for $E_{in} = 230$ kV/cm, and the transmitted fields for linear (LN), linear noparabolicity (LN-NP), nonlinear nointervalley (NL-NI), nonlinear parabolicity (NL-P), nonlinear (NL), respectively. The right panel (d)-(f) are the corresponding integral of the incident and transmitted fields, respectively.
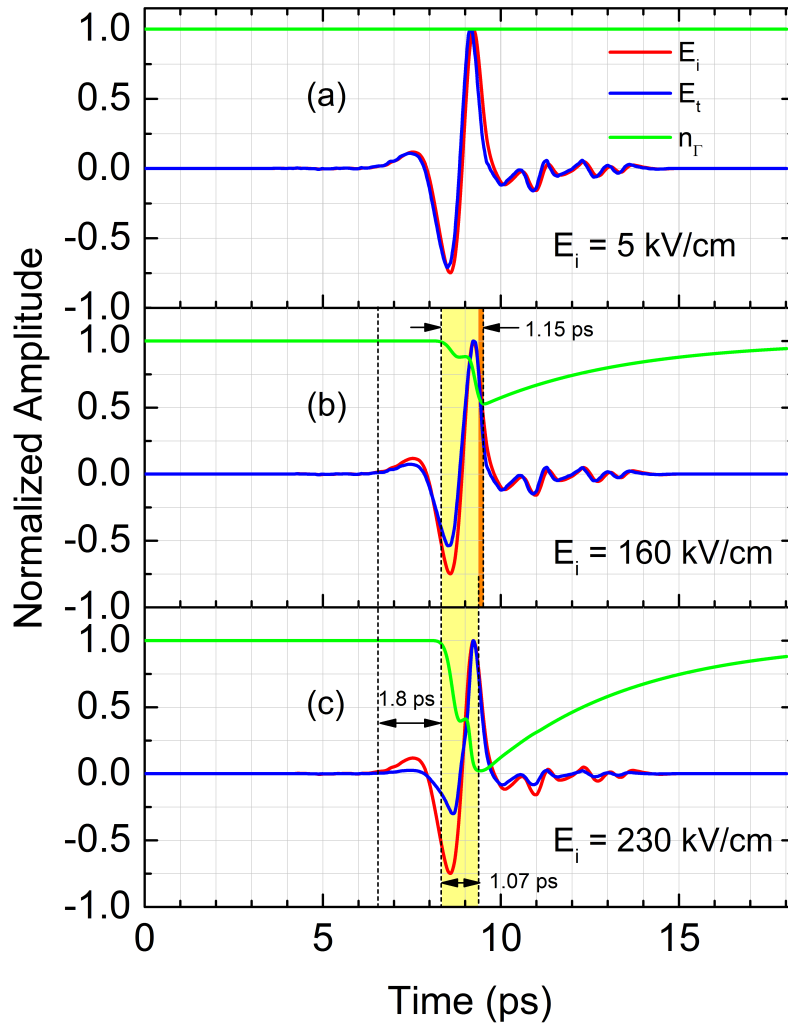
Figure 7.24: Transmitted THz pulse and carrier density of Γ-fraction at low (a), intermediate (b), and at high-THz electric field (c). In (b) and (c) the horizontal arrows indicate the duration of the transfer of electrons to satellite valleys due intervalley scattering and the vertical arrows indicated the shortening of the negative peak at high THz field results a unipolar driving field.

Table 7.3: Summary of the best fit parameters used in the model. $\alpha_\Gamma$ and $\alpha_L$ are the nonparabolicity factors (see Eq. 4.18) for $\Gamma$ and L-valleys, respectively.

| Parameter | symbol | Z-scan[1] | TPTP[2] | Transient Voltage $2\times10^{17}$ $(cm^{-3})$ | $2\times10^{18}$ $(cm^{-3})$ |
|---|---|---|---|---|---|
| Nonparabolicity factor (eV$^{-1}$) | $\alpha_\Gamma$ | 1.33 | 1.33 | 1.33 | 1.33 |
| | $\alpha_L$ | 0.59 | 0.59 | 0.59 | 0.59 |
| Scattering times ($10^{13}s^{-1}$) | $\tau_\Gamma^{-1}$ | 1.00 | 1.00 | 1.00 | 1.00 |
| | $\tau_L^{-1}$ | 1.67 | 1.67 | 1.67 | 1.67 |
| | $\tau_{\Gamma L0}^{-1}$ | 3.33 | 3.33 | 1.32 | 3.33 |
| | $\tau_{L\Gamma}^{-1}$ | 2.5 | 2.5 | 3.3 | 2.5 |
| Smooth parameter | b | $0.57\varepsilon_{th}$ | – | $0.95\varepsilon_{th}$ | $0.76\varepsilon_{th}$ |
| Correction factor | – | – | – | 0.765 | 0.3125 |

[1] Fit parameters of Z-scan result [Razzari et al. (2009)].
[2] Fit parameters used in TPTP [Blanchard et al. (2011)].

of carriers deviates from linear behavior. Figures 7.25 (c) and (d) shows the corresponding pk-pk measured voltage pulses for HD and LD InGaAs samples as a function of incident THz peak field. Figures 7.25 (e) and (f) show the corresponding log-log plot of (c) and (d), respectively. The dotted curve in Fig. 7.25 (c) and (d) shows the pk-pk measured transient voltage amplitude as a function of incident THz field strength for both HD and LD InGaAs samples, respectively. For the HD InGaAs sample, as illustrated in Fig. 7.25 (c), starting at intermediate fields of 150 kV/cm, the amplitude increases rapidly. However, for LD InGaAs sample, (see Fig. 7.25 (d)), starting at peak fields of 60 kV/cm the pk-pk voltage increases rapidly. The solid lines are Drude-based dynamic intervalley electron model fitting. As can be seen in Fig. 7.25 (c), the nonlinear simulations (both solid lines, blue and green) are reasonably consistent with the experimental data. However, for the lightly doped sample the fitting does well, roughly up to 150 kV/cm, and for high field strength the simulated data deviates from the experimental data. This might be due to the fact that at high field strength the carriers might scatter into both satellite valleys in which case the model doesn't account for the X-valley contribution.

In the linear plots, the Drude dynamic modeling reproduces the features observed experimentally for both HD and LD InGaAs samples as shown in Fig. 7.25 (b) and (e), respectively. However, in the lower field regime of mainly in the log-log plot the prediction
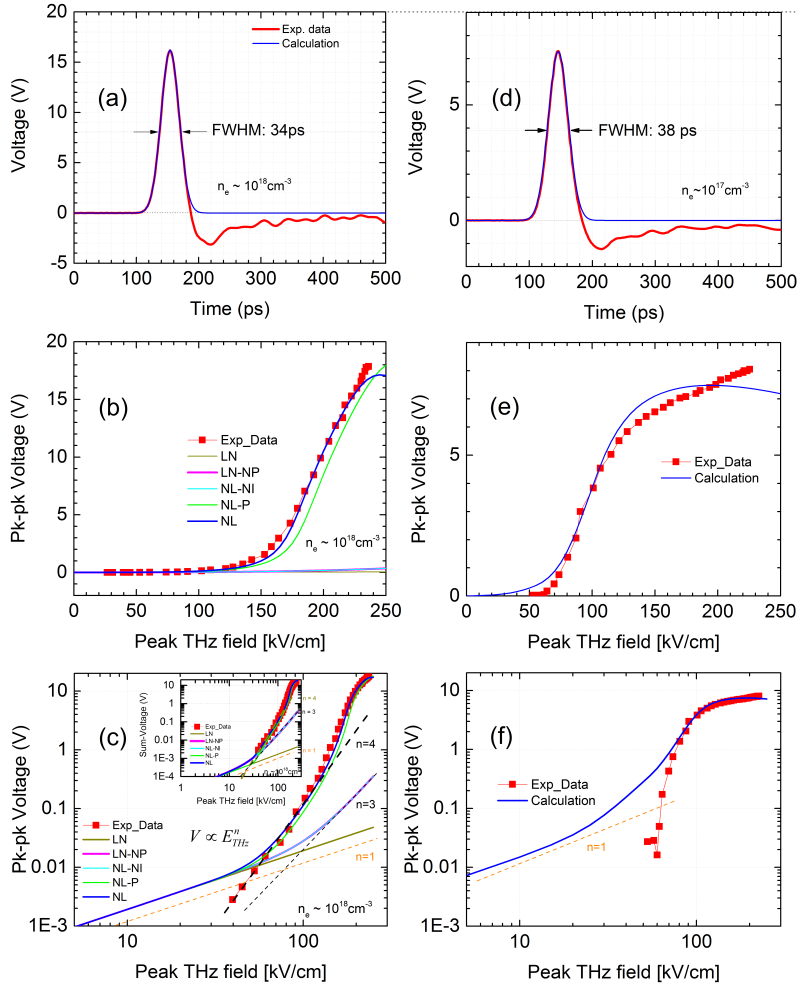
Figure 7.25: Amplitude of pk-pk voltage as a function of incident peak THz pulse field and fits to the model. To fit the simulated data with the experimental data, a scaling factor of 0.3125 and 0.765 are used for HD and LD InGaAs samples, respectively. (a) Voltage transient measured in HD InGaAs sample. (b) The linear plot of pk-pk voltage measured for HD sample as a function of peak THz field and a fitting based on the model. (c) Is the corresponding log-log plot of (b). (d) Voltage transient measured in LD InGaAs sample. (e) The linear plot of pk-pk voltage measured for LD sample as a function of peak THz field and a fitting based on the model. (f) Is the corresponding log-log plot of (d).
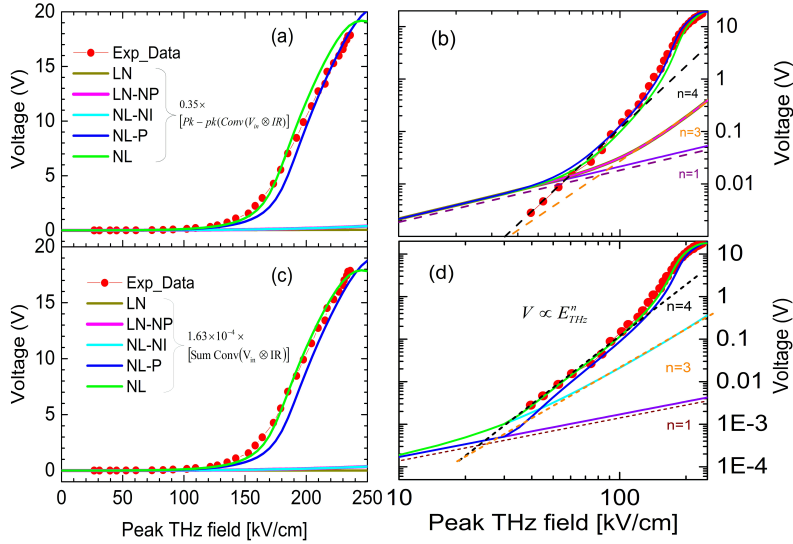
Figure 7.26: (a) and (b) are the same plot with Fig. 7.25 (b) and (c), in which the pk-pk of the convoluted voltage pulses fit with the experimental pk-pk voltage value. (c) For the same experimental data the sum of the convoluted voltage transients fit with the pk-pk data. (d) Corresponding log-log plot of plot (c). The correction factor for the convoluted pk-pk voltage transient is 0.3125 and it is $1.63 \times 10^{-4}$ for the sum of the convoluted voltage transients. Note: all solid lines represent results of model calculations.

deviates from the linear behavior. In this regime, the voltage pulse reverses sign for LD InGaAs samples, but such effect is not observed in the HD InGaAs sample. It could be explained based on the wire-grid polarizers used for adjusting the peak THz field. At low field region, the experimental data shows the phase and temporal shape of the incident THz field changes with respect to high field regime due to the nonideality of the THz wire-grid polarizers. However, the measured THz spectrum at low THz fields (close to the cross polarization condition) doesn't change significantly. The mechanism of deviation of the low-field regime from the Drude dynamic model is not fully understood. The origin of this behavior is still unclear. A fit to the data in Fig. 7.26 (b) or (d) reveals an exponential dependence of measured voltage transient changes from linear ($V \propto E_{THz}$) to power-law ($V \propto E_{THz}^{n}$) as shown in the log-log plots.

Taking the pk-pk of the estimated voltage transient (the convolution of the voltage pulse
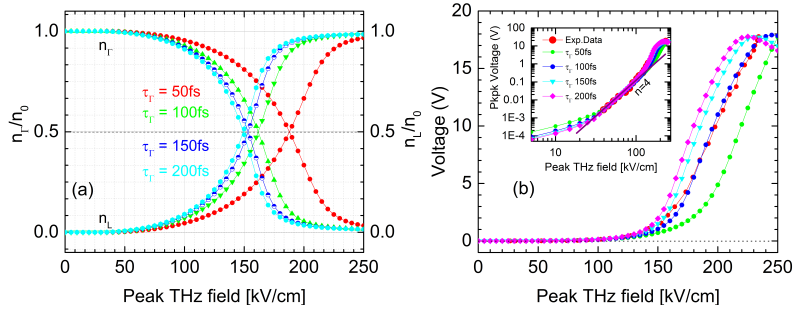
Figure 7.27: Fractional population of the Γ and L-valley versus applied electric field at different scattering times. As the applied field increases the temporal waveform shape of the transmitted field changes due to the modification of the THz sample interaction

.

induced at the sample position with the impulse response) at each peak electric field, one can directly determine a quantity proportional to the measured pk-pk voltage pulses. Although, taking the sum of the estimated voltage transient (the convolution of the voltage pulse induced at the sample position with the impulse response) at each peak electric field, one can retrieves indirectly a quantity proportional to the measured pk-pk voltage pulses. Such quantity can also be determined from the time integral of the voltage pulse simulated at the sample position (the product of the transmitted field with the pitch size ($\int E_{THz}d$)). The amplitude of the voltage increases nonlinearly with THz field. Our interpretation of the field dependence of the measured voltage peaks based on dynamic equation of motion are in agreement with the experimental data. High THz fields causes a fraction of electrons to scatter into higher satellite valleys. Figure 7.27 (a) shows fractional population of Γ and L-valleys calculated at different momentum scattering time of 50, 100, 150, and 200 fs that shifts the threshold peak field excitation to 188, 160, 153, and 150 kV/cm, respectively. In the fitting of Fig. 7.26 (a) and (c) the model uses a $\tau_\Gamma = 100$ fs, in which the fractional population balances about 150 kV/cm as shown in Fig. 7.27 (a). Consequently, the nonlinearity dependence of the experimentally measured THz-induced voltage pulses with peak THz field as shown in Fig. 7.27 (b) and 7.26 (a) and (c) starts at 150 kV/cm. The blue line in Fig. 7.27 (b) calculated at the scattering time of 100 fs. The pk-pk value of the measured transient voltage pulse is calculated as a function of momentum scattering rate in Fig. 7.27 (b). The inset in (b) shows the power-law dependences of the transient voltage on the driving field strength.

## 7.8 Limitation of the Drude dynamic intervalley electron model

Drude model has been successfully applied in extracting the frequency dependent conductivity of semiconductors, however, it is inadequate to describe the energetic carrier dynamics in detail in compound semiconductors. The model does not take into account the contributions of all the possible scattering mechanisms and the full band structure of the host crystal. All the scattering events are not included in the model. The description of the nonlinear ultrafast electron response requires more refined and complete models. This simple model depends only on the valley the electrons occupy and not on the details of the electron states within each valley [Stanton and Bailey (1992)]. For example, during intervalley scattering, the model does not account for states in the $\Gamma$-valley that are not energetically able to scatter into the L-valley. For both carrier densities, at low THz field excitation experimentally measured pk-pk THz-induced voltage dependence on the excitation THz field deviates from the Drude model. The mechanism for such effect is not fully understood. Similar observations were reported that at low charge densities the conductivity of n-type and p-type doped silicon samples departs from the Drude form in the THz spectral range [Ulbricht et al. (2011)]. The experiment is categorized as a many-body problem that needs a more complex ensemble Monte Carlo simulation to account for the full band structure and for all scattering effects, at every instant of carrier motion driven by THz field.

## 7.9 Conclusion

In conclusion, we used an intense THz pulses to modulate and probe the ultrafast time evolution of carrier dynamics by measuring the picosecond transient radiation produced by hot carriers in doped semiconductors. We successfully measured THz induced currents in n-doped semiconductors for time scales as short as 30 ps. The induced transient voltage is nonlinearly dependent on the THz field strength. The largest transient voltages are generated for the field polarization perpendicular to the contacts of the detector with sample. The nonlinearity is explained by intense THz-induced-intervalley scattering and band non-parabolicity. This study provides an enhanced understanding of nonlinear THz responses and ultrafast carrier dynamics in semiconductors which indicates promise towards the development of an ultrafast THz phtotodetector. We also gain insight into a possible physical explanation of the THz induced dipole radiation in InGaAs. We describe the experimental measurements with a Drude-based theoretical model for electrons driven by ultrashort intense THz transients and showed that intervalley scattering and band nonparabolicity are the leading effect for the nonlinear behavior of the measured voltage transients at high

field excitation. The model closely follow the experimental data and provides insight into the nonlinear behavior of the induced transient voltage pulses that arises due to intervalley scattering.

# CHAPTER 8

# Picosecond transient voltage pulse generation in photoexcited GaAs

## 8.1 Introduction

To further examine the THz pulse induced picosecond voltage transient dynamics, we conducted an optical pump-THz probe (OPTP) experiment to directly monitor the carrier density dependent dynamics in a semi-insulating gallium arsenide (SI-GaAs) sample. OPTP spectroscopy has emerged as a powerful and novel technique for probing ultrafast photoexcitation in semi-insulating semiconductors [Schall and Jepsen (2000); Beard et al. (2000); Huber et al. (2001); Lui and Hegmann (2001); Hegmann et al. (2002); Kadlec et al. (2004); Cooke et al. (2006); Su et al. (2009); Ulbricht et al. (2011); Jepsen et al. (2011)]. The unique advantage of OPTP is its ability to determine the resulting ultrafast photoconductivity response at each moment during and after photoexcitation with subpicosecond temporal resolution. In recent years, numerous studies on nonlinear ultrafast THz carrier dynamics on a time scale of picosends to subpicosenonds have been performed [Su et al. (2009); Hoffmann and Turchinovich (2010); Kampfrath et al. (2013)]. In this experimental technique, an ultrashort optical pulse excites the surface of a semiconductor to generate charge carriers, and the subsequent charge carrier dynamics are monitored by a THz probe pulse at some delay time $\Delta t$ after photoexcitation. The interactions among carriers and carriers with the host crystal lattice determine many of the ultrafast transient properties of photoexcited semiconductors. By varying the optical pump fluence, carrier-density-dependence of THz pulse induced ultrafast carrier dynamics can be studied.

Using this technique, we have demonstrated intense THz-field-induced picosecond transient voltage pulses in an unbiased photoexcited [100] SI-GaAs sample for the first time.

The THz-induced picosecond transient voltage is due to an interaction of a THz field with a nonequilibrium electron-hole plasma generated in the photoexcited SI-GaAs. We examined THz electric field, polarization and carrier density dependences of the magnitude of the measured transient voltage pulses. A simple Drude dynamic model of the hot electron transport as discussed in the preceding Chapters shows that the observed transient nonlinear shift current is due to THz-electric-field-induced intervalley scattering over sub-picosecond time scales as well as an increase in the intervalley scattering rate attributed to carrier heating.

## 8.2    OPTP current generation technique

The principle of OPTP experiment is illustrated in Fig. 8.1. The 800 nm optical pulse (red) with photon energy of 1.55 eV, exceeding the band gap, photoexcites the SI-GaAs sample to generate free electron-hole pairs by optical band-to-band transitions in a small region at the sample surface. Subsequently, the non-equilibrium dynamics of photogenerated carriers is then accelerated and probed by a single-cycle intense THz pulses to investigate a nonlinear THz induced voltage transients at different pump probe delay time that can range from zero to several hundreds of picosecond time. The electron momentum scattering is strongly dependent on the pump-probe delay time, and hence on the free carrier density [Mics et al. (2013)]. In our experiments, we have chosen an instantaneous (zero pump-probe delay time) and 20 ps delay time schemes as shown in Fig. 8.1 (a) and (b). Due to the existence of electrons and holes in a photoexcited sample, both contributes for the generation of the induced shift currents. The hole contribution comes from heavy holes (hh) and light holes (lh) (see Fig. 3.2). However, the excess kinetic energy of the optical pump power is possessed by electrons due to their effective mass, $m_e = 0.067m_0$, that is much lighter than that of the holes, $m_h = 0.45m_0$, $m_0$ is electron rest mass. Hence, the mobility of electrons exceeds that of holes. Thus, the induced current predominantly comes from electrons because of the small effective mass; as a result, we neglected hole currents as well as intravalley currents from side-valleys. Therefore, in this experiment the analysis of the experimental data as well as the physical interpretation of the carrier transport model were conducted with the considerations of electrons only. For a known optical excitation fluence the succeeding carrier density generated by the optical pulse can be inferred based on the optical penetration depth at the sample and amounts to $d = 900$ nm at 800 nm wavelength [Su et al. (2009)]. Review of carrier density calculation in photoexcited SI-GaAs sample is given in Appendix G.

Under the application of intense THz pulses, photogenerated carriers undergo ballistic acceleration for times shorter than the mean scattering time ($\sim 0.1$ ps) [Hu et al. (1995); Kuehn et al. (2010a)]. The average drift velocity reaches a maximum once carrier-carrier and
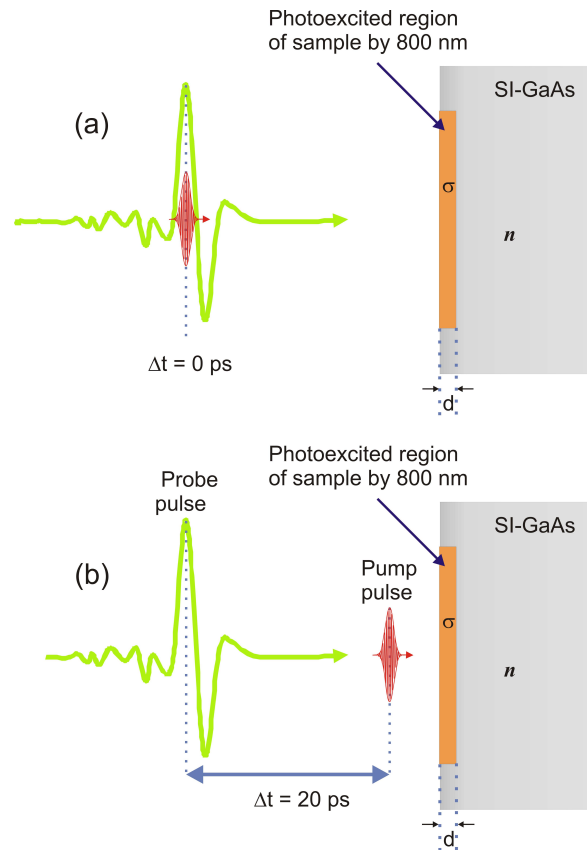
Figure 8.1: Schematic of optical pump THz probe nonlinear transient voltage pulse generation in a photoexcited SI-GaAs sample. (a) Pump-probe delay time $\Delta t = 0$ ps, where $\sigma$ is the photoconductivity induced in the sample, $n$ is the refractive index of the substrate at THz frequency and $d$ is the penetration depth. (b) Pump-probe delay time $\Delta t = 20$ ps. Practically, the optical beam is much shorter than what shown in the plot of (a) and (b).

carrier-phonon scattering processes set in and the acceleration of the carrier stops finally. In this case, the shift current has three distinct components related to the corresponding carrier transition processes in Fig. 3.2 that contributes to the net current generation in the photoexcited sample. These are the process of electron excitation, scattering, and recombination. The measured transient voltage is proportional to the induced current j(t).

## 8.3    Experimental details

The experimental setup is the same as the setup used in Chapter 7, except for photoexcitation, where an additional 800 nm beam line is introduced on the sample and the induced voltage transient pulses are detected using the SMA detector scheme as shown in Fig. 8.2. In our experiment, a piece of 0.5 mm-thick and $4 \times 9 \ mm^2$ semi-insulating [100] bulk gallium arsenide (SI-GaAs) is mounted on an SMA launcher, as shown in Fig. 8.2, and placed at the focus of the THz pulse and photoexcited at normal incidence with a 50 fs ultrashort laser pulses centered at 800 nm, with excitation pump fluence ranging from 0.177 to 32 $\mu J/cm^2$.

The THz spot size on the sample is 1.5 mm and the focal spot diameter of the optical pump beam is 4 times larger than that of the THz probe beam at the sample position. Hence, it is assumed that the probe beam sampled a uniform region of photoexcitation. The optical pump power varies from 0.05 mW to 9 mW using a $\lambda/2$-waveplate polarizer combination and the corresponding carrier density becomes $4.5 \times 10^{15} cm^{-3}$ and $8.5 \times 10^{17} cm^{-3}$ (see Appendix G for carrier density calculations). The maximal THz pump field strength at the focus was 220 kV/cm and its polarization and field strength were properly adjusted by a pair of metal wire-grid THz polarizers. The polarization state of the incident THz electric field was set to be perpendicular to the detection contacts (polarized along the [100] axes of the crystal) and the THz field is adjusted for field dependence measurements. The induced-transient voltage signals are directly coupled to SMA tab connectors; which is connected to the fast digital sampling oscilloscope using a transmission line with 50 $\Omega$ impedance to analyze and display the signals.
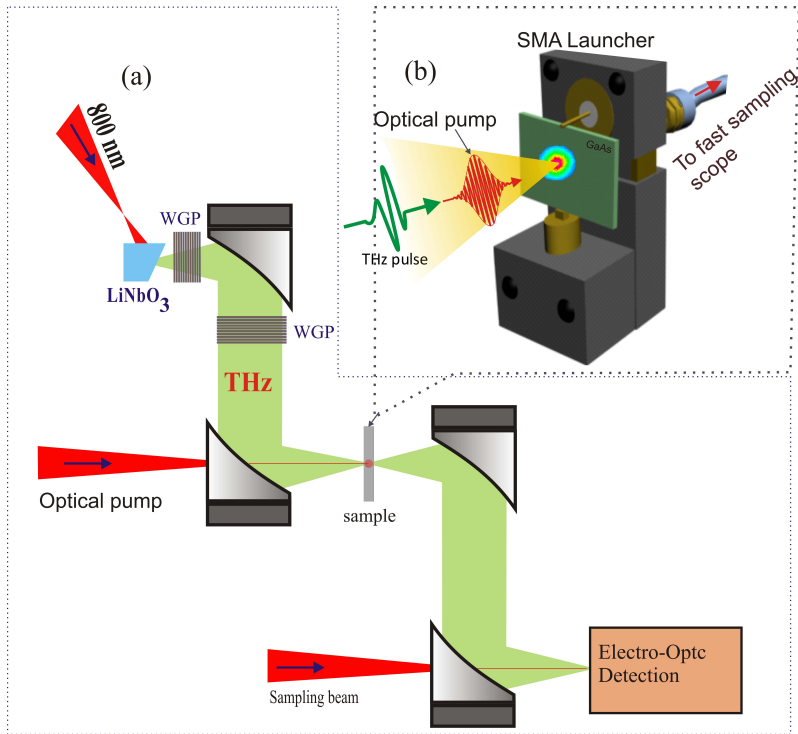
Figure 8.2: (a) Schematic of the experimental setup. (b) A piece of 0.5 mm thick and 4×9.0 mm$^2$ undoped SI-GaAs is mounted on a SMA launcher. The sample is photoexcited by the optical pump and probed by intense THz pulses generated from a tilted-pulse-front-scheme. Voltage transients generated by the intense THz pulse in the photoexcited SI-GaAs are measured by a fast digital sampling oscilloscope.

## 8.4 THz field dependence

Examples of THz electric field dependence of the THz-pulse-induced voltage transients at low and high carrier densities for pump probe delay times at $\Delta t = 0$ and $\Delta t = 20$ ps are displayed in Fig. 8.3. It is apparent from Fig. 8.3 that at low THz fields, the THz induced voltage signals are close to zero at $\Delta t = 20$ ps than zero delay time ($\Delta t = 0$). As expected, for both cases the voltage signal increases with the applied THz field strength. The temporal shift seen between the peaks of the voltage transients in both delay times is due to the different voltage reduction attenuators used during data acquisition. In photoexcited GaAs the THz absorption decreases with increasing THz pulse energy [Razzari et al. (2009); Su et al. (2009); Hebling et al. (2010)]. The long oscillatory tail in each voltage signals is due to the capacitive coupling and impedance mismatch as discussed in Chapter 7.

For $\Delta t = 0$, the THz-pulse-induced voltage transient increases linearly with THz probe field, as shown in Fig. 8.4 (a)-(c). Also, THz pulse induced voltage transient increases linearly with carrier density. As a result, very high THz probe field is required to induced large amplitude voltage transient pulses. For $\Delta t = 20$ ps, as the carrier densities are increased (see Fig. 8.4 (e) and (f)), the THz pulse induced transient voltage no longer scales linearly with THz electric field as it does at low carrier density, as shown in Fig. 8.4 (d). This is because, unlike, the THz probe pulse for $\Delta t = 20$ ps sees a roughly constant carrier density for the THz pulse duration. As a result, at low optical pump fluence (see Fig. 8.4 (d)), THz induced voltage transient response is linear. Also, the amplitude of the measured voltage transient is lower than by a factor of 2. However, as the carrier density increases in Fig. 8.4 (e) and (f), the dependence of the pk-pk voltage transient on peak THz field resembles the dynamics observed in the n-doped InGaAs samples as discussed in Chapter 7. For 20 ps delay time, the THz electric field dependence on the pk-pk voltage transient varies from linear (Fig. 8.4 (d)) to nonlinear (Fig. 8.4 (e) and (f)) with the strength of the THz pump field. The solid line in (d) is a linear fit and in (e) and (f) are Drude dynamic model fitting (see Sec. 8.6 ).
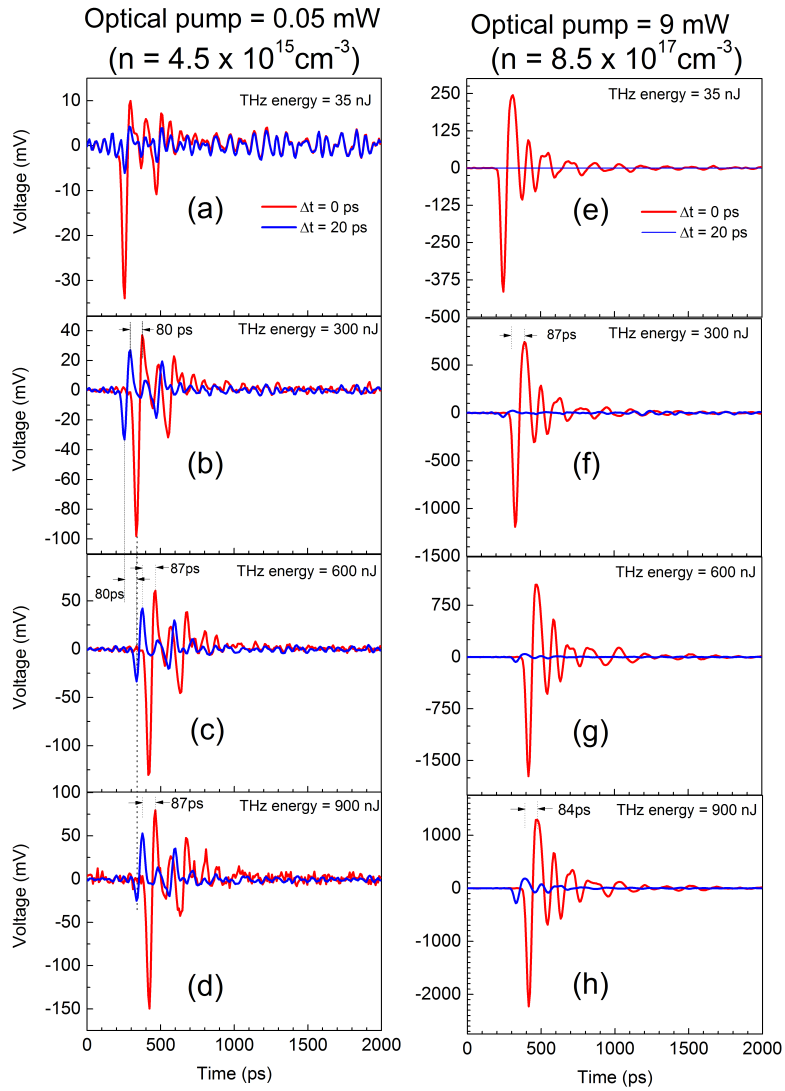
Figure 8.3: THz pulse-induced transient voltage pulses measured at different optical pump and THz probe energies. (a)-(d) the optical pump power 0.05 mW and (e)-(h) optical pump power is 9 mW. The temporal shift between transient signal at $\Delta t = 0$ ps and $\Delta t = 20$ ps are due to the differences in coaxial attenuators, inserted at the input of the high speed oscilloscope.

155
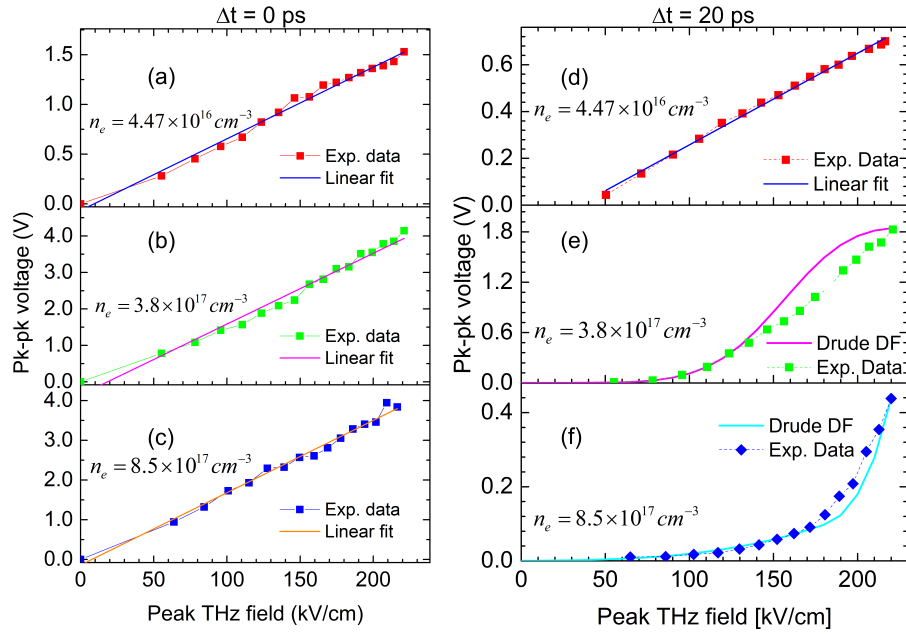
Figure 8.4: Peak-to-peak THz-pulse-induced transient voltage for different carrier densities as a function of peak THz field for a pump-probe delay time of $\Delta t = 0$ ps (a)-(c), and $\Delta t = 20$ ps (d)-(f). Solid lines in (a)-(d) are linear fits to the data and in (e) and (f) are Drude dynamic model fits (Drude DF) to the measured peak-to-peak voltage transients.

## 8.5  Carrier density dependence

To gain a better understanding of the physical mechanisms involved, a systematic study of the dependence of transient voltage generation on carrier density (excitation fluence) is necessary. Carrier-carrier interaction strongly depends on the carrier density. For example, Sharma et al. (2012) reported a carrier density dependent nonlinear terahertz absorption in photoexcited GaAs sample. Also, Mics et al. (2013) reported a reduction of momentum scattering time by a factor of 4 as the electron density increase over 4 order of magnitude.

In this section, the amplitude of the voltage transient at different incident THz pulse electric fields was investigated as a function of carrier density, $n_e$, for both pump-probe delay times. As discussed in Chapter 7, the THz pulse-induced transient voltage pulse depends on the amplitude of the transmitted THz pulse. Figures 8.5 clearly displays the typical carrier density dependent nonlinear dynamics observed experimentally. In Figs. 8.5 (a) and (b), a small population of photocarriers generated at low optical pump field is sufficient to produce measurable THz-induced transient voltage signals. For $\Delta t = 0$ ps, the fast increase of the voltage transient in the low carrier density regime followed by a saturation in the high carrier density regime is observed. As expected, for low carrier density region $\left(n_e < 2 \times 10^{17} cm^{-3}\right)$, the measured voltage transient increases with peak THz field; this is due to the applied strong THz field (47 kV/cm $<$ E $<$ 220 kV/cm) simultaneously transfer nearly all photoexcited electrons into the L-valleys, where they remain for the rest of the THz pulse [Tsuruoka, Hashimoto, and Ushioda (Tsuruoka et al.)], suggesting a fast $\Gamma \longrightarrow$L rate. Therefore, a strong voltage signal at the beginning is expected and saturated at high densities for the rest of the pulse.

Hence, with increasing carrier density at $\Delta t = 0$ ps the transient pk-pk voltage clearly saturates due to the sudden occupancy of the electronic states by non-equilibrium carriers and instantaneous probing of these carriers in the conduction band. As illustrated in Fig. 8.5 (a), the transient voltage amplitude saturation is present at all probe fields. The saturation effect can also be explained based on charge density screening effect and the back action of the induced radiation. The high carrier densities effectively screen the THz probe field and the back action of the accelerated free charge carriers on their own motion (the radiation signal from the shift current on the photoexcited carriers), which leads to a reduction in the strength of the driving field and thus to a reduction in the intense THz pulse induced transient voltage.

For 20 ps delay time scheme, there are three noticeable distinct peak-THz-field dependent regions in all conditions, as shown in Fig. 8.5 (b). In the low $n_e$ region ①, the voltage increases sharply due to high transmission of the THz fields. In the intermediate $n_e$ regime, ②, the voltage reaches a peak value before falling again at large $n_e$. In region ③, as
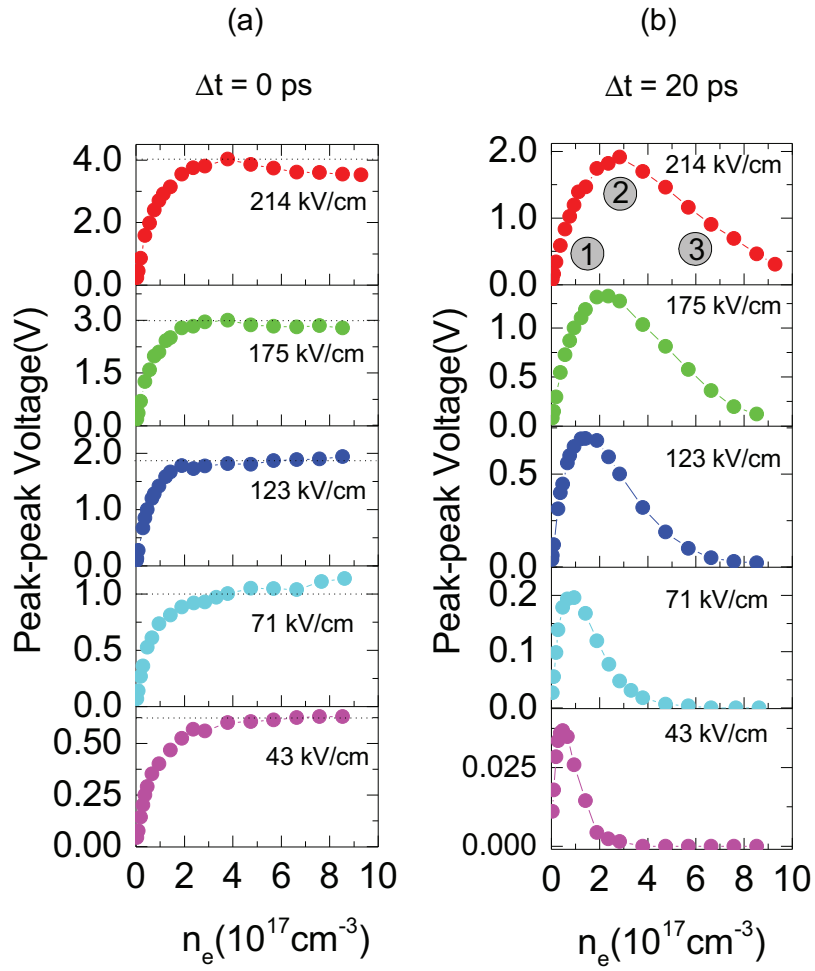
Figure 8.5: Peak-to-peak voltage transients as a function of carrier density for pump-probe delay times of (a) $\Delta t = 0$ ps and (b) $\Delta t = 20$ ps for different THz probe fields.

the carrier density increases, the sample becomes more conducting and shields the driving field (transmitted field through the sample) thereby reducing intervalley scattering and thus reducing the generated voltage with carrier density. After the THz pump pulse leaves the sample, the electrons scatter among the initial and side valleys, leading to a reduction in the average electron energy, and the absorption recovers [Hebling et al. (2010)]. Over time, the pk-pk of transient voltage gradually goes to zero once the carriers recombine after several hundred picoseconds.

## 8.6 Modeling the nonlinear THz response in photoexcited GaAs

To understand the THz induced nonlinear processes at different carrier densities in a photoexcited GaAs sample, a simple Drude-based dynamical numerical modeling was conducted similar to the model developed for n-type InGaAs in Chapter 4. The difference here is, the conductivity as well as the carrier density of the sample are time dependent. In our simple model, both heavy-hole and light hole bands contributions are ignored. The optical pump generates carriers instantaneously from band to band absorption. At $\Delta t = 0$ ps, the optical excitation pulse arrives at the same time as the THz probe at the sample (see Fig. 8.6 (a)). In this case, only the THz pulse after the main peak is affected by the time-dependent carrier density. Therefore, simulations were performed by changing the carrier density for different optical pump excitations.

For zero time delay, the THz response by photoexcited carriers arises from the half portion of the THz pulse after the peak as shown in Fig. 8.6 (a). The voltage transient measured in case of Fig. 8.6 (a) is the instantaneous polarization responses of carriers upon the half-cycle THz driving field. The time dependent conductivity, $\sigma(t)$, of the photoexcited sample is thus given by;

$$\sigma(t) = en(t)\mu(t) \tag{8.1}$$

where $n(\text{t})$ is the time dependent carrier density, $e$ is the electron charge and $\mu(\text{t})$ is the time-dependent mobility given as,

$$\mu(t) = \frac{e\tau_\Gamma}{m^*} \tag{8.2}$$

In our simple model, we use an energy dependent nonparabolic effective masses for $\Gamma$ and L-valleys ( $m_\Gamma^{**}(\varepsilon_\Gamma) = m_{\Gamma 0}^*(1 + \alpha_\Gamma \varepsilon_\Gamma)$ and $m_L^{**}(\varepsilon_L) = m_{L0}^*(1 + \alpha_L \varepsilon_L)$), but considered as constant with time, and energy dependent scattering time. Where $m_{\Gamma 0}^* = 0.067 m_0$ and $m_{L0}^* = 0.222 m_0$ are the effective masses at the bottom of the $\Gamma$ and $L$ -valleys, $\alpha_\Gamma$ and $\alpha_L$ are the nonparabolicity factors of the $\Gamma$ and $L$ -valleys, respectively. However, the effective
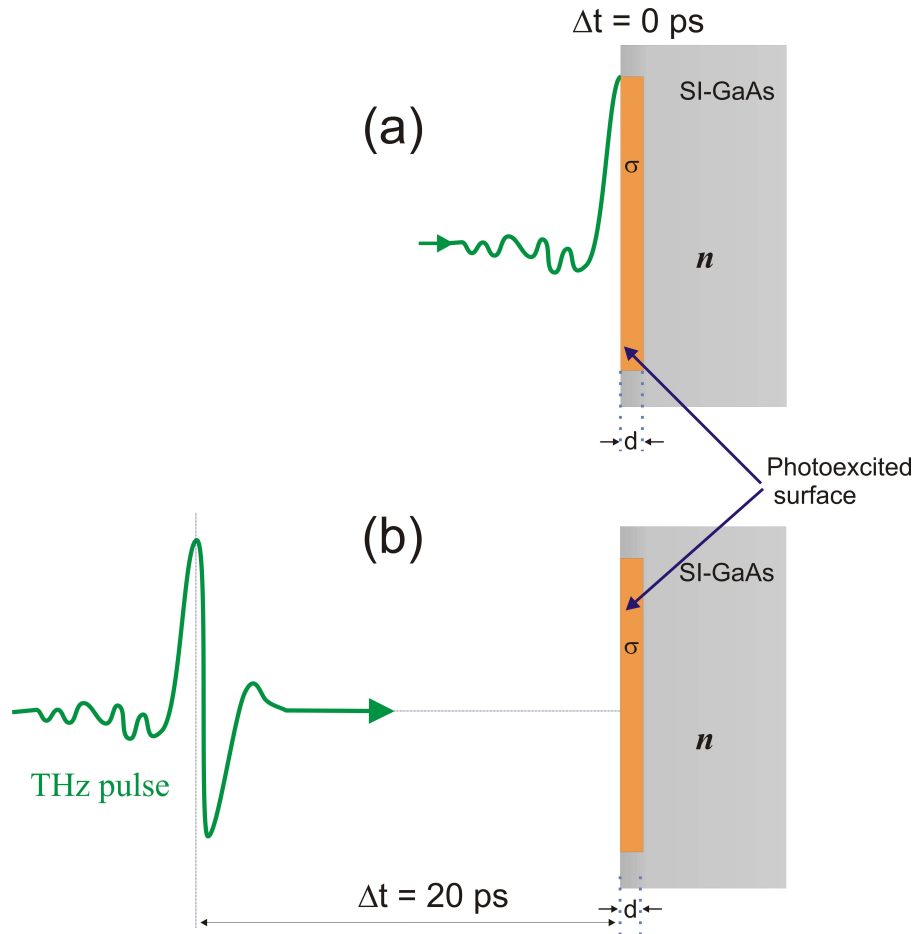
Figure 8.6: (a) Zero time delay between the THz peak and optical pump beam, hence the strong peak THz field instantaneously perturbs the nonequilibrium electron-hole plasma to generate the measured voltage signal. (b) For $\Delta t = 20$ ps, the peak of THz probe pulse arrives 20 ps after the optical pump pulse. As a result, a full single cycle THz probe pulse probes the photoexcited electron-hole plasma.

mass is time dependent due to the photoexcited electron distribution $f(E,t)$ itself is time dependent. The time dependent effective mass is given as,

$$m^*(t) = \frac{1}{\int f(E,t)\frac{1}{\hbar^2}\frac{d^2\varepsilon}{dk^2}dk} \tag{8.3}$$

The equation of monition of electrons given in Eq. 4.16 is modified as,

$$\frac{d(m^*(t)v(t))}{dt} = eE(t) - \frac{\langle m^*(t)v(t)\rangle}{\tau(\varepsilon(t))} \tag{8.4}$$

$$\hbar\frac{d\mathbf{k}_\Gamma(t)}{dt} = e\mathbf{E}(t) - \frac{\hbar\mathbf{k}_\Gamma(t)}{\tau_\Gamma} \tag{8.5}$$

where $m^*(t)v(t) = \hbar k(t)$ is the instantaneous electron momentum, $\langle\hbar k(t)\rangle$ is the average electron momentum, $E_{THz}(t)$ is the THz field, $m^*(t)$ is the time dependent electron effective mass, $\tau(t) = \frac{m^*(t)\mu(t)}{e}$ is the time dependent relaxation time. To model the zero delay time data there is a limitation to incorporate all the real time dependent dynamics. However, due to the saturation behavior observed for the measured data, the zero time delay data were fitted using a carrier density saturation fits based on the saturation fluence defined after Reference [Ropagnol et al. (2013)] as,

$$V \propto \beta\left(\frac{n_e}{n_e + n_{sat}}\right) \tag{8.6}$$

where $V$ is the voltage transient, $n_e$ is the carrier density, $n_{sat}$ is the saturation carrier density (SCD), and $\beta$ is a constant depends on the strength of the THz probe field. The solid lines in Fig. 8.7 (a) are carrier density saturation fits based on the saturation fluence fit using Eq. 8.6. The measured saturation carrier density is extracted from the fitting for all THz probe fields, as listed in Table 8.1. As mentioned in earlier, the saturation

Table 8.1: Carrier density saturation fluence for different THz probe fields.

| Parameter | Symbols | 214 kV/cm | 175 kV/cm | 123 kV/cm | 42 kV/cm |
|---|---|---|---|---|---|
| SCD | $n_{sat}$ | 0.4545±0.0063 | 0.4296±0.0059 | 0.3942±0.0054 | 0.5775±0.0061 |
| Scaling factor | $\beta$ | 4.0598±0.0077 | 3.1391±0.0060 | 2.0062±0.0037 | 0.6762±0.0012 |

carrier density fit affirms the THz probe field screening effect, in which the voltage transient saturated with increasing carrier density irrespective of the THz probe field strength. Also, this can be possibly explained as, intervalley scattering saturation due to the instantaneous probing of the photoexcited carriers. Hence, the half-strong THz field shown in Fig. 8.6
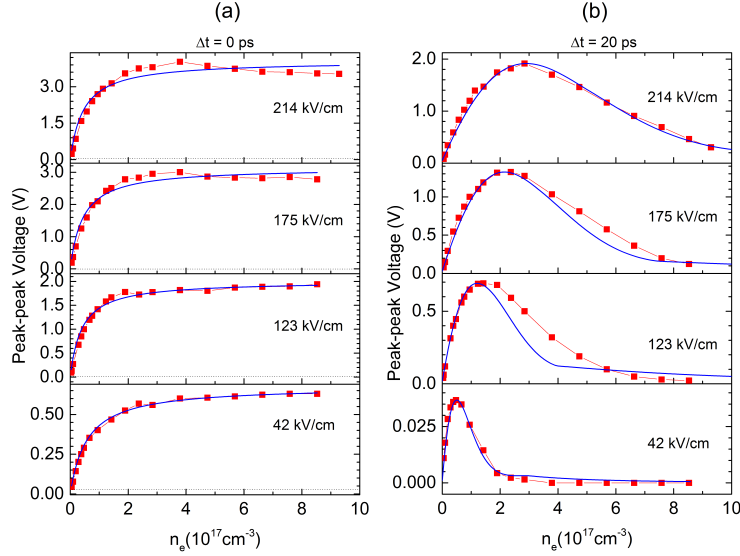
Figure 8.7: (a) Saturation carrier density fit to the measured voltage transients at $\Delta t = 0$ ps for different THz probe fields. (b) Drude dynamic model fit to the measured voltage transients at $\Delta t = 20$ ps.

see almost same conductivity within the duration of the probing pulse. However, the roll of intervalley scattering effect is not fully understood and more work is needed.

However, for 20 ps pump probe delay time, the electron population relaxes and scatters back to the $\Gamma$ valley, thus the THz pulse probes the time independent scattering rate independent of intervalley scattering rate rather than time-dependent scattering rates. Hence, the steady conductivity sees the effect of the full THz pulse, as shown in Fig. 8.6 (b). Thus, the carrier transport modeling is similar to the model used for the n-doped InGaAs sample. Besides some basic parameter changes for the GaAs sample, a number of assumptions were made to simplify the model: (1) only the effects of hot electron transport are taken into account, (2) only intervalley relaxation to the $\Gamma$-valley was taken into consideration, (3) the average mobility varies by changing the relative fraction of electrons in the $\Gamma$-valley. For the details of the model, see Chapters 4 and Appendix D and F.1.

Figure 8.7 (b) shows the Drude dynamic model fit with the measured carrier density dependent voltage transient amplitudes at $\Delta t = 20$ ps. The Drude dynamic fit is in good agreement with the experimental data for the range of THz probe fields and the fit parameters obtained from the model are consistent with our previous OPTP measurements [Su et al. (2009)]. Our model showed that the transmitted THz field that drives the carriers

162

Table 8.2: Summary of the fit parameters used in the model.

| Parameter | Symbols | OPTP[1] | $214(\frac{kV}{cm})$ | $175(\frac{kV}{cm})$ | $123(\frac{kV}{cm})$ | $42(\frac{kV}{cm})$ |
|---|---|---|---|---|---|---|
| Nonparabolicity factor | $\alpha_\Gamma$ | 0.061 | 0.061 | 0.061 | 0.061 | 0.061 |
|  | $\alpha_L$ | — | 0.54 | 0.54 | 0.54 | 0.54 |
| Scattering time (ps) | $\tau_\Gamma$ | 0.16 (low) | — | — | — | — |
|  |  | 0.051 (high) | 0.03 | 0.04 | 0.054 | 0.19 |
|  | $\tau_{\Gamma L0}$ | 0.022 | 0.022 | 0.022 | 0.022 | 0.022 |
|  | $\tau_{L\Gamma}$ | 3 | 3 | 3 | 3 | 3 |
| Threshold energy (eV) | $\varepsilon_{th}$ | 0.16 | 0.15 | 0.16 | 0.16 | 0.26 |
| Smooth parameter(eV) | b | — | 0.57 | 0.57 | 0.57 | 0.78 |

[1] Fit parameters used in OPTP result [Su et al. (2009)].

increases nonlinearly with incident electric field due to a decrease in conductivity of the sample as a result of intervalley scattering to satellite valleys and band non-parabolicity. Table 8.2 summarizes comparison of the best fit parameters used in the dynamic intervalley electron transfer model for incident peak THz field varying from 47 kV/cm to 214 kV/cm to the fit parameters used in reference [Su et al. (2009)]. For the nonzero time delay data, the observed carrier density dependent nonlinear dynamics at high carrier density is due to the increased shielding of the THz pulse transmission instead of the suppression in intervalley scattering because of electron-hole scattering as reported by Sharma et al. (2012). That is, in the low carrier density region the calculated voltage transient from the model sharply increased due to the high transmission of THz fields, which leads high driving field (see Eq. 7.6 and 7.7). In the high carrier density region shielding effect pronounced, which leads to low transmission of the THz fields, consequently leading to low voltage transients.

## 8.7 Conclusions

In conclusion, we have measured THz-field-induced picosecond transient voltage pulses in a piece of photoexcited SI-GaAs sample with pk-pk signals up to 4V using THz pulses. Very high THz probe field is required to induced large amplitude voltage transient pulses. Density-dependent transient current radiation from a photoexcited SI-GaAs sample is investigated. We found monotonic and power law dependence of the pk-pk transient voltage pulse on applied THz field at low and high carrier densities, respectively.

# CHAPTER 9

# Summary and Future Directions

The effects of optical pump pulse chirping on intense THz pulse generation via tilted-pulse-front optical rectification in $LiNbO_3$ has been investigated. By down-chirping the optical pump beam to the optimum pulse duration, intense single-cycle THz pulses with pulse energy up to 2.2 $\mu$J (uncalibrated) and field strength of 340 kV/cm capable of driving nonlinear dynamics in semiconductors have been generated. We are also the first to observe the optical pump polarization dependence of the generated THz pulse energies from a tilted-pulse-front $LiNbO_3$ source both experimentally and analytically. The experimental result is in agreement with predicted THz electric field derived from the nonlinear induced polarization and susceptibility tensors of $LiNbO_3$. Irrespective of the pump pulse polarization, the THz pulse energy will never have zero amplitude.

We have used such intense THz pulses to explore a series of novel ultrafast THz nonlinear carrier dynamics in doped and photoexcited semiconductors. For doped samples, we have used a single intense THz pulse to simultaneously perturb and probe the ultrafast time evolution of carriers, and an optical-pump/THz-probe technique is employed for photoexcited samples. We have demonstrated the experimental realization of an optical diode in the THz frequency range in an open aperture intense THz pulse Z-scan experiment. An asymmetrical nonlinear bleaching of THz pulse absorption through an n-doped InGaAs sample was observed by illuminating the conducting (InGaAs) and insulating (substrate) faces alternatively. We observed 52% higher normalized transmission modulation for an intense THz pulse propagating from insulating to conducting face than the reverse direction. We have derived an analytical expression of the transmitted THz fields based on the boundary conditions in a thin conducting film approximation and the Fresnel equations that affirms the transmission enhancement effect. Our study provides the development of a practical ultrafast optical diode analogous to current flow in an electronic diode. This finding is promising

and should be explored for a large number of available semiconductor materials for possible applications.

Moreover, using intense THz pulses we developed a new technique to measure ultrafast THz pulse-induced voltage transients for the first time in n-doped InGaAs and photoexcited SI-GaAs samples without external bias. We attribute the observed voltage transients to a shift current generated from the nonlinear THz dynamics of free electrons in the conduction bands. We measured voltage transients as high as 20 V and as fast as 30 ps wide followed by a slow response over several hundreds of picoseconds. The long oscillatory small amplitude tails of the voltage transient is attributed to a parasitic capacitive capacitances and inductances in the circuit and impedance mismatch between circuit elements. However, the THz-induced voltage transient bandwidths that are observed are limited not only by the frequency response of the detection system but also the impedance mismatch between the detector circuits. The observed transient voltage pulse width is limited by the bandwidth of the measurement setup and high speed oscilloscope. We anticipate even faster voltage transients are possible raising the possibility of applications as high speed THz photodetectors. Also, the response of the system varies with carrier density and detector position with respect to the sample face. The magnitude of the induced voltage is found to be nonlinearly dependent on the incident THz peak field and have a sinusoidal dependence on THz polarization, but it is independent of sample orientation. The modified Drude-based theoretical model for electrons driven by ultrashort intense THz pulse shows that intervalley scattering over ps time scales and band nonparabolicity are the dominant factors for the observed nonlinear behavior of the measured voltage transients at high field excitation. However, in the low field regime, the peak-to-peak value of the voltage transient deviates from a linear Drude model. The mechanism for such an effect is not fully understood. The full band structure of the sample and all the scattering effects should be considered in the model to fully understand the ultrafast nonlinear dynamics of carriers. Therefore, future test should include a more detailed many-body ensemble Monte Carlo simulation. One of the main potential future directions of the ultrafast THz pulse-induced transient voltage pulse scheme is to directly image the dipole radiation to identify the polarity of the induced shift current. Future plans are underway to conduct such measurements in the same experimental setup.

We further extended our study to directly monitor the transient carrier density dependence of the voltage transients in a photoexcited SI-GaAs sample using OPTP techniques. The generation mechanism is demonstrated for both zero and 20 ps delay times. The voltage transients at different incident THz pulse electric fields was investigated as a function of carrier density. In the low carrier density region, the voltage transient increases sharply due to high THz field transmission. With increasing carrier density the induced transient voltage tends to saturate for zero time delay scheme. However, for 20 ps delay time the voltage transient reaches a peak value in the intermediate region before falling again at large carrier

density due to increased shielding of the THz pulse transmission. This result suggests that the transmitted THz field that drives the carriers increases nonlinearly with incident electric field due to a decrease in conductivity of the sample as a result of intervalley scattering to satellite valleys and band non-parabolicity.

# Bibliography

Amnon Yariv, Pochi Yeh. *Optical Waves in Crystals: Propagation and control of Laser.* First edition. 1984.

Anile, A. Marcello and Simon D. Hern. "Two-valley Hydrodynamical Models for Electron Transport in Gallium Arsenide, Simulation of Gunn Oscillations." *VLSI Design* 15 (2002): 681–693.

Auston, D. H. "Picosecond optoelectronic switching and gating in silicon." *Applied Physics Letters* 26 (1975): 101–103.

Auston, D. H. and K. P. Cheung. "Coherent time-domain far-infrared spectroscopy." *J. Opt. Soc. Am. B* 2 (Apr 1985): 606–612.

Auston, D. H., K. P. Cheung, and P. R. Smith. "PICOSECOND PHOTOCONDUCTING HERTZIAN DIPOLES." *Applied Physics Letters* 45 (1984): 284–286.

Auston, D. H., K. P. Cheung, J. A. Valdmanis, and D. A. Kleinman. "Cherenkov Radiation from Femtosecond Optical Pulses in Electro-Optic Media." *Phys. Rev. Lett.* 53 (Oct 1984): 1555–1558.

Auston, D. H. and P. R. Smith. "GENERATION AND DETECTION OF MILLIMETER WAVES BY PICOSECOND PHOTOCONDUCTIVITY." *Applied Physics Letters* 43 (1983): 631–633.

Averitt, R D and A J Taylor. "Ultrafast optical and far-infrared quasiparticle dynamics in correlated electron materials." *Journal of Physics: Condensed Matter* 14 (2002): R1357.

Ayesheshim, K. Ayesheshim. *Terahertza imaging using full-field electrooptic sampling.* 2009.

Bartel, T., P. Gaal, K. Reimann, M. Woerner, and T. Elsaesser. "Generation of single-cycle THz transients with high electric-field amplitudes." *Opt. Lett.* 30 (Oct 2005): 2805–2807.

Beard, M. C., G. M. Turner, and C. A. Schmuttenmaer. "Transient photoconductivity in GaAs as measured by time-resolved terahertz spectroscopy." *Physical Review B* 62 (2000): 15764–15777.

Beard, Matthew C., Gordon M. Turner, and Charles A. Schmuttenmaer. "Subpicosecond carrier dynamics in low-temperature grown GaAs as measured by time-resolved terahertz spectroscopy." *Journal of Applied Physics* 90 (2001): 5915–5923.

Bieler, M., K. Pierz, and U. Siegner. "Simultaneous generation of shift and injection currents in (110)-grown GaAs/AlGaAs quantum wells." *Journal of Applied Physics* 100 (2006).

Bitzer, Andreas, Alex Ortner, Hannes Merbold, Thomas Feurer, and Markus Walther. "Terahertz near-field microscopy of complementary planar metamaterials: Babinet's principle." *Opt. Express* 19 (Jan 2011): 2537–2545.

Blanchard, F., D. Golde, F. H. Su, L. Razzari, G. Sharma, R. Morandotti, T. Ozaki, M. Reid, M. Kira, S. W. Koch, and F. A. Hegmann. "Effective Mass Anisotropy of Hot Electrons in Nonparabolic Conduction Bands of $n$-Doped InGaAs Films Using Ultrafast Terahertz Pump-Probe Techniques." *Phys. Rev. Lett.* 107 (Aug 2011): 107401.

Blanchard, F., L. Razzari, H. C. Bandulet, G. Sharma, R. Morandotti, J. C. Kieffer, T. Ozaki, M. Reid, H. F. Tiedje, H. K. Haugen, and F. A. Hegmann. "Generation of 1.5 mu J single-cycle terahertz pulses by optical rectification from a large aperture ZnTe crystal." *Optics Express* 15 (2007): 13212–13220.

Blanchard, F., X. Ropagnol, H. Hafez, H. Razavipour, M. Bolduc, R. Morandotti, T. Ozaki, and D. G. Cooke. "Effect of extreme pump pulse reshaping on intense terahertz emission in lithium niobate at multimilliJoule pump energies." *Opt. Lett.* 39 (Aug 2014): 4333–4336.

Blanchard, F., G. Sharma, L. Razzari, X. Ropagnol, H. C. Bandulet, F. Vidal, R. Morandotti, J. C. Kieffer, T. Ozaki, H. Tiedje, H. Haugen, M. Reid, and F. Hegmann. "Generation of Intense Terahertz Radiation via Optical Methods." *Ieee Journal of Selected Topics in Quantum Electronics* 17 (2011): 5–16.

Bosomworth, D. R. "THE FAR INFRARED OPTICAL PROPERTIES OF LiNbO$_3$." *Applied Physics Letters* 9 (1966): 330–331.

Bowlan, P., W. Kuehn, K. Reimann, M. Woerner, T. Elsaesser, R. Hey, and C. Flytzanis. "High-Field Transport in an Electron-Hole Plasma: Transition from Ballistic to Drift Motion." *Phys. Rev. Lett.* 107 (Dec 2011): 256602.

Budiarto, E., J. Margolies, S. Jeong, J. Son, and J. Bokor. "High-intensity terahertz pulses at 1-kHz repetition rate." *Ieee Journal of Quantum Electronics* 32 (1996): 1839–1846.

Cai, Y., I. Brener, J. Lopata, J. Wynn, L. Pfeiffer, J. B. Stark, Q. Wu, X. C. Zhang, and J. F. Federici. "Coherent terahertz radiation detection: Direct comparison between free-space electro-optic sampling and antenna detection." *Applied Physics Letter* 73 (1998): 444–446.

Carter, S. G., V. Birkedal, C. S. Wang, L. A. Coldren, A. V. Maslov, D. S. Citrin, and M. S. Sherwin. "Quantum Coherence in an Optical Modulator." *Science* 310 (2005): 651–653.

Chang, Guoqing, Charles J. Divin, Chi-Hung Liu, Steven L. Williamson, Almantas Galvanauskas, and Theodore B. Norris. "Power scalable compact THz system based on an ultrafast Yb-doped fiber amplifier." *Opt. Express* 14 (Aug 2006): 7909–7913.

Cheung, K. P. and D. H. Auston. "Excitation of Coherent Phonon Polaritons with Femtosecond Optical Pulses." *Phys. Rev. Lett.* 55 (Nov 1985): 2152–2155.

Chin, A. H., J. M. Bakker, and J. Kono. "Ultrafast Electroabsorption at the Transition between Classical and Quantum Response." *Phys. Rev. Lett.* 85 (Oct 2000): 3293–3296.

Chuang, Shun Lien, Stefan Schmitt-Rink, Benjamin I. Greene, Peter N. Saeta, and Anthony F. J. Levi. "Optical rectification at semiconductor surfaces." *Phys. Rev. Lett.* 68 (Jan 1992): 102–105.

Cocker, T. L., L. V. Titova, S. Fourmaux, G. Holloway, H.-C. Bandulet, D. Brassard, J.-C. Kieffer, M. A. El Khakani, and F. A. Hegmann. "Phase diagram of the ultrafast photoinduced insulator-metal transition in vanadium dioxide." *Phys. Rev. B* 85 (Apr 2012): 155120.

Cocker, Tyler L., Vedran Jelic, Manisha Gupta, Sean J. Molesky, A. J. BurgessJacob, Glenda De Los Reyes, Lyubov V. Titova, Ying Y. Tsui, Mark R. Freeman, and Frank A. Hegmann. "An ultrafast terahertz scanning tunnelling microscope." *Nat Photon* 7 (2013): 620–625.

Cook, D. J. and R. M. Hochstrasser. "Intense terahertz pulses by four-wave rectification in air." *Opt. Lett.* 25 (Aug 2000): 1210–1212.

Cooke, D. G., F. A. Hegmann, E. C. Young, and T. Tiedje. "Electron mobility in dilute GaAs bismide and nitride alloys measured by time-resolved terahertz spectroscopy." *Applied Physics Letters* 89 (2006).

Cooke, D. G., A. N. MacDonald, A. Hryciw, J. Wang, Q. Li, A. Meldrum, and F. A. Hegmann. "Transient terahertz conductivity in photoexcited silicon nanocrystal films." *Physical Review B* 73 (2006).

Cooke, David G. *Time-Resolved Terahertz Spectroscopy of Bulk and Nanoscale Semiconductors.* 2006.

Cote, D., N. Laman, and H. M. van Driel. "Rectification and shift currents in GaAs." *Applied Physics Letters* 80 (2002): 905–907.

Dai, Jianming, Nicholas Karpowicz, and X.-C. Zhang. "Coherent Polarization Control of Terahertz Waves Generated from Two-Color Laser-Induced Gas Plasma." *Phys. Rev. Lett.* 103 (Jul 2009): 023001.

Dai, Jianming, Xu Xie, and X.-C. Zhang. "Detection of Broadband Terahertz Waves with a Laser-Induced Plasma in Gases." *Phys. Rev. Lett.* 97 (Sep 2006): 103903.

Danielson, J. R., Yun-Shik Lee, J. P. Prineas, J. T. Steiner, M. Kira, and S. W. Koch. "Interaction of Strong Single-Cycle Terahertz Pulses with Semiconductor Quantum Wells." *Phys. Rev. Lett.* 99 (Dec 2007): 237401.

Dexheimer, Susan L. *Terahertz spectroscopy: Principles and applications.* First edition. CRC Press, Taylor and Francis Group, 2008.

Dougherty, Thomas P., Gary P. Wiederrecht, and Keith A. Nelson. "Impulsive stimulated Raman scattering experiments in the polariton regime." *J. Opt. Soc. Am. B* 9 (Dec 1992): 2179–2189.

Fan, Kebin, Harold Hwang, Mengkun Liu, Andrew Strikwerda, Aaron Sternbach, Jingdi Zhang, Xiaoguang Zhao, Xin Zhang, Keith Nelson, and Richard Averitt. "Nonlinear Terahertz Metamaterials via Field-Enhanced Carrier Dynamics in GaAs." *Phys. Rev. Lett.* 110 (May 2013): 217404.

Franken, P. A., A. E. Hill, C. W. Peters, and G. Weinreich. "Generation of Optical Harmonics." *Physical Review Letters* 7 (1961): 118–119.

Fuji, Takao and Toshinori Suzuki. "Generation of sub-two-cycle mid-infrared pulses by four-wave mixing through filamentation in air." *Opt. Lett.* 32 (Nov 2007): 3330–3332.

Fulop, J. A., L. Palfalvi, G. Almasi, and J. Hebling. "Design of high-energy terahertz sources based on optical rectification." *Optics Express* 18 (2010): 12311–12327.

Fulop, J. A., L. Palfalvi, S. Klingebiel, G. Almasi, F. Krausz, S. Karsch, and J. Hebling. "Generation of sub-mJ terahertz pulses by optical rectification." *Opt. Lett.* 37 (Feb 2012): 557–559.

Gaal, P., K. Reimann, M. Woerner, T. Elsaesser, R. Hey, and K. H. Ploog. "Nonlinear Terahertz Response of *n*-Type GaAs." *Phys. Rev. Lett.* 96 (May 2006): 187402.

Ganichev, S. D., E. L. Ivchenko, S. N. Danilov, J. Eroms, W. Wegscheider, D. Weiss, and W. Prettl. "Conversion of Spin into Directed Electric Current in Quantum Wells." *Phys. Rev. Lett.* 86 (May 2001): 4358–4361.

Ganichev, S. D. and W. Prettl. *Intense Terahertz Excitation of semiconductors.* second edition. Oxford University Press, 2006.

Glover, R. E. and M. Tinkham. "Conductivity of Superconducting Films for Photon Energies between 0.3 and $40kT_c$." *Phys. Rev.* 108 (Oct 1957): 243–256.

Gu, Bing, Ya-Xian Fan, Jin Wang, Jing Chen, Jianping Ding, Hui-Tian Wang, and Bin Guo. "Characterization of saturable absorbers using an open-aperture Gaussian-beam." *Phys. Rev. A* 73 (Jun 2006): 065803.

H. Hirori, M. Shirai S. Tani Y. Kadoya,K. Shinokita and K. Tanaka. "Extraordinary carrier multiplication gated by a picosecond electric field pulse." *Nat Commun* 2 (2011): 594.

Haché, A., Y. Kostoulas, R. Atanasov, J. L. P. Hughes, J. E. Sipe, and H. M. van Driel. "Observation of Coherently Controlled Photocurrent in Unbiased, Bulk GaAs." *Phys. Rev. Lett.* 78 (Jan 1997): 306–309.

Hamster, H., A. Sullivan, S. Gordon, W. White, and R. W. Falcone. "Subpicosecond, electromagnetic pulses from intense laser-plasma interaction." *Phys. Rev. Lett.* 71 (Oct 1993): 2725–2728.

Hebling, J., G. Almasi, I. Z. Kozma, and J. Kuhl. "Velocity matching by pulse front tilting for large−area THz-pulse generation." *Optics Express* 10 (2002): 1161–1166.

Hebling, J., K. L. Yeh, M. C. Hoffmann, B. Bartal, and K. A. Nelson. "Generation of high-power terahertz pulses by tilted-pulse-front excitation and their application possibilities." *Journal of the Optical Society of America B−Optical Physics* 25 (2008): B6–B19.

Hebling, János, Matthias C. Hoffmann, Harold Y. Hwang, Ka-Lo Yeh, and Keith A. Nelson. "Observation of nonequilibrium carrier distribution in Ge, Si, and GaAs by terahertz pump–terahertz probe measurements." *Phys. Rev. B* 81 (Jan 2010): 035201.

Hegmann, F. A., R. R. Tykwinski, K. P. H. Lui, J. E. Bullock, and J. E. Anthony. "Picosecond transient photoconductivity in functionalized pentacene molecular crystals probed by terahertz pulse spectroscopy." *Physical Review Letters* 89 (2002).

Hirori, H., A. Doi, F. Blanchard, and K. Tanaka. "Single-cycle terahertz pulses with amplitudes exceeding 1 MV/cm generated by optical rectification in LiNbO$_3$." Hirori, H. Doi, A. Blanchard, F. Tanaka, K. *Applied Physics Letters* 98 (2011).

Ho, I-Chen, Xiaoyu Guo, and X.-C. Zhang. "Design and performance of reflective terahertz air-biased-coherent-detection for time-domain spectroscopy." *Opt. Express* 18 (Feb 2010): 2872–2883.

Hoffmann, M. C. and J. A. Fulop. "Intense ultrashort terahertz pulses: generation and applications." *Journal of Physics D-Applied Physics* 44 (2011).

Hoffmann, M. C., B. S. Monozon, D. Livshits, E. U. Rafailov, and D. Turchinovich. "Terahertz electro-absorption effect enabling femtosecond all-optical switching in semiconductor quantum dots." *Applied Physics Letters* 97 (2010).

Hoffmann, Matthias C., János Hebling, Harold Y. Hwang, Ka-Lo Yeh, and Keith A. Nelson. "Impact ionization in InSb probed by terahertz pumpâĂŤterahertz probe spectroscopy." *Phys. Rev. B* 79 (Apr 2009): 161201.

Hoffmann, Matthias C. and Dmitry Turchinovich. "Semiconductor saturable absorbers for ultrafast terahertz signals." *Applied Physics Letters* 96 (2010): 151110.

Hu, B. B., E. A. de Souza, W. H. Knox, J. E. Cunningham, M. C. Nuss, A. V. Kuznetsov, and S. L. Chuang. "Identifying the Distinct Phases of Carrier Transport in Semiconductors with 10 fs Resolution." *Phys. Rev. Lett.* 74 (Feb 1995): 1689–1692.

Hu, B. B., X.-C. Zhang, D. H. Auston, and P. R. Smith. "Free-space radiation from electro-optic crystals." *Applied Physics Letters* 56 (1990): 506–508.

Huber, A. J., F. Keilmann, J. Wittborn, J. Aizpurua, and R. Hillenbrand. "Terahertz Near-Field Nanoscopy of Mobile Carriers in Single Semiconductor Nanodevices." *Nano Letters* 8 (2008): 3766–3770.

Huber, A. J., A. Ziegler, T. K öck, and R. Hillenbrand. "Infrared nanoscopy of strained semiconductors." *Nature Nanotechnology* 4 (2009): 153–157.

Huber, R., A. Brodschelm, F. Tauser, and A. Leitenstorfer. "Generation and field-resolved detection of femtosecond electromagnetic pulses tunable up to 41 THz." *Applied Physics Letters* 76 (2000): 3191–3193.

Huber, R., F. Tauser, A. Brodschelm, M. Bichler, G. Abstreiter, and A. Leitenstorfer. "How many-particle interactions develop after ultrafast excitation of an electronâĂŞhole plasma." *Nature Nanotechnology* 414 (2001): 286–289.

Hübner, J., W. W. Rühle, M. Klude, D. Hommel, R. D. R. Bhat, J. E. Sipe, and H. M. van Driel. "Direct Observation of Optically Injected Spin-Polarized Currents in Semiconductors." *Phys. Rev. Lett.* 90 (May 2003): 216601.

Jepsen, P.U., D.G. Cooke, and M. Koch. "Terahertz spectroscopy and imaging Modern techniques and applications." *Laser and Photonics Reviews* 5 (2011): 124–166.

Kadlec, F., H. Němec, and P. Kužel. "Optical two-photon absorption in GaAs measured by optical-pump terahertz-probe spectroscopy." *Phys. Rev. B* 70 (Sep 2004): 125205.

Kampfrath, Tobias, Koichiro Tanaka, and Keith A. Nelson. "Resonant and nonresonant control over matter and light by intense terahertz transients." *Nat Photon* 7 (2013): 680–690.

Karpowicz, Nicholas, Jianming Dai, Xiaofei Lu, Yunqing Chen, Masashi Yamaguchi, Hongwei Zhao, X.-C. Zhang, Liangliang Zhang, Cunlin Zhang, Matthew Price-Gallagher, Clark Fletcher, Orval Mamer, Alain Lesimple, and Keith Johnson. "Coherent heterodyne time-domain spectrometry covering the entire âĂIJterahertz gap." *Applied Physics Letters* 92 (2008).

Kim, K. Y., A. J. Taylor, J. H. Glownia, and RodriguezG. "Coherent control of terahertz supercontinuum generation in ultrafast laser-gas interactions." 10.1038/nphoton.2008.153. *Nat Photon* 2 (2008): 605–609.

Kim, Ki-Yong, James H. Glownia, Antoinette J. Taylor, and George Rodriguez. "Terahertz emission from ultrafast ionizing air in symmetry-broken laser fields." *Opt. Express* 15 (Apr 2007): 4577–4584.

Klarskov, Pernille, Andrew C Strikwerda, Krzysztof Iwaszczuk, and Peter Uhd Jepsen. "Experimental three−dimensional beam profiling and modeling of a terahertz beam generated from a two−color air plasma." *New Journal of Physics* 15 (2013): 075012.

Kress, Markus, Torsten Löffler, Susanne Eden, Mark Thomson, and Hartmut G. Roskos. "Terahertz-pulse generation by photoionization of airwith laser pulses composed of both fundamental and second-harmonicwaves." *Opt. Lett.* 29 (May 2004): 1120–1122.

Kuehn, W., P. Gaal, K. Reimann, M. Woerner, T. Elsaesser, and R. Hey. "Coherent Ballistic Motion of Electrons in a Periodic Potential." *Phys. Rev. Lett.* 104 (Apr 2010): 146602.

Kuehn, W., P. Gaal, K. Reimann, M. Woerner, T. Elsaesser, and R. Hey. "Terahertz-induced interband tunneling of electrons in GaAs." *Phys. Rev. B* 82 (Aug 2010): 075204.

Laman, N., M. Bieler, and H. M. van Driel. "Ultrafast shift and injection currents observed in wurtzite semiconductors via emitted terahertz radiation." *Journal of Applied Physics* 98 (2005).

Lange, C., T. Maag, M. Hohenleutner, S. Baierl, O. Schubert, E. R. J. Edwards, D. Bougeard, G. Woltersdorf, and R. Huber. "Extremely Nonperturbative Nonlinearities in GaAs Driven by Atomically Strong Terahertz Fields in Gold Metamaterials." *Phys. Rev. Lett.* 113 (Nov 2014): 227401.

Liu, Jingle, Gurpreet Kaur, and X.-C. Zhang. "Photoluminescence quenching dynamics in cadmium telluride and gallium arsenide induced by ultrashort terahertz pulse." *Applied Physics Letters* 97 (2010).

Lui, K. P. H. and F. A. Hegmann. "Ultrafast carrier relaxation in radiation-damaged silicon on sapphire studied by optical-pumpâĂŞterahertz-probe experiments." *Applied Physics Letters* 78 (2001): 3478–3480.

Lundstrom, Mark. *Fundamentals of carrier transport*. Second edition. Cambridge University Press, 2000.

Maiman, T. H. "Stimulated Optical Radiation in Ruby." *Nature* 187 (1960): 493–494.

Mathew, Reid and Robert Fedosejevs. "Quantitative comparison of terahertz emission from (100) InAs surfaces and a GaAs large-aperture photoconductive switch at high fluences." *Applied Optics* 44 (2005): 149–153.

Mics, ZoltÃąn, Andrea D, Angio, SÃ¿ren A. Jensen, Mischa Bonn, and Dmitry Turchinovich. "Density-dependent electron scattering in photoexcited GaAs in strongly diffusive regime." *Applied Physics Letters* 102 (2013).

Mittleman, D. *Sensing with Terahertz Radiation*. first edition. Springer Berlin Heidelberg, 2003.

Nahata, A., D. H. Auston, T. F. Heinz, and C. J. Wu. "Coherent detection of freely propagating terahertz radiation by electro-optic sampling." *Applied Physics Letters* 68 (1996): 150–152.

Nahata, Ajay, Aniruddha S. Weling, and Tony F. Heinz. "A wideband coherent terahertz spectroscopy system using optical rectification and electro−optic sampling." *Applied Physics Letters* 69 (1996): 2321–2323.

Nastos, F. and J. E. Sipe. "Optical rectification and shift currents in GaAs and GaP response: Below and above the band gap." *Phys. Rev. B* 74 (Jul 2006): 035201.

Nuss, M. C., D. H. Auston, and F. Capasso. "Direct Subpicosecond Measurement of Carrier Mobility of Photoexcited Electrons in Gallium Arsenide." *Phys. Rev. Lett.* 58 (Jun 1987): 2355–2358.

Osman, M.A., H.L. Grubin, P. Lugli, M.J. Kann, and D.K. Ferry. "Monte Carlo Investigation of Hot Photoexcited Electron Relaxation in GaAs." *Picosecond Electronics and Optoelectronics II*. Ed. FrederickJohn Leonberger, ChiH. Lee, Federico Capasso, and Hadis Morkoc. Volume 24 of Springer Series in Electronics and Photonics. Springer Berlin Heidelberg, 1987. 82–85.

Othonos, Andreas. "Probing ultrafast carrier and phonon dynamics in semiconductors." *Journal of Applied Physics* 83 (1998).

Peng, Bo, Sahin Kaya Ozdemir, Fuchuan Lei, Faraz Monifi, Mariagiovanna Gianfreda, Gui Lu Long, Shanhui Fan, Franco Nori, Carl M. Bender, and Lan Yang. "Parity-time-symmetric whispering-gallery microcavities." *Nature Physics* 10 (2014): 394–398.

Petersen, Poul B. and Andrei Tokmakoff. "Source for ultrafast continuum infrared and terahertz radiation." *Opt. Lett.* 35 (Jun 2010): 1962–1964.

Philip, Reji, M. Anija, Chandra S. Yelleswarapu, and D. V. G. L. N. Rao. "Passive all-optical diode using asymmetric nonlinear absorption." *Applied Physics Letters* 91 (2007): –.

Razzari, L., F. H. Su, G. Sharma, F. Blanchard, A. Ayesheshim, H. C. Bandulet, R. Morandotti, J. C. Kieffer, T. Ozaki, M. Reid, and F. A. Hegmann. "Nonlinear ultrafast modulation of the optical absorption of intense few-cycle terahertz pulses in n-doped semiconductors." *Physical Review B* 79 (2009).

Reimann, Klaus. "Table-top sources of ultrashort THz pulses." *Reports on Progress in Physics* 70 (2007): 1597–1632.

Rice, A., Y. Jin, X. F. Ma, X.âĂŘC. Zhang, D. Bliss, J. Larkin, and M. Alexander. "Terahertz optical rectification from ãĂĹ110ãĂĽ zincâĂŘblende crystals." *Applied Physics Letters* 64 (1994): 1324–1326.

Ropagnol, X., F. Blanchard, T. Ozaki, and M. Reid. "Intense terahertz generation at low frequencies using an interdigitated ZnSe large aperture photoconductive antenna." *Applied Physics Letters* 103 (2013).

Ruffin, A. B., J. V. Rudd, J. F. Whitaker, S. Feng, and H. G. Winful. "Direct Observation of the Gouy Phase Shift with Single-Cycle Terahertz Pulses." *Phys. Rev. Lett.* 83 (Oct 1999): 3410–3413.

S. Jha, Sudhanshu. *Perspectives in Optoelectronics.* First edition. 1995.

Schall, Michael and Peter Uhd Jepsen. "Photoexcited GaAs surfaces studied by transient terahertz time-domain spectroscopy." *Opt. Lett.* 25 (Jan 2000): 13–15.

Sharma, G., I. Al-Naib, H. Hafez, R. Morandotti, D. G. Cooke, and T. Ozaki. "Carrier density dependence of the nonlinear absorption of intense THz radiation in GaAs." *Optics Express* 20 (2012): 18016–18024.

Sheik-Bahae, M., A. A. Said, T. H. Wei, D. J. Hagan, and E. W. Van Stryland. "Sensitive measurement of optical nonlinearities using a single beam." *IEEE J. Quantum Electron.* 26 (Sep 1990): 125203.

Shen, Y., T. Watanabe, D. A. Arena, C.-C. Kao, J. B. Murphy, T. Y. Tsang, X. J. Wang, and G. L. Carr. "Nonlinear Cross-Phase Modulation with Intense Single-Cycle Terahertz Pulses." *Phys. Rev. Lett.* 99 (Jul 2007): 043901.

Singh, Jasprit. *Electronic and optoelectronic Properties of Semiconductr Structures*. First edition. Cambridge University press, 2003.

Srivastava, Ajit, Rahul Srivastava, Jigang Wang, and Junichiro Kono. "Laser-Induced Above-Band-Gap Transparency in GaAs." *Phys. Rev. Lett.* 93 (Oct 2004): 157401.

Stanton, C. J. and D. W. Bailey. "Rate equations for the study of femtosecond intervalley scattering in compound semiconductors." *Phys. Rev. B* 45 (Apr 1992): 8369–8377.

Stepanov, A. G., L. Bonacina, S. V. Chekalin, and J. P. Wolf. "Generation of 30 $\mu$J single-cycle terahertz pulses at 100 Hz repetition rate by optical rectification." *Optics Letters* 33 (2008): 2497–2499.

Stepanov, A. G., S. Henin, Y. Petit, L. Bonacina, J. Kasparian, and J. P. Wolf. "Mobile source of high-energy single-cycle terahertz pulses." *Applied Physics B* 101 (2010): 11–14.

Stepanov, Andrei G., János Hebling, and Jürgen Kuhl. "Efficient generation of subpicosecond terahertz radiation by phase-matched optical rectification using ultrashort laser pulses with tilted pulse fronts." *Applied Physics Letters* 83 (2003): 3000–3002.

Stevens, Martin J., Arthur L. Smirl, R. D. R. Bhat, Ali Najmaie, J. E. Sipe, and H. M. van Driel. "Quantum Interference Control of Ballistic Pure Spin Currents in Semiconductors." *Phys. Rev. Lett.* 90 (Apr 2003): 136603.

Su, F. H., F. Blanchard, G. Sharma, L. Razzari, A. Ayesheshim, T. L. Cocker, L. V. Titova, T. Ozaki, J.-C. Kieffer, R. Morandotti, M. Reid, and F. A. Hegmann. "Terahertz pulse induced intervalley scattering in photoexcited GaAs." *Opt. Express* 17 (Jun 2009): 9620–9629.

Titova, Lyubov, Tyler Cocker, David Cooke, Xiongyao Wang, Al Meldrum, and Frank Hegmann. "Ultrafast percolative transport dynamics in silicon nanocrystal films." *Phys. Rev. B* 83 (Feb 2011): 085403.

Titova, Lyubov V., Ayesheshim K. Ayesheshim, Andrey Golubov, Dawson Fogen, Rocio Rodriguez-Juarez, Frank A. Hegmann, and Olga Kovalchuk. "Intense THz pulses cause H2AX phosphorylation and activate DNA damage response in human skin tissue." *Biomed. Opt. Express* 4 (Apr 2013): 559–568.

Titova, Lyubov V., Ayesheshim K. Ayesheshim, Andrey Golubov, Rocio Rodriguez-Juarez, Rafal Woycicki, Frank A. Hegmann, and Olga Kovalchuk. "Intense THz pulses down-regulate genes associated with skin cancer and psoriasis: a new therapeutic avenue?." *Sci. Rep.* 3 (2013).

Tonouchi, Masayoshi. "Cutting-edge terahertz technology." *Nature Photonics* 1 (2007): 97–105.

Tsuruoka, T., H. Hashimoto, and S. Ushioda. "Real-space observation of electron transport in AlGaAs/GaAs quantum wells using a scanning tunneling microscope." *Thin Solid Films* 464âĂŞ465.

Turchinovich, Dmitry, Jorn M. Hvam, and Matthias C. Hoffmann. "Self-phase modulation of a single-cycle terahertz pulse by nonlinear free-carrier response in a semiconductor." *Physical Review B* 85 (2012).

Ulbricht, Ronald, Euan Hendry, Jie Shan, Tony F. Heinz, and Mischa Bonn. "Carrier dynamics in semiconductors studied with time-resolved terahertz spectroscopy." *Reviews of Modern Physics* 83 (2011): 543–586.

Wahlstrand, J. K. and R. Merlin. "Cherenkov radiation emitted by ultrafast laser pulses and the generation of coherent polaritons." *Phys. Rev. B* 68 (Aug 2003): 054301.

Wen, H., M. Wiczer, and A. M. Lindenberg. "Ultrafast electron cascades in semiconductors driven by intense femtosecond terahertz pulses." *Phys. Rev. B* 78 (Sep 2008): 125203.

Wu, Q. and X. C. Zhang. "FREE-SPACE ELECTROOPTIC SAMPLING OF TERA-HERTZ BEAMS." *Applied Physics Letters* 67 (1995): 3523–3525.

Xie, Xu, Jianming Dai, and X.-C. Zhang. "Coherent Control of THz Wave Generation in Ambient Air." *Phys. Rev. Lett.* 96 (Feb 2006): 075005.

Xu, L., X. C. Zhang, and D. H. Auston. "TERAHERTZ BEAM GENERATION BY FEM-TOSECOND OPTICAL PULSES IN ELECTROOPTIC MATERIALS." *Applied Physics Letters* 61 (1992): 1784–1786.

Yang, K. H., P. L. Richards, and Y. R. Shen. "Generation of Far−Infrared Radiation by Picosecond Light Pulses in LiNbO$_3$." *Applied Physics Letters* 19 (1971).

Yeh, K. L., J. Hebling, M. C. Hoffmann, and K. A. Nelson. "Generation of high average power 1 kHz shaped THz pulses via optical rectification." *Optics Communications* 281 (2008): 3567–3570.

Yeh, K. L., M. C. Hoffmann, J. Hebling, and K. A. Nelson. "Generation of 10 $\mu$J ultrashort terahertz pulses by optical rectification." *Applied Physics Letters* 90 (2007).

You, D., R. R. Jones, P. H. Bucksbaum, and D. R. Dykaar. "GENERATION OF HIGH-POWER SUB-SINGLE-CYCLE 500-FS ELECTROMAGNETIC PULSES." *Optics Letters* 18 (1993): 290–292.

Yun-Shik, Lee. *Principles of Terahertz Science and Technology.* second edition. Springler-New York: Springer, 2009.

Zhang, X.-C., Y. Jin, K. Yang, and L. J. Schowalter. "Resonant nonlinear susceptibility near the GaAs band gap." *Phys. Rev. Lett.* 69 (Oct 1992): 2303–2306.

Zhao, G., R. N. Schouten, N. van der Valk, W. T. Wenckebach, and P. C. M. Planken. "Design and performance of a THz emission and detection setup based on a semi-insulating GaAs emitter." *Review of Scientific Instruments* 73 (2002): 1715–1719.

Zhao, Hui, Xinyu Pan, Arthur L. Smirl, R. D. R. Bhat, Ali Najmaie, J. E. Sipe, and H. M. van Driel. "Injection of ballistic pure spin currents in semiconductors by a single-color linearly polarized beam." *Phys. Rev. B* 72 (Nov 2005): 201302.

# APPENDIX A

## THz pulse generation

### A.1 Photo-induced pulsed electromagnetic radiation in semiconductors

Terahertz pulse radiation from a transient carrier is illustrated in section 2.2.1 of chapter 2. Since velocity of carriers are less than velocity of light in semiconductors, the qualitative description of the emission of electromagnetic radiation by those accelerated photocarriers in semiconductors begins with a far-field dipole radiation approximation [S. Jha (1995)] [Chapter 3, p.95]. In the expression of dipole radiation the electric field component of the accelerated charged particle is expressed as;

$$\vec{E}(\mathbf{r}, t) = \frac{e}{4\pi c^2 r^3}\vec{r} + \frac{e}{4\pi c^2 r^3}\vec{r} \times \left(\vec{r} \times \frac{\partial \vec{v}}{\partial t}\right) + ... \tag{A.1}$$

where $e$ and $c$ denotes charge of an electron and peed of light in free space, respectively. $\vec{E}$ is the electric field component of an electromagnetic wave radiated by a dipole shown in Fig. A.1, and $v$ is charge velocity. The first and second terms in Eq. A.1 are the near field (Coulomb field) and the far-field (radiated field), respectively. The carrier velocity can be derived from the current density as

$$\vec{J} = ne\vec{v} \tag{A.2}$$

Thus, the rate of velocity charge oscillation becomes

$$\frac{\partial v}{\partial t} = \frac{1}{ne}\frac{\partial J}{\partial t} \tag{A.3}$$

Recall that the dipole oscillation is along the dipole axis and the velocity of the dipole oscillation is along z-axis, $\vec{v} = v\hat{z}$. In order to investigate the field direction of Eq. A.1 in
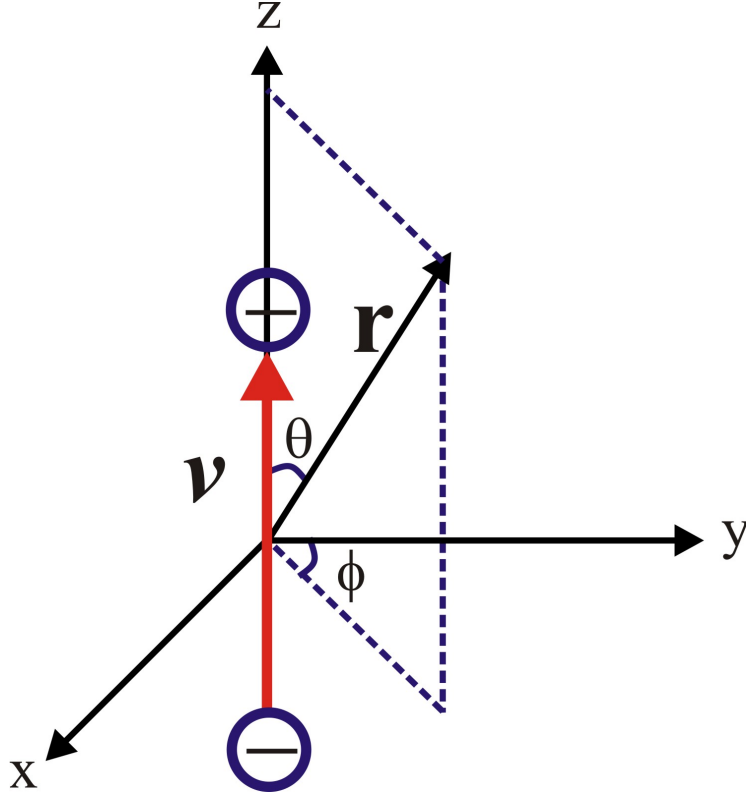


Figure A.1: Dipole radiation

spherical coordinator, each terms should be decomposed in spherical coordinate. Therefore, the unit vector along the dipole oscillation, $\hat{z}$, can be expressed as,

$$\hat{z} = \cos\theta\hat{r} - \sin\theta\hat{\theta} \tag{A.4}$$

where $\theta$ is the angle between the direction of dipole. Also, interns of the spherical coordinate unit vectors the velocity can be expressed as

$$\vec{v} = v\left(\cos\theta\hat{r} - \sin\theta\hat{\theta}\right) \tag{A.5}$$

And

$$\frac{\partial\vec{v}}{\partial t} = \left\{\cos\theta\hat{r} - \sin\theta\hat{\theta}\right\}\frac{\partial v}{\partial t} \tag{A.6}$$

The cross product of any two vectors $\vec{r} = r\hat{r}$ and $\vec{v} = v_r\hat{r} + v_\theta\hat{\theta} + v_\phi\hat{\phi}$ in spherical coordinate is given by

$$\vec{r} \times \vec{v} = \begin{bmatrix} r^2\sin\theta\hat{r} & \sin\theta\hat{\theta} & \frac{1}{\sin\theta}\hat{\phi} \\ r & 0 & 0 \\ v_r & v_\theta & v_\phi \end{bmatrix} = \sin\theta\hat{\theta}\left(rv_\phi - 0\right) + \frac{1}{\sin\theta}\hat{\phi}(rv_\theta) \qquad (A.7a)$$

And the cross product between $\vec{r}$ and $\frac{\partial\vec{v}}{\partial t}$ of the second term of Eq.A.1 yields,

$$\vec{r} \times \frac{\partial\vec{v}}{\partial t} = \begin{bmatrix} r^2\sin\theta\hat{r} & \sin\theta\hat{\theta} & \frac{1}{\sin\theta}\hat{\phi} \\ r & 0 & 0 \\ \cos\theta\frac{\partial v}{\partial t} & -\sin\theta\frac{\partial v}{\partial t} & 0 \end{bmatrix} = \frac{1}{\sin\theta}\left(-r\sin\theta\frac{\partial v}{\partial t}\right)\hat{\phi} \qquad (A.7b)$$

Hence, the vector products in the second term of Eq. A.1 becomes

$$\vec{r} \times \left(\vec{r} \times \frac{\partial\vec{v}}{\partial t}\right) = \begin{bmatrix} r^2\sin\theta\hat{r} & \sin\theta\hat{\theta} & \frac{1}{\sin\theta}\hat{\phi} \\ r & 0 & 0 \\ 0 & 0 & \frac{1}{\sin\theta}\left(-r\sin theta\frac{\partial\vec{v}}{\partial t}\right) \end{bmatrix} = -r^2\sin\theta\underbrace{\frac{1}{ne}\frac{\partial J}{\partial t}}_{\frac{\partial v}{\partial t}}\hat{\theta} \quad (A.7c)$$

The second term of Eq. A.1 combining with Eq. A.7c results a simplified angular component of far-field dipole radiation,

$$\boxed{\vec{E}(\mathbf{r}, t) \approx \left\{\frac{1}{4\pi nc^2 r}\sin\theta\right\}\frac{\partial J}{\partial t}\hat{\theta}} \qquad (A.7d)$$

Therefore, the emitted radiation of a dipole in the far-field is proportional to the first temporal derivative of induced transient current density $\mathbf{J}(t)$ [Jepsen et al. (2011)], as shown in Eq. A.7d. This derivation is for a single dipole radiation. However, for the entire complete radiation at the surface of optically illuminated portion of a semiconductor, Eq. A.7d should be integrated by incorporating the appropriate phase factor in the retarded current density. Thus, the emitted radiation from the surface of the illuminated cross sectional area of a semiconductor is given by

$$E_\theta = \frac{\sin\theta}{4\pi\kappa c^2}\frac{\partial}{\partial t}\int_A \frac{J_s}{|\vec{r} - \vec{r'}|}ds' \qquad (A.8)$$

## A.2   THz pulse generation by optical rectification

As discussed in Chapter 1, the interaction of ultrashort pulse with nonlinear media creates a time dependent polarization $\mathbf{P}(t)$. The oscillation of the transient dipole leads to electromagnetic wave radiation. The purpose of this appendix is to give you an overview of how the THz field is related to the second order transient polarization in time domain and to show how dc frequency component is obtained via mixing of different frequency components. It is ideal to begin with Maxwell's equations to describe the wave equations that governs the propagation of ultrashort femtosecond pulse through nonlinear media.

The macroscopic forms of Maxwell's equations have the form:

$$\vec{\nabla} \cdot \vec{D} = \rho \tag{A.9a}$$

$$\vec{\nabla} \times \vec{D} = -\frac{\partial \vec{B}}{\partial t} \tag{A.9b}$$

$$\vec{\nabla} \times \vec{H} = \vec{J} + \frac{\partial \vec{D}}{\partial t} \tag{A.9c}$$

where $\rho$ and $\vec{J}$ are the charge and current densities, respectively. $\vec{D}$ and $\vec{H}$ are the macroscopic fields and related to the fundamental fields of $\vec{E}$ and $\vec{B}$ as,

$$\vec{D} = \epsilon_0 \vec{E} + \vec{P} = \epsilon \vec{E} \tag{A.10a}$$

$$\vec{H} = \frac{1}{\mu_0} \vec{B} - \vec{M} = \frac{1}{\mu} \vec{B} \tag{A.10b}$$

$\vec{P}$ and $\vec{M}$ are the polarization and magnetization of the material, these contain the information about the macroscopic scale of EM properties of the media, $\epsilon$ and $\mu$ denote the electric permittivity and the magnetic permeability of the media. After applying the curl $\vec{\nabla} \times$ to both sides of Eq. A.9b with substituting of $\vec{D}$ and $\vec{H}$ given in equations A.10a and A.10b results the wave equation,

$$\nabla^2 \vec{E} - \mu\epsilon \frac{\partial^2 \vec{E}}{\partial^2 t} = \mu \frac{\partial}{\partial t} \vec{j} + \frac{1}{\epsilon} \vec{\nabla} \rho_f \tag{A.11}$$

For electrically neutral and nonmagnetic media, free charges and magnetic density doesn't exists, which are $\rho_f = 0$ and $\mathbf{M} = 0$. Therefore, the simplified wave form of Eq. A.11 is,

$$\nabla^2 \vec{E} - \mu\epsilon \frac{\partial^2 \vec{E}}{\partial t^2} = \mu \frac{\partial^2 \vec{P}}{\partial t^2} \tag{A.12}$$

where the term $\mu\epsilon = \frac{1}{v^2} = \{\frac{c}{n}\}^{-2}$ and $v$ is the speed of electromagnetic waves propagating through a homogeneous media and $J = J_f + \frac{\partial P}{\partial t}$ is the current density, $c$ is speed of light in

free space, and $n$ is the refractive index of the medium. Similarly, one can derive the wave equation for the magnetic field, $\vec{H}$ and reach with an identical form. However, the magnetic field effect is negligible compared with the electric field. Depending on the applied field, the polarization $\mathbf{P}$ can have both a linear $\varepsilon_0\chi\mathbf{E}$ and nonlinear $\mathbf{P}_{NL}$ components. For large amplitude of incident optical pulse the induced polarization $\mathbf{P}$ can be expanded into a Tyler series of the applied field as

$$\mathbf{P}(\mathbf{r},t) = \underbrace{\varepsilon_0\chi^{(1)}\mathbf{E}(\mathbf{r},t)}_{\textbf{Linear}} + \underbrace{\frac{1}{2}\varepsilon_0\chi^{(2)}\mathbf{E}(\mathbf{r},t)\mathbf{E}(\mathbf{r},t) + \frac{1}{6}\varepsilon_0\chi^{(3)}\mathbf{E}(\mathbf{r},t)\mathbf{E}(\mathbf{r},t)\mathbf{E}(\mathbf{r},t) + ...}_{\textbf{Nonlinear}} \quad \text{(A.13)}$$

where $\chi^{(1)}$ is linear susceptibility, $\chi^{(2)}$ is second order nonlinear susceptibility tensor and optical rectification occurs from this term, and higher order terms of $\chi^{(n)}$ are $n^{th}$ order susceptibility tensors. $\mathbf{E}(\mathbf{r},t)$ is incident field. Such that only up to $2^{nd}$ order terms are considered. Substituting Eq. A.13 to Eq. A.12 yields,

$$\boxed{\nabla^2\vec{E} - \mu_0\epsilon_0 n^2\frac{\partial^2\vec{E}}{\partial t^2} = \mu_0\frac{\partial^2\vec{P}_{NL}^{(2)}}{\partial t^2}} \quad \text{(A.14)}$$

Equation A.14 is an inhomogeneous nonlinear equation and the nonlinear polarization term on the right hand side $\mu_0\frac{\partial^2\vec{P}_{NL}^{(2)}}{\partial t^2}$ is a source term, which is responsible for generation of new frequencies ($\Omega$) in the THz range. If $\vec{P}_{NL}^{(2)} = 0$, Eq. A.14 becomes the well known EMW equation that propagating through vacuum and the solution is a monochromatic plane wave. To solve Eq. A.14, let's consider a short optical pulse incident normally on a thin electro-optic slab of thickness L, the far-infrared radiation field $\mathbf{E}_r(t)$ generated by the rectified polarization is obtained from the solution of Eq. Eq. A.14. In the far-field limit, the solution of the radiated field along the axis of propagation detected at distance z away from the emitter is proportional to the first time derivative of the induced surface current density [Yang et al. (1971)].

$$\mathbf{E}_r(t) = -\frac{A}{4\pi_0 c^2}\frac{\partial\mathbf{J}_s}{\partial t} \quad \text{(A.15)}$$

where $J_s$ is the surface current density and $A$ the emitter area. The transient polarization in OR is associated with a boundary current as,

$$J_s = J_f + \frac{\partial P}{\partial t} \quad \text{(A.16)}$$

where $\mathbf{P}$ is the induced nonlinear polarization, and $\mathbf{J}_f = \sigma\mathbf{E}$ is free current density. Consequently, the radiated field have the same form as the dipole far field approximation derived in Appendix A.1

$$\mathbf{E}_r(t) = \mathbf{E}_{THz} \propto \frac{\partial^2 P_{NL}^{(2)}}{\partial t^2} = \frac{\partial}{\partial t}\left(\frac{\partial P_{NL}^{(2)}}{\partial t}\right) = \frac{\partial J_s}{\partial t} \tag{A.17}$$

Therefore, far field radiated THz electric field is directly proportional to the first temporal derivative of the optical induced current density in photoconductive switch semiconductor substrates or the second temporal derivatives of the induced dipole moment in electrooptic crystals. Also, it can be expressed interns of incident light pulse intensity as

$$\mathbf{E}_r(t) = \mathbf{E}_{THz}\frac{\partial J_s}{\partial t} \propto \frac{\partial^2 P_{NL}^{(2)}}{\partial t^2} = \chi^{(2)}\frac{\partial^2 I(t)}{\partial t^2} \tag{A.18}$$

where $I(t) \propto \mathbf{E}(\mathbf{r}, t)\mathbf{E}(\mathbf{r}, t)$ is intensity of incident field. To investigate the OR scenario further, it is appropriate to express the nonlinear polarization in frequency domain as,

$$\mathbf{P}_{THz}^{(2)}\Omega = \varepsilon_0\left(\frac{1}{2}\chi^{(2)}\right)\mathbf{E}^*(\omega_1)\mathbf{E}(\omega_2) \tag{A.19}$$

where $\mathbf{P}_{THz}^{(2)}(\Omega)$ is the second order nonlinear polarization responsible for THz pulse radiation $\Omega$ is the difference frequency of generated field. A femtosecond optical pulse is a sum of monochromatic waves with frequencies occupying a spectral band surrounding the central frequency $\omega_o$. When the monochromatic frequency component propagates through the nonlinear media it can contribute to difference frequency generation or sum frequency generation. The difference frequency generation can cover frequencies from zero to the spectral bandwidth of the incident optical pulse and it can be obtained from any two frequency components of the pump pulse with angular frequencies of $\omega_1 = \omega$ and $\omega_2 = \omega + \Omega$. Therefore, THz pulse generation is the sum of all the pairs of the second order nonlinear polarization associated with the optical rectification [Amnon Yariv (1984)], which is given by

$$\mathbf{P}_{THz}^{(2)}(\Omega) = \varepsilon_0\sum_{jk}\chi_{ijk}^{(2)}(\Omega)\int\limits_{-\infty}^{\infty}\mathbf{E}_j(\omega + \Omega)\mathbf{E}_k(\omega)d\omega \tag{A.20}$$

Or in tensor form,

$$\mathbf{P}_i(\Omega) = \varepsilon_0\sum_{jk}d_{ijk}(\Omega)\mathbf{E}_j(\omega + \Omega)\mathbf{E}_k(\omega) \tag{A.21}$$

because the second order nonlinear susceptibility is a tensor. where, i, j, k = 1, 2, 3 denotes the dummy indices for x-, y-, and z-directions, respectively, in the crystallographic axis. Where $d_{ijk} = \frac{\partial^2 \mathbf{P}_i}{\partial E_j \partial E_k} = \frac{1}{2}\chi_{ijk}^{(2)}$ is the nonlinear susceptibility coefficient for the difference frequency generation, $\mathbf{E}_j(\omega + \Omega)\mathbf{E}_j(\omega)$ is the amplitude spectral component of the pump laser. The general form of Eq. A.21, of the induced polarization density due to difference frequency combination of the optical pump filed inside electro-optic crystals can be written

as,

$$
\begin{bmatrix} \vec{P}_x^{(2)}(\Omega) \\ \vec{P}_y^{(2)}(\Omega) \\ \vec{P}_z^{(2)}(\Omega) \end{bmatrix} = \begin{bmatrix} d_{11} & d_{12} & d_{13} & d_{14} & d_{15} & d_{16} \\ d_{21} & d_{22} & d_{23} & d_{24} & d_{25} & d_{26} \\ d_{31} & d_{32} & d_{33} & d_{34} & d_{35} & d_{36} \end{bmatrix} \begin{bmatrix} E_x(\omega_1)E_x(\omega_2) \\ E_y(\omega_1)E_y(\omega_2) \\ E_z(\omega_1)E_z(\omega_2) \\ E_y(\omega_1)E_z(\omega_2) + E_z(\omega_1)E_y(\omega_2) \\ E_z(\omega_1)E_x(\omega_2) + E_x(\omega_1)E_z(\omega_2) \\ E_x(\omega_1)E_y(\omega_2) + E_y(\omega_1)E_x(\omega_2) \end{bmatrix}
$$

$$(A.22)$$

At frequencies $\omega_1 = \omega_2$ the difference frequency generation creates a static induced polarization in the material, this effect is called optical rectification. Therefore, the term optical rectifiction is when the two optical frequency components are equal and their difference goes to zero, implies $\Omega \cong 0$. Hence, for OR, Eq. A.22 can be simplified as,

$$
\begin{bmatrix} \vec{P}_x^{(2)}(\Omega) \\ \vec{P}_y^{(2)}(\Omega) \\ \vec{P}_z^{(2)}(\Omega) \end{bmatrix} = \begin{bmatrix} d_{11} & d_{12} & d_{13} & d_{14} & d_{15} & d_{16} \\ d_{21} & d_{22} & d_{23} & d_{24} & d_{25} & d_{26} \\ d_{31} & d_{32} & d_{33} & d_{34} & d_{35} & d_{36} \end{bmatrix} \begin{bmatrix} E_x^2 \\ E_y^2 \\ E_z^2 \\ 2E_yE_z \\ 2E_xE_z \\ 2E_xE_y \end{bmatrix}
$$

$$(A.23)$$

Where $P_{x,y,z}^{(2)}$ and $E_{x,y,z}$ are the second order polarization and electric field of the optical pump along x, y, and z direction, respectively. Eq. A.23 is the general form of optical rectification polarization from electro-optic crystals. This equation applies to every electro-optic crystals and the nonlinear coefficient matrix will vary according to the symmetry properties of crystalline structures.

## A.3   Phase matching

Recall Eq. 5.3, for a slowly varying wavenumber, $k(\omega)$ can be approximated as,

$$k(\omega) \equiv k(\omega_0) + \frac{dk}{d\omega} \mid_{\omega_0} (\omega - \omega_0) + \frac{1}{2} \frac{d^2 k}{d\omega^2} \mid_{\omega_0} (\omega - \omega_0)^2 + \dots \tag{A.24}$$

$$k(\omega) - k(\omega_0) \approx \frac{dk}{d\omega} \mid_{\omega_0} (\omega - \omega_0) \tag{A.25}$$

$$\omega = \omega_0 + \Omega, k(\omega_0 + \Omega) - k(\omega_0) \approx \Omega \frac{dk}{d\omega} = \frac{\Omega}{c} n_{op} \tag{A.26}$$

185

and

$$k(\Omega) = \frac{\Omega}{c} n_{THz} \tag{A.27}$$

Hence, the phase matching condition given by Eq. 5.3 becomes,

$$\Delta k = k(\omega_{NIR} + \Omega_{THz}) - k(\omega_{NIR}) - k(\Omega_{THz}) = \frac{\Omega}{c}(n_{op} - n_{THz}) \tag{A.28}$$

Also, in terms of optical group velocity and THz phase velocity can be expressed as,

$$\Delta k = \frac{\Omega}{c}(n_{op} - n_{THz}) = \Omega(v_{op} - v_{THz}) \tag{A.29}$$

Therefore, the phase matching condition, $\Delta k = 0$, is fulfilled when $n_{op} = n_{THz}$ or $v_{op} = v_{THz}$.

# APPENDIX B

## THz pulse smoothing function

A Cosine taper Matlab function used to smooth the experimentally measured THz waveform is given below.

```matlab
1   clear all;
2   close all;
3   clc;
4   % Float32 x;
5   % X = start+i*increment;
6   % Window = (1/(1+exp((t1-x)/t0)))*(1-1/(1+exp((t2-x)/t0)))
7
8   % load p8interpolated_normalized.dat;
9   % load p8interpolated.dat;
10  load p8interpNormEt.dat;
11  % load p88.dat;
12  % p8 =p88;
13    p8 = p8interpNormEt;
14     E = p8(:,2);
15   time = p8(:,1);
16
17    j0 = length(E);
18    dt = 9.0114e-004;
19    T0 = time(20000,1);
20
21   mcc = 3000;
22   j00 = length(E)-mcc*2;
23   T00 = time(20000,1)-(dt*mcc*2);
24
25  %    t1 = time(1000,1);  % 0.900285592559615 ps
26  %    t1 = time(1500,1);  % 1.35087898222908  ps
27  %    t1 = time(2000,1);  % 1.80147237189854  ps
```

```matlab
28  %    t1 = time(2500,1);   % 2.252065761568    ps
29  %    t1 = time(3000,1);   % 2.252065761568    ps
30  %    t1 = time(3500,1);   % 3.15325254090693  ps
31     t1 = time(4000,1);   % 3.60384593057639  ps
32  %    t1 = time(4500,1);   % 4.05443932024588  ps
33
34  %    t1 = time(5000,1);   % 4.50503270991556  ps
35  %    t1 = time(5500,1);   % 4.95562609958525  ps
36  %    t1 = time(6000,1);   % 5.40621948925493  ps
37  %    t1 = time(6500,1);   % 5.85681287892462  ps
38  %    t1 = time(7000,1);   % 6.3074062685943   ps
39  %    t1 = time(7500,1);   % 6.75799965826399  ps
40  %    t1 = time(8000,1);   % 7.20859304793367  ps
41  %    t1 = time(8500,1);   % 7.65918643760336  ps
42  %    t1 = time(9000,1);   % 8.10977982727304  ps
43
44  %   t1 = time(10000,1);   % 2.49989212588621
45
46
47  %   t1 = time(2775,1);   % 2.49989212588621
48  %   t1 = time(3930,1);   % 3.54076285602267
49  %   t1 = time(7000,1);   % 4.50503270991556
50  %   t1 = time(5829,1);   % -0.0012441492
51
52  %  t1 = time(9000,1);      %
53  % wvtool(E)
54        ti = time(1,1);
55        tf = j0*dt;
56     theta = (2*pi)/(2*t1);
57
58  for it = 1:j00
59      t = (it-1)*dt;
60      if (ti <=t && t<=t1);
61          wc(it) = 1/2*(1-cos((theta)*t));
62      else
63          if (t1 <=t && t<=T00-t1);
64              wc(it) = 1;
65          else
66  %              if T0-t1<=t<T0
67              wc(it) = 1/2*(1-cos((theta)*(t-T00)));
68  %          end
69          end
70      end
71
72  end
73          wc = wc';
74        for it=1:j0
75          if (it <= mcc)
```

```matlab
76              wdc(it)=0.0;
77          elseif( it > mcc && it < j0—mcc)
78              wdc(it)=wc(it—mcc);
79          else( it ≥ j0—mcc)
80              wdc(it)=0.0;
81          end
82        end
83      wcc=wdc';
84 %       ifix=6000;
85 %       ishift =4000;
86 %       count=0;
87 %       wcc(1:j0)=1.0;
88 %       wcc(1:ifix)=wdc(1:ifix);
89 %       for it=:ishift
90 %       if(it
91 %       wcc(it+ifix+ishift)=wdc(it+ifix);
92 %       end
93 %       wcc=wcc';


96      wcp8=wcc.*p8(:,2);

98      p8windowed = [time wcp8];
99       p8windowedwcc = [time wcc];
100       p8windowedp8 = [time p8];
101      figure(1)

103 % subplot(311),plot(time,wcc),grid on
104 % legend('Forward Finite' ,'Backward Finite','1^{st} ODR','4^{th} ODR')
105 % title('Windowing function')
106 % xlabel('Time(ps)');
107 %  ylabel('Normalized Amplitude');
108 %  grid minor
109 %  hold all
110 % subplot(312),plot(time,p8(:,2)),grid on
111 % legend('Forward Finite' ,'Backward Finite','1^{st} ODR','4^{th} ODR')
112 % title('Original FSEOS THz waveform')
113 % xlabel('Time(ps)');
114 %  ylabel('Normalized Amplitude');
115 %  grid minor
116 %  hold all
117 % subplot(313),plot(time,wcp8,'r'),grid on
118 % legend('Forward Finite' ,'Backward Finite','1^{st} ODR','4^{th} ODR')
119 % title('Windowed THz waveform')
120 % xlabel('Time(ps)');
121 %  ylabel('Normalized Amplitude');
122 %  grid minor
123 %  hold all
```
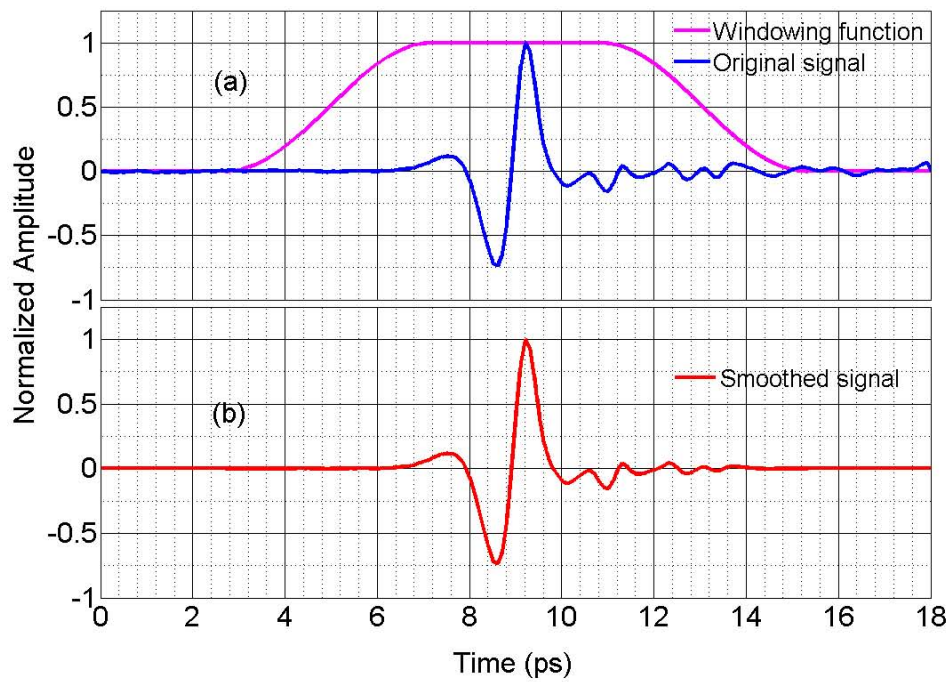
Figure B.1: Cosine taper smoothing function

```
124  subplot(211),plot(time,wcc, time,p8(:,2)),grid on
125  legend('Windowing function' ,'FSEOS  signal')
126  title('Windowing function & FSEOS  signal')
127  xlabel('Time(ps)');
128   ylabel('Normalized Amplitude');
129   grid minor
130   hold all
131
132  subplot(212),plot(time,wcp8,'r'),grid on
133  legend('Windowed THz waveform')
134  title('Windowed THz waveform')
135  xlabel('Time(ps)');
136   ylabel('Normalized Amplitude');
137   grid minor
138   hold all
139  save p8smoothed.mat  p8windowed  wcp8;
140  % figure(2)
141  % plot(t, int(time,wcp8))
142  % plot(time,wc
```

# APPENDIX C

## Pyroelectric Detector

The pyroelectric detector (SPJ-D-8 digital USB joule meter from Spectrum Detector Inc.) used for THz pulse energy measurement is designed to incorporate into a single or dual channel system to connect to analog or digital output to measure laser pulse energy with digital precision. Photograph of the SPJ-D-8 pyroelectric detector is shown in Fig. C.1 with the analog and digital reading is plotted in Fig. C.2. Therefore, it provides digital and analog readings. The pyro-electric detector has 7.8 $\times$7.8 mm$^2$ square active pyro-electric detector element and it is calibrated at 1.06 $\mu$m. The pyroelectric parameters are given in Table C.1. The maximum analog output of the SPJ-D-8 is set to 2 V for a given energy range. The ranges are 2 $\mu$J, 20 $\mu$J, 200 $\mu$J, and 2 mJ. For each of the voltage reading ranges the maximum reading of SPJ-D-8 is scaled to give an output voltage of 2.0 V. The analogue conversion of the pyro-detector is given in Table. C.2. If one makes a measurement using the 2 mJ range of the SPJ-D-8 and the reading on the software display is 1.50 mJ, someone should see a peak voltage output of 1.5V on the oscilloscope. If one measures a peak voltage

Table C.1: Pyroelectric detector specification

|  | SPJ-D-8 |
| --- | --- |
| Wavelength Range | 0.1-1000 $\mu$m |
| Energy Range | 2 $\mu$J-20 mJ |
| Energy Resolution | 10 nJ |
| Max Rep Rate | 1000 PPS |
| Detector Size | 7.8$\times$ 7.8 mm$^2$ |
| Detector or coating Type | Pyro/Chrome |
| Analog Voltage Output | 0-2 V |
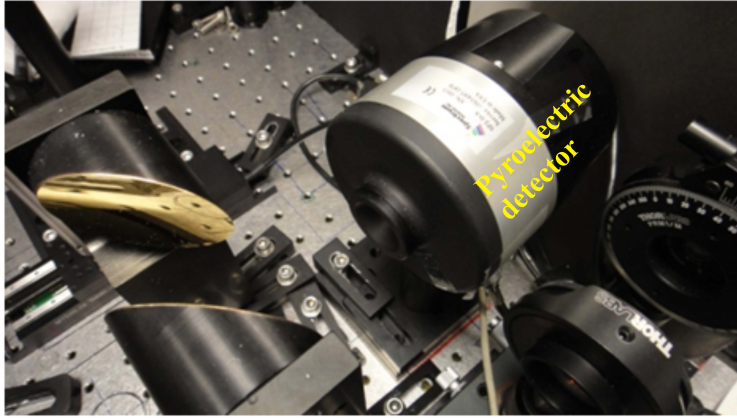
Figure C.1: Photograph of pyroelectric detector used for THz pulse energy measurement.
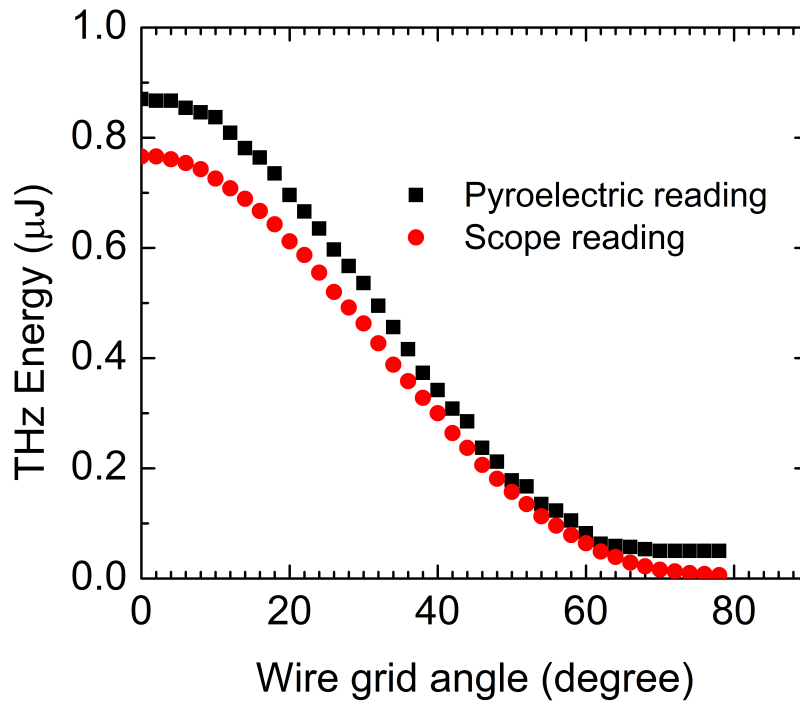


Figure C.2: Comparison pyroelectric digital THz pulse energy reading vs. analog reading.

Table C.2: SPJ-D-8 analog conversion

| Energy range | Analog conversion | Output |
|---|---|---|
| 2 $\mu$J | 2 V/2 $\mu$J | 1 mV / nJ |
| 20 $\mu$J | 2 V/20 $\mu$J | 100 mV / $\mu$J |
| 200 $\mu$J | 2 V/200 $\mu$J | 10 mV / $\mu$J |
| 2 mJ | 2 V/2 mJ | 1 mV / $\mu$J |

of 1.5 mV on 200 $\mu$J range the peak voltage observed on the scope will be 1.50 V.

### C.0.1 Infrared Camera (PV320: Electronics Inc.)

The PV320 infrared camera is a color thermal imaging camera with video and USB output. The focus has to be done manually. The camera has an array of 320×240 pixels with array size of 15.52×11.64 mm (HV), and pixel size of 48.5 $\mu$m$^2$. THz spot size is evaluated from the intensity profiles of the spot dimension ($1/e^2$) of 1.5 mm. The FWHM THz pulse duration is found to be 1.4 ps.

## C.1 THz peak field calculation

The peak THz field can be calculated either from the total pulse energy measured by the pyroelectric detector discussed in Chapter 5 or from the THz pulse modulation measured by balanced photodiode detectors. To keep the detectors in the linear regime, a set of Si attenuators were introduced on the collimated section of the THz beam. After attenuation to decrease the applied THz field to the EO sampling detector, the polarization modulation given in Eq. 2.5 in Chapter 2 is modified to be,

$$\frac{I_A - I_B}{I_A + I_B} = \sin\theta = \frac{2\pi}{\lambda_0} n_0^3 r_{41} t_D t_{Si} E_{THz} L \tag{C.1}$$

where t$_D$ and t$_{Si}$ are Fresnel transmission coefficients of the detector (ZnTe) and attenuator (silicon wafers) used to attenuate the THz intensity to keep the EO detection in the linear regime, respectively. The refractive index of the detecting crystal (ZnTe) for a THz frequency range of 0.3-1 THz is n$_{THz} \approx 3.16$. For normal incidence the Fresnel loss in terahertz power from reflection at the air-ZnTe interface is $\left(\frac{n_{THz}-1}{n_{THz}+1}\right)^2 = 27\%$. The associated Fresnel THz field reflection loss at the face of the ZnTe crystal is the square root of THz power, which is

about 51 %. To map out the time evolution of the transient EO signal, the time between the optical gate pulse and THz pulse at the detector crystal is varied via an optical time delay. Comparison of peak THz field calculation using THz modulation and directly calculated from the average energy of a THz pulse is given below.

Example of a THz pulse modulation after using two 2 Si wafer is displayed in Fig. C.3 The linearity of the photodiode THz pulse detectors are confirmed by plotting the modulation (A-B vs A+B) THz Energy after background subtracted measured using the pyroelectric detector was: 1.13 $\mu$J Transmitted THz energy through 2 Si wafers : 0.484 $\mu$J

$$sin^{-1}\left(\frac{I_A - I_B}{I_A + I_B}\right) = \frac{2\pi n_0^3 r_{41} t_D t_A E_{THz} L}{\lambda_0} \tag{C.2}$$

where $t_D$ and $t_A$ are the Fresnel transmission coefficient of the detector and attenuator crystals, respectively, at THz frequencies. $I_A$ and $I_B$ are the optical intensity measured by the photodetectors without the presence of THz pulse at the ZnTe detector. Intensity levels are labeled by $A$ and $B$ as shown in Fig. C.4.

| Detector | $n_0$ (800 nm) | $n_{THz}$ | $t_{THz}$ | $r_{41}$ ($10^{-10}$ cm/V) | Thickness (cm) | Attenuator | $\frac{I_A - I_B}{2I_A}$ |
|----------|------|-----------|-----------|------|-----------|------------|------|
| ZnTe | 2.853 | 3.16 | 0.48 | 4.04 | $5\times10^{-2}$ | 2Si | 0.512 |
| GaP | 3.2 | 3.34 | 0.46 | 0.88 | $3\times10^{-2}$ | 2Si | 0.135 |

Peak THz field calculation using modulation Eq. C.2 given as;

$$\boxed{|E_{THz}| = \frac{\lambda_0}{2\pi n_0^3 r_{41} t_{GaP} t_{Si}^2 L} sin^{-1}\left(\frac{I_A - I_B}{I_A + I_B}\right)} \tag{C.3}$$

Therefore, the simplified version of THz electric field modulation calculation using ZnTe and GaP detector for the parameters given in Table C.1 depending on number of Si wafer attenuator becomes:

$$ZnTe : E_{THz}(kV/cm) = 1.36 \left(\frac{Modulation}{t_{ZnTe} t_{Si}^n L(cm)}\right) \tag{C.4}$$

and

$$GaP : E_{THz}(kV/cm) = 4.415 \left(\frac{Modulation}{t_{GaP} t_{Si}^n L(cm)}\right) \tag{C.5}$$

where

$$Modulation = sin^{-1}\left(\frac{I_A - I_B}{I_A + I_B}\right)$$

194
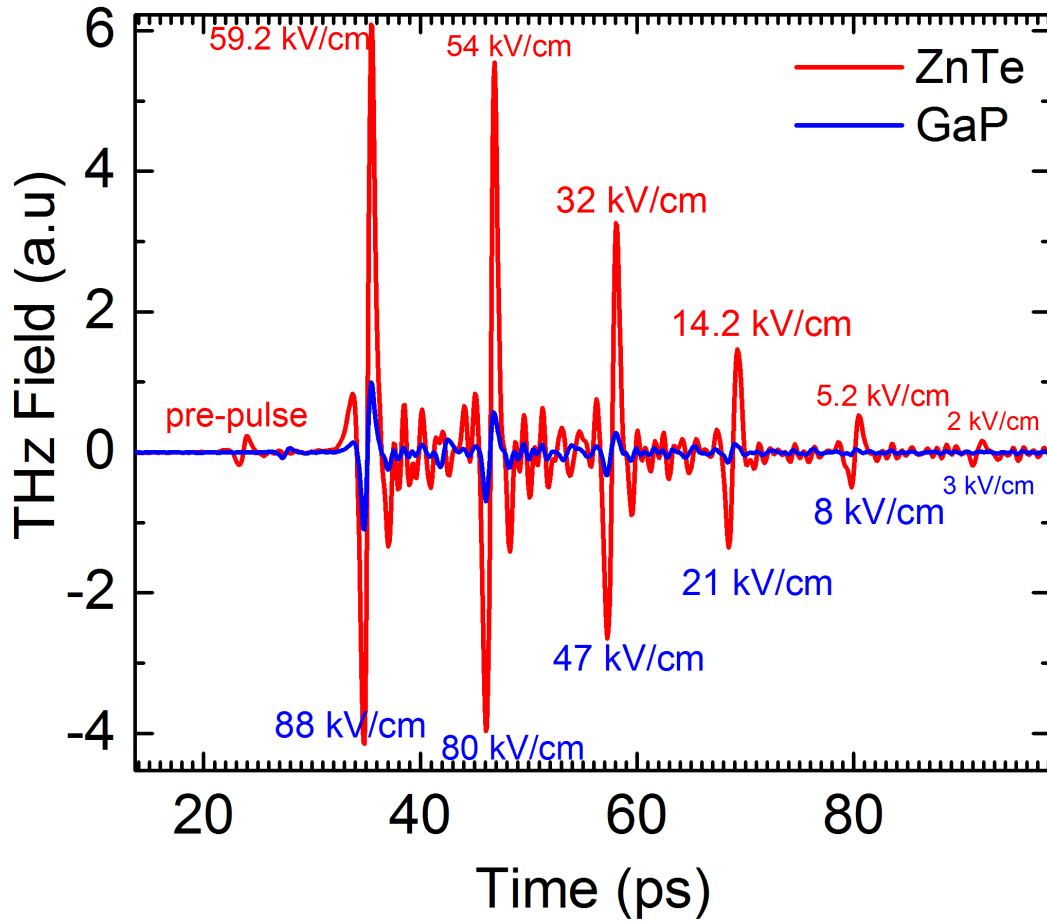
Figure C.3: Corresponding THz pulse measured using 500 $\mu$m thick ZnTe (red signal) and 300 $\mu$m thick GaP (blue signal) after 2Si wafers are inserted on the collimated section of the THz pulse to attenuate the intensity to keep the photodetectors in the linear regime
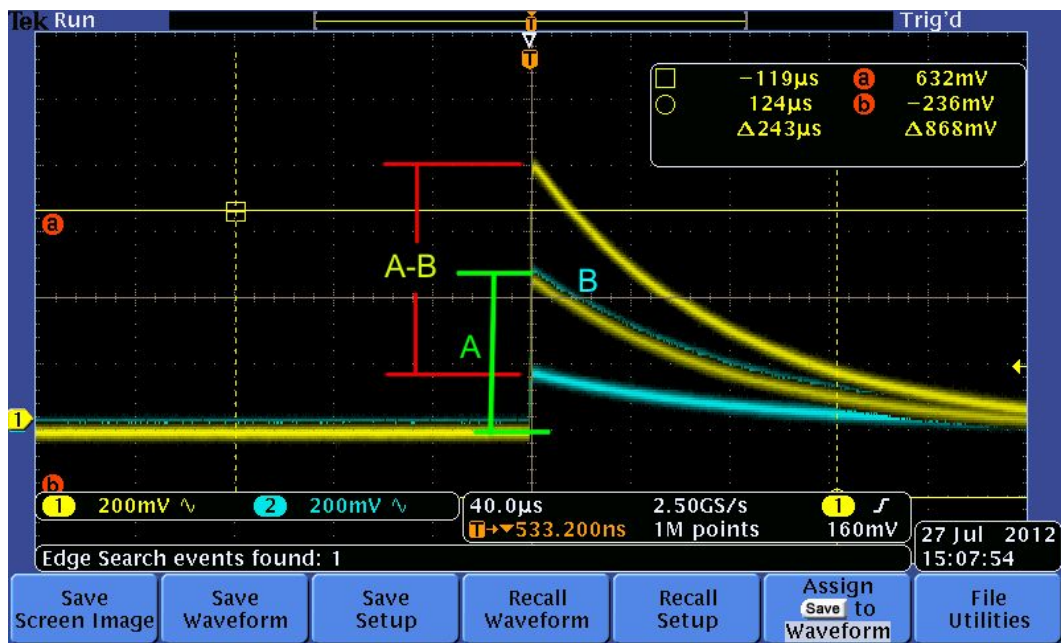
Figure C.4: THz pulse modulation using 0.5 mm thick ZnTe detector at a THz pulse energy of 0.484 $\mu$J after a 1.134 $\mu$J THz pulse energy is attenuated using two silicon wafers.

Recall the THz peak field calculation directly from the measured THz pulse energy using Eq. 5.31 in Chapter 5, at 0.484 $\mu$J it results, **157** kV/cm. However, the peak THz field calculated from the modulation detected by ZnTe and GaP whose parameters given in Table C.1 and using the corresponding equations C.4 and C.5 provides **59** kV/cm and **88** kV/cm, respectively. Both the modulation calculations are less by a factor of 2.65 and 1.8 from the calculation using THz pulse energy for ZnTe and GaP. The discrepancy of the THz field calculation based on electrooptic signal modulation with calculation based on measured THz pulse energy is not fully understood.

# APPENDIX D

## Drude dynamic model flowchart

Complete steps of the dynamic Drude intervalley scattering model is given in the flowchart.
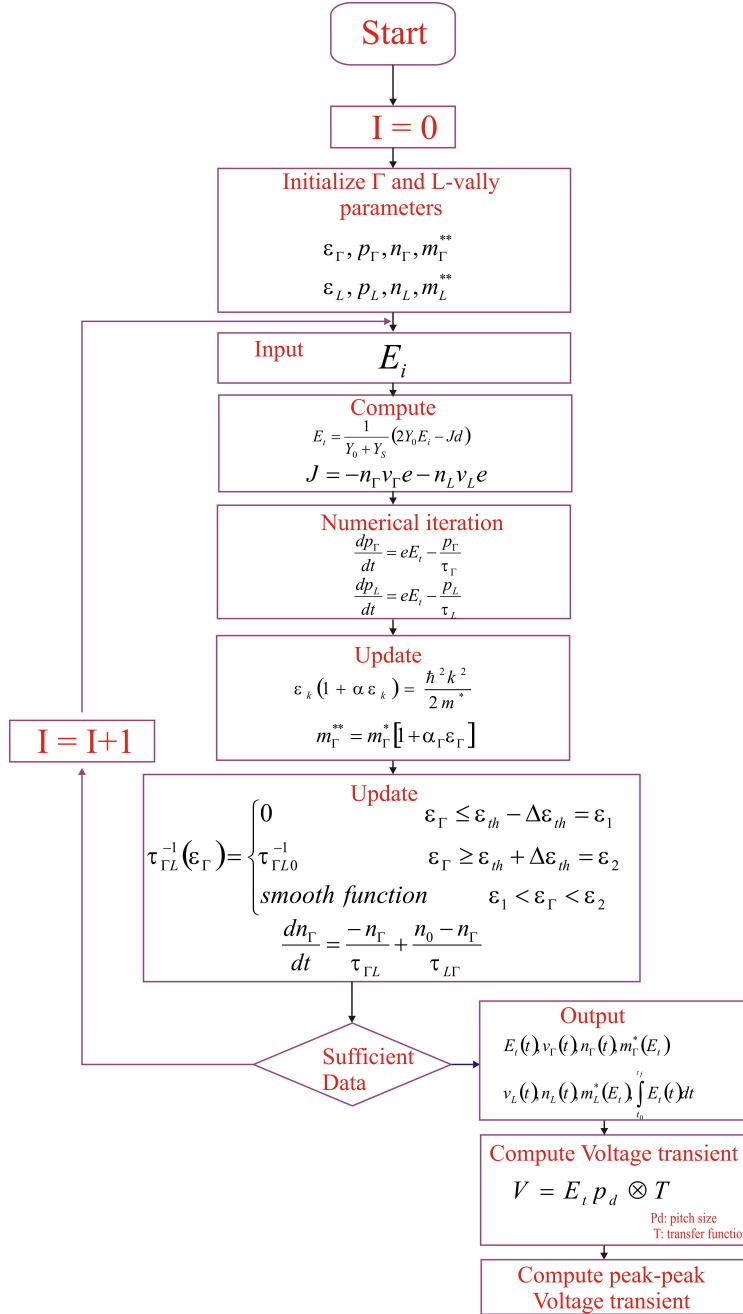
Figure D.1: Drude dynamic intervalley model flowchart.

# APPENDIX E

## Tilted pulse front technique

The following Matlab code is used to calculate the basic parameters to develop a tilted pulse front scheme for different grating grove density.

```matlab
function wavefront_tilt(demagnification,grating_groove,lens_focus)
   wavelength = 800;  % WAVE LENGTH OF THE OPTICAL BEAM in nm
  %(1) littrow_omega is the littrow angle
littrow_omega = asin(grating_groove*wavelength*1e-6/2)*180/pi

% For Littrow configuration alpha = beta, implies the grating equation
% becaomes m*lamda/(2* groove separation) = sin(littrow_omega)

     n_index = 2.26; % Index of LiNbO3 at optical wave length
  crystal_beam = 1.00; % spot size on crysal is 1.0mm
incident_beam = demagnification*crystal_beam;
% b/c demagnification = incident beam spot/beam spot at the crystal
     crystal_angle = 63;
     gamma_crystal = 63;
  gamma_outside_tan = tan(gamma_crystal*pi/180)*n_index;

% (2) gamma_outside is the tilt angle before LiNbO3, i.e., gamma
     gamma_outside = atan(gamma_outside_tan)*180/pi


  tilt_grating_tan = gamma_outside_tan/demagnification;

% gamma_outside = gama_after lens = gama2, tan(gama2)/tan(gama1)=demag
% where tan(gama1) is tilt pulse front before lens...
% therefore, tan(gama1)= tilt_grating_tan = gama_outside/demag
% (3) gtilt_grating is the tilt angle after grating, i.e., gamma1
tilt_grating = atan(tilt_grating_tan)*180/pi
```

```matlab
28
29 % (4) littrow_tilt is the littrow angle, i.e., alpha=beta
30 % littrow_tilt = atan(2*tan(littrow_omega*pi/180))*180/pi
31 littrow_tilt = atan(tan(littrow_omega*pi/180)/2)*180/pi
32 % in littrow configuration alpha=beta, but cos(alpha)*tan(gama1)=
33 % sin(alpha)+sin(beta)=2sin(alpha)
34 % Therefore, littrow_tilt = atan((tan(littrow_omega*pi/180)/2*(180/pi)
35
36 % grating equation and tilt equation%
37
38 % grating_groove*wavelength*1e—6=sin(alpha)+sin(belta)
39 % cos(belta)*tan(gamma)=sin(alpha)+sin(belta)
40            cos_beta = grating_groove*wavelength*1e—6/tilt_grating_tan;
41            sin_beta = sqrt(1—cos_beta^2);
42        sin_beta_neg = —sqrt(1—cos_beta^2);
43
44           sin_alpha = grating_groove*wavelength*1e—6—sin_beta;
45           dev_angle = asin(sin_alpha)*180/pi—asin(sin_beta)*180/pi
46      incident_angle = asin(sin_alpha)*180/pi
47        output_angle = asin(sin_beta)*180/pi
48              %in mm
49      image_distance = lens_focus*(demagnification+1)/demagnification
50     object_distance = demagnification*image_distance
51              %in inch
52  image_distanceinch = image_distance/25.4
53 object_distanceinch = object_distance/25.4
54                demag = object_distance/image_distance
55
56               AngleofIncidence =incident_angle
57               DiffractionAngle = output_angle
58               DeviationAngle =dev_angle
59                TiltAngleAfterGrating = tilt_grating
60               TiltAngleBeforeCrystal = gamma_outside
61               TiltAngleInsideCrystal = 63
62 %To run the program write as follows on the command line
63 % >> wavefront_tilt(Demag,groove density,focal length of lens)
64 % >> wavefront_tilt(1.7,1800,150)
65 % >> wavefront_tilt(4.9,1100,75)
66 % >> wavefront_tilt(4.65,1100,75)
67 % >> wavefront_tilt(4.6,1100,75)
68 % >> wavefront_tilt(4.8,1100,75)
69 % >> wavefront_tilt(4.9,1100,75)
70 %%%%
```

# APPENDIX F

# DSA response function

In principle the transient voltage displayed on the fast scope is down scaled by the transfer function or impulse response of the system. The simulation by itself does not account the impulse response or capacitive coupling of the detection systems (such as, SMA cables, attenuators, and the fast digital scope). Hence there are two approaches to scale the simulated transient voltage with the experimentally measured voltage signals by accounting the impulse responses of the system: (1) The first approach is to represent the impulse response of the system by a simple low pass filters. (2) The second approach is convolution of the voltage transient at the sample position with an impulse response of the system. The impulse response is represented by a Gaussian envelope having the same pule width with the measured transient voltage pulses.

### F.0.1   Capacitive coupled signal

In this approach, all the responses including the impedance mismatch of the SMA cable from the detector head to the oscilloscope, and the impulse response of the oscilloscope can be represented by a second order RCR low pass filter. As discussed in Chapter 7 transient voltage at the sample position is simply the transmitted field multiplied by the pitch size (THz spot), $V_{sample} = E_t * d$.

Figure F.1 shows a schematic representation of second order RCR low pass filter representing the impulse response of the oscilloscope. As illustrated in Fig. F.1 the voltage induced at the sample is filtered by the capacitive coupled circuit after propagating through the SMA cable that connected the detector to the scope. $V_{in}$ represents the input voltage from the sample position, $V_{in} = V_{sample}$, and $V_{out}$ represents the output voltage at the oscilloscope position. Thus, the scaling factor of the displayed signal on the oscilloscope
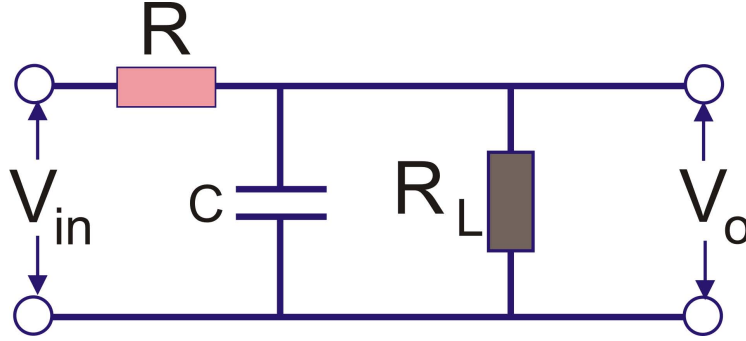
Figure F.1: Low pass filter represents the impulse response of the digital oscillo-scope. $V_{in}$ is the input signal, that is the voltage signal at the sample position, $V_{in}$ = $E_{tr} * d$, and $V_{out}$ is the capacitive signal displayed on the scope.

with respect to the signal at the sample position is then determined in a frequency or time domain. In frequency domain, the analytical equivalent out put signal after the low pass filter is given by:-

$$V_0(\omega) = \frac{1}{2 + j\omega RC} V_{in} \tag{F.1}$$

and in time domain

$$RC\frac{dV_0(t)}{dt} = V_{in}(t) - 2V_0(t) \tag{F.2}$$

Once the capacitive signal is determined, the shape of the displayed signal on the oscilloscope can be retrieved by convolving the capacitive coupled signal with the impulse response of the scope. Figure F.2 shows an example of a capacitive coupled electric fields calculated using 200 kV/cm incident field by both the frequency and time domain equations, Eq. F.1 and Eq. F.2, respectively. Thus, to calculate both $V_{in}$ and $V_{out}$ in Fig. F.1, all the signals displayed in Fig. F.2 should be multiplied by the pitch size of the detector or roughly by the THz spot diameter at the sample position. Figure F.3 shows the voltage signals simulated at the sample position and the corresponding capacitive coupled signal at the oscilloscope. The temporal shape of the capacitive coupled signal calculated based on a simple RCR low pass filter doesn't resemble the experimentally measured voltage transients. The simple RCR low pass filter doesn't completely represent the impulse response of the oscilloscope as well as the impedance mismatch between coaxial cables with the system.
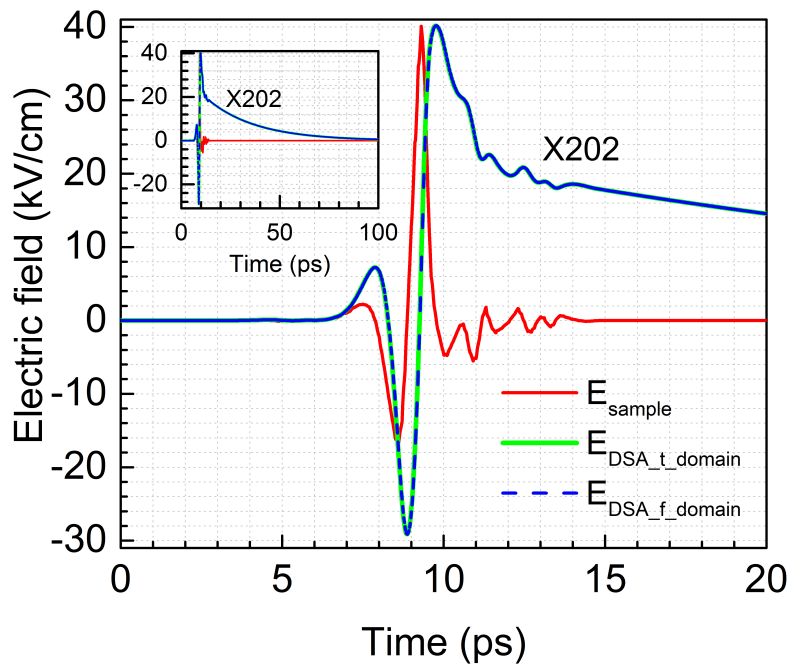
Figure F.2: Red signal is the calculated transmitted field using an input THz field of 200 kV/cm. The blue and and green signals are the capacitive coupled signals calculated using Finite Difference in frequency and time domain after scaled by 202, respectively. The inset show the corresponding long term.
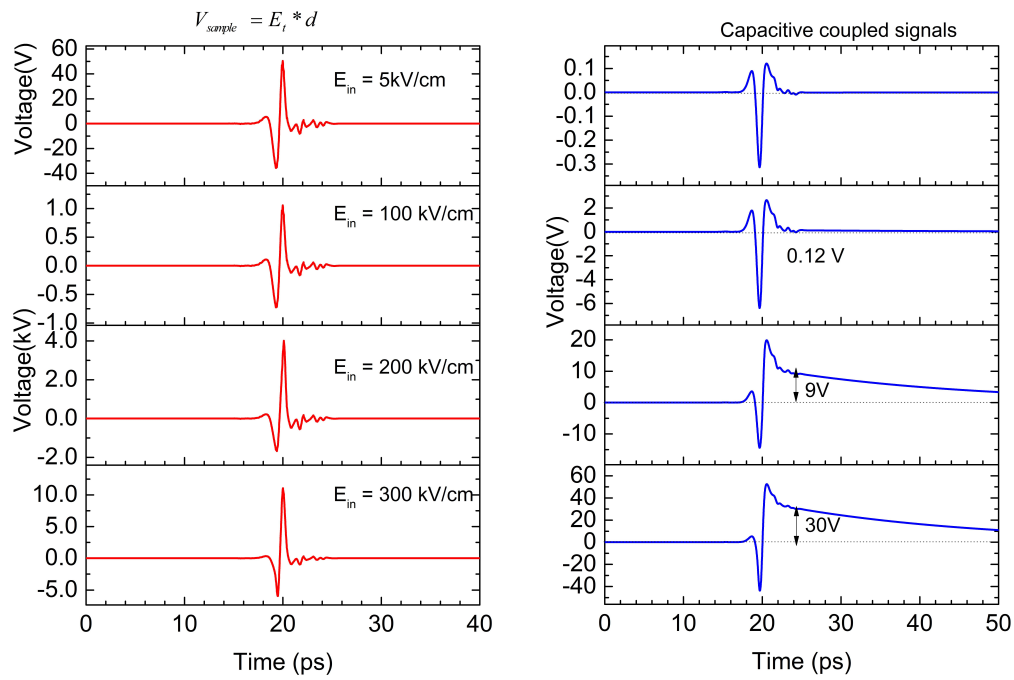
Figure F.3: The left panel plot is the calculated voltage transients at the sample position using the incident field shown in each plot. The right hand side plot is the corresponding capacitive coupled voltage signals, evaluated using a time domain calculation given in Eq. F.2.

## F.0.2 Adjustment of the amplitude of Gaussian response using step function

For the fitting a Gaussian pulse envelope with pulse duration equivalent to experimentally measured transient voltage pulses are chosen to perform the convolution. This voltage pulse should be convoluted with the impulse response of the fast scope to retrieve the shape and magnitude of the calculated voltage pulse to experimentally measured voltage pulse. The impulse response represented by the Gaussian function is given by

$$G(t) = \frac{1}{2\sigma\sqrt{2\pi}} exp\left\{-\frac{1}{2}\left(\frac{t-\mu}{\sigma}\right)^2\right\}$$
(F.3)

where $\sigma = \frac{FWHM}{\sqrt{2ln2}}$, and $\mu$ is the center of the peak. Interms of FWHM, the Gaussian function becomes:-

$$G(t) = \frac{2}{FWHM}\sqrt{\frac{ln2}{\pi}} exp\left\{-4ln2\left(\frac{t-\mu}{FWHM}\right)^2\right\}$$
(F.4)

We need to normalize Eq. F.4 by the time resolution, dt, to get the same peak with the step function after convolution with Gaussian response. That is given by

$$dG(t) = dt\left(\frac{2}{FWHM}\sqrt{\frac{ln2}{\pi}}\right) exp\left\{-4ln2\left(\frac{t-\mu}{FWHM}\right)^2\right\}$$
(F.5)

The validity of the impulse response represented by the Gaussian function is checked by convolving with a step function of magnitude unity. Convolution of the Gaussian pulse given by Eq. F.5 with a step function gives the same amplitude as shown in Fig. F.4 and F.5.
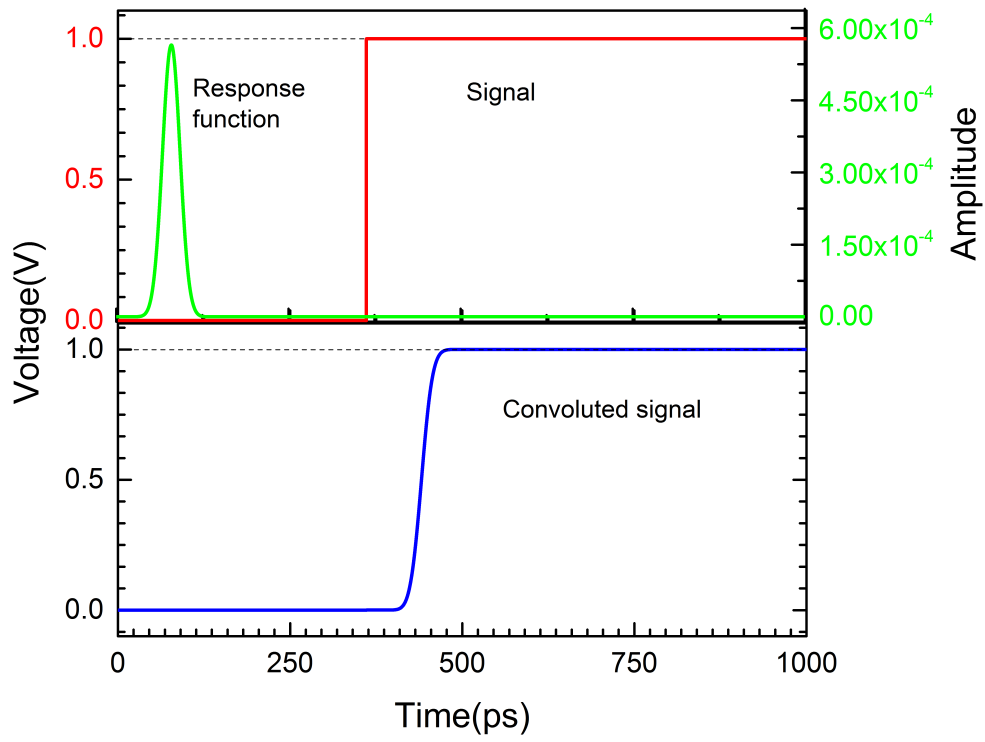
Figure F.4: Convolution of the test Gaussian response with a step function of amplitude unity. Green signal is the response function and red signal is the step function with amplitude of unity. Blue line signal is the result of response function convoluted with the step function.
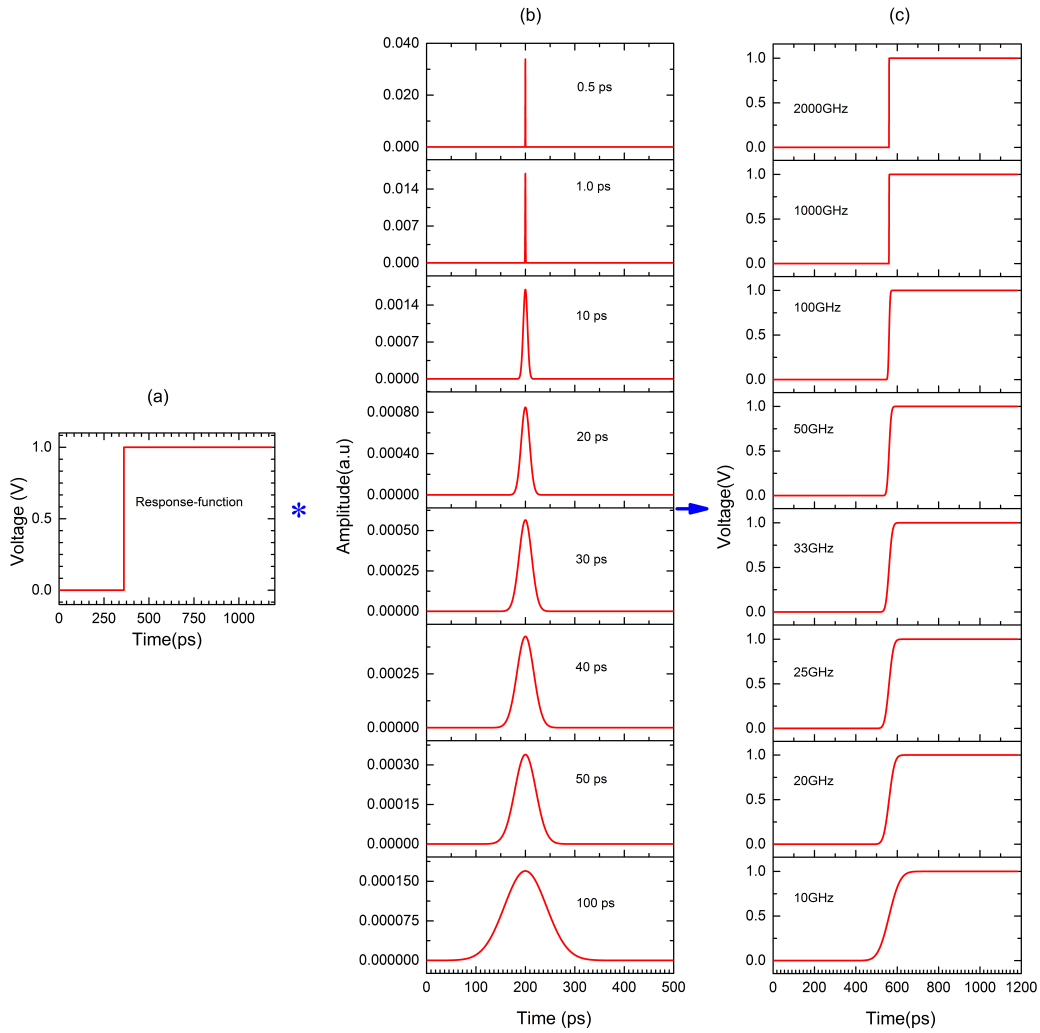
Figure F.5: A step function of magnitude 1 convoluted with different pulse duration of impulse response. (a) Response step function with amplitude of 1 V. (b) Different pulse width of Gaussian signals convoluted with a step function of peak voltage 1V in (a) always gives a convoluted signal peak of 1V. (c) Convoluted voltage signals of (a) and (b)

## F.1 Dynamic intervalley electron matlab Code

The following Matlab code is used to simulate the nonlinear Transient voltage induced in doped-and photoexcited semiconductors using a single electron Drude dynamic intervalley model.

```matlab
1  function ...
       [Integ_J,Integ_Jn1,Integ_v_g1,Integ_v_g2,Integ_v_g,Integ_E,Integ_Eem,E,Eem,r12,v1, ...
       v2,vd,n1,en1,en2,t,current,pk_pk,Eempkpk]= voltage_stuffkvector_main(Et,peak)
2
3  %─────────────────── constants─────────────────────────────
4         e0 = 1.60217653e-19;
5         me = 9.109389e-31;
6
7         kB = 1.380658e-23;
8         T0 = 300;
9
10          c = 3e8;
11         h0 = 1.054572e-34;
12 %───────────────────sample parameters ─────────────────────
13         m1 = 0.04*me;% m1 = 0.037*me;      %m1=0.037*me
14         m2 = 0.26*me;
15
16      n_InP = 3.001;
17
18    d_thick = 5e-7;           %film thickness
19         Z0 = 377;            %impedance of free space
20 n_electron = 2e24;
21   switch_intervalley = 0;%w  hen switch_intervalley=0, it is switched as drude ...
          model
22 intervalley_velocity = 1;%when intervalley_velocity = 0; that is linear case
23 format long;               % Display extra precision for example up to 6 decimal ...
      places
24
25
26 %%% EXPERIMENTALLY DETERMINED PARAMETERS FOR InGaAs SAMPLE BY LUYBOV
27 %%% TAU = 200 fs INSTEAD OF TAU = 100 fs AND CARRIER DENSITY = 1.13e18 cm^3
28 %%% m* = 0.04me
29
30
31 %───────────────nonparabolic is taken into account─────────────────
32 %nonparabolic parameters: T valley: a1=1.33eV-1; L valley: a2=0.59eV-1
33 % %
34 a1 = 1.33/e0;    % 1.33eV-1, 1.167 should be 1.686125454545454/e0
35 a2 = 0.59/e0;    % if a1 and a2 is zero, it is parabolic energy valley
36
```

```matlab
37   %   a1 = 0.0/e0;    % 1.33eV—1, 1.167 should be 1.686125454545454/e0
38   %   a2 = 0.0/e0;
39
40   %===========calculated as dt = (Et(20000,1)—Et(1,1))/20000=================
41
42     dt = (9.0114172e—4)*1e—12;%P8interpNorm,  & p8smoothed
43   %%%%%%%% Au—CONTACTED DATA BEST FITTING PARAMETERS : ne=2x 10^18 cm^—3 AND
44        enth = 0.165*e0;   %enth—2%enth = 0.1617  ===enth+2%enth = 0.1683; ...
                enth+5%enth = 0.17325
45           b = 0.76*enth;  %0.798
46       tp120 = 0.03e—12;          tp21 = 4e—12;    %intervalley momentum ...
             scattering rate
47       tn120 = tp120;             tn21 = tp21;       %intervalley electron ...
             population scattering rate
48   %    te120 = 2*tp120;te21=tp21;                   %intervalley energy ...
         scattering rate
49
50   %————————————————intravalley momentum scattering rate————————————————
51        tp11 = 0.10e—12; % 0.10e—12 highfield;   0.4ps lowfield          ...
             %tp11 G—valley scattering rate
52        tp22 = 0.6*tp11; % tp22 = 0.060e—12;
53   % % *****************************Au_contacted*************************
54    b1 = 0.1*e0;
55    b2 = 0.1*e0;
56   BB1 = (0.5/tn120)/((—3*b^3)*(—b—2*b1)*(3*b+2*b1)*(—b—2*b1—2*b2)*(3*b+2*b1+2*b2));
57   %————————————————————————————————————————————————————————————————————
58          j0 = length(Et);  %the length of vector for incident pulse
59   E_incident = 1e5*peak*Et; %the input electric field is normalized, peak is the ...
         peak with kV/cm units
60                          %1e5 is to convert to V/m
61                          %Since the input is normalized then it should ...
                             multiplied by peak
62          sigma_dc = n_electron*e0^2*tp11/m1;
63     %====================for THz pulse propagating from air to film to
64          tf_lowfield = 2/(n_InP+1+Z0*sigma_dc*d_thick); % electric field ...
             transmission through epilayer
65                 E = E_incident*tf_lowfield;           % electric pulse inside ...
                     sample
66            %E_tsub = 2*n_InP/(1+n_InP)*E;
67            %E_tsub = (2*n_InP)/(1+n_InP))*tf_lowfield*E_incident;
68        tf_filmandsub = tf_lowfield*2*n_InP/(1+n_InP);   % Transmission from film ...
             to substrate
69
70   inside_electricfield = tf_lowfield*peak;           % estimate the inside ...
         the electric field before calculation
71   'the electric field inside sample is (unit kV/cm):'
72   inside_electricfield
73   %%%%%%%%%%%%%%%%%%%%%%%%%%%%%%%%%%%%%%%%%%%%%%%%%%%%%%%%%%%%%%%%%%%%%%%%%
```

```matlab
74 %—————————————————————————————————————————
75 %index 1 is Gamma valley parameters; index 2 is L valley parameters;
76 %—————————————————————————————————————————
77 %veloccity, v1 correspond to Gamma valley velocity, v2 is L valley velocity
78       Y1 = 1/377;
79    Yplus = Y1+Y1*n_InP;
80 %      E = (1/Yplus)*(2*Y1*(E_incident)); % J = 0 to start with
81        E = (1/Yplus)*(2*Y1*(E_incident—E_incident));
82      Eem = E—E_incident;
83
84       v1 = E—E; %v1(1)=zeros(1,j0+1)
85       v2 = v1;
86       vd = v1;
87      nv2 = v1;   %nv2 is n2*v2
88 %population
89       n1 = 0.999999999999999+v1;
90 %scattering function
91      r12 = v1;   %G—L valley scattering rate
92 %electron average energy
93      en0 = 1.5*kB*T0;
94      en1 = v1+en0;
95      en2 = v1+en0;
96       T1 = en1;
97       T2 = en2;
98
99 h0k1 = sqrt(2*m1*en1.*(1+a1*en1)); %p1 G—valley
100 h0k2 = sqrt(2*m2*en1.*(1+a2*en2)); %p2 L—valley
101
102 %============nonparabolical effective masses for G & L valleys============
103      nm1 = v1+m1;
104      nm2 = v2+m2;%should be v1 + m2
105     nm1x = v1+m1;
106     nm1y = nm1x;
107     nm2x = v1+m2;
108     nm2y = v2+m2;
109 %————————————————————differential variable————————————————————
110   diff_v1 = v1;
111  diff_nv2 = v1;
112   diff_v2 = v1;
113  diff_en1 = v1;
114  diff_en2 = v1;
115   diff_p1 = v1*m1;
116   diff_p2 = v2*m2;
117 momentum1 = v1*m1;
118 momentum2 = v1*m2;
119 %       p1 = h0*kk1;
120 %       p2 = h0*kk2;
121        p1 = v1.*h0k1;
```

```matlab
122         p2 = v1.*h0k2;
123   momentum = momentum1;
124    current = v1;
125       v_g1 = v1;
126       v_g2 = v1;
127        v_g = v1;
128      E_rad = v1;
129          d = 0.1;%separation of gold strips in cm
130   %————————————————starting the calculation——————————————————————
131      t = 0.0:dt*1e12:(j0—1)*dt*1e12; %the incident pulse is delayed by 0.8 ps ...
             by substrate
132                                  %save ttt.mat t
133     Integ_J = 0; % used to initialize the integeral of Current density
134    Integ_Jn1 = 0; % used to initialize the integeral of the product of carrier ...
          density and velocity
135   Integ_v_g1 = 0;
136   Integ_v_g2 = 0;
137    Integ_v_g = 0;
138      Integ_E = 0;
139    Integ_Eem = 0;
140        Epeak = 0;
141           ti = 0.0;
142       tf = (j0—1)*dt*1e12;
143      % here t is in ps
144   for j = 1:j0—1; % with the initialization parameters @ t0 it becomes a total ...
        of 20000 pts
145       current(j) = —(n1(j)*n_electron*e0*v1(j))—(n_electron*e0*(1—n1(j))*v2(j));
146         E_rad(j) = current(j)*d/(2*Y1); %RADIATIED FIELD REF. PRL ——
147           Integ_J = Integ_J + current(j)*dt;
148   %————————————————for THz pulse propagating from air to film to substrate——————
149             E(j) = (1/Yplus)*(2*Y1*E_incident(j)—d_thick*current(j)); %IN V/m
150           Integ_E = Integ_E+E(j); %IN V/m
151   % if E>Epeak
152   %      Eempkpk ;
153   % else
154   %     Epeak =Epeak
155   %             Epeak = max
156   %%%%%%%%%%%%%%%%%%%%%%%%%%%%%%%EMITTED FIELD%%%%%%%%%%%%%%%%%%%%%%%%%%%%%%%%%%%%%%
157   % E_incident(j)
158      Eem(j) = (E(j)—E_incident(j));
159    % Eem(j) = E_incident(j)—E(j); %emitted field is transmitted field minus ...
          insident field J(t) = —env(t)=—2Eem(t)/(Z0*d)
160   Integ_Eem = Integ_Eem + Eem(j);
161   %———————————————————————effective mass aclculation——————————————————
162         nm1(j) = m1*(1+a1*(en1(j)—1.5*kB*T0));
163         nm2(j) = m2*(1+a2*(en2(j))—1.5*kB*T0);
164   %————————————————————————An isotropic——————————————————————
165   % nm1x(j)=m1*(1+2*a1*(en1(j)—1.5*kB*T0));
```

```matlab
166  % nm1y(j)=m1*(1+2*a1*(en1(j)-1.5*kB*T0))^3;
167  %
168  % nm2x(j)=m1*(1+2*a2*(en2(j)-1.5*kB*T0));
169  % nm2y(j)=m1*(1+2*a2*(en2(j)-1.5*kB*T0))^3;
170  %---------------------------Kinetic Energy NON-PARABOLIC--------------------------
171  %          en1(j) = ((sqrt(1+2*a1*p1(j)^2/m1)-1)/(2*a1))+1.5*kB*T0;
172  %          en2(j) = ((sqrt(1+2*a2*p2(j)^2/m2)-1)/(2*a2))+1.5*kB*T0;
173   %%%%%%%%%%%%%%%%%%%%%%%%%MAIN%%%%%%%%%%%%%%%%%%%%%%%%%%%%%%%%%%%%%
174        en1(j) = ((sqrt(1+2*a1*p1(j)^2/nm1(j))-1)/(2*a1))+1.5*kB*T0;
175        en2(j) = ((sqrt(1+2*a2*p2(j)^2/nm2(j))-1)/(2*a2))+1.5*kB*T0;
176  %+++++++++++++++++++FOR PARABOLIC a1 = 0, and a2 = 0; +++++++++++++++++++
177  %
178  %        en1(j) = (p1(j)^2/(2*nm1(j)))+1.5*kB*T0; % nm1(j) = m1
179  %        en2(j) = (p2(j)^2/(2*nm2(j)))+1.5*kB*T0; % nm2(j) = m2
180  %        en1(j+1) = (p1(j+1)^2/(2*nm1(j+1)))+1.5*kB*T0; % nm1(j) = m1
181  %        en2(j+1) = (p2(j+1)^2/(2*nm2(j+1)))+1.5*kB*T0; % nm2(j) = m2
182  %        en1(j) = (p1(j)^2/(2*m1))+1.5*kB*T0;
183  %        en2(j) = (p2(j)^2/(2*m2))+1.5*kB*T0;
184  %        en2(j) = 1/2*nm2(j)*v2(j)^2+1.5*kB*T0;
185
186  %++++++++++++++++++++WAVE VECTOR FOR G & L VALLEY++++++++++++++++++++++++
187           h0k1(j) = sqrt(2*m1*en1(j)*(1+a1*en1(j)));
188           h0k2(j) = sqrt(2*m2*en2(j)*(1+a2*en2(j)));
189  %         vd(j) = n1(j)*v1(j)+nv2(j);%calculate the average velocity
190  %           vd(j) = n1(j)*v1(j)+(1-n1(j))*v2(j);
191          r12(j) = inter_scattering(en1(j),enth,b,tn120);%calculate the ...
                intervalley scattering rate
192  %     p1(j)=h0k1(j);
193  %     p2(j)=h0k2(j);
194  %===============calculate G valley carrier momentum====================
195          t1 = (intervalley_velocity*r12(j)...
196                +switch_intervalley*((1-n1(j))/n1(j))*(1/tn21));
197  diff_p1(j) = -e0*E(j)-p1(j)*(1/tp11+t1);
198          k1 = dt*diff_p1(j);
199          k2 = dt*(-e0*E(j)-(p1(j)+1/2*k1)*(1/tp11+t1));
200          k3 = dt*(-e0*E(j)-(p1(j)+1/2*k2)*(1/tp11+t1));
201          k4 = dt*(-e0*E(j)-(p1(j)+k3)*(1/tp11+t1));
202    p1(j+1) = p1(j)+(1/6)*(k1+2*(k2+k3)+k4);
203  %==========calculate L valley  momentum==================================
204           t2 = intervalley_velocity/tp21;
205    diff_p2(j) = -e0*E(j)-p2(j)*(1/tp22+t2);%-intervalley_velocity/tp21);
206           c1 = dt*diff_p2(j);
207           c2 = dt*(-e0*E(j)-(p2(j)+1/2*c1)*(1/tp22+t2));
208           c3 = dt*(-e0*E(j)-(p2(j)+1/2*c2)*(1/tp22+t2));
209           c4 = dt*(-e0*E(j)-(p2(j)+c3)*(1/tp22+t2));
210
211      p2(j+1) = p2(j)+(1/6)*(c1+2*(c2+c3)+c4);
212  %=====================================================================
```

```matlab
213 %        v1(j+1)  = p1(j)/(nm1(j)*sqrt(1+(2*a1*p1(j)^2)/nm1(j)));
214 %        v2(j+1)  = p2(j)/(nm2(j)*sqrt(1+(2*a2*p1(j)^2)/nm2(j)));
215 %        v1(j+1)  = p1(j)/(nm1(j)*(1+2*a1*en1(j)));
216 %        v2(j+1)  = p2(j)/(nm2(j)*(1+2*a2*en2(j)));
217        v1(j+1)  = p1(j)/(m1*sqrt(1+(2*a1*p1(j)^2)/m1));
218        v2(j+1)  = p2(j)/(m2*sqrt(1+(2*a2*p1(j)^2)/m2));
219      % v2(j+1)  = 0; %Linear case
220        vd(j)  = v1(j)*n1(j) + v2(j)*(1-n1(j));
221 %————————calculate the electron population percentage at G valley—————————
222      n1(j+1) = n1(j)+dt/tn21-n1(j)*dt*(r12(j)+1/tn21);
223 %%&&&&&&&&&&LINEAR CASE^^^^^^^^dn/dt = 0, and ...
        a1=a2=0^^^^^^^^^^^^^^^^^^^^^^^^^^^^^^^^^^^
224    % n1(j+1) = 0.999999999999999;      %      Linear case
225 %%&&&&&&&&&&^^^^^^^^^^^^^^^^^^^^^^^^^^^^^^^^^^^^^^^^^^^^^^^^^^^^^^^^^^^^^^^^^^^^^^^^^
226    Integ_Jn1 = Integ_Jn1 + v1(j)*n1(j)*e0;
227   Integ_v_g1 = Integ_v_g1 + v1(j)*n1(j)*e0;
228 %   end
229   Integ_v_g2 = Integ_v_g2 + v2(j)*(1-n1(j))*e0;
230    Integ_v_g = Integ_v_g + vd(j)*e0;
231 end
232    pk_pk = max(E)+abs(min(E));
233 % %   Eempkpk = max(E-E_incident)+ abs(min(E-E_incident)); %emitted field
234   Eempkpk = max(E-E_incident)+ abs(min(E-E_incident)); %emitted field
235     v_g1 = p1./(m1*sqrt(1+2*a1*p1(j).^2/m1));
236     v_g2 = p2./(m2*sqrt(1+2*a2*p1(j).^2/m2));
237     v_g = v1.*n1  + v2.*(1-n1);
238     n2 = 1-n1;
239   save  E_t.mat t n1 n2 Integ_J Integ_E v_g1 v_g2 v_g E Eem current ...
240        en1 en2 h0k1 h0k2 nm1 nm2 E_rad
241
242 save Ev1.mat t n1 n2 E v1 v2 vd en1 en2 r12 h0k1 h0k2 nm1 nm2 E_rad
243 %————————————————————————————end the loop————————————————————————————
244   eletric_inside = peak*max(E)/max(E_incident);
245 %    E_reference = E_incident*(2/(1+n_InP));
246 %       E_radiated_f = E-E_incident;
247 % plot(t,E_radiated_f)
248 % % % % figure(1)
249 % % % % plot(t,E*1e-5)
250 % % % % ylabel('E_{t}(kV/cm)')
251 % % % % set(gcf, 'paperpositionmode','auto','color','white');
252 % % % % ...
       set(gca,'box','on','fontsize',18,'fontweight','normal','linewidth',2,'layer','top')
253 % % % % % grid on
254 % % % % set(gca,'GridLineStyle','-');
255 % % % % % grid on
256 % % % % % grid minor
257 % % % % hold all
258
```

```
259  figure(1)
260   plot(t,n1,t,E/max(E))
261  %plot(t,Eem/max(Eem),t,E/max(E))
262  set(gcf, 'paperpositionmode','auto','color','white');
263  set(gca,'box','on','fontsize',18,'fontweight','normal','linewidth',2,'layer','top')
264  %grid on
265  set(gca,'GridLineStyle','—');
266  % grid on
267  % grid minor
268  hold all
269  % % % figure(2)
270  % % % plot(t,n1,t,1—n1,t,E/max(E))
271  % % %
272  % % % xlim([0 18.25])
273  % % % xlabel('Time(ps)','fontsize',16);
274  % % % ylabel('Normalized E_{t},n_{e}','fontsize',16);
275  % % % set(gcf, 'paperpositionmode','auto','color','white');
276  % % % ...
            set(gca,'box','on','fontsize',18,'fontweight','normal','linewidth',2,'layer','top')
277  % % % % grid on
278  % % % set(gca,'GridLineStyle','—');
279  % % % % grid on
280  % % % % grid minor
281  % % % hold all
282
283  % figure(3)
284  % plot(E_incident,v1/max(v1),E_incident,v1/max(v1))
285  % set(gcf, 'paperpositionmode','auto','color','white');
286  % ...
            set(gca,'box','on','fontsize',18,'fontweight','normal','linewidth',2,'layer','top')
287  % % grid on
288  % set(gca,'GridLineStyle','—');
289  % % grid on
290  % % grid minor
291  % hold all
292  Efield = E*1e—5;
293     v11 = —v1*1e—5;
294     v22 = —v2*1e—5;
295     vdd = vd*1e—5;
296  %————————————intervalley scattering function————————————————
297  function y = inter_scattering(en,enth,b,tn120)
298  e0 = 1.60217653e—19;
299  %——————————————————————————————————————————————————————————
300  %smooth function:
301  %r12=A1(en1—enth)(en1—2b—enth)(en1+2b—enth)(en1—enth+b1)(en1—enth—b1)(en1—e
302  %nth—b2)(en1—enth+b2)+r120/2
303   b1 = 0.1*e0;
304   b2 = 0.1*e0;
```

```
305  BB1 = (0.5/tn120)/((−3*b^3)*(−b−2*b1)*(3*b+2*b1)*(−b−2*b1−2*b2)*(3*b+2*b1+2*b2));
306  %────────────────────────────────────────────────────────
307   if en ≤ (enth−b);      %b=0.57e0
308       y = 0;
309     else
310        if en ≥ (enth+b);
311             y = 1/tn120;
312        else
313          y = ...
                BB1*(en−enth)*(en−enth−2*b)*(en−enth+2*b)*(en−enth−2*b−2*b1)*(en−enth+2*b+2*b1)*(en−enth−2
314        end
315     end
316  %────────────────────────────────────────────────────────
```

## Input functions

Inputs of the smoothed iterated THz pulse, peak THz field ranges, and experimental datas
are loaded in the following Matlab function to compare with the simulation result.

```
1   function input_voltage_stuffkvector_main_main()
2   % % h = actxserver('matlab.application')
3   % %
4   % % % COM.matlab.application
5   % % % To quit MATLAB, type:
6   % % %
7   % % % h.Quit;
8   % creating the automation manually
9   % "C:\Program Files\MATLAB\R2006a\bin\win32\MATLAB.exe /Automation"
10  % hold all
11
12  load p8interpolated_normalized.dat;
13  load p8interpolated.dat;
14  load R_THz_at960nJ_normalized.dat;
15  load T_THzpulse_at960nJ_normalized.dat;
16  load Ref_THzpulse_at960nJ__normalized_time.dat;
17
18  % load sin_gaussian.dat;
19  load Ref_THzpulse_at960nJ.dat;
20  % load input_pulse.dat;
21  load input_pulse1.dat;
22  load testfun_mu9_z14.dat;
23  load pulse_normalized_pos_peak.dat; % it has 2 column
24  load pulse_normalized_neg_peak.dat; % it has 2 column
25
26  %%^^^^^^^^^^^^^^^^^^^^^^^^^^%%%%%%%%%%%%%%%%%%%^^^^^^^^^^^^^^^^^^^^^^^^^%%%%%%%%%%%
```

216

```
27
28  %+++++++++++EXPERIMENTAL DATA+++++++++++++++++++++++++++++++++++++++++++++++
29  load pkpk_n18_MWP_pyro_NoCalibrationF.dat;
30  load pkpk_n18_MWP_scope_NoCalibrationF.dat;
31
32  load pkpk_n18_SMA_DSA_digital_NoCalibrationF.dat;
33  load pkpk_n18_SMA_DSA_scope_NoCalibrationF.dat;
34  load pkpk_n18_SMA_curssor_digital_NoCalibrationF.dat;
35  load pkpk_n18_SMA_curssor_scope_NoCalibrationF.dat;
36
37  load pkpk_n17_SMA_DSA_digital_NoCalibrationF.dat;
38  load pkpk_n17_SMA_DSA_scope_NoCalibrationF.dat;
39  load pkpk_n17_SMA_curssor_digital_NoCalibrationF.dat;
40  load pkpk_n17_SMA_curssor_scope_NoCalibrationF.dat;
41
42  % load PkPk_n18_MWP_extzero_NoCalibrationF.dat;
43  load Expvoltage_NoCalibrationF.dat;
44
45  % load test.dat;
46  %+++++++++++++++++++New experimental dat+++++++++++++++++++++++++++++++++++++
47  load pkpk_n18_may10_NoCalibrationF.dat;
48  load pkpk_n17_may10_NoCalibrationF.dat;
49
50  load pkpk_n17_may19_NoCalibrationF.dat;
51  load pkpk_n18_may19_NoCalibrationF.dat ;
52  %++++++++++++++++++++++++++++++++++++++++++++++++++++++++++++++++++++++++++++
53  load n17MWP_June03_NoCalibrationF.dat; %June 03/04/2012 DATA
54  load n18MWP_June03_NoCalibrationF.dat;
55  %++++++++++++++++++++++++++++++++++++++++++++++++++++++++++++++++++++++++++++
56  %%^^^^^^^^^^^^^^^^^^^%%%%%%%%%%%%%%%%%%%%%%%%^^^^^^^^^^^^^^^^^^^^^^^^^%%%%%%%%%
57  %^^^^^^^^^^^^^^^^^^^^^^^^%%%%%%%%%%%%%%%%%%^^^^^^^^^^^^^^^^^^^^^^^^^^%%%%%%%%%%
58
59  %+++++++++++EXPERIMENTAL DATA+++++++++++++++++++++++++++++++++++++++++++++++
60  load pkpk_n18_MWP_pyro_WithCalibrationF.dat;
61  load pkpk_n18_MWP_scope_WithCalibrationF.dat;
62
63  load pkpk_n18_SMA_DSA_digital_WithCalibrationF.dat;
64  load pkpk_n18_SMA_DSA_scope_WithCalibrationF.dat;
65  load pkpk_n18_SMA_curssor_digital_WithCalibrationF.dat;
66  load pkpk_n18_SMA_curssor_scope_WithCalibrationF.dat;
67
68  load pkpk_n17_SMA_DSA_digital_WithCalibrationF.dat;
69  load pkpk_n17_SMA_DSA_scope_WithCalibrationF.dat;
70  load pkpk_n17_SMA_curssor_digital_WithCalibrationF.dat;
71  load pkpk_n17_SMA_curssor_scope_WithCalibrationF.dat;
72
73  % load PkPk_n18_MWP_extzero_WithCalibrationF.dat;
74  load Expvoltage_WithCalibrationF.dat;
```

```matlab
 75
 76  % load test.dat;
 77  %+++++++++++++++++++New experimental dat+++++++++++++++++++++++++++++++++++
 78  load pkpk_n18_may10_WithCalibrationF.dat;
 79  load pkpk_n17_may10_WithCalibrationF.dat;
 80
 81  load pkpk_n17_may19_WithCalibrationF.dat;
 82  load pkpk_n18_may19_WithCalibrationF.dat ;
 83  %++++++++++++++++++++++++++++++++++++++++++++++++++++++++++++++++++++++++++
 84  load n17MWP_June03_WithCalibrationF.dat; %June 03/04/2012 DATA
 85  load n18MWP_June03_WithCalibrationF.dat;
 86  %++++++++++++++++++++++++++++++++++++++++++++++++++++++++++++++++++++++++++
 87  %%^^^^^^^^^^^^^^^^^^%%%%%%%%%%%%%%%%%%%%%%%%^^^^^^^^^^^^^^^^^^^^^^^%%%%%%%%%
 88  load Au_n18_NoCalibF_June04.dat;
 89
 90
 91  load p8smoothed4000.dat;
 92
 93  %++++++++++++++++++++++++++++++++++++++++++++++++++++++++++++++++++++++++++
 94
 95
 96   Et = p8smoothed4000;
 97
 98  %++++++++++++++++++++++++++++++++++++++++++++++++++++++++++++++++++++++++++
 99
100    a1 = 1.33;
101    a2 = 0.59;
102
103  % ==================Voltage_stuff_Input==================================
104  %%%NONCALIBRATED%%%%%%%%%%%%
105
106        minpeak = 0.0;
107        maxpeak = 250.0;
108   %%%%%%%%%%%%%%%%%%%%%%%%%%%%%%%%%%%%%%%%%%%%%%%%%%%%%%%%%%%%%%%%%%%%%%%%%%%%%
109   %%%WITHCALIBRATED FACTOR%%%%%%%%%%%%%%%%%%%%%%%%%%%%%%%%%%%%%%%%%%%%%%%%%%%%%%
110
111  %        minpeak = 0.0;
112  %        maxpeak = 365.0;
113   %%%%%%%%%%%%%%%%%%%%%%%%%%%%%%%%%%%%%%%%%%%%%%%%%%%%%%%%%%%%%%%%%%%%%%%%%%%%%%
114  %      minpeak = 0.0;
115  %      maxpeak = 350.0;
116   thz_incident = Et;
117
118  ipeak = minpeak:5:maxpeak;
119  %        ipeak(1:41) = 0:5:200;
120              [nn,npeak] = size(ipeak);
121                  E_DCt = zeros(npeak,1);
122
```

```matlab
123
124                     ngamma = [];
125         current_density = []; %current density
126
127                   v_gamma = [];
128             v_satelite = [];
129                 v_drift = [];
130               scat_rate = [];
131 %         Etpad = [];
132
133   tf = 18.021933258280001;    %in picosecond
134   dt1 = 9.0114172e-004;
135   t1 = 0:dt1:tf ;
136
137   tf = 18.021933258280001;     %in picosecond
138   dt2 = tf/999;
139   ti = 0:dt2:tf;
140
141 %   interp1000 = interp1(t1,Etran,ti);
142
143   ti = 0:dt2:tf;
144
145       Etran = []; %transmitted field
146   E_radiated = [];
147         for i = 1:npeak
148
149          peak = ipeak(i);
150
151
152 [Integ_J,Integ_Jn1,Integ_v_g1,Integ_v_g2,Integ_v_g,Integ_E,Integ_Eem,E_tran,E_emi,r_G_L,v_G, ...
        v_L_valley, v_drif, n_gamma,time,Jcurrent,Et_pkpk,Eempkpk]= ...
        voltage_stuffkvector_main(Et,peak);
153 %
154 %                    Etran = [Etran E_tran/max(E_tran)];
155             interp1000i = interp1(t1,E_tran,ti);% To interpolate 20000 data ...
                  points to 1000 data points
156             Etran = [Etran interp1000i'];
157 %                Etran = [Etran E_tran];
158
159             interp1000ii = interp1(t1,E_emi,ti);
160             E_radiated = [E_radiated interp1000ii'];
161             % E_radiated = [E_radiated E_emi];
162
163             ngamma = [ngamma n_gamma];
164
165      ngammaMax = max(ngamma);
166      ngammaMin = min(ngamma);
167
```

```matlab
168
169          peaktopeakngamma = ngammaMax + abs(ngammaMin);
170                    n1pkpk = peaktopeakngamma';
171  %
172          current_density = [current_density Jcurrent];
173
174                  sum_E(i) = Integ_E;
175
176              sum_Eem(i) = Integ_Eem;
177
178                sum_V(i) = Integ_J;
179              sum_Jn(i) = Integ_Jn1;
180
181            sum_v_g1(i) = Integ_v_g1;
182            sum_v_g2(i) = Integ_v_g2;
183             sum_v_g(i) = Integ_v_g;
184
185             Etr_peak(i) = Et_pkpk*10^-5; %in kV/cm
186             Eem_pkpk(i) = Eempkpk;
187
188                 v_gamma = [v_gamma v_G];
189              v_satelite = [v_satelite v_L_valley ];
190                 v_drift = [v_drift v_drif];
191               scat_rate = [scat_rate r_G_L];
192
193
194       EtranMax = max(Etran);
195       EtranMin = min(Etran);
196
197
198    peaktopeakEtran = EtranMax + abs(EtranMin);
199
200             n1pkpk = peaktopeakEtran'; % Peak to peak of transmitted field
201
202          end
203           integration_J = [ipeak' sum_V'];
204          integration_Jn = [ipeak' sum_Jn'];
205
206         integration_vg1 = [ipeak' sum_v_g1'];
207         integration_vg2 = [ipeak' sum_v_g2'];
208          integration_vg = [ipeak' sum_v_g' ];
209
210  %        integration_E = [ipeak' sum_E'];%% in V/m
211           integration_E = [ipeak' 1e-3*sum_E'];%% in V/m , 1e-3 is the 1mm gap ...
                 of the MWP convert to meter
212       % integration_E = [Etr_peak' sum_E']; %% in V
213
```

```matlab
214         integration_Eem = [ipeak' 1e-3*sum_Eem'];%% in V/m , 1e-3 is the 1mm ...
                gap of the MWP convert to meter
215
216 %         transm_field = [time' Etran*1e-3]; % FACTOR OF 1E-5 IS TO CHANGE TO ...
       V, because 1e-3m = 1mm gap of the MWP detector
217         transm_field = [ti' Etran*1e-3]; % FACTOR OF 1E-3 IS TO CHANGE TO V
218
219         radiated_field = [ti'  E_radiated*1e-3];
220
221         currentdensity = [time' current_density];
222         carrierdensity = [time' ngamma];
223
224             Edrivepeak = [ipeak' Etr_peak'];
225                 pkpkEem = [ipeak' Eem_pkpk'];
226
227             Gamma_v = [time' v_gamma*1e-5];   % factor 1e-5 is in cm/s
228                 L_v = [time' v_satelite*1e-5];
229             drift_v = [time' v_drift*1e-5];
230         scattering_rate = [time' scat_rate*1e-13]; % factor 1e-13 is the ...
                scattering rate in 1e-13
231 %                 dt = (9.0114172e-004);
232
233 %+++++++++++++++++++NORMALIZATION++++++++++++++++++++++++++++++++++++++++++
234
235         IntegEx = integration_E(:,1);
236 %       IntegEy = integration_E(:,2)*max(test(:,2))/max(integration_E(:,2));
237 %         testx = test(:,1)*maxpeak/max(test(:,1));
238 %         testy = test(:,2);
239 %+++++++++++++++++++++PLOT+++++++++++++++++++++++++++++++++++++++++++++++++
240
241 %++++++++++++++++++++++++++++++++++++++++++++++++++++++++++++++++++++++++++
242 %++++++++++++++++++++++++++++++++++++++++++++++++++++++++++++++++++++++++++
243
244     save IntegralE.mat integration_E transm_field radiated_field currentdensity...
245         sum_V  sum_Jn sum_v_g1 sum_v_g2 sum_v_g...
246         integration_J integration_Jn integration_vg1...
247         integration_vg2 integration_vg carrierdensity pkpkEem...
248         Gamma_v L_v drift_v scattering_rate  integration_Eem
249
250 %++++++++++++++++++++++++++++++++++++++++++++++++++++++++++++++++++++++++++
251 %++++++++++++++++++++++++++++++++++++++++++++++++++++++++++++++++++++++++++
252
253 % %+++++++++++NORMALIZE X-AXIS OF EXPERIMENTAL DATA 10^18cm^-3+++++++++++++
254
255         IncidentPeak = integration_E(:,1);
256             IncidJ = integration_J(:,1);
257
```

```
258          Expvoltage_NoF = ...
                 Expvoltage_NoCalibrationF(:,1)*max(IncidentPeak)./(max(Expvoltage_NoCalibrationF(:,1)));
259        Expvoltage_WithF = ...
                 Expvoltage_WithCalibrationF(:,1)*max(IncidentPeak)./(max(Expvoltage_WithCalibrationF(:,1)));
260
261  %++++++++++++++++++++++++++++++++++++++++++++++++++++++++++++++++++++++++
262  %    MWP_n18_PyroMay10  = ...
         pkpk_n18_may10(:,1)*max(IncidentPeak)./max(pkpk_n18_may10(:,1));
263  %     MWP_n18_PyroMay19 = ...
         pkpk_n18_may19(:,1)*max(IncidentPeak)./max(pkpk_n18_may19(:,1));
264
265                  %NoF = no correction factor
266                 %WithF = with correction factor 1.5
267     MWP_n18_PyroMay10_NoF  = pkpk_n18_may10_NoCalibrationF(:,1);    %THz field ...
            max is 232kV/cm
268      MWP_n18_PyroMay19_NoF  = pkpk_n18_may19_NoCalibrationF(:,1);    %THz field ...
            max is 243kV/cm
269
270   MWP_n18_PyroMay10_withF  = pkpk_n18_may10_WithCalibrationF(:,1);   %THz field ...
          max is 348kV/cm
271    MWP_n18_PyroMay19_withF = pkpk_n18_may19_WithCalibrationF(:,1);   %THz field ...
          max is 365kV/cm
272  %++++++++++++++++++++++++++++++++++++++++++++++++++++++++++++++++++++++++
273  %           MWP_n18_Pyro = ...
         pkpk_n18_MWP_pyro(:,1)*max(IncidentPeak)./max(pkpk_n18_MWP_pyro(:,1));
274  %          MWP_n18_scope = ...
         pkpk_n18_MWP_scope(:,1)*max(IncidentPeak)./max(pkpk_n18_MWP_scope(:,1));
275
276          MWP_n18_Pyro_NoF = pkpk_n18_MWP_pyro_NoCalibrationF(:,1);     %THz ...
               field max is 210kV/cm
277          MWP_n18_scope_NoF = pkpk_n18_MWP_scope_NoCalibrationF(:,1);    %THz ...
               field max is 197kV/cm
278
279         MWP_n18_Pyro_WithF = pkpk_n18_MWP_pyro_WithCalibrationF(:,1);  %THz ...
               field max is 315kV/cm
280        MWP_n18_scope_WithF = pkpk_n18_MWP_scope_WithCalibrationF(:,1); %THz ...
               field max is 296kV/cm
281
282       %  MWP_n18_PyroNew = ...
             Newdata_10_18cm_3(:,1)*max(IncidentPeak)./max(Newdata_10_18cm_3(:,1));
283
284  %       SMA_n18_CursPyro = ...
         pkpk_n18_SMA_curssor_digital(:,1)*max(IncidentPeak)./max(pkpk_n18_SMA_curssor_digital(:,1));
285  %       SMA_n18_CursScope = ...
         pkpk_n18_SMA_curssor_scope(:,1)*max(IncidentPeak)./max(pkpk_n18_SMA_curssor_scope(:,1));
286  %
287  %       SMA_n18_DSA_Pyro = ...
         pkpk_n18_SMA_DSA_digital(:,1)*max(IncidentPeak)./max(pkpk_n18_SMA_DSA_digital(:,1));
```

```matlab
288  %      SMA_n18_DSA_scope = ...
        pkpk_n18_SMA_DSA_scope(:,1)*max(IncidentPeak)./max(pkpk_n18_SMA_DSA_scope(:,1));
289
290    SMA_n18_CursPyro_NoF = pkpk_n18_SMA_curssor_digital_NoCalibrationF(:,1);
291   SMA_n18_CursScope_NoF = pkpk_n18_SMA_curssor_scope_NoCalibrationF(:,1);
292
293    SMA_n18_DSA_Pyro_NoF = pkpk_n18_SMA_DSA_digital_NoCalibrationF(:,1);
294   SMA_n18_DSA_scope_NoF = pkpk_n18_SMA_DSA_scope_NoCalibrationF(:,1);
295
296  SMA_n18_CursPyro_WithF = pkpk_n18_SMA_curssor_digital_WithCalibrationF(:,1);
297 SMA_n18_CursScope_WithF = pkpk_n18_SMA_curssor_scope_WithCalibrationF(:,1);
298
299  SMA_n18_DSA_Pyro_WithF = pkpk_n18_SMA_DSA_digital_WithCalibrationF(:,1);
300 SMA_n18_DSA_scope_WithF = pkpk_n18_SMA_DSA_scope_WithCalibrationF(:,1);
301
302 %%%FOR AU-CONTACT FITTING ETH = 0.2eV
303
304         Au_n18_june04 = Au_n18_NoCalibF_June04(:,1);
305       pkpk_n18_Au_cont = Au_n18_NoCalibF_June04(:,2);
306
307 %  MWP_n18_PyroMay10 = ...
        pkpk_n18_may10(:,1)*max(IncidentPeak)./max(pkpk_n18_may10(:,1));
308 %  MWP_n18_PyroMay19 = ...
        pkpk_n18_may19(:,1)*max(IncidentPeak)./max(pkpk_n18_may19(:,1));
309
310   % % =================NORMALIZED Y-AXIS OF CALCULATED DATA================
311 % %         IntegJ = ...
        -integration_J(:,2)*max(pkpk_n18_MWP_pyro(:,2))./max(-integration_J(:,2));
312      IntegExpvoltage = ...
            integration_E(:,2)*max(Expvoltage_NoCalibrationF(:,2))./max(integration_E(:,2));
313
314 %++++++++++++++++++++++++++Integral of J++++++++++++++++++++++++++++++++++++
315         IntegJMWP = ...
                integration_J(:,2)*max(pkpk_n18_MWP_pyro_NoCalibrationF(:,2))./max(integration_E(:,2));
316
317      IntegExpvoltage = ...
            integration_E(:,2)*max(Expvoltage_WithCalibrationF(:,2))./max(integration_E(:,2));
318
319 %++++++++++++++++++++++++++Integral of J++++++++++++++++++++++++++++++++++++
320         IntegJMWP_WithF = ...
                integration_J(:,2)*max(pkpk_n18_MWP_pyro_WithCalibrationF(:,2))./max(integration_E(:,2));
321
322
323 %++++++++++++++++++++++++++10^18 cm-^3 May 10 and 19++++++++++++++++++++++++
324 %    IntegMWP_n18_PyroMay10 = ...
        integration_E(:,2)*max(pkpk_n18_may10(:,2))./max(integration_E(:,2));
325 %    IntegMWP_n18_PyroMay19 = ...
        integration_E(:,2)*max(pkpk_n18_may19(:,2))./max(integration_E(:,2));
```

```
326
327        IntegMWP_n18_PyroMay10_NoF = pkpk_n18_may10_NoCalibrationF(:,2);
328        IntegMWP_n18_PyroMay19_NoF = pkpk_n18_may19_NoCalibrationF(:,2);
329
330     IntegMWP_n18_PyroMay10_WithF = pkpk_n18_may10_WithCalibrationF(:,2);
331     IntegMWP_n18_PyroMay19_WithF = pkpk_n18_may19_WithCalibrationF(:,2);
332
333 %++++++++++++++++++++++++++Integral of transmitted field++++++++++++++++++++
334 %         IntegEMWP_pyro = ...
        integration_E(:,2)*max(pkpk_n18_MWP_pyro(:,2))./max(integration_E(:,2));
335 %         IntegEMWP_scope = ...
        integration_E(:,2)*max(pkpk_n18_MWP_scope(:,2))./max(integration_E(:,2));
336
337      IntegEMWP_pyro_NoF = pkpk_n18_MWP_pyro_NoCalibrationF(:,2);
338      IntegEMWP_scope_NoF = pkpk_n18_MWP_scope_NoCalibrationF(:,2);
339
340      IntegEMWP_pyro_WithF = pkpk_n18_MWP_pyro_WithCalibrationF(:,2);
341     IntegEMWP_scope_WithF = pkpk_n18_MWP_scope_WithCalibrationF(:,2);
342
343 %   IntegSMA_CursPyro = ...
        integration_E(:,2)*max(pkpk_n18_SMA_curssor_digital(:,2))./max(integration_E(:,2));
344 %   IntegSMA_CursScope = ...
        integration_E(:,2)*max(pkpk_n18_MWP_curssor_scope(:,2))./max(integration_E(:,2));
345
346 %   IntegSMA_CursPyro = ...
        integration_E(:,2)*max(pkpk_n18_SMA_curssor_digital(:,2))./max(integration_E(:,2));
347 %   IntegSMA_CursScope = ...
        integration_E(:,2)*max(pkpk_n18_SMA_curssor_scope(:,2))./max(integration_E(:,2));
348 %
349 %   IntegE_SMA_DSApyro = ...
        integration_E(:,2)*max(pkpk_n18_SMA_DSA_digital(:,2))./max(integration_E(:,2));
350 % IntegE_SMA_DSAScope = ...
        integration_E(:,2)*max(pkpk_n18_SMA_DSA_scope(:,2))./max(integration_E(:,2));
351
352     IntegSMA_CursPyro_NoF = pkpk_n18_SMA_curssor_digital_NoCalibrationF(:,2);
353    IntegSMA_CursScope_NoF = pkpk_n18_SMA_curssor_scope_NoCalibrationF(:,2);
354
355     IntegE_SMA_DSApyro_NoF = pkpk_n18_SMA_DSA_digital_NoCalibrationF(:,2);
356    IntegE_SMA_DSAScope_NoF = pkpk_n18_SMA_DSA_scope_NoCalibrationF(:,2);
357
358
359    IntegSMA_CursPyro_WithF = pkpk_n18_SMA_curssor_digital_WithCalibrationF(:,2);
360   IntegSMA_CursScope_WithF = pkpk_n18_SMA_curssor_scope_WithCalibrationF(:,2);
361
362   IntegE_SMA_DSApyro_WithF = pkpk_n18_SMA_DSA_digital_WithCalibrationF(:,2);
363  IntegE_SMA_DSAScope_WithF = pkpk_n18_SMA_DSA_scope_WithCalibrationF(:,2);
364
365
```

```matlab
366 %  %+++++++++++++++++++++PLOT OF 10^18 CM^-3++++++++++++++++++++++++++++++++
367 % % % % figure(1)
368 % % % % ...
        subplot(211),plot(IncidentPeak,IntegExpvoltage,'or',ExpvoltageX,Expvoltage(:,2),'*b');
369 % % % % ...
        subplot(212),semilogy(IncidentPeak,IntegExpvoltage,'or',ExpvoltageX,Expvoltage(:,2),'*b');
370 % % %
371 % % % %  %+++++++++++++++++++++SCALE FACTOR++++++++++++++++++++++++++++++++++++++++
372 % % % % figure(1)
373 % % % %    integrationE = 1.5e-7*integration_E(:,2);
374 % % % % integrationESMA = 2.5e-9*integration_E(:,2);
375 % % %
376 %    integrationE = integration_E(:,2);
377 % integrationESMA = integration_E(:,2);
378
379
380 %for ne = 1.15x10^18cm^-3
381 %    integrationE = 2.5e-7*integration_E(:,2);
382 % integrationESMA = 3.5e-9*integration_E(:,2);
383
384 %for ne = 1.15x10^18cm^-3
385 %    integrationE = 2e-7*integration_E(:,2);
386 % integrationESMA = 3e-9*integration_E(:,2);
387
388    integrationE = 2e-7*integration_E(:,2);%THE FACTOR 1e-3 IS THE MWP GAP TO ...
           CONVERT IN TO  V
389 integrationESMA = 3e-9*integration_E(:,2);
390
391        IntegE1 = integrationE/max(integrationE);
392
393 %          IncidentPeak = integration_E(:,1);
394 %               IncidJ = integration_J(:,1);
395
396
397 % integrationEt = 1e-3*integration_E(:,2); %integral of Et in V, 1e-3 is the ...
        size of the gap of the microwave probe detector in meter
398
399 figure(12)
400 subplot(211),plot(IncidentPeak,1.03e-5*integration_E(:,2),'*-r', ...
        Au_n18_june04,pkpk_n18_Au_cont,'*-b');
401 title('Au-contacted: DSAscope reading')
402 text(40, 15, 'SF = 1.03x10^{-5}', 'Color', ...
        'k','fontsize',20,'fontweight','normal','linewidth',3);
403 xlabel('Time(ps)','fontsize',16);
404 ylabel('Voltage(V)','fontsize',16);
405 set(gcf,'paperpositionmode','auto','color','white');
406 set(gca,'box','on','fontsize',18,'fontweight','normal','linewidth',2,'layer','top')
407 set(gca,'GridLineStyle','-');
```

```
408

409

410  subplot(212),loglog(IncidentPeak, 1.03e—5*integration_E(:,2),'*—r', ...
            Au_n18_june04,pkpk_n18_Au_cont,'*—b');title('Loglog plot')
411  title('Loglog plot')
412  xlabel('Time(ps)','fontsize',16);
413  ylabel('Voltage(V)','fontsize',16);
414  set(gcf, 'paperpositionmode','auto','color','white');
415  set(gca,'box','on','fontsize',18,'fontweight','normal','linewidth',2,'layer','top')
416  grid on
417  set(gca,'GridLineStyle','—');
418  grid on
419  grid minor
420  hold all
421
422  integrationEem = 1e—3*integration_Eem(:,2); %integral of Et in V, 1e—3 is the ...
            size of the gap of the microwave probe detector in meter
```

## Convolution: $\{(V_{sample}) \otimes (Impulse response)\}$

The convolution of matlab function that convolute the calculated voltage signal at the sample ($V_{sample}$) with the impulse response of the DSA is given in the following matlab fucntion.

```
1   clear all;
2   close all;
3
4   input_voltage_stuffkvector_main()
5
6   load Au_contact_Et0_230_n17.dat;
7   load Au_contact_Et0_230_n17_BETTER.dat;
8
9   load HIGHEST_VOLTAGE.dat;
10  load BARE_InGaAs.dat;
11
12
13  load IntegralE.mat;
14
15  format long
16
17  %%%%%%%%TRANSMITTED FIELD^^^^^^^^^^^^^^^^^^^^^^^^
18  Etransmf = transm_field*1.25E—3;      %IN VOLT; 1.25e—3 is the pitch ...
         separation in m and the transm_field is in V/m
19      t = transm_field(:,1);          %Et25_250_enth163_b0754_tG01ps(:,1);
20  %%%%%%%%RADIATED FIELD^^^^^^^^^^^^^^^^^^^^^^^^^
```

```matlab
21
22  %               tt = radiated_field(:,1); t = tt
23
24
25  load Au_n18_NoCalibF_June04.dat;
26
27          Au_n18_june04 = Au_n18_NoCalibF_June04(:,1);
28      pkpk_n18_Au_cont = Au_n18_NoCalibF_June04(:,2);
29
30          dt = t(2,1)—t(1,1);   % dt = 0.018039973231511 ps
31  [ii jjj] = size(Etransmf); % 20000 52
32
33          t1 = 0;
34
35  %       j0 = 1.108649095169654e+004; %dt*J0 = 200ps time window%
36
37          j0 = 5.543245475848269e+004;        %dt*J0 = 1000ps time window%
38          j01= 2.771622737924133e+004;        %dt*J0 = 500ps time window%
39      for ii = 1:(j0)
40      t1(ii) = dt*(ii—1); %t(ps)
41      end
42      [nt,npeak] = size(t1');
43            nx = pow2(nextpow2(nt)); %2^16
44
45            t2 = 0;
46      for jj = 1:(nx)
47      t2(jj) = dt*(jj—1); %t(ps)
48      end
49
50            peaktopeak = zeros(51,1);
51
52
53    ConvEt = [];
54      pkpk = [];
55
56  for j = 2:jjj % since Etransmf first and second coluns are time, and zero coluns
57  % for j = 5:5
58      Etr = Etransmf(:,j);   % IN V
59  % %     d = 0.154;            % DIAMETER OF THZ SPOT IN CM
60  %       d = 1e—3;             % GAP OF MICROWAVE PROBE OR SEPARATION OF GOLD ...
        TRANSMISSION LINE in meter
61  %      Et = Etr*d;           % TRANSMITTED FIELD IN V, the factor 1000 is to ...
        convert form kV to V
62
63
64    %PADDING ZEROS
65
```

227

```matlab
66  % Etpaded = padarray(Et,32268,'both' );%size of nx is 16384, (65536—1000)/2 = ...
        32268
67
68  % % % %  Etpadpre = padarray(Etr,20000,'pre' );         % size of nx is 16384, ...
        (16384—1000)/2 = 7692
69  % % % %  Etpaded = padarray(Etpadpre, 44536,'post' );  % size of nx is 16384, ...
        (16384—1000) = 15384
70
71    Etpadpre = padarray(Etr,32763,'pre' );          % size of nx is 16384, ...
          (16384—1000)/2 = 7692
72    Etpaded = padarray(Etpadpre, 32763,'post' );    % size of nx is 16384, ...
          (16384—1000) = 15384
73
74  % Etpadpre = padarray(Etr,20000,'pre' );          % size of nx is 16384, ...
        (16384—1000)/2 = 7692
75  %  Etpaded = padarray(Etpadpre, 25536,'post' ); % size of nx is 16384, ...
        (16384—1000) = 15384
76
77    % Transmitted field in  V
78        Vin = Etpaded;              % Transmitted field in  V
79
80  %%%&&&&&&&&&&&&&&&&&&&&&&&&&&&&&&&&&&&&&&&&&&&&&&&&&&&%%
81    %%FOR Au—contacted INGAAS sample VOLTAGE READING
82      MU = 200;
83    FWHM = 34; %FWHM of measured voltage signals for Au—contact is 30ps
84  %%%%%%%%%%^^^^^^^^^^^^^^^^^^^^^^^^^^^^^^^^^^^^^^^^%%%%%%%%%%%%%%%%%%%%%%%%%%%%
85      A = (2/FWHM)*(sqrt((log(2))/pi));
86      C = (—4*log(2))/(FWHM)^2;
87      y = dt*A*exp(C*((t2—MU).^2)); %THE FACTOR 100 COMES FROM THE RESOLUTION dtt
88      G = y';
89    MaxG = max(G)/2;
90
91        ConvTEt = conv(G,Vin); % SIZE Vin is 65536x1
92    ConvTEt_65536 = ConvTEt(1:65536,1);
93
94
95
96  %   if (j==2)
97  %           maxi = find(ConvTEt==max(ConvTEt));
98  %           mini = find(ConvTEt==min(ConvTEt));
99  %
100 %     MaxConvTEt = 0;
101 %     MinConvTEt = 0;
102 %
103 %   else
104 %           maxi = find(ConvTEt==max(ConvTEt));
105 %           mini = find(ConvTEt==min(ConvTEt));
106 %
```

```matlab
107 %       MaxConvTEt = ConvTEt(maxi);
108 %       MinConvTEt = ConvTEt(mini);
109 %
110 %     end
111 %   peaktopeak(j-1) = MaxConvTEt +abs(MinConvTEt);
112   if (j==2)
113             maxi = find(ConvTEt_65536==max(ConvTEt_65536));
114             mini = find(ConvTEt_65536==min(ConvTEt_65536));
115
116       MaxConvTEt = 0;
117       MinConvTEt = 0;
118
119   else
120             maxi = find(ConvTEt_65536==max(ConvTEt_65536));
121             mini = find(ConvTEt_65536==min(ConvTEt_65536));
122
123 %       MaxConvTEt = ConvTEt(maxi);
124 %       MinConvTEt = ConvTEt(mini);
125       MaxConvTEt = ConvTEt_65536(maxi);
126       MinConvTEt = ConvTEt_65536(mini);
127     end
128   peaktopeak(j-1) = MaxConvTEt + abs(MinConvTEt);
129   % peaktopeak(j-1) = MaxConvTEt + (MinConvTEt);
130 %             maxi = find(ConvTEt_65536==max(ConvTEt_65536));
131 %             mini = find(ConvTEt_65536==min(ConvTEt_65536));
132 %
133       %  MaxConvTEt = ConvTEt_65536(maxi);
134       %  MinConvTEt = ConvTEt_65536(mini);
135
136   % peaktopeak(j-1) = MaxConvTEt -(MinConvTEt);
137
138             ConvEt = [ConvEt ConvTEt_65536];
139 %           ConvEt = [ConvEt ConvTEt];
140
141     conv_Et = ConvTEt(1:65536); % size of t2
142
143   %   save convolution.mat t2 ConvTEt conv_Et;
144
145       tConv = t2(24946:38804)-t2(24946);
146      ConvTE = ConvTEt(24946:38804);
147
148    Exp_data = HIGHEST_VOLTAGE;
149   Exp_data2 = BARE_InGaAs;
150
151  figure(1)
152  % ...
       plot(t2(16631:49904)-415.5,ConvTEt(16631:49904)*0.35,'b',Exp_data(:,1),Exp_data(:,2),'r','linewidth',
153  plot(t2(35839:63485)-646.51656067091,ConvTEt(35839:63485)*0.35,'b',Exp_data(:,1),Exp_data(:,2),'r','linew
```

```matlab
154  xlim([0 500])
155  xlabel('Time(ps)','fontsize',16);
156  ylabel('Voltage(V)','fontsize',16);
157  set(gcf,'paperpositionmode','auto','color','white');
158  set(gca,'box','on','fontsize',18,'fontweight','normal','linewidth',2,'layer','top')
159  set(gca,'GridLineStyle','−');
160  hold on
161  %        time = t2(13637:41577)−t2(13637);
162
163  ConvTEt_t2 = ConvTEt(1:65536);% same size with t2
164
165  %%%%%%%%%%^^^^^^^^^^^^^^^^^^^^^^^^^^^^^^^^^^^^^^%%%%%%%%%%%%%%%%%%%%%%%%%%%%
166  %%%%%%%%%%^^^^^^^^^^^^^^^^^^^^^^^^^^^^^^^^^^^^^^%%%%%%%%%%%%%%%%%%%%%%%%%%%%
167  %%FOR HIGHEST VOLTAGE FITTING
168
169  %%EXPERIMENTAL DATA
170      t_shift = 415.5;
171        t_exp = Exp_data(:,1);
172  Exp_result = Exp_data(:,2);
173
174  %%SIMULATED DATA
175            t_sim = t2(22174:49891)−t_shift;
176      ConvTEt_final = ConvTEt(22174:49891)*0.43; %0.43 is the scaling factor
177
178  % save fitting.mat t_sim ConvTEt_final t_exp Exp_result
179
180  %%%%%%%%%%^^^^^^^^^^^^^^^^^^^^^^^^^^^^^^^^^^^^^^%%%%%%%%%%%%%%%%%%%%%%%%%%%%
181      t_shift2 = 383.5;
182        t_exp2 = Exp_data2(:,1);
183  Exp_result2 = Exp_data2(:,2);
184
185  %%SIMULATED DATA
186
187              t_sim2 = t2(22174:49891)−t_shift2;
188        ConvTEt_final2 = ConvTEt(22174:49891)*0.025; %0.025 is the scaling factor
189
190  % save fitting2.mat t_sim2 ConvTEt_final2 t_exp2 Exp_result2
191
192  %%%%%%%%%%^^^^^^^^^^^^^^^^^^^^^^^^^^^^^^^^^^^^^^%%%%%%%%%%%%%%%%%%%%%%%%%%%%
193  %  save pkpkpk.mat peaktopeak
194  end
195
196  IncidentPeak = 0:5:250;
197
198  save transferf.mat t t2 Etr Vin ConvTEt G ConvEt IncidentPeak peaktopeak ...
          ConvTEt_t2...
199          MaxConvTEt MinConvTEt
200
```

```matlab
201  figure(3)
202  % subplot(211),plot(IncidentPeak,0.35*(peaktopeak-peaktopeak(6,1)),'*-r', ...
          Au_n18_june04,pkpk_n18_Au_cont,'*-b');
203  subplot(211),plot(IncidentPeak,0.35*(peaktopeak),'*-r', ...
          Au_n18_june04,pkpk_n18_Au_cont,'*-b');
204
205  title('Au-contacted: DSAscope reading')
206  text(40, 15, 'SF = 0.35', 'Color', ...
          'k','fontsize',20,'fontweight','normal','linewidth',3);
207  xlabel('Time(ps)','fontsize',16);
208  ylabel('Voltage(V)','fontsize',16);
209  set(gcf,'paperpositionmode','auto','color','white');
210  set(gca,'box','on','fontsize',18,'fontweight','normal','linewidth',2,'layer','top')
211  set(gca,'GridLineStyle','-');
212
213  subplot(212),loglog(IncidentPeak,0.35*peaktopeak,'*-r', ...
          Au_n18_june04,pkpk_n18_Au_cont,'*-b');title('Loglog plot')
214  title('Loglog plot')
215  xlabel('Time(ps)','fontsize',16);
216  ylabel('Voltage(V)','fontsize',16);
217  set(gcf, 'paperpositionmode','auto','color','white');
218  set(gca,'box','on','fontsize',18,'fontweight','normal','linewidth',2,'layer','top')
219  grid on
220  set(gca,'GridLineStyle','-');
221  grid on
222  grid minor
223  hold all
```

# APPENDIX G

## Free carrier density calculation in photoexcited GaAs

The pump pulse is 800 nm and the optical spot size is about 6 mm in diameter. Therefore the area of the optical spot becomes $\pi r^2 = 28.274 \times 10^{-2}\ mm^2$. The optical pump power of 800 nm pulse varies from 9 mW to 0.05 mW, the equivalent optical pump energy ranges from 9 $\mu$J to 0.05 $\mu$J, and the THz pulse duration is 1 kHz.

The fluence will be calculated as:

$$Fluence = \frac{E_{pump}}{A} \tag{G.1}$$

Hence, at 9.0 and 0.05 $\mu$J, the fluence becomes 32 $\mu J/cm^2$ and 0.177 $\mu J/cm^2$, respectively. The index of refraction of GaAs at 800 nm is 3.6 ($n_{GaAs} = 3.6$), therefore, the total reflection of 800 nm at the surface of the GaAs sample is given by: $R = |\frac{1-n}{1+n}|^2 = 0.319$, then number of photons absorbed by GaAs at 9 $\mu J$ pump energy is:

$$N_{photon} = \frac{fluence * (1-R)}{1.55eV} = \frac{31.8\mu J/cm^2 \times 0.681}{1.55 \times 1.602 * 10^{-13}\mu J} = 8.72 \times 10^{13} cm^{-2} \tag{G.2}$$

For 0.05 $\mu J$,

$$N_{photon} = \frac{fluence * (1-R)}{1.55eV} = \frac{0.177\mu J/cm^2 \times 0.681}{1.55 \times 1.602 \times 10^{-13} cm^{-3}\mu J} = 4.8 \times 10^{11} cm^{-2} \tag{G.3}$$

It is assumed that one optical photon create one pair of free carrier (electron-hole) and the free carrier penetration depth for 800 nm is about d = 900 nm Su et al. (2009). The free carrier density, n$_e$, becomes:

$$n_e = \frac{N_{photon}}{d} = \frac{8.72 \times 10^{13} cm^{-2}}{9 \times 10^{-5} cm} = 9.68 \times 10^{17} cm^{-3} \tag{G.4}$$
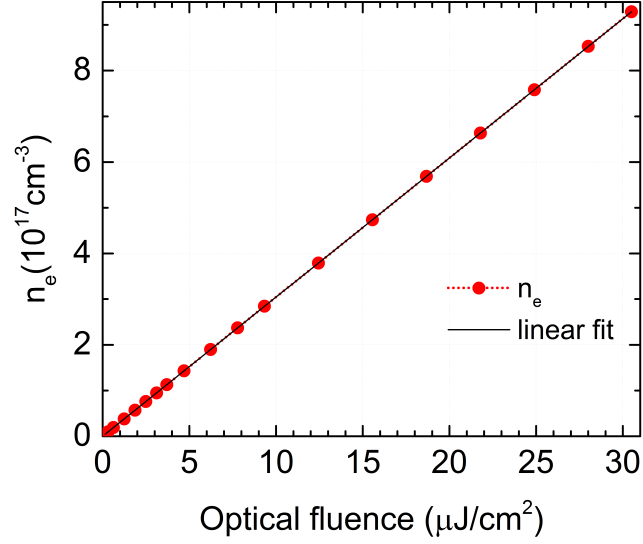
Figure G.1: Optical fluence dependent carrier density generated in the photoexcited GaAs sample

for 9 $\mu J$ pump and $5.33\times10^{15} cm^{-3}$.

Also, carrier density can be easily evaluated from Drude fit result, $\sigma_{dc} = 12000\ \Omega.m, \tau = 0.2$ ps. Thus, free carrier density becomes

$$n = \frac{m^*(\sigma_{dc})^{-3}}{e^2\tau} \tag{G.5}$$

Equation G.5 results $1.427\times10^{17} cm^{-3}$. The linear dependence of carrier density generated in a photoexcited GaAs sample as a function of optical fluence is given in Fig. G.1.